SENSING THE DYNAMICS OF SEVERE WEATHER USING 4D GPS TOMOGRAPHY IN THE AUSTRALIAN REGION

A thesis submitted in fulfilment of the requirements for the degree of Doctor of Philosophy

Toby Manning
B App Sci (Surveying) Honours Class 1

School of Mathematical and Geospatial Sciences
College of Science, Engineering and Health
Royal Melbourne Institute of Technology (RMIT) University
Melbourne, Australia
December, 2013

Declaration

I certify that except where due acknowledgement has been made, the work is that of the author alone; the work has not been submitted previously, in whole or in part, to qualify for any other academic award; the content of the thesis is the result of work which has been carried out since the official commencement date of the approved research program; any editorial work, paid or unpaid, carried out by a third party is acknowledged; and, ethics procedures and guidelines have been followed.

Toby Manning

December, 2013

Acknowledgements

I would like to express my appreciation and respect to my supervisors: Prof. Kefei Zhang and Dr. David Silcock for all their significant contributions to my PhD research. Especially to Prof. Kefei Zhang for his invaluable supervision and support throughout the duration of my candidature. Many thanks to Dr. David Silcock for his ongoing mentoring and editing of my thesis. A very special thanks to Dr. Witold Rohm for his technical guidance and collaboration in multiple research projects. Also, I would like to thank Dr. Suqin Wu for her editing and advice on the final stages of my thesis.

I would also like to thank my colleges at SPACE Research Centre. Special thanks to Dr. Robert Norman, Dr Carl Wang and Dr Erjiang Fu for their technical guidance during my candidature. I would also like to thank Dr Shaocheng Zhang, Ms Ying Li, Dr Brett Carter, Mr Lucas Holden, Mr Rodney Deakin, Mrs Sarah van Rooyen, Mr Brain Bai and Mr Yunbin Yuan for their ongoing team support. Also, thanks to Prof. John Le Marshall from the Australian Bureau of Meteorology for his support and research collaboration.

I would also like to thank the institutions and researchers that have given me access to their data and software systems, which are critical to this research. Many thanks to Prof. Alain Geiger, Dr. Donat Perler and Mr. Fabian Hurter from the Geodesy and Geodynamics Lab, ETH Zurich, Switzerland for providing the AWATOS 2 software package and for their ongoing technical support. I would also like to acknowledge Mr. Fabian Hurter for his support in relation to the AWATOS 2 software and for collaboration in multiple research projects. Thank you to the Australian Bureau of Meteorology for providing the NWP analysis, radiosonde and cumulative rainfall data. Also, the Department of Environment and Primary Industries for providing the raw GPSnet data.

I would also like to express many thanks to my family Trevor Manning, Paula Mobach, Jack Manning and Nicholas Manning for their personal support. And many thanks to my special friends Eamon, Eugene, Cameron, Hayley, Becky, Chris, Scott, Greg, Xenon, Ashley, Meagan, Brendan, Gearoid, Matthew and Jeremy.

Abstract

The Earth's climate and weather is a highly dynamic and complex system. Monitoring and predicting meteorological conditions with a high accuracy and reliability is, therefore, a challenging task. Furthermore, climate change and the enhanced greenhouse effects have become a major challenge for the sustainable development of the Earth and environment. The by-product of such effects includes increasing weather extremes in time and space. Therefore, intensive global research is of paramount importance to enhance the measurements and understanding of atmospheric processes and its projected implications. The dynamics of water vapour (WV) have a strong influence on weather and climate due to the large energy transfers in the hydrological processes. This particularly correlates to WV dynamics during the formation and lifecycle of severe mesoscale convective storm and precipitation systems. Contrary to its importance, WV remains poorly understood and inadequately measured both spatially and temporally, especially in Australia and the southern hemisphere where meteorological data are sparse. Ground-based and space-borne GPS (global positioning system) meteorology are currently regarded as leading atmospheric remote sensing instruments for numerical weather prediction (NWP) and climatology due to their high spatio-temporal resolutions, multiple observing platforms and continuous operability. It is therefore vital for Australia to develop innovative GPS meteorology platforms for the assimilation of GPS measurements into NWP models to ultimately attain a more robust solution in view of safety, and social and economic benefits.

The GPS signals are delayed and bent due to the refractive index of the ionosphere and troposphere. This tropospheric path delay can be separated into dry and wet integral components, with the latter proportional, using a scale factor, to the integrated precipitable water vapour (PWV) in the vertical column above the GPS stations. These wet delay measurements can also be combined using a network of GPS stations to resolve the spatial distribution of WV. This method is called GPS tomography, which is a promising and developing method of reconstructing dynamically changing four dimensional (4D) wet refractivity fields. This takes advantage of the high density and homogeneity of ground-based GPS Continuously Operating Reference Station (CORS) networks to provide accurately resolved WV profiles in space and time.

Ground-based GPS tomography has the potential to utilise the dense ground-based infrastructure in Australia providing continuous wet refractivity field solutions. This research develops ground-based GPS meteorology and introduces a Kalman filter based 4D GPS tomographic model to the Victorian region with a view of improving weather forecasting and early detection and prediction of severe weather. The GPS tomographic software AWATOS 2 (Perler, 2011) is customised for the Victorian GPS infrastructure – GPSnet. This software implements a trilinear parameterisation method in the Kalman filter processing strategy.

GPS tomographic simulations are analysed using multiple synthetic wet refractivity fields to statistically optimise the tomographic model and parameter settings for the GPSnet. The optimal voxel grid discretisation for the GPSnet is investigated and found to be 0.5° horizontal resolution and 15 exponentially increasing height layers. This configuration presented the fastest solution convergence and error stabilisation based on the evolution of the solution RMS error. Furthermore, additional synoptic network and profile observation methods are introduced into the simulated observation model to assess the influence of additional observations and relevant observation

geometries on the wet refractivity solution. The speed of the solution convergence is improved by a factor of 3.3 and 4.3 when including the synoptic network and profile observations, respectively.

Investigations into GPS-derived PWV estimates confirmed both a high accuracy and a high time resolution plus a sensitivity to the precursors of severe weather via mapping the integrated amount of WV in the vertical column above ground-based GPS stations. Sharp, excessive increases in PWV indicated the formation of humid convective processes several hours prior to intense precipitation with sharp decreases in PWV directly after. This trend phenomena between PWV and cumulative rainfall is evident in two case studies conducted during the March 2010 and January 2011 severe weather events in Victoria. GPS-derived PWV estimates are validated against radiosonde observations with RMS errors of 2.00 mm and 1.68 mm, respectively. This research concludes that PWV is highly sensitive to the precursors during the formation of severe weather and has the potential to increase the accuracy of NWP analysis and forecasts. However, the monitoring of mesoscale convective processes in severe weather remains relatively ambiguous when using PWV estimates. Therefore, 4D methods of reconstructing wet refractivity fields using GPS tomography are investigated for the Australian region.

A distinct trend between the 4D reconstructed wet refractivity fields using GPS tomography and the formation and lifecycle of severe storm and precipitation systems was found. Sharp gradients are evident up the vertical layers providing the wet refractivity trend of convection, with high gradient falls through the vertical layers after the storm system passed. Radiosonde is used as a reference to validate the GPS tomographic model with final accuracies of the March 2010 and January 2011 case studies presenting 8.58 and 9.36 ppm RMS errors, respectively. A wet refractivity index adopted for the GPS tomographic wet refractivity profiles showed an excessive increase above the planetary boundary layer as a response to the formation of a supercell thunderstorm. Finally, horizontal and vertical 2D cross sections, investigating the evolution of the March 2010 severe weather event concludes a high correlation between the highly dynamic spatial and temporal changes of wet refractivity, modelled using 4D GPS tomography with precipitation intensities measured using weather radars images. These gradient solutions from GPS tomography are able to identify the spatial and temporal structure of the mesoscale convective and stratiform processes during severe weather.

Final investigations analyse the influence of additional observational methods introduced into the observation model of the GPS tomographic processing. This analysis is conducted during the formation and lifecycle of severe weather of the January 2011 case study. A statistical analysis compares additional observational methods including: radiosonde, synoptic weather station networks and GPS radio occultation and then the influence of all observation methods combined. The results are compared against radiosonde-derived wet refractivity estimates as the reference data to conclude RMS errors of 9.36, 8.03, 8.14, 8.56 and 7.57 ppm, respectively. These results have shown that the introduction of accurate additional information into the tomographic solution lead to a significant increase in accuracy and more robust results than the original method containing no additional data. These improvements are in the order of 14.29%, 13.09%, 8.57% and 19.15%, respectively.

The major objectives of this research are satisfied by developing ground-based GPS meteorological platforms in the Australian region including the introduction of 4D tomographic reconstruction methods to the GPSnet. These developments are in view of assimilation methods for nowcasting and NWP to provide a more robust platform for early detection and prediction of severe weather and precipitation extremes.

Table of contents

Chapter 1. Introduction

1.1. GPS meteorology

The dynamics of water vapour (WV) has a strong influence on the climate, weather processes and formation and lifecycle of severe storm systems. This is due to large energy transfers in the hydrological processes. Contrary to its importance, WV remains poorly understood and inadequately measured both spatially and temporally, especially in the southern hemisphere where meteorological data are sparse. WV also accounts for 60% of the natural greenhouse effects and therefore provides a valuable parameter for modelling the enhanced greenhouse effects of climate change (Mockler, 1995; Schneider et al., 1999; Genio and Hanson, 2001; Soden et al., 2002; Solomon et al., 2007; Isaac and Van Wijngaarden, 2012). Therefore, improved spatial and temporal monitoring and understanding of WV will lead to higher accuracy and more robust observation methods for forecasting, early prediction of severe weather anomalies, precipitation prediction, climatology and improved monitoring and prediction of the enhanced greenhouse effects on climate change (Lambeck, 2010).

The global positioning system (GPS) has been extensively used as a robust tool for measuring the integrated amount of WV in the atmosphere with high accuracy and under all weather conditions. It is currently regarded as one of the most important atmospheric remote sensing instruments for weather forecasting and climatology due to the rapid development and deployment of GPS continuously operating reference station (CORS) networks, the development of space-borne GPS technologies, and the continuous operability (Bevis et al., 1992; Rocken et al., 1995; Tregoning et al., 1998; Gradinarsky et al., 2002; Le Marshall et al., 2010; Zhang et al., 2011). Furthermore, unlike conventional methods of meteorological observations, existing ground-based GPS permanent stations are able to estimate tropospheric WV continuously at almost no further costs.

GPS meteorology can be divided into two observation methods:

- *Ground-based GPS CORS networks* are currently used to produce two different data products. Firstly, the integrated quantity of precipitable water vapour (PWV) in the zenith direction above each GPS station can be accurately estimated using path delay measurements of the GPS observations between a satellite and a receiver (Bevis et al., 1992; Rocken et al., 1995; Tregoning et al., 1998; Gradinarsky et al., 2002). Secondly, the 4 dimensional (4D) spatial and temporal distribution of wet refractivity is able to be reconstructed using accurate measurements of path delays between each satellite-and-receiver link over the GPS network.

This method is called GPS tomography and takes advantage of the multiple integrated measurements passing through a finite 3D grid field to reconstruct a time evolving model of wet refractivity (Seko et al., 2000; Flores et al., 2000; Troller et al., 2002; Bender and Raabe, 2007; Lutz 2008; Perler et al., 2011).

- *Space-borne RO* is an observation method that takes advantage of GPS receivers' on-board low Earth orbiting (LEO) satellites that rise or set in view of GPS satellites. As the GPS signal propagates through the various layers of the atmosphere, it is retarded and bent due to the index of refraction. The geometry of the LEO satellite rising or setting behind the Earth's atmospheric limb creates a profile of raw observations, which can be transformed into refractivity profiles relating to meteorological parameters in the neutral atmosphere (Anthes et al., 2008; Fu et al., 2009; Zhang et al., 2011; Le Marshall et al., 2012).

Due to the sparse nature of ground-based atmospheric observation systems in the southern hemisphere, the development of alternate methods for observing the spatial and temporal structure of the atmosphere is of high priority (Fu et al., 2009; Le Marshall et al., 2010; Choy et al., 2011). Currently, the Satellite Positioning for Atmosphere Climate and Environment (SPACE) Research Centre at RMIT University and Australian Bureau of Meteorology has a longstanding joint collaboration which has provided the research platform for the implementation of space-borne GPS meteorological information into the current numerical weather prediction (NWP) models in an operational capacity (Le Marshall et al., 2010; Zhang at al., 2011).

Kalman filtering based GPS tomography is a promising method of reconstructing dynamically changing 4D wet refractivity fields. This method takes advantage of the high density and homogeneity of the ground-based GPS Continuously Operating Reference Station (CORS) networks. Ground-based GPS tomography has the potential to utilise the dense ground-based infrastructure in Australia providing wet refractivity field solutions at a high spatial and temporal resolution. The premise of this research is to introduce and optimise parameters for a robust model algorithm of GPS tomography by utilising the Victorian ground-based GPS infrastructure for the reconstruction of wet refractivity and in the context of severe weather.

A National Positioning Infrastructure (NPI) project is currently in development, which will potentially provide 2 cm positional accuracy anywhere in the Australian region in real-time. This accuracy is assisted by the current constellation of GPS (USA) and the new systems for next generation GNSS including Galileo (EU), GLONASS (Russia), Compass (China), QZSS (Japan) and IRNSS (India). The development of this infrastructure will provide a world-class benchmark for innovation and will potentially enhance the capability of this research in GPS meteorology for national applications in the future.

1.2. Australian climate and weather

The Earth's climate and weather system is a highly dynamic and complex environment. Monitoring and predicting meteorological conditions with a high accuracy and reliability is, therefore, a challenging task. WV has a strong influence on the Earth's weather and climate systems due to the large energy transfers in the hydrological process. However, it remains poorly understood and inadequately (spatially and temporally) measured, especially in the southern hemisphere where ground-based data are very sparse and only limited meteorological information is available.

WV is the most important greenhouse gas in the climate system of the Earth. It also plays a major role in weather processes due to the large energy transfers related to water evaporation and vapour condensation (Bai, 2004). This cycle of water termed the hydrologic cycle, describes the continuous movement of water on, under or above the Earth's surface. The physical characteristics of WV in the atmosphere are highly variant. WV has a major influence on meteorological processes, particularly having a significant impact on the mesoscale systems such as convective storms and the development of weather fronts.

The spatial and temporal distribution of WV also has a strong influence on the dynamics of clouds and rainfalls. Due to the large energy transfers associated with the phase change process of water, the distribution of WV plays a critical role in the vertical stability of the atmosphere and in the structure and evolution of atmospheric storm systems. The transport mechanism of WV and its latent heat by the general circulation of the atmosphere is an important component of the Earth's meridional energy balance. In addition, water plays a critical role in many chemical reactions that occur in the atmosphere (Bevis et al., 1992).

The Australian continent is a unique environment as it covers a vast geographical surface area and encompasses a large range of climatic regions and conditions. The range of latitude for the Australian region inevitably means that the country holds both dry and tropical areas, including areas prone to drought, excessive rain, cyclones, bushfires, etc. These environmental and natural hazards affect all aspects of life. A large proportion of the population lives in coastal regions because nearly all major cities are situated on the coastline. Therefore, customised methodologies and algorithms must be developed to fit the unique parameters of Australia (and the southern hemisphere), to improve both measurement methods and improve our understanding of the dynamics of WV in the troposphere.

At present, the observation of WV over the Australian continent and surrounding oceans is very limited. Only a few radiosonde stations exist throughout the extent of the country and low accuracy vertical sounding from orbiting satellites are available (Fu et al., 2009; Zhang et al., 2011; Choy et al., 2011). The outlook of this research is in the development of GPS meteorological platforms to improve

our current understanding of WV dynamics in view of forecasting and severe weather prediction in the Australian region.

1.2.1. Severe weather in Australia

Severe weather in the Australian continent can encompass many atmospheric weather extremes, ranging from isolated thunderstorms to intense, large low pressure systems affecting thousands of square kilometres. In turn, these low pressure systems have the potential to cause widespread flash flooding and gale force winds.

Severe weather processes include thunderstorms of various strength and cell structure, intense low pressure systems, lightening, hail, storm wind gusts and occasionally tornados. Crompton and McAneney (2008) estimated that severe weather events cost $820 million (2006) per annum in Australia. In terms of insured costs, severe storms were responsible for more damage than tropical cyclones, earthquakes, floods or bushfires. This was half the average annual cost of natural disasters in Australia.

The formation of severe storms are caused by a large scale, low pressure system triggering atmospheric instability due to high pressure gradients. Intense low-pressure systems and their associated cold fronts can generate strong winds and heavy rain over large areas. Thunderstorms form in unstable atmospheric environments when warm, moist air rises due to unstable air mass. The warmer the air-mass (less dense), the greater the acting upward-directed buoyant force, and in turn the stronger the convection. The forcing mechanisms needed to start air moving upward may be: unequal heating at the surface; the effect of terrain, or the lifting of air along shallow boundaries of converging surface winds; diverging upper-level winds, coupled with converging surface winds and rising air; and warm air rising along a frontal zone. Usually, a combination of several mechanisms is needed together with vertical wind shear to generate severe thunderstorms (Ahrens and Samson, 2010).There are three recognised types of thunderstorms (Geoscience Australia, 2011):

- *Singlecell thunderstorms,* which are of limited size and lifespan and can produce short bursts of severe weather;
- *Multicell thunderstorms,* which are more persistent and have a greater impact; and,
- *Supercell thunderstorms,* which are even more persistent with a constant rotating updraft known as a mesocyclone.

Supercell thunderstorms are uniquely characterised during the mature stage by the ratio of cold air downdraft being undercut by moist air updraft. This causes horizontal spin of a singular violent updraft, which develops a supercell. These storms have the ability to suspend hailstones of considerable size, produce high speed winds and heavy precipitation threatening significant damage

and flash flooding. These mesoscale convective storm systems contain regions of both convective and stratiform precipitation. The convective region consists of intense, vertically extending cores, while the stratiform region hold a more stabilised lighter precipitation (Houze, 2004), as shown in Figure 1.1.

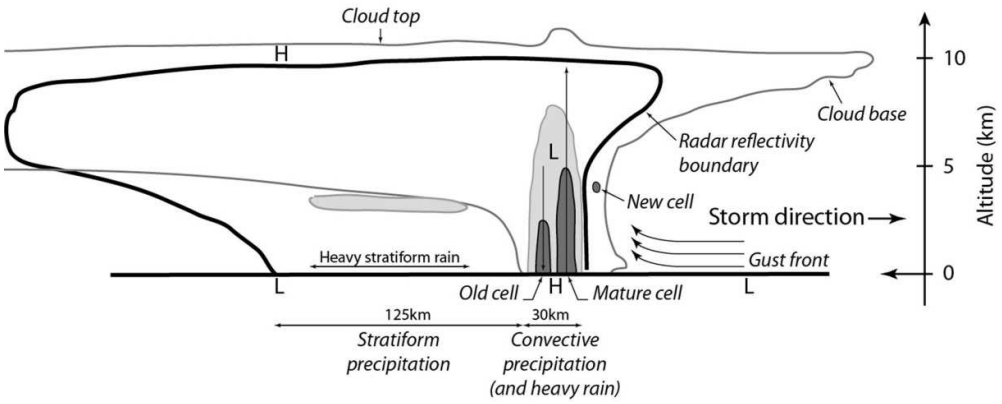

Figure 1.1 2D profile of a severe convective supercell thunderstorm. Radar reflectivity boundary presented as thick black line, and the horizontal scale of convective and stratiform precipitation regions identified (based on Houze, 2004).

After the heavy precipitation, the storm becomes dominated by downdraft. This process cuts off the inflow and updraft and the storm begins to dissipate (Ahrens and Samson, 2010). The fundamental elements of the storm structure require a much finer resolution where the mature cell and convective region can cover less than 30 km. The stratiform on the other hand is much larger with a spatial coverage of approximately 125 km (Houze, 2004).

Lightening comes as a residual of nearly all thunderstorms and has the potential to start bush fires, which can be detrimental to the communities in dry parts of Australia. An example is the Victorian Black Saturday bushfires of 2009. Hail and strong winds can both be considered as other residual effects of severe thunderstorms with possible consequential dangers to civilians, immense commercial and residential damage, and vast traffic and transport delays. An example of severe hail, severe winds and flash flooding is the March 2010 supercell thunderstorm, which passed over greater Melbourne (Choy et al 2011; Manning et al. 2012).

1.3. The hydrological process and greenhouse effect

The Earth's climate is able to support life primarily due to the atmospheric greenhouse effects and the workings of the hydrological cycle, in which water in the gaseous phase i.e. WV is a key element (Mockler, 1995; Lambeck, 2010). The hydrological cycle defines the movement of water, in all three phases, below, on and above the surface of the Earth, encompassing the oceans, continents and

atmosphere (Trenberth, 1999). The three physical states of water (H_2O) are liquid, vapour and ice. These physical transformations can occur at various stages in the hydrological cycle. Water vapour is the state of water in the gaseous phase. It has a high temporal variation in the atmosphere and transfers large amounts of thermal energy due to the process of evaporation and recondensation.

WV is constantly cycling through the atmosphere, evaporating from the surface, condensing to form clouds transported horizontally by the winds, and subsequently returning to the Earth as precipitation. Heat from the Sun evaporates water, and this heat is transferred into the air when the water condenses into clouds and precipitates. This evaporation-condensation cycle is an important mechanism for transferring heat energy from the Earth's surface to its atmosphere and in moving heat around the Earth.

There are many atmospheric greenhouse gases, some naturally occurring and some resulting from industrial activities. WV is involved in an important climate feedback loop. As the temperature of the Earth's surface and atmosphere increases, the atmosphere is able to hold more WV. The additional WV, acting as a greenhouse gas, absorbs energy that would otherwise escape to space and so causes further warming. This basic picture is complicated by important interactions between WV, clouds, atmospheric motion, and radiation from both the Sun and the Earth. There are some aspects of the role of WV as a greenhouse gas that are not well understood. This is due to a lack of sufficient quality observations of WV content in space and time. Through the implementation of high accuracy long-term WV monitoring, climate variations and trends will be detected and predicted with much higher confidence (Mockler, 1995; Lambeck, 2010).

There have been multiple scientific technologies developed to measure the vertical and horizontal distribution of WV. The radiosonde is a balloon-borne instrument that detects temperature, humidity and pressure at increasing altitudes and transfers the data via radio signals to the ground. There are some advantages to this instrument including good accuracy and high vertical resolution, however, the pivotal disadvantage to this technology is the high cost of these devices restricting the number of launches to twice daily (typically 00:00 and 12:00 UTC) at a limited number of stations. Thus, radiosonde measurements result in low temporal and spatial resolution variability of WV.

1.4. Developments of GPS meteorology

1.4.1. Developments of WV monitoring

WV is a key quantity in the modelling and prediction of atmospheric and weather dynamics due to mechanisms of the hydrological energy transfers. Therefore accurate, high density and

homogeneously distributed observations of WV are integral for the initialisation, forward prediction and validation of atmospheric modelling.

GNSS is a promising observation platform, which can deliver operational ground-based and space-borne observation geometries for estimating WV density with a high temporal and spatial resolution. It has been proven that GPS observations contain information on the integrated amount of PWV in the total GPS signal path delay, which is estimated by stochastic filtering of raw GPS observations during post processing (Bevis et al., 1992; Rocken et al., 1995; Tregoning et al., 1998; Gradinarsky et al., 2002; Wolfe and Gutman, 2002). GPS-derived PWV are currently regarded as one of the most important data types for the improvement of precipitation modelling and mesoscale NWP (Houze, 2004; Ishikawa, 2012). Leading meteorological institutes are successfully assimilating GPS zenith total delays (ZTD) or integrated PWV data into NWP models with a quantifiably enhanced result. These institutes include:

1. *The National Center for Atmospheric Research and the NOAA Forecast Systems Laboratory*, Boulder, USA (Gutman et al., 2004; Smith et al., 2007);
2. *The UK Meteorological Office* (Bennitt and Jupp., 2012);
3. *German Weather Service (DWD)* (Kopken, 2001);
4. *GFZ, Potsdam, in collaboration with the DWD* (Gendt et al., 2001; Grzeschik et al., 2006); and,
5. *Japan Meteorological Agency* (Nakamura and Shimpo, 2004; Seko et al., 2004; Seko et al., 2010; Ishikawa, 2012)

The Australian Bureau of Meteorology has assimilated space-borne GPS RO profiles from the Constellation Observing System for Meteorology, Ionosphere and Climate (COSMIC) low earth orbiting (LEO) constellation into the operational Australian Community Climate and Earth-System Simulator (ACCESS) NWP model (Le Marshall et al., 2010; Norman et al., 2013a; Zhang et al., 2013). Currently no ground-based GPS-derived PWV are assimilated into the operational ACCESS model.

Research initiatives by Australian academic communities into the concept, development, potential benefits and operational use of GPS for meteorology and climatology have rapidly grown. These are primarily supported by the Australian Space Research Project (ASRP) and by the Australian Research Council (ARC) grants both funded by the Australian Federal Government. This research project is funded by the ARC linkage grant (LP0883288) awarded to the SPACE Research Centre at RMIT University and the Australian Bureau of Meteorology. The collaborative research proposed for this platform contributes to the enhancement of capabilities for GNSS technologies in the meteorological

domain. Prior to this collaboration, limited academic research was undertaken for the Australian region. Recent achievements of GPS meteorological research in Australia include:

- Investigations into radio wave propagation and the resultant effects due to refractive index was presented by Rueger (2002). These investigations presented a new benchmark in accuracy for radio wave refractive index formulae, identifying limitations in the widely used Thayer's formula of 1974. Three-term formulae were presented for estimating both dry and wet refractivity. Two coefficient methods were also developed: one based on 'best available' coefficients and the other based on 'best average' coefficients.
- Bai (2004) introduced a near-real-time feasibility study using the Australian regional GPS network (ARGN) along with additional interpolated observations from the automatic weather station network that were standardised against radiosonde observations. This research demonstrated the feasibility of GPS technologies for estimating PWV and its potential benefits to significantly improve numerical weather and storm prediction.
- Fu et al. (2007, 2009) and Zhang et al. (2011) presented initial investigations into GPS RO for the Australian region. The RO events within Australia from the CHAMP and FORMOSAT-3/COSMIC constellations provided temperature profiles for evaluation at 16 pressure levels with data from co-located radiosonde stations. Results showed that the mean temperature difference between radiosonde and CHAMP is 0.39° C (std. dev.=1.20°C) and 0.37° C (std. dev. = 1.24°C) for comparison between radiosonde and FORMOSAT-3/COSMIC.
- Le Marshall et al. (2010, 2012) presented results on the assimilation of GPS RO profiles into the Australian NWP forecast model in an operational capacity. A month of COSMIC RO events, together with a smaller number of RO events from the Meteorological Operational satellite (MetOp) and Gravity Recovery and Climate Experiment (GRACE) spacecrafts for the greater Australian region, have been assimilated into the global ACCESS system run by the Australian Bureau of Meteorology. Le Marshall et al. (2010, 2012) used 4D variational assimilation (4DVAR) to introduce the RO profiles and other data into the global ACCESS system (ACCESS-G), which was used to provide forecasts for up to five days. For the period studied, the accuracy was evaluated using the same operation assimilation without RO profiles. The forecasts using RO data were improved in all the lower, middle and upper troposphere. "These results, combined with the relatively unbiased nature of the RO observations indicate their use has the potential to improve operational analysis and forecasting in the Australian region and also to assist in important tasks such as a regional reanalysis and climate monitoring" (Le Marshall et al., 2010).
- Choy et al. (2011) applied methods of retrieving PWV estimates using ground-based GPS and a precise point positioning (PPP) processing method during a severe weather event in the greater Melbourne region. This case study focused on a severe mesoscale supercell

convective system that passed over greater Melbourne during March 2010. This initial result identified the ability of GPS state-wide networks in Australia to map the passage of WV in the pre- and post-frontal air mass with a high spatial and temporal resolution continuously in the outlook for severe weather.

- Zhang et al. (2011) provided an investigation of atmospheric temperature profiles in the Australian region using GPS RO and co-located radiosonde data. The joint research collaboration between the SPACE Research Centre and the Australian Bureau of Meteorology implemented GPS RO data into the operational ACCESS model (see Le Marshall et al., 2010).

1.4.2. Developments of GNSS tomography for atmospheric modelling

To further enhance the benefit of GPS as a platform for meteorology and climatology, information on the vertical profile of WV is needed. This is especially true for meteorological modelling and forecasting. GNSS tomography is an emerging method for reconstructing the 4D distribution of WV in the troposphere using a local GPS network. Integrated measurements of wet delays are extracted from each satellite-to-station link, which are used as the primary observable through a finite 3D ellipsoidal grid field to estimate the 3D structure of WV with a time evolving variable. Concept studies have identified the potential benefit for tropospheric tomography including Rocken et al. (1993), Ware et al. (1997), Flores (1999); Seko et al. (2000), Kruse (2001), MacDonald et al. (2002), Braun et al. (2003) and Bender and Raabe (2007).

The tomographic technique is a modification of the inverse theory utilising integral measurements of a finite field from different positions and orientations to reconstruct a 3D WV distribution (Gradinarsky and Jarlemark, 2004). The origin and the main application of tomographic imaging are in medicine (Jain, 1989), which successfully reconstructed 2D and 3D images by utilising a source-detector assembly rotating around an object to extract projection views of the media from different angles. Tomography is also used in geophysical applications such as seismology where acoustic vibrations of the subsurface media are sourced and received from accurately established surface positions in order to provide the input observables for the 2D or 3D reconstruction (Nolet, 1987). In more recent years, tomography was introduced to atmospheric modelling (initially for the ionosphere and then for the troposphere) utilising the observations of GPS.

The tomography technique has been used extensively in ionospheric research. The ionosphere extends from approximately 50 km to 1000 km altitude with an observational parameter of Total Electron Density (TEC). Using GPS post processing the integrated amount of electron density (i.e. TEC) is extracted from each zero-difference satellite to receiver link creating a large number of ray paths

traversing through the ionospheric media (Norman et al., 2013b). Tomography is then used to reconstruct images of TEC from ionospheric modelling (Rius et al., 1997; Ruffini et al., 1998).

The same concept is used for the troposphere with total path delays between each satellite and receiver link used as the observables in the reconstruction of wet refractivity or WV field using GPS tomography. Major research developments for GPS tropospheric tomography include:

- Flores (1999) and Flores et al. (2000) presented a simulation and real data investigation into 4D tropospheric tomography using GPS observations. The tomography software package, called local tropospheric tomography software (LOTTOS), was developed for this research using a stochastic approach. The real data analysis used the Kilauea network in Hawaii with the voxel grid discretisation covering an area of 400 km² and 15 km in height. The software was improved to include a Kalman filtering technique in the processing procedure, which is highly advantageous for estimating the evolution of dynamically changing parameters (Gradinarsky and Jarlemark, 2004).
- An alternate method presented in Nilsson et al. (2004), Nilsson (2005) and Nilsson and Gradinarsky (2006) used raw GPS phase measurements directly for the reconstruction of WV distribution. This method was tested using simulations where the horizontal and vertical voxel resolution, observation noise and additional GNSS constellations were varied and optimised. Results indicated high accuracy in the modelling of wet refractivity in lower layers, however, its limitation was found in resolving layers above 4000 m altitude.
- Seko et al. (2000) investigated the benefits of GPS tomography for modelling mesoscale precipitation systems. The model was designed on the premise that the grid system would move in relation to the vector of horizontal wind velocity. This investigation was further developed by Song et al. (2006). It was concluded that GPS tomographic solutions can improve the initial WV field for short term NWP predictions and forecasting.
- Braun et al. (2003) and Braun (2004) explored GPS tomography using low-cost single-frequency GPS receivers and the inclusion of Lidar images to constrain the vertical structure providing complementary information for the solutions. The discretisation was set to 1 km horizontally and 500 m vertically with a time resolution of 30 minutes. Results indicated difficulties in validation due to the small scale.
- Nicholson et al. (2005) presented an alternate approach, which used double difference (DD) residuals directly into the tomographic model without first recovering single-path slant wet delay (SWD) information. Temporal variations between epochs were modelled using a Kalman filter approach. The innovative aspect of this investigation is that it has been developed for use with an existing, real-time precise positioning software package, MultiRef and DD SWD observables can be incorporated directly into the model without post-

processing to create single path observations. Simulations indicated that integrating through estimated wet refractivity fields to extract zenith wet delays (ZWD) agreed with truth data to better than 1 mm when network station heights vary by 400 m. Flat GPS network geometries agreed better than 3 mm.

- Bender and Raabe (2007) provided an extensive analysis on the preconditions and constraints of ground based GPS WV tomography. Results suggest that the spatial resolution is limited by the density of the ground-based GPS networks and the number of available GNSS satellites. To optimise horizontal resolution the humidity fields would be restricted to the mean inter-station distance of the GPS network. Another important parameter presented is the elevation cutoff angle, the number of available rays increases heavily with a decreasing elevation cutoff angle and in return provides much more information on the lower troposphere.
- Bosy et al., (2010) and Rohm and Bosy (2009, 2011) presented investigations into the concept of near-real-time atmospheric model construction based on the GNSS and meteorological observations from the ASG-EUPOS stations. This application is in view of nowcasting and provides accurate comparisons with NWP analysis models.

1.4.3. Developments of AWATOS

The software package AWATOS (Atmospheric Water Vapour Tomography Software) was developed by the Geodesy and Geodynamics Lab (GGL), ETH Zurich (Kruse, 2001; Troller et al., 2002; Troller, 2004; Troller et al., 2006; Lutz, 2008). This software uses the least squares method for estimating the 3D wet refractivity field using DD tropospheric delays as the primary observables. AWATOS was tested with various campaigns. These include:

- Kruse (2001) developed a method of using the DD tropospheric residuals from Bernese GPS processing as a pioneer study in the initial development of the AWATOS software package at the GGL, ETH Zurich.
- Troller et al. (2002), Troller (2004) and Troller et al. (2006) further investigated the influence of additional observations and constraints on the tomographic solution. Additional observations such as ground meteorological sensor networks, radiosonde and NWP data were introduced as apriori information. The influence of inter-voxel constraints were also investigated with overall positive results. However, the key limitations of the method were found in detecting sharp refractivity gradients due to smoothing effects.
- Lutz (2008) investigated high-resolution tomography over mountainous regions in the Swiss Alps in view of hazard mitigation. A total of 30 GPS stations were used over a two week campaign in July 2005 and October 2005. The optimal grid resolution was concluded to be 3

km horizontally (mean inter-station distance) with 43 exponentially increasing height layers up to 15km altitude.

AWATOS was reprogrammed and enhanced to include new methods of parameterisation and introduced a Kalman filtering approach for the second edition, called AWATOS 2 (Perler et al., 2011; Perler, 2011). AWATOS 2 has the ability to assimilate any refractivity measurements as either point or integral observations. The new version supports tropospheric gradients and enhanced statistical models, and includes sophisticated simulation scenarios including both point and integral observations. Due to these characteristics it has been used in this thesis. Investigations were based on the Victorian CORS network (GPSnet) as a wide geographic scale analysis for severe weather. Studies using AWATOS 2 include:

- Perler et al. (2011) and Perler (2011) investigated the long-term operability and overall accuracies of a constant, trilinear and bilinear/spline parameterisation method using the Kalman filter based AWATOS 2. The accuracy of the tomographic solution is quantified by the inter-quartile rang (IQR), which is decreased by 10 – 20% when using the trilinear and bilinear/spline methods when compared with the constant parameterisation approach.
- Manning et al. (2012) presented a case study investigation into early detection of severe mesoscale convective systems in the Australian region using GPS tomography. Results were based on real data analysis with a strong correlation between the processed tomography profiles and the truth radiosonde profiles and RADAR image intensities. Also strong indications of lift and convection along with the formation of the stratiform region were evident in tomographic solutions over time.
- Manning et al. (2013) presented results on a new study in Australia for discretising the atmosphere in the Victorian region using 4D GPS tomographic solutions for wet refractivity processed by AWATOS 2. This research presented simulation studies into parameter optimisation methods for resolution and geometry of the GPSnet.

In contrast to the sparse distribution of radiosonde and radiometer stations, GPS and GNSS tomography has the potential for providing WV distribution with a high spatio-temporal resolution. This technique has the potential to enhance nowcasting, detection and prediction of severe weather and long-term climate analysis.

1.5. Objective and main contributions

1.5.1. Aims and objectives

The primary aim of this thesis is to develop advanced GPS meteorological platforms, including a 4D ground-based GPS tomography technique using CORS networks for severe weather analysis in Australia. This research takes advantage of the homogeneity and high density of the GPSnet. This aim is in view of providing an additional observation platform, which yields high spatial and temporal resolution, for the assimilation into nowcasting and NWP models. This has the potential to strengthen early detection and prediction of severe weather events. Two severe weather events: March 2010 super cell storm and January 2011 severe precipitation system will be used as case studies for the analysis of these objectives.

The specific objectives of this research are as follows:

- To adopt advanced methods of accurately estimating tropospheric delay parameters and DD residuals of ground-based GPS observations using the Bernese Processing Engine for the GPSnet infrastructure. Optimisation of apriori models and mapping functions are to be investigated.
- To develop methods for obtaining optimal ZWD from the Bernese GPS processing of tropospheric ZTD using an optimal dry modelling function. Adopt optimal method to attain GPS-derived PWV estimates. Radiosonde observations will be converted to integral PWV for accurate validation and accuracy analysis of co-located stations.
- To statistically optimise parameters for modelling 4D tropospheric wet refractivity fields using GPSnet. Multiple simulation studies will be investigated using an exponential synthetic refractivity field based on average radiosonde profiles and the inclusion of observation noise.
- To analyse the dynamics of wet refractivity using GPS tomography during the formation and lifecycle of a severe convective supercell storm anomaly in the Victorian region using *case study 1* (March 2010). This is to identify a correlation between the 4D dynamics of the reconstructed wet refractivity fields with the mesoscale mechanisms of severe weather phenomena.
- To analyse the influence of including additional point observations into the observation matrix of the 4D GPS tomography modelling strategy under severe weather conditions using *case study 2* (January 2011). These include:
    - Radiosonde profiles;
    - GNSS RO events; and,
    - Ground-based synoptic weather observation networks.

1.5.2. Contributions and benefit of this research

Ground-based and space-borne GPS has become one of the most important observational sources for operational NWP. It is therefore significant for Australia to continue to develop GPS meteorological platforms for safety, economic and social aspects. The main benefits of this research include:

- An operational methodology for the processing of ground-based GPS observations for the estimation of tropospheric delay parameters with a high accuracy applied to GPSnet location, geometry and density in view of near-real-time and real-time applications.
- A developed methodology for attaining GPS-derived PWV using GPSnet during severe weather phenomena.
- Parameter optimisation for 4D GPS tomographic modelling with respect to the Victorian region and GPSnet geometry.
- A robust and operational 4D GPS tomographic algorithm for the Victorian region and GPSnet geometry for reconstructing the highly dynamic wet refractivity fields in view of severe weather phenomena.
- A methodology for monitoring the mesoscale convective and stratiform mechanisms of severe weather using 4D GPS tomography.
- Comprehensive analysis of a multi-observational GPS tomographic strategy evaluating the influence of additional profile and point observation methods within the observation model under severe weather conditions. An optimised observation model strategy is developed.

1.6. Thesis structure

The structure of the remainder of this thesis is as follows:

CHAPTER 2: Introduces the current laws of microwave signal propagation in Earth's atmosphere and the fundamentals of modelling wet refractivity in the troposphere. The governing equations for GPS processing are described including relevant mapping functions, along with path delay measurements and their relationship with meteorological parameters. The Bernese GPS processing software is introduced focusing on parameter settings and Bernese Processing Engine (BPE) strategies. Finally the formula for optimal determination of the PWV estimates based on additional information is introduced.

CHAPTER 3: Presents the observation systems used for this research. This includes spatial and temporal distribution, accuracy and developments of each observation system. A case study on the validation of GPS-derived PWV estimates using integrated radiosonde PWV estimates is presented.

CHAPTER 4: Introduces the theory of GPS tropospheric tomography and its application in reconstructing wet refractivity fields. The algorithms, models and observations used in AWATOS 2 are then presented. This is the fundamental processing platform used for this research.

CHAPTER 5: Presents the analysis and results of multiple GPS tomographic simulation studies using AWATOS 2 to determine the optimal parameters of the model system.

CHAPTER 6: Outlines *case study 1*, which investigates the functionality of the GPS tomography algorithm and solution during severe weather phenomena. The accuracy and evolution of the 4D wet refractivity fields developed using GPS tomography is analysed during a severe mesoscale convective storm system to investigate the capability of monitoring the mesoscale structure.

CHAPTER 7: Presents *case study 2*, which is used to analyse the influence of additional profile and point observation methods introduced as apriori observations to support the DD SWD observations for modelling wet refractivity using 4D GPS tomography. This analysis is tested during the formation and lifecycle of a severe weather event. A statistical analysis is conducted for 5 separate test scenarios, which independently implement radiosonde profiles, synoptic weather station data and GPS RO profiles into the GPS tomography. The final test scenario assimilates all additional observation methods.

CHAPTER 8: Discusses the conclusions, recommendations and outlook for this direction of research.

Chapter 2. GPS meteorology fundamentals

2.1. Overview

In recent years, GPS has been used to attain measurements of the physical parameters within the ionosphere and neutral atmosphere by estimating the delay and bending of the propagating microwave signals of GPS satellites. Ground-based and airborne GPS meteorology takes advantage of the GPS microwave signal delay and bending due to the refractive index of the troposphere, which extends from the ground to the tropopause (approximately 15 km in middle latitudes).

The physical parameters retarding the GPS microwave signals as they pass through different media in the troposphere are pressure, temperature and humidity. These parameters must be measured with sufficient accuracy, resolution, plus spatial and temporal coverage to improve NWP models and thus improve our knowledge of the fundamental processes involved in global change (Kursinski et al., 1997; Soden et al., 2002; Solomon et al., 2007; Isaac and Van Wijngaarden, 2012). GPS meteorology provides a robust technology for the improvement of resolving the spatial and temporal variability of WV within the neutral atmosphere, due to the high accuracy, high spatial and temporal resolution and all weather working capability (Bevis et al., 1992).

2.2. Physics of the atmosphere

2.2.1. Microwave propagation in the atmosphere

In theory, to obtain perfect ranging measurements from GPS, signals must travel at exactly the speed of light as they travel from a satellite to a receiver through the various layers of the atmosphere. In order for the signal to travel at the speed of light along the ray path, the media the signal travels through must hold an index of refraction equal to 1, i.e. the speed of light in a vacuum. In addition, the exact position and velocity of each satellite would need to be known at each point of broadcast. Also, ideally the satellite and receiver clocks would need to be perfectly synchronised to measure the exact time displacement. In reality, there are many affecting factors of the propagating signal. The ionospheric and tropospheric delays are two of the most notorious error sources, and are usually eliminated through a GPS DD procedure that is used in geodetic and high precision positioning. However, the delays have become a valuable source of information for meteorological applications.

This research investigated the meteorological processes, which were mainly attributed to the dynamics and distribution of WV in the troposphere (Figure 2.1). The ionosphere is a dispersive medium due to its electron density. It is essential to mitigate all other error sources so that the tropospheric propagation effects can be isolated and ultimately the magnitudes of GPS-derived PWV can be estimated accurately. GPS-derived tropospheric path delay estimates were also used as a primary input observable for the 4D tomographic reconstruction of WV fields. This is necessary in order to study WV trends and dynamics in the troposphere.

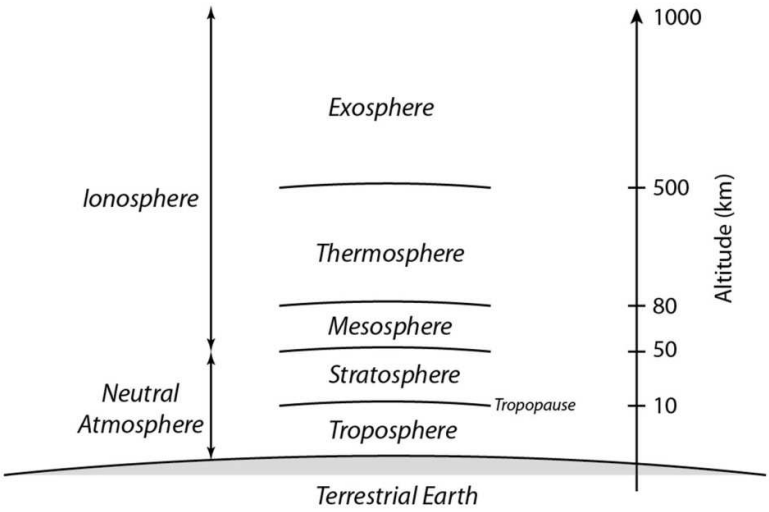

Figure 2.1: Profile view of the ionosphere and neutral atmosphere in respect to approximate altitude.

2.2.2. Modelling refractivity in the neutral atmosphere

As electromagnetic signals at radio wavelengths propagate through both the Earth's ionosphere and neutral atmosphere they are delayed and bent due to the variations in refractive index thus causing displacement in GPS phase and amplitude observations. GPS measurements are derived by precisely determining the scalar distance between each satellite in view and a GPS receiver. The delays and amplitude variations caused by the atmospheric refractive medium adversely affects the accuracy of these range measurements, and thus to degrade the accuracy of the derived position of the receiver. However, this can then provide the means for observing atmospheric information. This is why GPS has now become one of the most important and globally distributed atmospheric sensing instruments for weather forecasting and climatological studies.

Refractivity has both dispersive and non-dispersive effects. The dispersive effect on radio wavelengths is caused by the electron density in the ionosphere, and is frequency dependent. This means that a linear combination of two frequency GPS observations can eliminate the dispersive ionospheric effect. This combination is called the ionosphere-free linear combination. The non-

dispersive component is associated with the refractive index of the neutral atmosphere, i.e. the troposphere. The propagation of radio wavelengths through this medium is independent of carrier frequency variations. The refractivity within the troposphere is usually calculated using empirically determined constants k_1, k_2, k_3 and three meteorological parameters: partial air pressure P_d , temperature T, and WV pressure e (Essen and Froome, 1951):

$$N = (n - 1) \cdot 10^6 \tag{2.1}$$

$$N = k_1 \frac{P_d}{T} \cdot Z_d^{-1} + k_2 \frac{e}{T} \cdot Z_w^{-1} + k_3 \frac{e}{T^2} \cdot Z_w^{-1} \tag{2.2}$$

where

N	is the total refractivity (ppm)
n	is the index of refraction
k_1, k_2, k_3	are the empirically determined constants
Z_d	is the compression factor of dry air
Z_w	is the compression factor of wet air

The empirically determined constants have been continuously refined and updated (Essen and Froome, 1951; Smith and Weintraub, 1953; Owens, 1967; Thayer, 1974; Bevis et al., 1994 and Rueger, 2002). Assuming a condition of ideal gas behaviour in the troposphere, then both compression factors Z_d and Z_w are equal to 1 and eliminated from Eq. (2.2). In this study the empirical constants for microwave refractivity derived by Rueger (2002) were used because they are currently considered the most accurate (Table 2.1).

Table 2.1: Empirical constants for microwave refractivity derived by Rueger (2002).

	k_1	k_2	k_3
Value	77.689	71.295	375463

The accuracy of the dry air refractivity N_{dry} component is about 0.02% of N_{dry} and for the wet refractivity N_{wet} component the accuracy is approximately 0.15% of N_{wet}. The empirical values can be substituted into Eqs. (2.2) for total refractivity *N* of microwave electromagnetic frequencies in the troposphere (Rueger, 2002).

$$N = 77.689 \frac{P_d}{T} + 71.295 \frac{e}{T} + 375463 \frac{e}{T^2} \tag{2.3}$$

N can be further separated into a dry refractivity N_{dry} and a wet refractivity N_{wet} (i.e. Eqs. (2.4) and (2.5), respectively), representing the contribution from the dry atmosphere, and the part associated to WV, respectively.

$$N_{dry} = 77.689 \frac{P_d}{T} \tag{2.4}$$

$$N_{wet} = 71.295 \frac{e}{T} + 375463 \frac{e}{T^2} \tag{2.5}$$

2.2.3. Tropospheric delay estimation

In order to attain high accuracy GPS positioning for geodetic applications, all error sources need to be identified and accounted for. As stated previously, the ionospheric effect on a GPS signal can be resolved using an ionosphere-free linear combination approach. However, the effect of the neutral atmosphere can only be modelled and derived using optimal estimation techniques and additional meteorological parameters. The slant path delay (SPD) $\Delta\rho_a^x$ of a GPS signal due to the tropospheric refractivity from receiver a to satellite x can be expressed as (Bevis et al., 1992):

$$\Delta\rho_a^x = \int_a^x (n-1)ds = 10^{-6} \cdot \int_a^x N \, ds \tag{2.6}$$

where

$\Delta\rho_a^x$ is the SPD from station a to satellite x (m)

ds is the integral length from station a to satellite x

The integral of Eq. (2.6) is performed for the total refractivity N along the straight path between satellite x and receiver a with respect to the scalar length ds, and can be separated into N_{dry} and N_{wet} components.

2.2.4. Saastamoinen models

The Saastamoinen model is currently the most accurate and widely used empirical tropospheric model to compute the tropospheric refraction or SPD. It needs accurate meteorological measurements of temperature, pressure and WV at the Earth's surface along with the associated elevation angles in the observed direction for the total path delay (Saastemoinen, 1972, 1973; Hofmann-Wellenhof et al., 2001; Lutz, 2008). Full details on the derivations of the Saastamoinen model can be found in Saastemoinen (1972).

$$\Delta\rho_{saas} = \frac{0.002277}{\cos(z)} \cdot \left(P_d + \left(\frac{1255}{T} + 0.05 \right) \cdot e - B \cdot \tan^2(z) \right) + \delta_R \qquad (2.7)$$

where

$\Delta\rho_{saas}$	is the SPD approximated by the Saastamoinen model (m)
z	is the zenith angle of the satellite (radians) ($z = 90° - \varepsilon$)
B, δ_R	are the height and zenith angle dependent corrections, respectively.

B and δ_R are correction variables dependent on the height of the instrument and zenith angle of the satellite (see tabulated values in Saastamoinen (1973) and Hofmann-Wellenhof et al. (2001)).

Similar to Eq. (2.3) the separation of the dry and wet components of the total refractivity N, the Saastamnoinen Eq. (2.7) can also be separated to model both dry and wet delays. The dry component $\Delta^{dry}\rho_{saas}$ representing the contribution from the dry atmosphere is directly proportional to the atmospheric pressure gradient. The wet component $\Delta^{wet}\rho_{saas}$ representing the WV contribution is an inhomogeneous field and thus cannot be modelled accurately (Thayer, 1974; Remondi, 1984; Herring, 1992 and Lutz, 2008).

$$\Delta^{dry}\rho_{saas} = \frac{0.002277}{\cos(z)} \cdot \left(P_d - 0.155471 \cdot e - B \cdot \tan^2(z) \right) + \delta_R \qquad (2.8)$$

$$\Delta^{wet}\rho_{saas} = \frac{0.002277}{\cos(z)} \cdot \left(\frac{1255}{T} + 0.205471 \right) \cdot e \qquad (2.9)$$

2.3. Estimation of tropospheric delay using GPS data

2.3.1. GPS observations

The NAVSTAR GPS is a space-based global navigation satellite system that can be used to determine accurate (3-dimensional) position and time at any point on or close to the Earth's terrestrial surface. The GPS was pioneered by the United States Department of Defence with the first satellite of NAVSTAR launched into orbit in 1978, and was used for advanced positioning and navigation purposes. This technology proved to be a fundamental tool for military intelligence as it provided real-time, highly accurate point positioning, velocity, time and navigation data, anywhere on the Earth, at any time, and in any weather conditions (McDonald, 1999; Dach et al., 2007; Dach and Walser, 2013).

GPS is made up of three segments: space, control and user. The space segment consists of the GPS satellite constellation framework, currently consisting of approximately 32 satellites at 6 different orbital planes. Each satellite takes approximately 12 hours to complete one orbit around the Earth. The average altitude of each orbiting GPS satellite is ~20,200 km above the Earth's terrestrial surface at an inclination angle of 55^0. The control segment consists of five tracking stations, three ground antennas, and a master control station. The monitoring stations track continuous data from each satellite in view. The data is processed at the master control station for determination of satellite orbits, clocks errors and to updating the navigation message of each satellite. The data is updated and sent to each satellite via the ground antennas. The user segment includes a GPS antenna and receiver to collect GPS observations for obtaining positioning, velocity and precise timing to users (Dach et al., 2007; Dach and Walser, 2013).

Traditionally, the GPS signals are transmitted on two different L-band radio frequencies: L_1 and L_2 (see Table 2.2). Coded information is carried on these signals and provides information on satellite identification, time, position and status for each satellite, along with parameters for a simple ionospheric model used for correction of the ionospheric delays. Three of these pseudo-random noise ranging codes are in operation, including:

1. The course/ acquisition (C/A) code is used primarily to acquire the P-code. It has a 1.023 MHz chip rate, and a period of 1 millisecond (ms);
2. The precision (P) code is the principle military navigation raging code. It has a 10.23 MHz chip rate, and a period of 7 days; and,
3. The Y-code is for anti-spoofing (A/S) and is used in place of the P-code.

The C/A code is active on the L1 frequency and the P-code and Y-code are available on both L1 and L2 frequencies. Each satellite transmits a navigation message containing orbital parameters, clock corrections, system time and status messages. In addition, approximated information on the orbits and positions of all active satellite is also given to assist the receiver to find all satellites in view once the first has been identified.

Table 2.2: L-band carrier frequencies for GPS signals.

	Frequency	**Wavelength**
f_1	1575.42 MHz	19.05 cm
f_2	1227.60 MHz	24.45 cm

Although the GPS was developed primarily to enhance the US military's positional and navigation capabilities, it quickly expanded to provide significant benefits to a wide and diverse range of global users. This was due to the associated high accuracy, continuous operability, all weather working and global coverage. As a direct result of these benefits, U.S Vice President Al Gore announced a GPS

modernisation effort in January 1999 to further the capabilities of the existing GPS constellation (McDonald, 1999). This investment has seen a unified global expansion of GPS applications. The various domains for GPS applications include industry, military, transportation, science and research, personal navigation and mobility, sport and agriculture. The application of GPS into different technologies has been developing over the past two decades and continues to expand. The diverse scientific applications of GPS technologies include atmospheric and space science, geodesy, geodynamics and geophysics, hydrography, oceanography and wildlife studies. This research will focus on GPS-meteorology for atmospheric science and more specifically WV modelling in the troposphere.

2.3.1.1. GPS observation equations

GPS observations have two types: pseudo-range and carrier phase. The phase measurements hold a very low noise level and are very precise in comparison to the pseudo-range measurements that have an accuracy of a few metres. As a result, the phase measurements are used as the primary observable in precise GPS positioning and the pseudo-range are treated as auxiliary observations and primarily used for synchronising receiver clocks and aiding ambiguity resolution.

The basic form of the (zero difference (ZD)) carrier phase observation equation can be broken down into different parameter effects for both frequencies f_1 and f_2 (Remondi, 1984; Dach et al., 2007).

Code on L1

$$P_{1,a}^{x} = \rho_a^x + c\delta_a - c\delta^x + I_a^x + \Delta\rho_a^x + \varepsilon \tag{2.10}$$

Code on L2

$$P_{2,a}^{x} = \rho_a^x + c\delta_a - c\delta^x + \frac{f_1^2}{f_2^2}\cdot I_a^x + \Delta\rho_a^x + \varepsilon \tag{2.11}$$

Phase on L1

$$L_{1,a}^{x} = \rho_a^x + c\delta_a - c\delta^x - I_a^x + \Delta\rho_a^x + \Lambda_1 n_{1,a}^x + \varepsilon \tag{2.12}$$

Phase on L2

$$L_{2,a}^{x} = \rho_a^x + c\delta_a - c\delta^x - \frac{f_1^2}{f_2^2}\cdot I_a^x + \Delta\rho_a^x + \Lambda_2 n_{2,a}^x + \varepsilon \tag{2.13}$$

where:

P_1 is the code measurement on f_1

P_2 is the code measurement on f_2

L_1 is the phase measurement on f_1

L_2 is the phase measurement on f_2

ρ_a^x is the true geometric path distance from receiver a to satellite x

$c\delta_a$	is the clock error of receiver a
$c\delta^x$	is the clock error of satellite x
I_a^x	is the ionospheric delay at frequency L1
f	is the carrier frequency
$\Delta\rho_a^x$	is the tropospheric SPD
Λ	is the wavelength
n_a^x	is the initial integer ambiguity
n_a^x	is the initial integer ambiguity
ε	is the observation noise

2.3.1.2. GPS DD approach

The carrier phase observations expressed in Eqs. (2.12) and (2.13) hold several common parameters and common error effects. To achieve high accuracy GPS positioning or, in the case of this research accurate meteorological data, the DD technique needs to be applied to the GPS data processing in order to cancel out these common unknown parameters. The geometric structure of DD is shown in Figure 2.2.

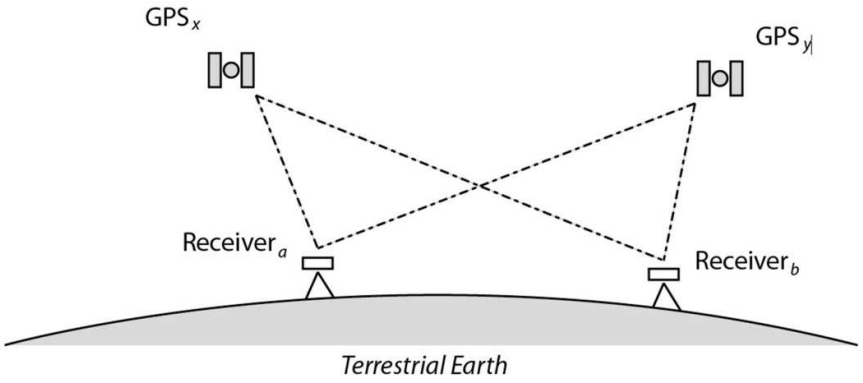

Figure 2.2: GPS DD geometry using two receivers (a & b) and two satellites (x & y)

The DD approach starts from a single-differencing (SD) of the simultaneous one-way measurements from one satellite to the two ground receivers. This eliminates the satellite clock error, and if the receivers are close to each other the atmospheric refraction effects can be cancelled out due to the correlation nature of the atmosphere. Then, differencing the two single-differenced observations gives a DD observation, which eliminates the two receivers' clock errors. The SD equation for two

receivers a, b and one common satellite x is expressed as (Hofmann-wellenhof et al., 2001 and Bai, 2004):

$$SD_{a,b}^{x} = L_{2,b}^{x} - L_{2,a}^{x} \tag{2.14}$$

By combining two single-difference equations we obtain the DD equation ($DD_{a,b}^{x,y}$):

$$DD_{a,b}^{x,y} = SD_{a,b}^{y} - SD_{a,b}^{x} = \left(L_{2,b}^{y} - L_{2,a}^{y}\right) - \left(L_{2,b}^{x} - L_{2,a}^{x}\right) \tag{2.15}$$

In the DD equation the satellite and receiver clock errors are eliminated (Hofmann-wellenhof et al., 2001).

Code:

$$P_{1,a,b}^{x,y} = \rho_{a,b}^{x,y} + I_{a,b}^{x,y} + \Delta\rho_{a,b}^{x,y} + \varepsilon \tag{2.16}$$

$$P_{2,a,b}^{x,y} = \rho_{a,b}^{x,y} + \frac{f_1^2}{f_2^2} \cdot I_{a,b}^{x,y} + \Delta\rho_{a,b}^{x,y} + \varepsilon \tag{2.17}$$

Phase:

$$L_{1,a,b}^{x,y} = \rho_{a,b}^{x,y} - I_{a,b}^{x,y} + \Delta\rho_{a,b}^{x,y} + \Lambda_1 n_{1,a,b}^{x,y} + \varepsilon \tag{2.18}$$

$$L_{2,a,b}^{x,y} = \rho_{a,b}^{x,y} - \frac{f_1^2}{f_2^2} \cdot I_{a,b}^{x,y} + \Delta\rho_{a,b}^{x,y} + \Lambda_2 n_{2,a,b}^{x,y} + \varepsilon \tag{2.19}$$

If the linear combination of dual frequency carrier phase measurements is used in the DD observations for eliminating the ionospheric effect. The DD phase observations ($L_{3,ab}^{xy}$) may be further reduced to:

$$L_{3,ab}^{xy} = \rho_{ab}^{xy} + \frac{1}{f_1^2 - f_2^2} \cdot \left(f_1^2 \Lambda_1 n_{1,ab}^{xy} - f_2^2 \Lambda_2 n_{2,ab}^{xy}\right) + \Delta\rho_{ab}^{xy} + \varepsilon \tag{2.20}$$

2.3.1.3. Niell mapping functions

The magnitude of SWD from satellite x to receiver a can be derived using an averaged PWV or ZWD plus an associated mapping function using the satellite elevation angle (Figure 2.3). In the processing of GPS observations using the DD approach (Eq. (2.20)), all SPD during a specified time span were averaged to form a ZTD for each GPS station. As will be described in Section 2.5, the dry component N_{dry} or hydrostatic delay at the zenith (ZHD) represents the contribution from the dry atmosphere. This can be accurately estimated using a dry delay model (Saastamoinen, 1973), together with accurate surface meteorological parameters, latitude and height variables. The SWD at the radio

wavelength is then a function of the elevation angle and is the sum of the isotropic and non-isotropic terms (Niell, 1996; Braun, 2004 and Lutz, 2008).

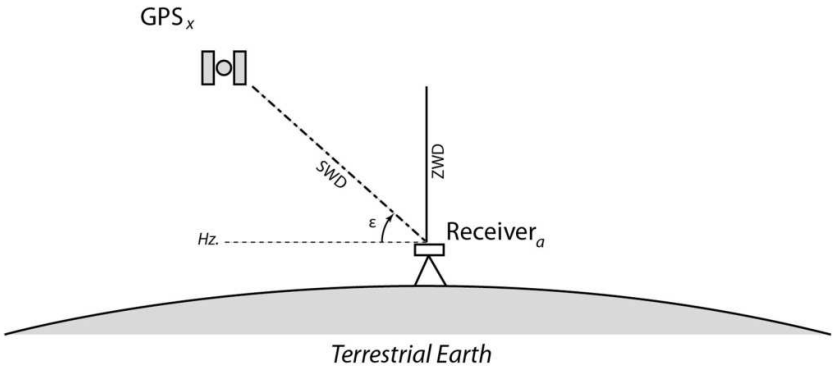

Figure 2.3: Geometry of SWD and elevation angle (ε) of a receiver (a) and a satellite (x), the vertical component is the ZWD of the station to be estimated.

$$\Delta^{wet}\rho_a^x = \mathrm{ZWD}_a \cdot m_{wet}(\varepsilon_a^x) + S_a^x \tag{2.21}$$

where

$\Delta^{wet}\rho_a^x$	is the SWD from station a in the direction of satellite x
ZWD_a	is the zenith wet delay at station a
$m_{wet}(\varepsilon_a^x)$	is the wet mapping function
ε_a^x	is the elevation angle of satellite x from station a
S_a^x	is the non-isotropic component of the SWD

Mapping functions have been developed over the years for improved accuracy of the approximation model. The mapping functions originally were simple localised mapping functions ($m\ (\varepsilon)$), in which a flat planar Earth was assumed. The simplest mapping function for the slant delay being mapped to the zenith is:

$$m\ (\varepsilon) = \frac{1}{\sin(\varepsilon)} \tag{2.22}$$

This function provided good approximations for elevation angles above ~15^0. However, this function was not accurate since the earth's curvature needs to be taken into account. The Marini mapping function (Niell, 1996) was developed to account for this, which was later improved by introducing an increased amount of parameters including ray bending. As the elevation angle approaches the horizontal, error increases exponentially due to temperature and humidity dynamics within the planetary boundary layer and also the increasing scalar length of atmosphere through which the signal

propagates (Stull, 1999; Lutz, 2008). The parameters of a mapping function are based on geographical and meteorological observations. Currently, the most widely used mapping function was developed by Niell (1996), in which coefficients a, b and c are geographical latitude dependent and are based on global radiosonde data (Herring, 1992; Niell, 1996; Mendes and Langley, 1998; Niell 2003; Shrestha, 2003; Troller, 2004 and Lutz, 2008). In this research we use the Neil mapping function for both wet and dry delays. The Neil wet mapping function $NMF_{wet}(\varepsilon)$ is expressed as (Niell, 1996):

$$NMF_{wet}(\varepsilon_a^x) = \frac{1 + \dfrac{a_{wet}(\phi)}{1 + \dfrac{b_{wet}(\phi)}{1 + c_{wet}(\phi)}}}{\sin(\varepsilon_a^x) + \dfrac{a_{wet}(\phi)}{\sin(\varepsilon_a^x) + \dfrac{b_{wet}(\phi)}{\sin(\varepsilon_a^x) + c_{wet}(\phi)}}} \tag{2.23}$$

where

a_{wet}, b_{wet} and c_{wet} are the coefficients derived from the station's latitude (ϕ) and a table developed by Neil (1996)

The Neil hydrostatic (dry) mapping function $NMF_{dry}(\varepsilon)$ is geographically dependent, i.e. latitude (tabulated values a_{avg} and a_{amp}) and also time dependent, i.e. day of year (t_{DOY}) (Neil, 1996). The parameter a_{dry} at time t_{DOY} is expressed using notation from Lutz (2008):

$$a_{dry}(\phi, t_{DOY}) = a_{avg}(\phi) - a_{amp}(\phi) \cdot \cos\left(2\pi \cdot \frac{t_{DOY} - T_a}{365.25}\right) \tag{2.24}$$

where T_a is the phase, which is usually set to January 28 (DOY = 28). A correction term $\Delta m(\varepsilon)$ is added in Eq. (2.25) (with the corresponding coefficients), which is related to the height H of the station above mean sea level (km):

$$NMF_{dry}(\varepsilon_a^x) = \left(\frac{1 + \dfrac{a_{dry}(\phi)}{1 + \dfrac{b_{dry}(\phi)}{1 + c_{dry}(\phi)}}}{\sin(\varepsilon_a^x) + \dfrac{a_{dry}(\phi)}{\sin(\varepsilon_a^x) + \dfrac{b_{dry}(\phi)}{\sin(\varepsilon_a^x) + c_{dry}(\phi)}}} \right) + \Delta m(\varepsilon) \tag{2.25}$$

where

$$\Delta m(\varepsilon) = H \cdot \left(\frac{1}{\sin(\varepsilon)} - \frac{1 + \dfrac{a_{ht}}{1 + \dfrac{b_{ht}}{1 + c_{ht}}}}{\sin(\varepsilon) + \dfrac{a_{ht}}{\sin(\varepsilon) + \dfrac{b_{ht}}{\sin(\varepsilon) + c_{ht}}}} \right) \tag{2.26}$$

It should be noted that the coefficients a_{ht}, b_{ht} and c_{ht} are all height dependent.

2.3.2. Bernese GPS processing

Bernese Version 5.0 is the latest version of a globally used GPS processing software package developed by the Astronomical Institute at the University of Berne, Switzerland. It is a high performance, accurate, flexible and comprehensive GPS/GNSS post processing package. The software provides state-of-the-art modelling, all relevant processing options, powerful automatic tools, dynamic adoption to international standards, and intrinsic flexibility. Uses of the Bernese GPS software include (Dach and Walser, 2013):

- Rapid processing of small-size single and dual frequency receivers
- Automatic processing of permanent networks
- Processing data from a large number of receivers
- Combination of different receiver types, accounting for variations in phase centre parameters
- Ambiguity resolution on long baselines (>2000 km)
- Ionospheric and tropospheric monitoring
- GNSS satellite orbit determination and estimation of Earth orientation parameters

An automated Bernese processing engine (BPE) is used for the post-processing strategy for daily GPS campaigns. This strategy uses resident GNSS processing programs such as CODSPP, SINGDIF and MAUPRP. The program GPSEST is used for the final step to obtain estimates of the GPS receiver coordinates, ZTDs, horizontal gradients and DD residuals.

In this section, the methodology for this post-processing strategy in order to determine optimal estimates of ZTD, horizontal gradients and DD residuals using the DD approach for the geodetic GPSnet station infrastructure is explained.

2.3.2.1. Processing parameters

For high accuracy positioning and path delay solutions, multiple parameters need to be included in the processing strategy. Precise orbital data is collected from the International GNSS Service (IGS) and used in the processing to provide precise position and velocity data for each satellite.

Input data includes:

- Ground-based GPS data collected from each CORS station of GPSnet, at a sample rate of 30 seconds and in RINEX format.
- Precise orbital files: daily files from the International GNSS Services (IGS).
- Axis rotation correction files: weekly files from the IGS.

- Solid Earth tide: Fluctuation height as the land mass rises and falls due to the rotation of the Earth and gravitational effects. There is a default equation used in the Bernese software package to account for this.
- ITRF coordinates for fixed stations position at time (t) with velocity information. These stations are ideally recognised in the IGS network (see Section 3.2.1).
- Station information including station name, antenna type, receiver type, relevant offsets, etc.

RINEX GPS observation format

The flow of programs in the pre-processing procedure needs the explicit format of the GPS observation files. All GPS data from GPSnet used in this research was provided by the Department of Environment and Primary Industries in the RINEX format. Daily files were needed for this research to comply with the input needs of Bernese V5.0. There are three types of RINEX files provided by each station/receiver: observation files, broadcast ephemeris or navigation message files, and meteorological data files. Only the RINEX observation files were used for processing since we use IGS precise orbit products.

The file contains a header containing all metadata concerning both the stations and the GPS receiver information. The basic observations are for code and phase observations listed alongside the corresponding epoch. The RINEX observation files will be converted into binary (Bernese) format for processing using the Bernese GPS software.

2.3.2.2. Bernese Processing Engine (BPE)

The BPE is a powerful automated Bernese processing strategy that combines successive modules in the pre- and post- processing sequence. The BPE processing tasks are defined by the user in so-called Process Control Files. The BPE can run multiple tasks simultaneously on different CPUs, and can even allocate a single task to different CPUs. Initially the sequence of modules and parameters are constructed and input file paths identified from which the BPE server calls on this information in sequential order.

The program uses an ionosphere-free linear combination in a standard least squares adjustment to compute unknown parameters, such as the receiver clock corrections, and coordinates of GPS stations.

Code single point positioning (CODSPP)

This CODSPP program uses the ZD code observations to resolve the receiver clock errors to ultimately synchronise with satellite clocks and GPS time. It also provides the aposterori RMS error

on the 3D relative position estimation. The program stores the clock-offset data in the phase observation files for further processing.

Single difference (SINGDIF)

The SINGDIF program computes the SD code and phase observables and outputs them into files, which will be used to form the DD in the final estimation program GPSEST. SINGDIF then creates the baselines between all active receivers in each session of the campaign and stores that output data in the SD files. The baseline processing strategy is defined in SINGDIF.

MAUPRP

The MAUPRP program performs three steps of processing. It first detects cycle slips that may have occurred during observation. Cycle slips are caused by an interruption in the measured (integrated) carrier phase resulting from a temporary loss of lock between the satellite and receiver. This may be caused by physical obstructions such as vegetation, buildings, etc. that block the satellite-receiver link. The ambiguities caused by the cycle slips must be repaired before processing the DD. The MAUPRP program involves the following three main processing steps:

1. Automatic cycle slip detection: the program corrects large discontinuities due to loss of lock using the SD values.
2. Smoothing: The CODCHK algorithm detects time intervals in which no cycle slips occur.
3. Triple-difference processing: the triple difference solution using the processed baselines in a standard least square adjustment is used to detect and isolate the undetected cycle slips.

With the successful completion of the MAUPRP processing steps, the GPSEST program can be run to compute the final tropospheric, gradient and DD residual parameter estimates.

GPS estimation (GPSEST)

The GPSEST program uses DD solutions and a standard least squares adjustment for each station to estimate ZTD parameters, gradient parameters and DD residuals. The program undertakes the following four processing iterations:

1. The first iteration uses basic DD carrier phase observations to estimate initial coordinates of each station using the IF linear combination without an ambiguity resolution. Earth rotation parameters and ocean loading corrections are used as input parameters in this iteration. This step solves the initial residuals. All output data is saved for the next step.
2. Initial coordinates and residuals are used as apriori information in this second iteration to compute more accurate coordinates and initial tropospheric delays. The output results are again stored for the next iteration.

3. The ambiguities are resolved for all baselines separately using tropospheric and ionospheric corrections. The coordinates and initial tropospheric delays from the previous iteration are used as apriori values in this step.
4. The fourth and final iteration generates final estimates of coordinates of each station, ZTD parameters, tropospheric gradient parameters and DD residuals for every epoch using the IF linear combination. The L1 and L2 ambiguities solved in the previous iteration are then used in the final least squares adjustment.

This research used the hourly ZTD, DD residuals and coordinate estimates from the final output for further analysis on the structure and distribution of WV in the troposphere. Both the 1D and 4D structure of WV were reconstructed with a high temporal resolution. PWV estimation defining the amount of WV in the vertical column above the GPS station provided a 1D resolution over the network (see Section 2.4.1). The 4D structure was reconstructed using a Kalman filter based GPS tomographic modelling technique (see Chapter 4).

2.4. WV estimation

2.4.1. Ground-based GPS estimation of PWV

Ground-based GPS measurements have been proven to provide a robust measure of the integrated amount of WV in the atmosphere with a high accuracy, continuous and with an all-weather observing capability. The integrated amount of WV at the zenith has been validated by microwave WV radiometers (WVRs) to an agreement of 1 – 2 mm RMS (Rocken et al., 1995). Similar validation results have been carried out using radiosonde PWV estimates (Tregoning et al., 1998). Quantification studies for line-of-sight integrated WV estimates to a GPS satellite have also been investigated. The GPS slant integrated WV (SIWV) estimates and WVR estimates agreed to an accuracy of 1.3 mm RMS (Alber et al., 2000; Braun et al., 2003).

A study by Bai (2004) explored the feasibility and near-real-time (NRT) capability of ground-based GPS sensing of atmospheric PWV within the Australian region. The Australian Regional GPS Network (ARGN) was used to assess the performance of GPS derived PWV estimates against radiosonde PWV solutions. The final results and accuracies reflect those attained in the original proof of concept studies: Bevis et al. (1992), Rocken et al. (1995) Tregoning et al. (1998), Gradinarsky (2002) and Braun (2004).

GPS signals are delayed and bent due to the variations in refractive index when they propagate through different layers of the atmosphere to a ground receiver. There are dispersive effects within the

ionosphere, which can be eliminated using an ionosphere-free linear combination of the dual frequency measurements (see section 2.3.1.2). The remaining average ZTD can be divided into hydrostatic and wet delay mapped to the zenith (Niell, 1996). The Saastamoinen hydrostatic delay model can be used to accurately estimate the magnitude of the delay caused by the hydrostatic component in the zenith direction (Saastamoinen, 1972), i.e. it can be extracted from the total tropospheric delay. The remaining component is attributed to the ZWD and is an estimate of the total delay due to WV content in the troposphere. This is proportional to the integrated amount of PWV (Hofmann-Wellenhof et al., 2001).

The Bernese GPS data processing software package is used to process the final ZTD from all path delays during a time period (t) at a GPS station (a) by eliminating all other errors (Dach et al., 2007). The ZHD is subtracted from the ZTD to obtain the ZWD:

$$\mathrm{ZTD}_a = \mathrm{ZWD}_a + \mathrm{ZHD}_a \tag{2.27}$$

Using the surface pressure measurements from synoptic weather stations and the associated mean sea level height (H) and geographic latitude (ϕ) of the GPS station (a), the ZHD can be computed via the following equation (Saastamoinen, 1972),

$$\mathrm{ZHD_a} = [(0.0022768 \pm 0.0000015)\mathrm{m\ hPa^{-1}}] \cdot \frac{\mathrm{p_0}}{\mathrm{f}(\phi, \mathrm{H})} \tag{2.28}$$

using,

$$\mathrm{f}(\phi, \mathrm{H}) = 1 - 0.002652\cos(2\phi) - 0.000285\mathrm{H} \tag{2.29}$$

where

$\mathrm{p_0}$	is the pressure at the antenna height of (a) in hPa
ϕ	is the latitude of the GPS station (a) in degrees
H	is the height of the GPS antenna above MSL (m)

Pressure measurements at the height of the GPS receiver are imperative to the accuracy of the hydrostatic model and consequentially the accuracy of the ZWD determination. Surface pressure and temperature measurements are provided by the synoptic weather observation station infrastructure and interpolated values from NWP models.

Once the ZWD is obtained from the ZTD, the PWV estimate can be computed using the following factor Π (Bevis et al., 1992; Kleijer, 2004; Bai, 2004 and Lutz, 2008).

$$\Pi = \frac{10^6}{\rho_w \cdot R_v \left(\frac{k_3}{T_m} + k'_2\right)} \tag{2.30}$$

where,

Π	is the scale factor (kgm^{-3})
ρ_w	is the density of liquid water (kgm^{-3})
R_v	is the specific gas constant of WV ($Jkg^{-1}K^{-1}$)
m_w	is the molar mass of WV (m_w=18.01528 $kgkmol^{-1}$)
k_3	is the physical constant (K^2hPa^{-1})
k'_2	is the physical constant ($KhPa^{-1}$)
T_m	is the mean weighted temperature at the zenith above station (a) (K)

T_m is the mean weighted temperature of the atmosphere along the zenith profile above the antenna, which is modelled as.

$$T_m = 70.2 + 0.72T_0 \quad (2.31)$$

where T_0 is the temperature at GPS antenna (K).

Therefore, PWV can be expressed as:

$$PWV = ZWD \cdot \Pi \quad (2.32)$$

The ratio of PWV to ZWD is approximately in the order of 1:1.66, meaning a PWV value of 1 mm would correspond to a ZWD value of 6.5 mm (Braun, 2004). See Figure 2.4.

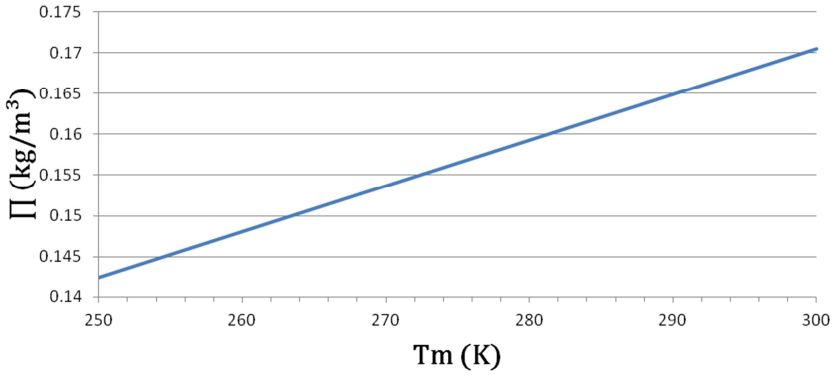

Figure 2.4: Ratio between ZWD and PWV with respect to mean temperature (Tm). The relationship is linear.

2.4.2. Radiosonde estimation of PWV

It is possible to use radiosonde profile observations to estimate the integrated value of PWV in the direction of the station's zenith. In order to provide comparisons with GPS, the Australian radiosonde network was used (see Section 3.3.1). An averaging approach was adopted for this research, which uses an integration method for the radiosonde profile.

Chapter 3 will present a validation study for the GPSnet estimates of PWV in the Victorian region over a one month period. This time span also covers the formation and evolution of a severe weather event. Radiosonde observations from the Melbourne International Airport (MELB) were used as truth data for the comparison and quality control in this thesis. Two secondary radiosonde stations located at Wagga Wagga (WAWA) and Mt Gambier (MTGA), were used for the study of PWV estimates from GPSnet.

The radiosonde balloon attains a direct measurement of pressure (P), temperature (K) and relative humidity (%) at associated geopotential heights, creating a vertical profile. This vertical profile can be integrated to produce an estimate of PWV above the radiosonde station, which is then used as the truth data for the GPS comparison. To calculate PWV, the integrated WV (IWV) along the path of the sounding balloon needs to be determined using the expression below:

$$IWV = \int \rho_v \cdot dh \tag{2.33}$$

where ρ_v is the density of WV.

IWV can then be mapped to the zenith to attain PWV using the following formula:

$$PWV = \frac{IWV}{\rho_w} \tag{2.34}$$

where ρ_w is the density of the liquid water.

The equation for WV density (ρ_v) is defined as:

$$\rho_v = \frac{P_v}{R_v \cdot T} \tag{2.35}$$

where R_v= 461.*495* $J{\cdot}K^{-1} \cdot kg^{-1}$ is the specific gas constant for WV, and P_v is the partial pressure of WV. P_v is computed using relative humidity (*RH*) as a percentage and absolute temperature (*T*) in Kelvin using the following formula (Bai, 2004).

$$P_v = RH \cdot \exp(-37.2465 + 0.213166 \cdot T - 2.56908 \cdot 10^{-4} \cdot T^2) \tag{2.36}$$

Using the discrete series of measurements along the sounding balloon path the radiosonde data profile can be divided into layers between each geopotential height. P_v *and* T are used to determine the WV density for each discrete layer. This study assumes linear WV density variation in each layer. The integrated approximation of PWV can be calculated via:

$$PWV = \frac{1}{\rho_w} \sum \frac{(h_{j+1} - h_j)(\rho_v^{j+1} + \rho_v^{j})}{2} \tag{2.37}$$

where j+1 and j represent the top and bottom values of each layer for height and WV density.

2.4.3. Co-location of datasets

Theoretically, the meteorological sensor and the GPS antenna should be physically located at the same point in order to attain optimal GPS-derived PWV estimates. In this study however, each co-located station incurs a few kilometres separation. Furthermore, there are also separations between the GPS and radiosonde stations for every co-located pair. A perfect co-location of the two data sets will ensure a sound benchmark for the experimental comparison and provide minimal bias. However, the separations mentioned above are minimum for this study and have almost negligible effect on results.

Geographically, there is a horizontal and vertical difference between the GPS station and radiosonde launch site. Theoretically, both lateral and vertical separation should be accounted for, however in this study only the height component is co-located since the lateral component is deemed to have no practical temperature or pressure change due to the very slight lateral separation.

The following provides temperature and pressure estimates for the GPS station site using radiosonde solutions (Bai, 2004).

$$PP_{QNH} = P_o \left\{ \left(\frac{P_{QFE}}{P_0} \right)^{Ru/g} + \frac{H_{stn} u}{T_0} \right\}^{g/Ru} \tag{2.38}$$

where:

P_{QNH} is the QHE pressure (mbar), and is the pressure measured at station then reduced down to mean sea level pressure

P_{QFE} is the QHE pressure (mbar), and is the mean sea level pressure corrected for temperature, adjusted for a specific site or datum

R = 287.04 $m^2/°Csec^2$

u = 0.0065 m/sec^2

g = 9.80655 m/sec^2

H_{stn} is the station height in metres

T_0 = 288.16°K

The co-location equation T_{rad} and P_{QNH} are used to estimate the temperature (T_{GPS}) and pressure (P_{GPS}) for the GPS station.

The T_{GPS} is approximated using the following equation:

$$\Delta T = \beta \cdot \Delta H \tag{2.39}$$

Where β is the temperature lapse rate and ΔH is the height difference between stations. Bai (2004) concluded that a height difference of 45 m produced very minimal difference to the PWV solution. Therefore the temperature changes due to height were not considered and so this study assumes T_{rad} to be used as T_{GPS}.

2.5. Summary

This chapter introduced GPS meteorological fundamentals and the theory of GPS microwave signal propagation in the atmosphere. Atmospheric refractivity can be modelled using these propagating GPS signals as they are delayed and bent due to the variations in refractive index of the ionosphere and troposphere causing displacement in phase and amplitude. This theory is fundamental to this research as accurate SPD estimates can be extracted from ground-based GPS observations using the Bernese GPS processing software and the DD approach. These path delay estimates are the primary parameter for ground-based GPS meteorology.

This chapter also introduced fundamental empirical atmospheric models including the most commonly used Saastamoinen model. The key aspects of the Bernese GPS processing software and associated BPE were presented. Finally, the theory of integrating radiosonde measurements to estimate measurements of PWV was also introduced.

The fundamentals of GPS meteorology presented in this chapter provide the theoretical background for this new study of severe weather in Australia. The ensuing tropospheric delay estimates were used in this research to attain, 1) estimates of PWV for an integral measurement of WV in the vertical column above the GPS station, and 2) a reconstruction of 4D dynamics of wet refractivity using GPS tomography.

Chapter 3. WV observation systems

3.1. Overview

This section first introduces the various observation systems used in this research and defines their key features, including: affiliation, availability, temporal resolution, geometric distribution, and main parameters. The observation systems used for this research include:

- Ground-based GPS CORS networks;
- Space-borne RO;
- Australian radiosonde network;
- Synoptic weather observation network; and,
- NWP analysis model.

The ground-based GPS data is provided by Vicmap position - GPSnet from the Department of Environment and Primary Industries, GPS RO data is obtained from COSMIC, and radiosonde, synoptic weather observation network and NWP analysis data from the Australian Bureau of Meteorology.

Secondly, analysis and results are presented on an investigation into the accuracy of ground-based GPS-derived PWV estimates using the GPSnet. This accuracy analysis is conducted from 15 Dec. 2010 to 15 Jan. 2011. The GPS-derived PWV estimates are validated against radiosonde estimates. The final results reflect the high accuracy and sensitivity of measuring PWV content in 1D over time during stable and unstable atmospheric conditions, and the potential benefit for severe weather monitoring applications.

3.2. GPS platforms

GPS observation systems have rapidly advanced and are currently used for many different applications, globally. As stated previously, GPS has been used as a robust tool for measuring the integrated amount of WV in the atmosphere with high accuracy, under all weather conditions and continuous operability. It is currently regarded as one of the most important atmospheric remote sensing technologies available for weather forecasting and climatology research due to the rapidly increasing density of GPS CORS networks, the development of space-borne GPS technologies, and

the continuous operability (Bevis et al., 1992; Ware et al., 1998; Tregoning et al., 1998; Gradinarsky, 2002; Le Marshall et al., 2010).

3.2.1. Ground-based GPS CORS networks

Ground-based GPS CORS networks are the combination of collaborative GPS sites that support Global Navigation Satellite Systems (GNSS) users in the capacity of real-time or post processing. These networks are established on local, state, national and international scales. Three GNSS networks relevant to this research include:

- International GNSS Service (IGS);
- National Positioning Infrastructure (NPI); and,
- Victorian GPS CORS network GPSnet.

The framework and parameters associated with each network are described below.

International GNSS Service (IGS)

The IGS is a federation of more than 200 collaborative worldwide agencies that combine resources and permanent GPS and GLONASS station data to generate precise GPS and GLONASS products. The IGS aims to provide the highest quality data and products as the standard for Global Navigation Satellite Systems (GNSS) in support of Earth science research, multidisciplinary applications, and education. Currently the IGS includes GPS and the Russian GLONASS, and intends to incorporate future GNSS (Dow et al., 2009). Figure 3.1 shows the IGS network as of Oct 2012.

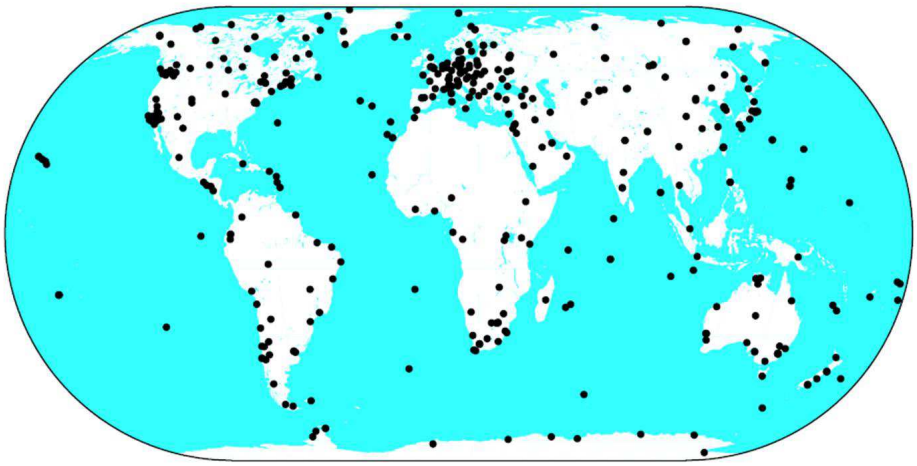

Figure 3.1: The current IGS Reference Frame (RF) stations (2012) (based on Daw et al., 2009).

National Positioning Infrastructure (NPI)

Currently Australia and New Zealand are establishing a NPI, which will potentially provide 2 cm positional accuracy anywhere in the Australian/New Zealand regions in real-time. This accuracy is subject to the operability of the existing GPS system (USA) plus the new systems of Galileo (EU), GLONASS (Russia), Compass (China), QZSS (Japan) and IRNSS (India). The NPI will also have a network of permanent satellite navigation tracking stations. The infrastructure will provide a world-class benchmark for innovation in such sectors as agriculture, mining, construction and climate change. It will also provide the basis for logistics, navigation, transport, emergency management and security.

Precise positioning for geodetic, surveying and machine guidance applications requires a substantial investment in ground infrastructure in the form of GPS CORS. The Australian federal government and state governments as well as the government of New Zealand are currently establishing CORS networks in high-value commercial markets. The foundation infrastructure in Australia is funded under the AuScope initiative, and there are now more than 250 stable CORS across Australia and New Zealand as part of this effort (Ball, 2011). This initiative will significantly enhance the capability of GNSS for meteorological purposes, due to the larger coverage, higher density and the imminent inclusion of additional GNSS satellite constellations.

Victorian GPS CORS network GPSnet

GPSnet is a Victorian State government initiative and comprises of approximately 110 dual-frequency geodetic grade GPS receivers in continuous operation (Department of Environment and Primary Industries, 2013). Dual frequency measurements are the key to high accuracy GPS positioning and ultimately GPS meteorology. The network is highly dense for Australian standards and is one of the most sophisticated in the southern hemisphere. Therefore, it has the potential to be a major resource for meteorological data. Figure 3.2 presents the distribution of the current GPSnet infrastructure. In this research, ground-based GPS-derived PWV were estimated using the GPSnet. This infrastructure was also used for the tomographic testing of simulated and real data.

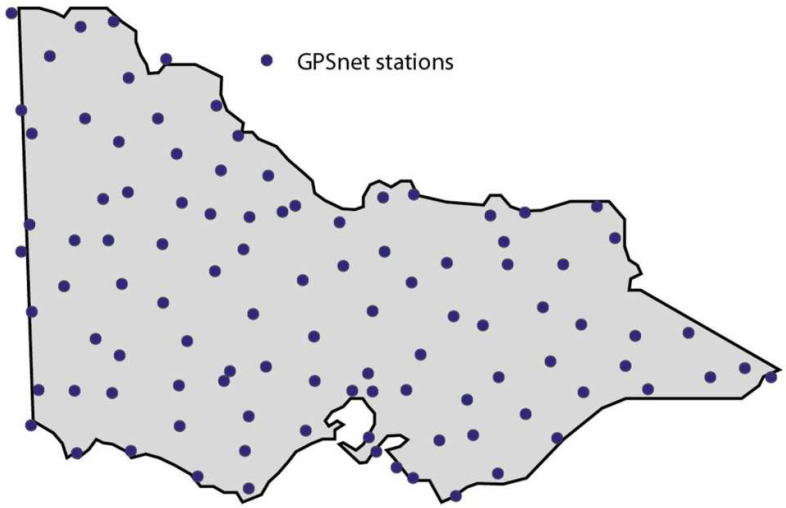

Figure 3.2: Distribution of stations for the Victorian GPSnet CORS state-wide network (Department of Environment and Primary Industries, 2013).

3.2.2. Space-borne GPS RO

The development of high-performance GPS instrumentation on-board LEO satellites has created an operational method of remotely sensing the Earth's atmosphere using the tested theory of GPS RO (Kursinski et al., 1995; Wickert et al., 2001). The first theoretical and practical studies where carried out by the Jet Propulsion Lab (JPL) and described in Melbourne et al. (1994) and Kursinski et al. (1995, 1997, 2001).

GPS RO techniques are predominantly used to determine excess phases and bending of the occulted GPS signals in relation to the Earth's atmospheric limb. As a GPS satellite rises or sets behind the Earth's atmospheric limb the transmitted microwave signal is delayed and bent due to the gradient of refractive index associated with the ionosphere and the neutral atmosphere (Figure 3.3). This delay and bending can be inverted with an Abel integral inversion to obtain profiles of refractivity in the ionosphere and neutral atmosphere with a high accuracy and also a high vertical resolution (Hajj et al., 2002). Further processing with additional background models can produce profiles of temperature and WV in the troposphere. Each occultation event has a time period of 1 – 2 minutes as the sounding plane sweeps (approximately) vertically through the atmospheric layers. The profiles are derived from the accurately measured L1 and L2 phase delays on the occulting signals. The magnitude of this delay caused by the atmosphere only is termed the excess atmospheric phase delay (Kursinski, 1997; Kuo et al., 2004).

GPS RO observations can be input as an additional profile information source in the observation matrix for GPS tomographic modelling using AWATOS 2 in order to analyse the potential benefits in the reconstruction of wet refractivity fields (see Chapter 7).

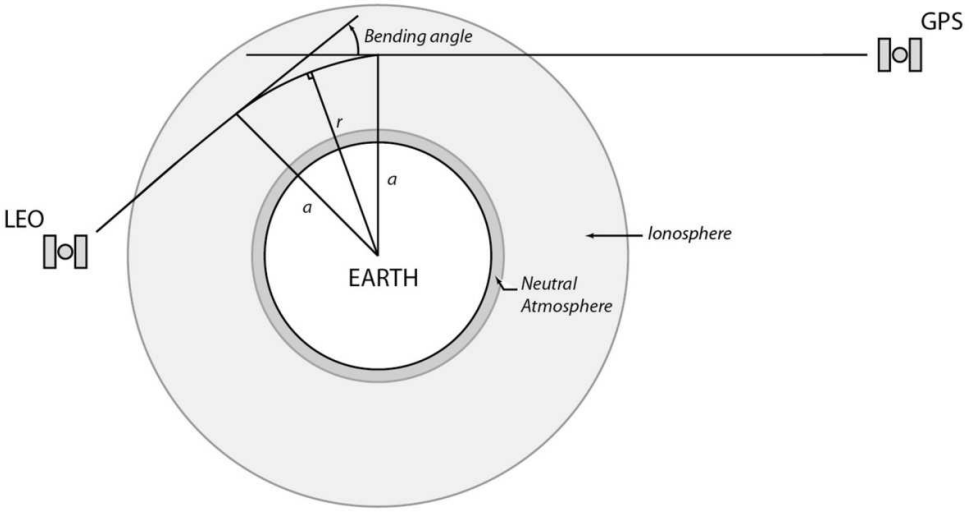

Figure 3.3: GPS RO geometry of the occulted propagating signal and significance of bending angle due to the effects of refractivity in the atmospheric layers.

3.2.3. Combination of GPS platforms

GPS has become one of the most important observing systems for weather forecasting and climatology. The ground-based and space-borne GPS technologies are complementary in many ways. These include:

- *Horizontal and vertical information capture:* Ground-based GPS atmospheric sounding resolves the horizontal spatial distribution of PWV at each station with a high accuracy and reliability. This horizontal resolution is complemented by space-borne GPS RO profiles, which provide a high vertical resolution due to the near vertical sounding geometry and helps define the vertical structure of the tomographic model to optimise accuracy.
- *Spatial and temporal continuity:* Ground-based GPS observations can provide continuous data, whereas space-borne GPS RO soundings are events from which the distribution is determined by the geometry of both LEO and GPS constellations. Spatial and temporal continuity will be advantageous in the context of severe weather monitoring.
- *Heterogeneity/homogeneity:* Ground-based GPS observations are restricted to land and therefore, cannot provide any solutions over oceans, while space-borne GPS RO events are global and tend to be geographically homogenous.

This research studies the complementary nature of various observation methods to enhance and construct a robust observation platform for resolving the spatio-temporal distribution of WV and wet refractivity.

3.3. Meteorological sensors

In this research two major meteorological sensors were used for modelling parameters, assimilation as additional observations and validation purposes. They are:

- The Australian radiosonde network; and,
- Ground-based synoptic weather observation network.

Both the radiosonde network and synoptic weather observation network data were provided by the Australian Bureau of Meteorology. Radiosonde profiles were used throughout this research to provide truth data for evaluation methods because of its high accuracy and vertical resolution. Unfortunately, the density of the ground-based synoptic weather observation network is insufficient for this research, as precise meteorological parameter observations were needed at the antenna of every GPSnet station. These are necessary for precise estimation and elimination of the hydrostatic delay component of the total path delay as discussed in Section 4.3.3. For this reason interpolated NWP analysis data was used for the estimation of meteorological parameters for the GPSnet network as discussed in Section 3.4.

3.3.1. The Australian radiosonde network

The radiosonde technique is able to deliver profiles of meteorological parameters with a high accuracy and vertical resolution using a sensor attached to an automatic radio-sounding balloon. Data collected by the sensor is transmitted via radio link back to a ground receiving station. Accurate observations of pressure, temperature and relative humidity can be detected at increasing altitudes from the ground up to approximately 30 km. Because of the high vertical resolution of this direct measurement method, radiosonde is a very important observational tool that can be assimilated with forecast models and also used for evaluation studies of WV retrieval using ground and remote sensing techniques. Radiosonde WV measurements are also used in the context of climate research, including studies of trends in upper tropospheric WV, and stratospheric dehydration and tropospheric-stratospheric exchange processes (Miloshevich et al., 2006 and Zhang et al., 2011).

Figure 3.4 presents the current Australian radiosonde network as well as the sites located in the greater Victorian region. The limitation of radiosonde is its restricted coverage and low spatial and temporal resolution of data due to the high maintenance and cost to keep a site operational. Many

regions including polar, mountains, desert and unpopulated areas around the globe experience similar problems with ground-based observation networks (Kuo et al., 2004 and Fu, 2011). Figure 3.4 also depicts the sparse distribution of radiosonde stations nationally, especially in the centre of Australia where the region is dominated by desert. A bias exists for stations located towards the coastline where most of the population reside. Only 3 radiosonde stations were operational in the greater Victorian region – located in Melbourne (MELB), Wagga Wagga (WAWA) and Mt Gambier (MTGA). These sites were used in this research as truth data for a validation study of three co-located GPS stations. A poor temporal resolution is also a major limitation, with two radiosonde observations per day, typically occurring at 11:00 and 23:00 (UTC).

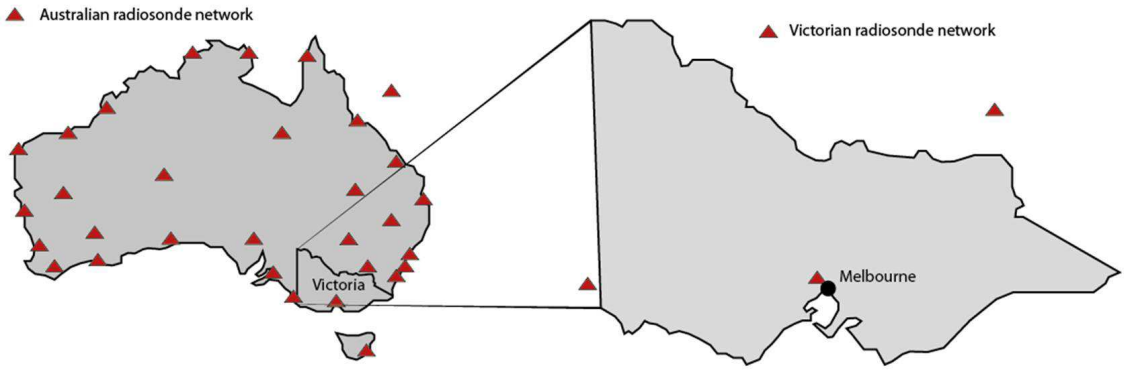

Figure 3.4: Distribution of the Australian radiosonde network (left) and, radiosonde sites in the greater Victorian region (right).

Table 3.1 presents the associated accuracies at increasing altitudes of each meteorological parameter detected using radiosonde. The radiosonde technique is highly accurate for observations of the troposphere with a 1 – 2 hPa accuracy for pressure, 0.5°C accuracy for temperature and 5% accuracy for relative humidity.

Table 3.1: Radiosonde measurement accuracies (National Oceanic and Atmospheric Administration, 1997)

Variable	**Range**	**Accuracy**
Pressure	~1000 hPa (surface) – 100 hPa	1 – 2 hPa
	100 – 10 hPa	2 %
Temperature	~1000 hPa (surface) – 100 hPa	0.5 °C
	100 – 10 hPa	1 °C
Relative Humidity	Troposhere	5 %

As mentioned previously, radiosonde profiles from stations within the greater Victorian region were used in this thesis as truth data for evaluation purposes due to high accuracy and vertical resolution. This profile data will also be tested as an additional point observation input for the observation model of the GPS tomography processing (see Chapter 7).

3.3.2. Ground-based synoptic weather observation network

The synoptic weather observation station network within Victoria consisted of 69 operational stations (Figure 3.5). Data from these automatic weather stations are provided by the Australian Bureau of Meteorology, with a temporal resolution of 3 hours. The synoptic network provides pressure (hPa), temperature (K) and partial WV pressure (hPa) parameters.

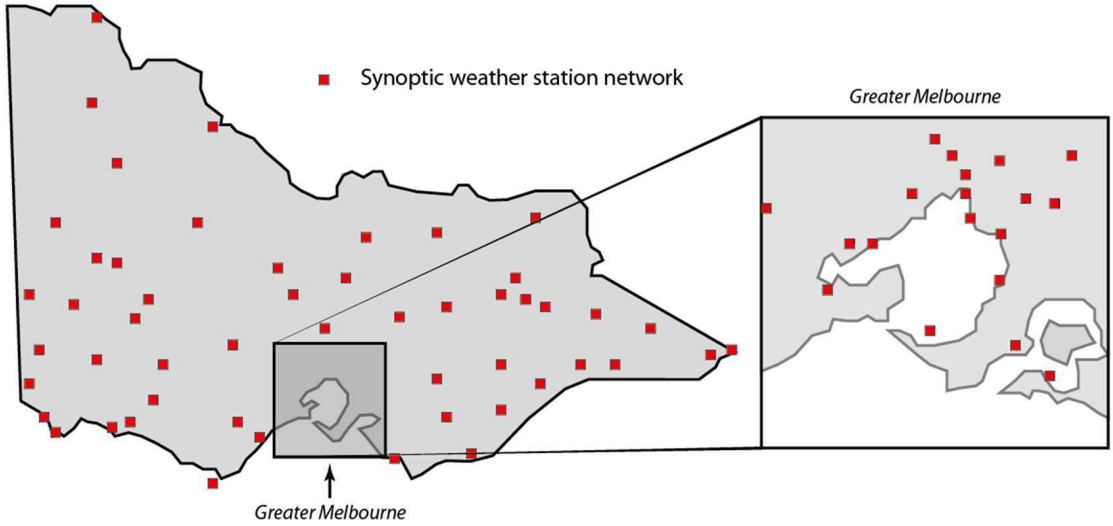

Figure 3.5: Distribution of the Victorian synoptic weather station network.

These observations, when co-located with the GPS receiver, can provide sufficient ground meteorological information to eliminate the hydrostatic delay from the GPS path delay to extract the wet delay component relating to WV. In theory, it would be preferable to have every CORS GPS station equipped with a synoptic meteorological sensor, however, in Australia and more relevantly Victoria, this is far from the case. During the Jan 2011 campaign (see Section 3.5) only 20% of CORS GPS receivers had a co-located synoptic station within a 20 km radius. For the PWV estimates at each station and the tomographic modelling procedures (Chapter 6 and 7) accurate meteorological values of temperature, pressure and relative humidity were needed at the location of every GPSnet station in order to estimate SWD. Therefore, an interpolation method is adopted using grid data from the Australian NWP model ACCESS-R (see Section 4.3).

The synoptic data however, was used for the Saastamoinen modelling of hydrostatic delay (Eq. (2.28)) in the estimation of GPS-derived PWV for the ground-based validation (Section 3.5).

Figures 3.6, 3.7 and 3.8 present the synoptic observations of pressure (hPa), temperature (K) and WV partial pressure (hPa) from the Melbourne observatory (MOBS) over a 60-day period from 1 Dec 2010 to 31 January 2011. These measurements were limited to ground observations and present the relative trend for the Melbourne region at surface level. It should be noted that unstable atmospheric conditions occurred from 8 – 15 Jan 2011 due to a severe weather phenomena.

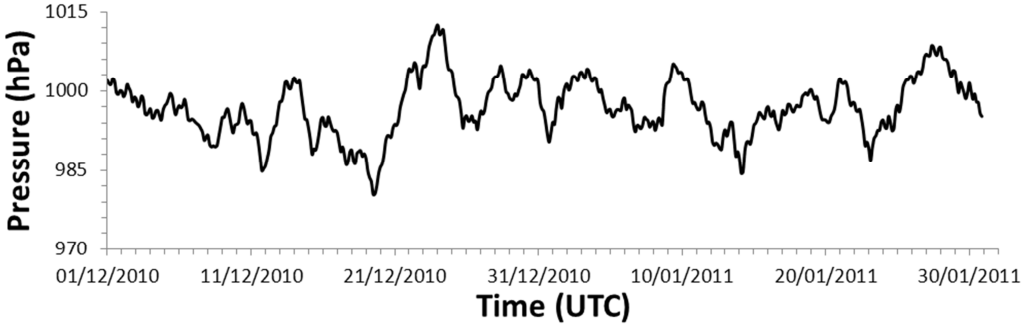

Figure 3.6: Pressure profile from the Melbourne Observatory (MOBS) synoptic station from 1 Dec 2010 to 31 January 2011. Data is produced with a temporal resolution of 3 hours.

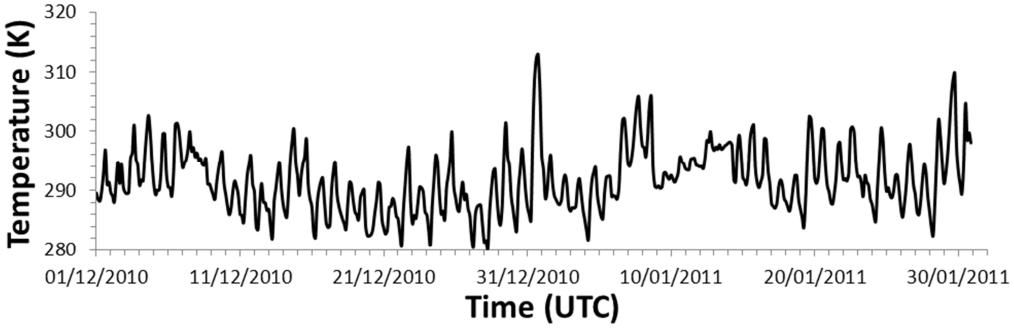

Figure 3.7: Temperature profile from the Melbourne Observatory (MOBS) synoptic station from 1 Dec 2010 to 31 January 2011. Data is produced with a temporal resolution of 3 hours.

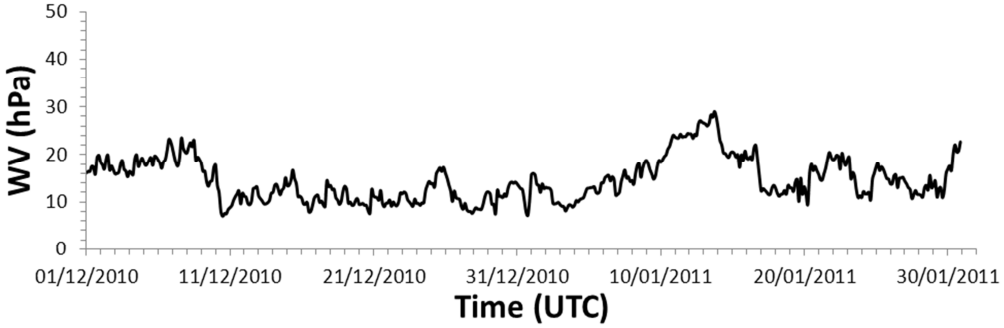

Figure 3.8: Water vapour profile from the Melbourne Observatory (MOBS) synoptic station from 1 Dec 2010 to 31 January 2011. Data is produced with a temporal resolution of 3 hours.

These meteorological measures can be used to estimate the dry and wet effects within the troposphere represented as the sum of total refractivity. Figures 3.9, 3.10 and 3.11 present the application of these meteorological observations in the segregated form of total, dry and wet refractivities, respectively. The trend of dry refractivity is quite stable and is not affected by varying densities of WV as opposed to wet refractivity, which was dominated by these densities.

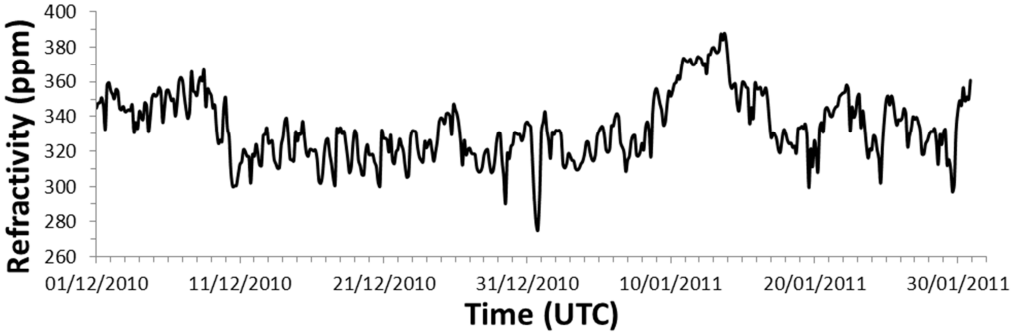

Figure 3.9: Refractivity estimates using synoptic measurements with the Saastamoinen model. Synoptic data is from the Melbourne Observatory (MOBS) station from 1 Dec 2010 to 31 January 2011. Data is produced with a temporal resolution of 3 hours.

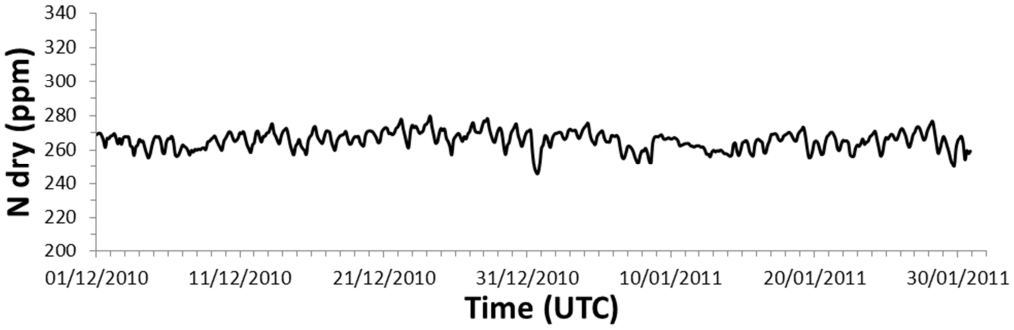

Figure 3.10: Dry refractivity estimates using synoptic measurements with the Saastamoinen model. Synoptic data is from the Melbourne Observatory (MOBS) station from 1 Dec 2010 to 31 January 2011. Data is produced with a temporal resolution of 3 hours.

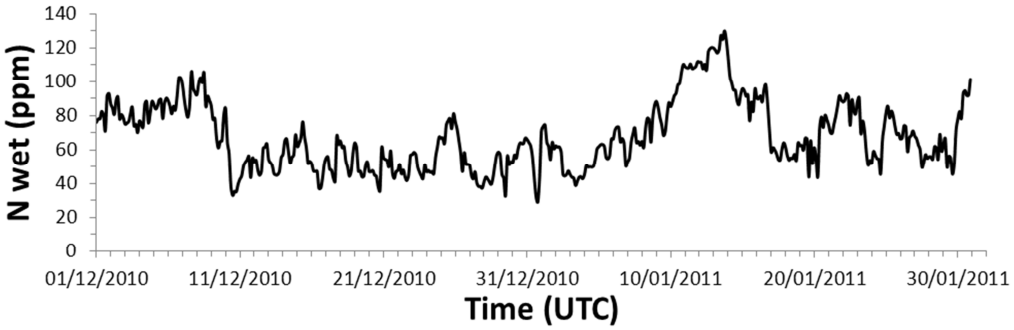

Figure 3.11: Wet refractivity estimates using synoptic measurements with the Saastamoinen model. Synoptic data is from the Melbourne Observatory (MOBS) station from 1 Dec 2010 to 31 January 2011. Data is produced with a temporal resolution of 3 hours.

3.4. NWP model

3.4.1. The Australian ACCESS grid model

The Australian NWP model named ACCESS was tested by the Centre for Australian Weather and Climate Research (CAWCR) and implemented operationally by the Operational Development Subsection of National Meteorological & Oceanographic Centre (NMOC) from the Australian Bureau of Meteorology. Table 3.2 lists the available ACCESS suite of models, domain and resolution with the domains presented in Figure 3.12.

For this research the ACCESS-R analysis data available with 6-hour resolution is used for the interpolation of meteorological parameters for each GPS antenna location. This is for the modelling of hydrostatic delay in the zenith direction to extract the wet component as per Eq. (2.28).

Table 3.2: ACCESS model type, domain and resolution.

Model	**Domain**	**Resolution**
ACCESS-G	Global	~80 km
ACCESS-T	Tropical	0.375° (~37.5 km)
ACCESS-R	Regional	0.11° (~12 km)
ACCESS-A	Australia	0.11° (~12 km)
ACCESS-C	City	0.05° (~5 km)

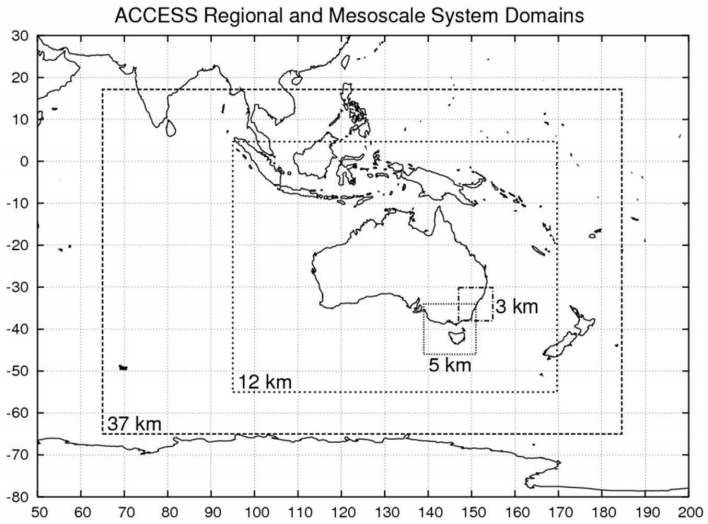

Figure 3.12: Location of ACCESS model domains and resolutions with respect to Australia

3.4.2. Interpolation procedure for ACCESS-R

Due to the co-location problem with the current ground-based synoptic weather observation network as discussed in section 3.3.2, the ACCESS-R analysis data were used to interpolate meteorological parameters to the height of the GPS station. This data was used to eliminate the hydrostatic delay in the observation equation (see Eq. (2.28)) for all ZTD estimates. This information was also used for all tomographic processing presented in this thesis. The interpolated meteorological parameters from NWP analysis were also tested as an additional point observation input for the observation model of the GPS tomography processing strategy (see Chapter 7).

As discuss previously, the Australian NWP model: ACCESS-R analysis is structured in a geopotential grid format with a horizontal resolution of 12 km. The meteorological parameters for the closest 4 grid nodes were used for the interpolation (Bosy et al., 2010). The value for a particular location's parameter is interpolated as a weighted average:

$$\bar{s} = \frac{\sum_{i=1}^{n} s_i w_i}{\sum_{i=1}^{n} w_i} \tag{3.1}$$

where w_i is the weight value and is calculated differently for temperature (T), relative humidity (RH) and pressure (P) using empirical formulae given by Borkowski et al. (2002).

- Temperature (T):

$$w_i = (h - h_i)^{-4} \tag{3.2}$$

where h and h_i are the heights of the interpolated point and ACCESS grid points, respectively.

- Relative Humidity (RH):

$$w_i = \sqrt{[(x - x_i)^2 + (y - y_i)^2 + (z - z_i)^2]} \quad (3.3)$$

where x and y are the horizontal coordinates of the interpolated point and x_i and y_i are coordinates of the ACCESS grid point used for the interpolation.

- Pressure (P):

$$w_i = \sqrt{[(x - x_i)^2 + (y - y_i)^2]} \quad (3.4)$$

In this case the values of pressure are calculated from ACCESS grid data using barometric levelling formula (Rankine and Bamber, 2009):

$$\log P_i = \log P_{COA_i} + \frac{h_i - h}{18400\left(1 + \frac{T + T_i}{546}\right)} \quad (3.5)$$

The weighted average is then determined from the calculated values (Bosy et al. 2010).

Values of temperature, pressure and relative humidity were interpolated for the location of every GPSnet station in Victoria at a temporal resolution of 1 hour.

3.5. Ground-based GPS validation study

Sensing WV using GPS meteorology is fundamental to this research. Therefore, a validation study was investigated to determine the accuracy of using ground-based GPS for depicting PWV in the Victorian region. This study compared 3 GPS CORS stations, Keilor Park (KEPK), Albury (ALBU), and Nelson (NELN) from the GPSnet, with three co-located radiosonde stations operated by the Australian Bureau of Meteorology. Ground-based GPS-derived PWV estimates from these 3 GPSnet stations were computed over a 1-month period (15 Dec. 2010 to 15 Jan. 2011) and provided approximately 700 measurements per station. Both KEPK and ALBU incurred 2-days of down time while NELN experienced 3. The 3 co-located radiosonde stations used for this investigation were Melbourne International Airport (MELB), Wagga Wagga (WAWA) and Mt Gambier (MTGA), respectively. Two radiosonde observations per day were obtained from the MELB station and one per day from both the WAWA and MTGA stations. The position of each co-located GPS and radiosonde pairing for validation of GPS-derived PWV is presented in Figure 3.13. Formulae for computing the GPS and radiosonde estimates of PWV, including a data co-location method, can be found in Section 2.4.1 and 2.4.2, respectively.

The validation campaign was tested in both stable and unstable atmospheric conditions. A severe weather event occurred from the 8 – 15 January 2011, which tested the durability of GPS-derived PWV during severe weather.

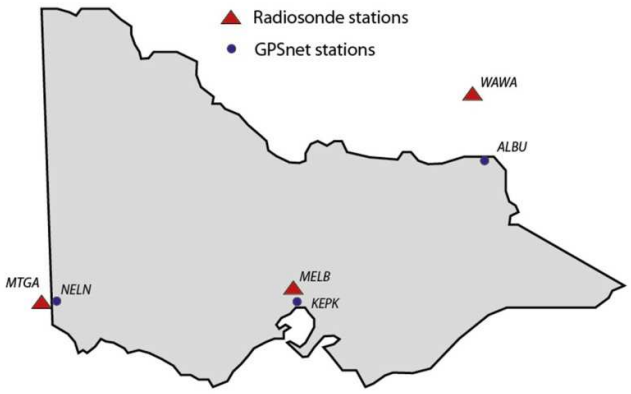

Figure 3.13: locations of each GPS and radiosonde pairing for validation of PWV estimates.

Table 3.3 provides the MGA map coordinates and Australian height datum (AHD) heights (E, N, H) of all GPS and radiosonde stations in the experiment and the horizontal and vertical separations between sites is also highlighted. The largest horizontal separation is approximately 112 km and the largest vertical separation is 0.05 km. The results showed no adverse errors due to these geographical differences so all three pairs of stations were safely assumed to be co-located.

Table 3.3: MGA coordinates and separation for each GPS & radiosonde validation pair.

Instrument	**Station**	**Easting (m)**	**Northing (m)**	**Height (m)**
GPS	KEPK	310 323	5 822 951	90
Radiosonde	MELB	308 617	5 828 582	141
Separation			**6 km**	**51 m**
GPS	ALBU	492 396	6 007 452	197
Radiosonde	WAWA	542 069	6 108 684	212
Separation			**112 km**	**15 m**
GPS	NELN	500 536	5 788 883	10
Radiosonde	MTGA	480 079	5 822 514	63
Separation			**39 km**	**53 m**

Parameters of the Bernese GPS processing were adopted for this validation analysis and were expressed in Table 3.4. A daily BPE was created for the automated processing of the 30-day campaign.

Table 3.4: Parameters of the Bernese GPS processing software

Parameter *GPS processing*	**Value**
Processing period	15 Dec. 2010 – 15 Jan. 2011
Processing method	Double difference
Number of stations	78
Baseline strategy	Maximum number of observations
Estimation period	Daily
Ionosphere correction	Ionosphere free linear (L_3) combination
Orbits	IGS precise orbits
Sampling rate	30 s
Cutoff angle	5°
Additional corrections	Ocean loading, solid Earth tide, axis rotation corrections
A priori model	Saastamoinen dry model
Mapping function	Niell mapping function

The ZTDs from GPS processing were estimated every hour using Bernese V5.0. Surface meteorological data from the Victorian synoptic weather station network were then used to calculate the dry component in the total delay, leaving the ZWD (Δ_a^{ZWD}) to be solved for. These were then converted into PWV using the dimensionless conversion factor Π (Bevis et al., 1992).

As discussed in Section 2.4.2, radiosonde observations can also be used to estimate PWV through integrating the vertical profile of meteorological measurements. As a result, radiosonde data were used as a reference for this comparison. The theoretical accuracy of the radiosonde-derived PWV estimates has been estimated to be 1.2 mm (Liu, 2000; Bai, 2004).

3.5.1. Results and discussion

Figures 3.14, 3.15 and 3.16 present the results from the 30-day PWV analysis of the aforementioned 3 co-located GPS stations. Each time series shows the evolution of GPS-derived PWV estimates with a one hour resolution against the co-located radiosonde-derived PWV integral. It appears that the two observation methods are robust. It is also evident that the GPS-derived PWV estimates have a much higher temporal resolution. This method quickly identifies early rises in unstable conditions due to humid air convection in the formation of severe weather. Figure 3.14 shows the results for MOBS and radiosonde PWV estimates with 1 and 12 hour resolutions, respectively. The initial increase in warm, moist air during the unstable conditions of severe weather is evident from 8 Jan 2011. This is because the dynamics of severe convection drives WV up through the atmospheric layers creating

higher moisture content in the vertical column integral. Consequently, PWV rises from an average of 17 mm during a stable atmosphere to a maximum of 62 mm during the severe thunderstorm and unstable atmosphere period. This initial result highlights the ability of GPS state-wide networks to map the continuous passage of PWV in the pre-frontal air mass that is a precursor to severe weather at a high spatial and temporal resolution. This could lead to significant benefits in the early detection and monitoring of the formation and evolution of severe storm convection and precipitation systems.

Figures 3.15 and 3.16 present the results for ALBU and NELN GPS stations, respectively. The temporal resolution of GPS-derived PWV is again one hour, however, the radiosonde stations only produced one radiosonde observation every 24 hours. Therefore, a bias was introduced based on a singular time of day comparison. Again, pronounced increases in PWV are evident during the severe weather period.

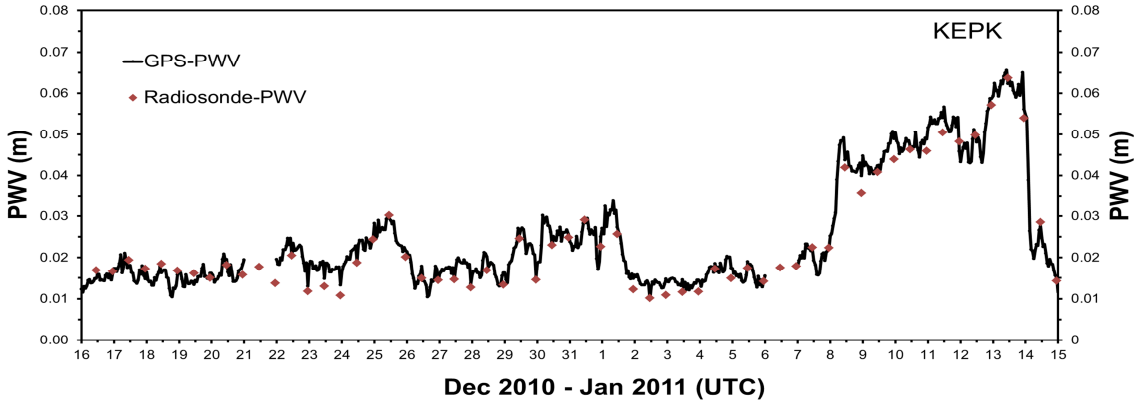

Figure 3.14: GPS-PWV estimates from the KEPK station from 15 Dec 2010 to 15 Jan 2011 with hourly temporal resolution (black) against co-located radiosonde-PWV estimates during the same period with a 12 hour resolution (red).

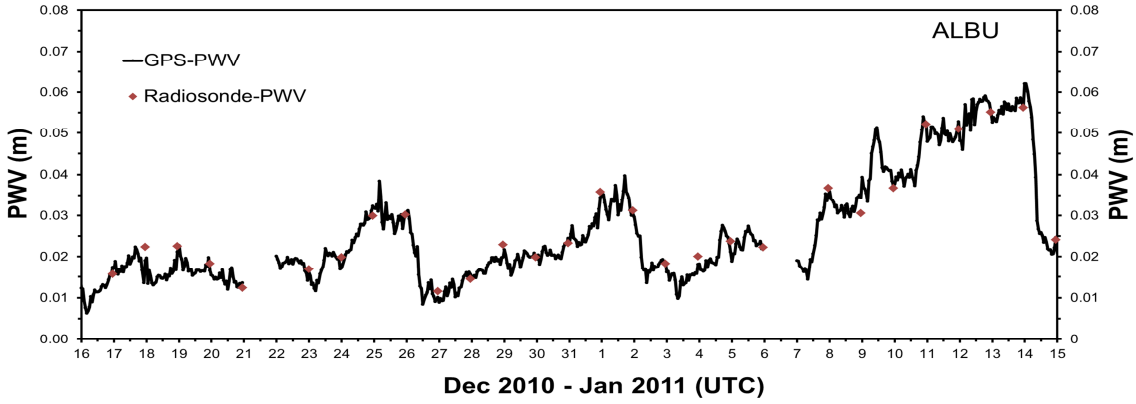

Figure 3.15: GPS-PWV estimates from the ALBU station from 15 Dec 2010 to 15 Jan 2011 with hourly temporal resolution (black) against co-located radiosonde-PWV estimates during the same period with a 24 hour resolution (red).

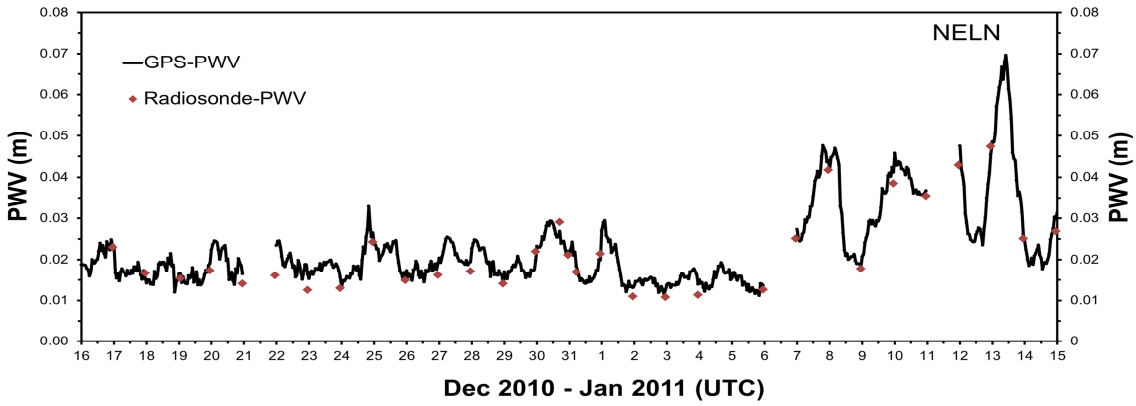

Figure 3.16: GPS-PWV estimates from the NELN station from 15 Dec 2010 to 15 Jan 2011 with hourly temporal resolution (black) against co-located radiosonde-PWV estimates during the same period with a 24 hour resolution (red).

It should be noted that each station displays a distinct rise in PWV estimates, depicting mechanisms of warm, moist lift due to the convective process of severe mesoscale storm systems. These sudden increases of PWV to unusually high levels occur several hours before the passing of the mature storm system over each station. These findings are consistent with Champollion et al. (2005), Boniface et al. (2009) and Seko et al. (2004, 2010) where the time series of ZWD forms distinct patterns of significant increases several hours prior to the storm system. After these initial indications of convective lift, there is a significant decrease in PWV, due to the passing of the severe weather and heavy precipitation systems.

Figure 3.17 presents the comparison between GPS-derived PWV estimates and associated radiosonde-derived PWV estimates for 3 GPS stations over the 30-day period. A summary of the number of comparisons, maximum ($\boldsymbol{\Delta}_{max}$) and minimum ($\boldsymbol{\Delta}_{min}$) PWV difference, RMS error, bias and standard deviation for each analysis are presented in Table 3.5. The KEPK, ALBU and NELN stations concluded RMS errors of 1.64, 1.61 and 1.53 mm, respectively, i.e. an average RMS value of 1.59 mm. This result is consistent with final results of PWV from previous research that achieved accuracies in the order of 1 – 2 mm RMS (Bai, 2004; Gutman et al., 2004; Song et al., 2006; Boniface et al., 2009). These convert to accuracies of 5 – 10 mm for ZWD. A positive bias is identified for the KEPK and the NELN comparisons of 0.52 mm and 0.80 mm, respectively. These biases are small compared with the average PWV value of 31 mm. However, when compared with the overall RMS, the bias magnitude is in the order of 32% and 50%, respectively. There are still some errors associated with the PWV estimates using radiosonde profiles because of the averaging approach of computing an integrated value as shown in section 2.4.2, and a dry bias evident in the radiosonde profile observations. It should also be noted that the inaccuracies in modelling the ZHD due to the

errors in the surface meteorological data and in the Saastamoinen hydrostatic equation (Eq. (2.28)) are not accounted for as being contributors to the overall uncertainties of the GPS-derived PWV estimates.

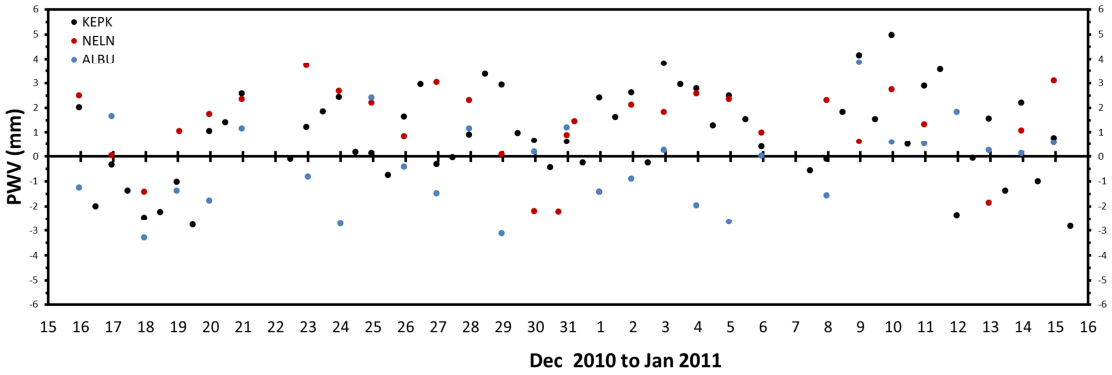

Figure 3.17: Difference between GPS- and radiosonde-derived PWV estimates for KEKP, ALBU and NELN co-located stations from 16 Dec 2010 – 15 Jan 2011.

Table 3.5: Statistical results for the differences between GPS-derived PWV and radiosonde-derived PWV estimates for 3 Victorian GPSnet stations over a one-month period.

Station	Comparisons	$\Delta_{max}(mm)$	$\Delta_{min}(mm)$	RMS	Bias	Std. Dev.
KEPK	60	4.96	-3.21	1.64	0.52	1.47
ALBU	30	3.85	-3.97	1.61	-0.07	1.51
NELN	30	3.97	-2.96	1.53	0.80	1.36

3.5.2. Conclusion

The results for this validation study presented a high accuracy for GPS-derived PWV estimates from the GPSnet. This result has proven that ground-based GPS observations are robust and can provide a platform of assimilation into NWP models in the Australian region.

The GPS processing strategy used a longest baseline DD approach to produce final ZTD estimated as part of the stochastic filtering every hour. As mentioned previously, 78 GPSnet CORS stations were included in the campaign over a 1-month period from which 3 were co-located with radiosonde stations and used for this validation study. Conclusions from these final results:

- The accuracy of GPS-derived PWV estimates from the 3 co-located GPS stations produced an RMS error of 1.59 mm when compared with radiosonde-derived PWV.
- GPS-derived PWV estimates produced a mean positive bias of 0.31mm and a standard deviation of 1.45 mm.

- GPS-derived PWV estimates during the severe weather event from 8 – 15 Jan 2011 produced an RMS error of 1.9 mm

This validation study provided the fundamentals for the GPS-derived PWV estimation process in Victoria. It also provided a further opportunity for assimilation into the Australian NWP model for improved forecasting and nowcasting. The advantages include a high temporal resolution of measurements in comparison with radiosonde, a highly dynamic capability for detecting sharp changes in PWV at the zenith and a high accuracy. These complement the highly dynamic nature of the unstable atmosphere during severe weather and thus has the potential to be a valuable additional observation source for NWP prediction and analysis. The major limitation, however, is the inability to provide any information on the vertical structure of WV in the troposphere. The PWV estimates are integral measurements that estimate the amount of WV evident in the column directly above the station. Therefore, results in this study depict the inability of PWV estimates for detecting mechanisms of convection due to lift of warm, moist air masses and the size, shape and direction of the severe weather event. The 1D PWV estimate is limited to the accurate detection of the magnitude increases and decreases in the total WV content of the vertical column above a specific station.

The final RMS error for the three co-located stations was 1.59mm, which converts to approximately 5mm for ZWD. This standard error of 5mm (ZWD) will be used as the input error for the GPS tomographic simulation studies (see Chapter 5), where an additive Gaussian error is applied to each observation.

3.6. Summary

This chapter introduced the operational observation systems used for this research. The spatio-temporal distribution for each alternate system was presented with their advantages and limitations in observing the dynamics of WV for the troposphere over the Victorian region. The GPSnet infrastructure was also introduced and described as an advanced and highly dense CORS network in the Australian region.

A validation study concluded that GPS-derived PWV estimates present a high accuracy when compared with integral estimates of PWV from radiosonde. This result identified the potential for ground-based GPS meteorology to have a positive influence on future NWP analysis and forecasting due to the high resolution of observations in space and time.

Chapter 4. Modelling wet refractivity with GPS tomography

4.1. Overview

This chapter discribes the theory of GPS tropospheric tomography and how it is applied to a finite field of the atmosphere in order to model the 4D distribution of wet refractivity. AWATOS 2 was used for this research, which implements a trilinear parameterisation technique and a Kalman filter based processing strategy.

This section provides the fundimentals of the models and algorithms implemented in AWATOS 2 including:

- GPS DD observations
- Kalman filter (KF) processing
- Parameterisation techniques
- Prediction and observation models in the KF system

The theory of simulation analysis using AWATOS 2 includes:

- Synthetic refractivity fields
- Simulated observations
- Forward and backward model processing

4.2. Fundamentals of GPS tropospheric tomography

Tomography is a method of applying the inverse theory to modelling applications. As discussed previously, tomographic modelling originated and is most commonly used for seismology and medical imaging. The development of SWD and PWV estimates from GPS observations has provided a platform for further development in atmospheric modelling using tomography due to the high density and continuous operability of ground-based GPS networks.

The application of tomography to the atmosphere requires multiple GPS-derived SWD estimates from different locations and orientations through a finite space in order to infer its spatio-temporal structure. The fundamentals of GPS tomography, which include the optimal preconditions and

constraints for reconstructing atmospheric wet refractivity fields have been demonstrated in multiple studies using SWD as the input observables (Flores 1999; Gradinarsky, 2002; Braun, 2004; Nilsson, 2005; Rohm et al., 2011, Van Baelen et al., 2011) and DD SWDs (Nicholson et al., 2005; Troller et al., 2006; Skone and Hoyle, 2005; Lutz, 2008; Perler et al., 2011, Manning et al. 2012).

Current studies continue to investigate optimal methods for the reconstruction process to ultimately attain a robust algorithm with a high accuracy and reliability. Preconditions and constraints were used to resolve the ill-posed problem along with apriori and pseudo information to strengthen the solution. This research aims to further develop and customise GPS tomography for the Australian climate using AWATOS 2. Discretisation and parameter optimisation was analysed for GPSnet (see Chapter 5), along with extensive analysis of tomographic results under severe weather conditions (see Chapter 6). The influence of additional observational methods input into the Kalman filter system on the GPS tomographic solution (see Chapter 7).

4.3. The AWATOS 2 software package

4.3.1. Overview of software

The tomographic inversion used in this project was processed using the C++ software package AWATOS 2 (Perler, 2011). As discussed previously, AWATOS 2 is an extended version of the original tomographic software package AWATOS developed by Kruse (2001) from ETH, Zurich. The configuration file for running the software integrated a succession of modules that called on all input data to estimate the predicted and update solution of wet refractivity using a KF model which reconstructed the spatio-temporal dynamics. AWATOS 2 is capable of logistically handling and assimilating multiple observation types within the finite media using three parameterisation methods. The major contributions to this software from the Geodesy and Geodynamics Lab (GGL) ETH can be found in Kruse (2001), Troller (2004), Lutz (2008) and Perler (2011).

4.3.2. Voxel model

A 3D grid model was used to divide the atmosphere into a finite resolution to solve an unknown wet refractivity parameter at each grid point. This discretised grid setup is commonly referred to as a voxel (volume pixel) model. The constructed voxel model over GPSnet was referenced using the WGS84 ellipsoid. The vertical voxel spacing was constructed using increasing height levels, which were determined by an exponential layer function. The horizontal discretisation follows curvilinear

ellipsoidal boundary surfaces for each level using geodetic coordinates (i.e. latitude, longitude and height) to define each voxel corner point. It should be noted that the horizontal extremities of the voxel model are 5° boundary zones to ensure that all rays tracing from satellites to receivers pass through the top of the model. No rays pass completely or partly outside the model. In the vertical direction the finite media is discretised into increasing height layers from the ellipsoidal surface to 15000 m altitude. For a stable atmosphere the wet refractivity above 10000 m altitude is assumed to be 0 ppm (Troller et al., 2006; Lutz, 2008; Perler et al., 2011). The exponential spacing technique uses a constant growth factor (w) at the i^{th} layer. The height subdivision can be expressed as $\Delta h_i = \Delta h_0 w^i$, where Δh_i is the thickness of layer i and Δh_0 is the thickness of the first layer. Figure 4.1(a) and (b) presents the optimal positioning and spatial resolution of the horizontal and vertical voxel grid discretisation, respectively. This optimal voxel grid resolution was found using a simulation analysis presented in Section 5.5. The horizontal distribution of GPSnet (Figure 4.1(a)) is quite homogeneous with no real spatial bias. The vertical distribution of GPSnet (Figure 4.1(b)), however, is relatively flat with only 8 stations above 500 m altitude and a maximum station height of ~1900 m.

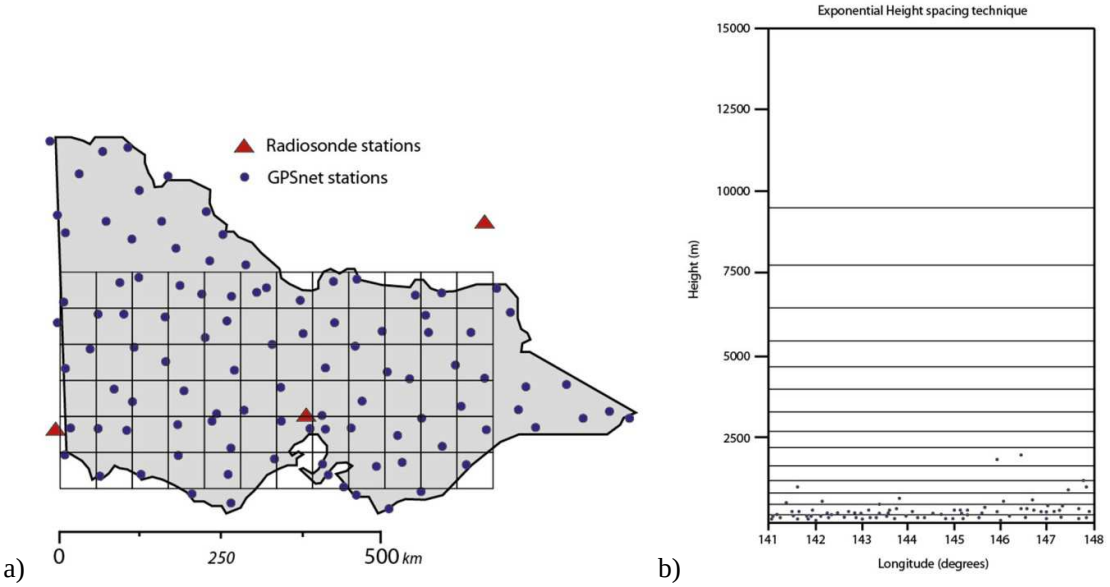

Figure 4.1: Presents the GPSnet, radiosonde sites and horizontal discretisation of the voxel grid model (a), and, vertical layer structure defined with an exponential spacing technique (b). This spatial resolution for the voxel construction is used in real data processing.

4.3.3. GPS DD observations

GPS satellite signals are delayed and bent due to the variations in refractive index as they propagate through different layers of the atmosphere to a ground receiver. As discussed previously, a linear combination of two frequencies can effectively eliminate the ionospheric contribution leaving only

the dry and wet effects of the troposphere represented as refractivity (Rueger, 2002), using the equations found in Section 2.2.2.

The concept of GPS meteorology was first presented in Bevis et al. (1992) who proposed to utilise the properties of the signal delays caused by the lower atmosphere to the estimates of total zenith WV content or PWV.

The GPS tomographic inversion process involves estimating the scalar field of wet refractivity values within a finite curvilinear grid from multiple integrated values passing through the media at different positions and orientations (Gradinarsky and Jarlemark, 2004). The key aspect in GPS tomography is a linear relation between path delays, which are an integrated measure of the signal delays, and the refractivity within the finite voxel model. This same relation holds true for dry and wet refractivity. The integration refractivity (N) along the SPD Δ^{PD} between satellite (x) and receiver (a) can be expressed as (Troller et al., 2006):

$$\Delta^{PD}{}_{a}^{x} = 10^{-6} \int_{a}^{x} N \cdot ds = SHD + SWD \tag{4.1}$$

where SWD and SHD are the slant wet and slant hydrostatic delays (m), respectively.

Ray bending is neglected and a cut-off elevation angle of 5 degrees is commonly used (Bender et al., 2008). The Bernese GPS software was used to attain the ZTD, DD phase residuals $\Delta\Phi_{a,b}^{x,y}$ and coordinates using a shortest distance baseline strategy (see section 2.3.2) and the DD approach. The DD SPD can be expressed as a function of 4 zero difference observations (see Eq. (2.15)). A DD SPD $\Delta^{2,PD}{}_{a,b}^{x,y}$ (Eq. (4.3)) can be reconstructed between two satellites (x and y) and two receivers (a and b) using the ZTDs from the receivers which are mapped to the corresponding elevations of the satellites using the Niell mapping function (Niell, 1996) $m(el_a^x)$ (see section 2.3.1.3) with the addition of DD residuals (see Eqs (4.3) and (4.4)) .

$$\Delta\nabla^{2,PD}{}_{a,b}^{x,y} = \left(\Delta^{PD}{}_{b}^{x} - \Delta^{PD}{}_{a}^{x}\right) - \left(\Delta^{PD}{}_{b}^{y} - \Delta^{PD}{}_{a}^{y}\right) \tag{4.2}$$

Separation of the total path delay

In this study the wet refractivity is of interest, since the dry component can be calculated and eliminated using a dry empirical model, e.g. in this study the dry Saastamoinen model (Saastamoinen, 1972) was used. This model incorporates surface pressure measurements and the associated geoid height (H) and geographic latitude (ϕ) of the GPS station (a) to estimate ZHD (see Eq. (2.28)). The ZHD estimate is subtracted from the ZTD to estimate the ZWD (see Eq. (2.27)). For full details see Section 2.4.1.

DD SWD equation

The final DD SWD equation (Troller et al., 2006; Lutz, 2008; Perler, 2011) reads as:

$$\Delta\nabla SWD_{a,b}^{x,y} = \overline{\Delta\nabla SWD_{a,b}^{x,y}} + \Delta\nabla\Phi_{a,b}^{x,y} \tag{4.3}$$

where,

$\overline{\Delta\nabla SWD_{a,b}^{x,y}}$ is the isotropic DD constructed using the isotropic SWDs. This can be expressed as:

$$\overline{\Delta\nabla SWD_{a,b}^{x,y}} = \left(\overline{\Delta_b^{ZWD}} \cdot m(el_b^x) - \overline{\Delta_a^{ZWD}} \cdot m(el_a^x)\right) - \left(\overline{\Delta_b^{ZWD}} \cdot m\left(el_b^y\right) - \overline{\Delta_a^{ZWD}} \cdot m\left(el_a^y\right)\right) \tag{4.4}$$

$\overline{\Delta_a^{ZWD}}$ is the ZWD at station a

$m(el_a^x)$ is the Niell wet mapping function from station a to satellite x

DD SWDs are constructed and used as the input integral observations through the finite voxel model for this research. This method takes advantage of automatic elimination of the satellite and receiver clock biases (Ware et al., 1997; Troller et al., 2006; Lutz, 2008 and Perler et al., 2011).

4.3.4. Parameterisation methods using AWATOS 2

Using the AWATOS 2 software package, the wet refractivity can be discretised into an ellipsoidal voxel grid using latitude, longitude and height coordinates on the WGS84 datum. Three voxel parameterisation methods were developed by Perler (2011).

1. *Constant parameterisation*: the refractivity is assumed to be constant within each voxel. The number of parameters to be estimated equals the number of grid voxels in the model as follows:

$$n_{total} = n_\lambda \times n_\phi \times n_h \tag{4.5}$$

where $n_\lambda, n_\phi,$ and n_h are the number of longitude voxels, latitude voxels, and height voxels, respectively.

2. *Trilinear parameterisation*: the refractivity at a point (λ, ϕ, h) is determined by a weighted sum of the 8 refractivity values at the 8 corners of the voxel. The interpolation function is defined by:

$$N_{(\lambda,\phi,h)} = \omega^T N_{voxel,i,j,k} \tag{4.6}$$

where ω is the weight matrix of the 8 corners' refractivity values. This is defined by:

$$\omega = \begin{bmatrix} \frac{\lambda_{i+1} - \lambda}{\lambda_{i+1} - \lambda_i} & \frac{\phi_{j+1} - \phi}{\phi_{j+1} - \phi_j} & \frac{h_{k+1} - h}{h_{k+1} - h_k} \\ \frac{\lambda - \lambda_i}{\lambda_{i+1} - \lambda_i} & \frac{\phi_{j+1} - \phi}{\phi_{j+1} - \phi_j} & \frac{h_{k+1} - h}{h_{k+1} - h_k} \\ \vdots & \vdots & \vdots \\ \frac{\lambda - \lambda_i}{\lambda_{i+1} - \lambda_i} & \frac{\phi - \phi_j}{\phi_{j+1} - \phi_j} & \frac{h - h_k}{h_{k+1} - h_k} \end{bmatrix}$$

and

$$N_{voxel,i,j,k} = \begin{bmatrix} N_{i,j,k} \\ N_{i+1,j,k} \\ \vdots \\ N_{i+1,j+1,k+1} \end{bmatrix}$$

The parameters for this approach to be estimated are for the refractivity value of every corner of the voxel, which means the number of parameters to be estimated equates to:

$$n_{total} = (n_\lambda + 1)(n_\phi + 1)(n_h + 1) \tag{4.7}$$

3. *Bilinear/spline parameterisation*: this method uses direction dependent parameterisation techniques. On the horizontal plane a bilinear technique is used and in the vertical direction natural splines are used. An interpolation method is incorporated using the 4 adjoining vertical profiles. The refractivity at a point (λ, ϕ, h) is expressed by their refractivities and their second derivatives in the vertical direction at the corners of the corresponding voxels:

$$N_{(\lambda,\phi,h)} = \begin{bmatrix} N_k(\lambda, \phi) \\ N_{k+1}(\lambda, \phi) \\ N_k^{"}(\lambda, \phi) \\ N_{k+1}^{"}(\lambda, \phi) \end{bmatrix} \tag{4.8}$$

where,

$$\omega = \begin{bmatrix} 1 - \frac{h - h_k}{dh_k} \\ \frac{h - h_k}{dh_k} \\ \frac{(h - h_k)^2}{2} - \frac{dh_k(h - h_k)}{3} - \frac{(h - h_k)^3}{6dh_k} \\ \frac{(h - h_k)^3}{6dh_k} - \frac{dh_k(h - h_k)}{6} \end{bmatrix}$$

where dh_k is the thickness of the kth layer, $N_k(\lambda, \phi)$ and $N_k^{"}(\lambda, \phi)$ are the bilinear interpolation and second derivative of the refractivity at height h_k, respectively.

The trilinear and bilinear/spline parameterised approaches provide far superior solutions to the non-parametric constant approach. A long-term tomographic test scenario completed in Switzerland

concluded that the trilinear approach was more robust and provided a higher accuracy (Perler, 2011). Based on this conclusion, all simulated and real data analysis in this research used a trilinear parameterisation approach.

4.3.5. Kalman filter based processing

Reconstructing the 3D field of wet refractivity is a challenging task. This is due to a restricted and noisy measurement geometry of ground-based GPS observations and the highly dynamic and variable nature of the atmosphere. Previous studies have incorperated a Kalman filtering technique to effectivily utilise the statistical analysis of a tomographic solution (Flores, 2001; Gradinarsky and Jarlemark, 2004; Troller, 2004; Nilsson, 2006; Perler et al., 2011; Rohm et al., 2013). The Kalman filtering is a powerful processing procedure and is highly advantageous for estimating the evolution of dynamically changing parameters. In this study a Kalman filtering technique was used.

As mentioned previously, the wet refractivity field is discretised by an ellipsoidal voxel. The time evolving refractivity field is assumed to be a Gaussian random walk. The benefit of this is its simplicity and high sample rate of the observations compared to the comparitively slow evolution of the synoptic atmospheric processes. The stochastic differential equation (SDE) is used to model the random walk.

The current true state of this field is denoted by $\mathbf{N}_{wet}$ with estimate $\widehat{\mathbf{N}}_{wet}$. The Kalman filter system consists of two steps: the "prediction" and "update" steps (Grewal and Weill, 2002; Grewal et al., 2007).

The *prediciton step* (time or temporal updates) updates the estimate and estimation uncertainty, based on uncertanty of the dynamic system over the update time t_{k-1} to t_k between measurements.

Predicted state vector:

$$\widehat{\mathbf{N}}_{wet\,k}(-) = \mathbf{F}_k \widehat{\mathbf{N}}_{wet\,k-1}(+) \tag{4.9}$$

Predicted state covariance:

$$\mathbf{P}_k(-) = \mathbf{F}_k \mathbf{P}_{k-1}(+) \mathbf{F}_k^{\boldsymbol{T}} + \mathbf{Q}_{k-1} \tag{4.10}$$

The *update step* (measurement or observational updates) redefines the estimate and estimate uncertainty based on new observational information.

Update state estimate:

$$\hat{\mathbf{N}}_{wet\,k}(+) = \hat{\mathbf{N}}_{wet\,k}(-) + \bar{\mathbf{K}}_k \left(\mathbf{z}_k - \mathbf{H}_k \hat{\mathbf{N}}_{wet\,k}(-)\right) \tag{4.11}$$

Update state coverience matrix:

$$\mathbf{P}_k(+) = \mathbf{P}_k(-) - \bar{\mathbf{K}}_k \mathbf{H}_k \mathbf{P}_k(-) \tag{4.12}$$

With the Kalman Gain:

$$\bar{\mathbf{K}}_k = \mathbf{P}_k(-)\mathbf{H}_k^T \left(\mathbf{H}_k \mathbf{P}_k(-)\mathbf{H}_k^T + \mathbf{R}_k\right)^{-1} \tag{4.13}$$

where:

$\hat{\mathbf{N}}_{wet\,k}(-)$	is the predicted state vector
$\mathbf{P}_k(-)$	is the predicted covariance matrix of the predicted state vector
$\hat{\mathbf{N}}_{wet\,k}(+)$	is the updated state estimate
$\mathbf{P}_k(+)$	is the updated covariance matrix of the updated state vector
$\mathbf{F}_k$	is the state transition matrix
$\mathbf{Q}_k$	is the uncertainty matrix of the process
$\mathbf{z}_k$	is the observation matrix
$\mathbf{H}$	is the design matrix
$\bar{\mathbf{K}}$	is the Kalman gain matrix
$\mathbf{R}_k$	is the measurment noise covariance matrix

The state transition matrix (F_k) in AWATOS 2 is implemented as an identity matrix. The initial state provided by the background model is predicted using Eq. (4.9) and updated using Eq. (4.11) based on the Kalman gain matrix ($\bar{K}$) in every estimation step. This procedure is identical for the prediction (Eq. (4.10)) and update (Eq. (4.12)) of the covariance matrices. The initialisation of the Kalman filter uses an exponential refractivity model and parameters established for the GPSnet.

4.3.6. Prediction model

The AWATOS 2 uses a Gaussian random walk for modelling the time evolving wet refractivity field. The advantage of this method is the simplicity in computation for high sample rate of observations in comparison to the temporal evolution of atmospheric processes. This method is particularly beneficial

for modelling the highly variable and unstable atmospheric conditions of severe convective storm and precipitation systems due to the highly dynamic nature of the prediction model. The SDE of the random walk model is denoted by (Grewal and Weill, 2002; Grewal et al., 2007):

$$dX_t = \mathbf{B}dW_t \tag{4.14}$$

where:

X_t is the n-dimensional multivariate random variable predicting the refractivity field with respect to time t

B is a n × n matrix

W_t is the vector of uncorrelated standard Brownian motions

4.3.7. Observation model

The observation model incorporates integral, point and pseudo observation types. The observation matrix $\mathbf{z}_k$ and associated covariance matrix $\mathbf{R}_k$ are included in the update step (Eqs. (4.11) and (4.12)) of the Kalman filter in order to estimate the wet refractivity field and its uncertainties using new observations. The observation equations for the aforementioned 3 types of observations using the trilinear parameterisation method are defined below.

Integral observations

GPS integral measurements of slant and zenith delays (Eq. 4.3) were used as the primary observational input into the update step of the Kalman filter (see Eqs. (4.11) and (4.12)) using the Kalman gain. The GPS integrals are subdivided into sections, by the graduations of the voxel boundaries (see Figure 4.2). A ray-tracing algorithm is used to determine the intersection point of the GPS ray and the voxel faces. The discretisation of GPS integral measurements through a finite ellipsoidal voxel field is expressed using a trilinear parameterisation method (see Eq. (4.16)).

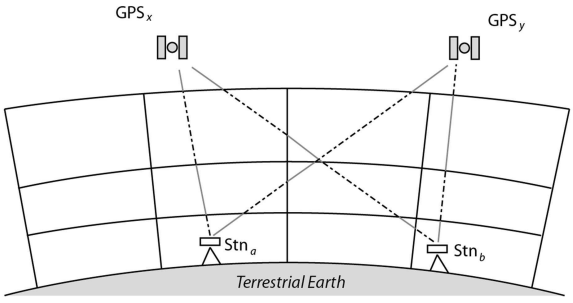

Figure 4.2: The discretisation of GPS DD observations from GPS satellites (x & y) to stations (a & b) through finite ellipsoidal voxel grids.

If a simple non-parametric approach is adopted, the SWDs (Δ^{SWD}) can be expressed using Eq. (4.15) as the sum of the distances a ray propagates through each voxel (Δs) along its path multiplied by the wet refractivity $\mathrm{N_{wet}}$ of the corrisponding voxel (i) (Flores 1999; Gradinarsky, 2002; Braun, 2004; Nilsson, 2005; Troller et al., 2006; Lutz, 2008; Rohm et al., 2011, Van Baelen et al., 2011):

$$\Delta^{SWD}{}_a^x = 10^{-6} \sum_i N_{wet,i} \Delta s_i{}_a^x \tag{4.15}$$

If a parameterised field is adopted, the algorithm becomes more complex. The Newton-Cotes quadratic function is used to solve the weighted integral. Using a trilinear parameterised field the algorithm of AWATOS 2 expresses the DD SWD observations as a weighted sum of the grid nodes (Perler, 2011, Manning et al., 2012). The weighted sum of the N_{wet} is used at the voxel corners to solve the integral, i.e.

$$\Delta^{SWD}{}_a^x = 10^{-6} \sum_i \int_{s_i}^{s_{i+1}} N_{wet,i} ds_i{}_a^x \tag{4.16}$$

Eq. (4.16) is used to combine four ZD SWD equations to form a DD SWD observation as per Eqs. (4.2), (4.3) and (4.4). The resulting DD SWD equation is a weighted sum of refractivities, which are used in the observation matrix ($\mathbf{z}_k$). Due to the geometry of integrated views through the finite media being restricted to ground observations, the tomographic inversion is ill-posed, so resolving the vertical structure of wet refractivity becomes a challenging task. To resolve this issue pseudo observations in the form of apriori information and inter-voxel constraints are applied to smooth and stabilise the update process (see Section 4.3.8).

Point observations

Previous tomographic research into using ground-based GPS to model the 3D WV distribution (see Section 1.5) suggests that apriori information about the state of the wet refractivity field can improve the accuracy and reliability of resolving the vertical structure of the true field (Braun et al., 2003; Troller, 2004; Bender and Raabe, 2007). Point observations supply the fundamental apriori information, and along with their associated covariances, can assist in the reconstruction of the wet refractivity state. The geometric properties of point observations may be provided as vertical profiles or ground network geometries. Additional meteorological point observations may include radiosonde profiles and Lidar measurements (see Skone and Hoyle (2005); Nicholson et al. (2005); Braun et al. (2003); Rocken (2003)). These may provide a highly resolved vertical structure for the assimilation into the tomography solution. Standard atmospheric models and NWP fields are also used to provide an encompassing 3D structure of the atmospheric state for an apriori field in the observation model.

Synoptic ground meteorological data can also be used as apriori data providing surface wet refractivity values to the observation model (see Troller, 2004 and Lutz, 2008).

Point observations are entered into the observation matrix in the form:

$$N = N_{(\lambda,\phi,h)} \tag{4.17}$$

where N is the refractivity point observation at geographical coordinates (WGS84) and incorporated into the voxel parameterisation method using $N_{(\lambda,\phi,h)}$.

For the trilinear parameterisation method used in this study, the $N_{(\lambda,\phi,h)}$ is implemented using Eq. (4.6).

4.3.8. Inter-voxel constraints

A partly ill-conditioned inversion system may exist in the tomographic equation system due to GPS rays not passing through every voxel in the voxel model. Inter-voxel constraints may be introduced in the form of pseudo-observations to strengthen this condition. There are two types of inter-voxel constraints constructed in AWATOS 2.

Neighbourhood averaging constraints

For each voxel or grid point an observation equation is included. The wet refractivity of the voxel or grid point is therefore equal to the weighted sum of the six wet refractivity values of the neighbouring voxels or grid points. This constraint is introduced as a covariance function between two points in the voxel model (see Troller, 2004):

$$\Phi_{i,j} = \frac{\sigma_0^2}{1 + \left[\left(\frac{x_i - x_j}{\Delta x_0}\right)^2 + \left(\frac{y_i - y_j}{\Delta y_0}\right)^2 + \left(\frac{z_i - z_j}{\Delta z_0}\right)^2\right]} \tag{4.18}$$

where

$\Phi_{i,j}$	is the covariance function between voxels *i* and *j*
σ_0^2	is the apriori variance of the signal
$\Delta x_0, \Delta y_0, \Delta z_0$	is the correlation length of the individual components

The covariance functions of all voxels are combined into a row vector $\overrightarrow{\Phi_i}$ with size *k* equal to the total number of voxels and included into the design matrix. Each element *x* of this vector is defined as:

$$\overrightarrow{\Phi_i} : x = \begin{cases} -1, & \text{if } j = i \\ \dfrac{\Phi_{i,j}}{\Phi_{sum,i}}, & \text{if } j \text{ is neighbouring to } i \\ 0, & \text{in all other cases} \end{cases} \tag{4.19}$$

where

$$\Phi_{sum,i} = \sum_{j=1}^{k} \Phi_{i,j} \tag{4.20}$$

Spatial gradient constraints

It is also possible to individually constrain the single spatial derivatives of the refractivity field in AWATOS 2. This spatial gradient constraint is separated into horizontal and vertical derivatives and is modelled on a stable average exponential model with no horizontal gradients. The horizontal derivatives are set to zero whereas the vertical derivatives are constrained to the exponential model $N_0 \exp\left(-\frac{h}{h_s}\right)$ where N_0 is the surface refractivity value and h_s is the scale height. This constraint is expressed as:

Horizontal constraint equation

$$N_{i+1,j,k} - N_{i,j,k} = 0 \tag{4.21}$$

$$N_{i,j+1,k} - N_{i,j,k} = 0 \tag{4.22}$$

Vertical constraint equation

$$N_{i,j,k+1} - N_{i,j,k} = N_0 \cdot \left[\exp\left(-\frac{h_{k+1}}{h_s}\right) - \exp\left(-\frac{h_k}{h_s}\right)\right] \tag{4.23}$$

Both inter-voxel constraint methods are entered into the observation equation independent of each other. The weight for each pseudo-observation type can be specified and its reciprocal is introduced into the covariance matrix $\mathbf{R}_k$ (see Eq. (4.13)).

4.3.9. Tomographic matrix equation system

GPS tomography is inherently under-determined and highly correlated due to the restricted geometry of integrated rays passing through the finite atmosphere. This leaves a number of individual voxels without any rays passing through and thus an ill-posed problem with the inversion of the equation system infers. To overcome this problem, inter-voxel constraints and apriori information are

introduced as pseudo observations. Furthermore, singular value decomposition is also used to solve the ill-posed problem (see Troller, 2004).

The DD SWDs, ZWDs, apriori point observations and smoothing inter-voxel constraints as pseudo observations are combined to form the fundamental tomographic equation system.

$$\begin{pmatrix} \Delta\nabla SWD_{a,b}^{x,y} \\ ZWD_a \\ N_{(\lambda,\phi,h)} \\ 0_i \end{pmatrix} = H \cdot \begin{pmatrix} \widehat{N}_1 \\ \widehat{N}_2 \\ \widehat{N}_3 \\ \widehat{N}_4 \\ \widehat{N}_5 \\ \widehat{N}_6 \\ \vdots \end{pmatrix} \tag{4.24}$$

where:

$\Delta\nabla SWD_{a,b}^{x,y}$	is the GPS DD SWD (m)
ZWD_a	is the ZWD in (m)
$N_{(\lambda,\phi,h)}$	is the point observation of refractivity (ppm) at point (λ, ϕ, h)
0_i	is the inter-voxel constraints added to voxel i
H	is the design matrix

4.4. AWATOS 2 simulation theory

Synthetic data may be used for GPS tomographic simulations, to test the capability of new configurations and parameter arrangements on specific atmospheric states in a controlled environment. Simulation experiments conducted in this project were undertaken to optimise the configuration strategy, voxel and height resolution. Simulated observations (forward model) from a pre-determined field were used to evaluate the solution convergence behaviour of the reconstructed wet refractivity field (backward model) using a Kalman filtering solution. This section introduces the simulation process for GPS integral observations and additional point observations through predefined synthetic refractivity fields. Model functions are used to define these predetermined fields.

4.4.1. Synthetic refractivity fields

Synthetically defined refractivity fields were used for the statistical optimisation of the tomographic model setup. An exponential function was used to approximate the trend of wet refractivity from radiosonde observations. Furthermore, a spike layer function was used to test the capability of

resolving the rapid increase in wet refractivity within a vertical layer. This may help model the convective processes during severe weather phenomena.

Exponential refractivity function

An exponential function is used to approximate an average distribution of wet refractivity along a vertical profile using an exponentially decreasing wet refractivity field with reference to increasing height. A scale height function is used to approximate the average troposphere profile observed using radiosonde. This exponential function is expressed as:

$$N_{wet} = N_{wet\,0} \cdot \exp(-\frac{h}{h_s}) \tag{4.25}$$

where $N_{wet\,0}$ is the surface refractivity and h_s is the scale height constant for the gradient of the exponential function.

Spike refractivity function

The main limitation of GPS tomography is its poor ability to reconstruct the vertical profile due to the restricted satellite to ground observation geometry (Braun et al., 2003; Troller, 2004; Bender and Raabe, 2007; Rohm and Bosy, 2009). This function defines a sharp vertical spike in refractivity, which tests the capability of resolving the anomaly. This allows for the optimal vertical resolution of the voxel model to be resolved by varying the height and thickness of the spike along with the vertical resolution of the voxel model. The function is defined as:

$$N_{wet} = \begin{cases} N_{wet\,h} & if\ h \in [h_{lower}, h_{upper}] \\ 0 & all\ else \end{cases} \tag{4.26}$$

where $N_{wet\,h}$ is the wet refractivity value assigned to layers from the two boundaries of h_{lower} to h_{upper}.

4.4.2. Simulation process for observations

GPS DD SWD observations may be formed using simulated integral measurements from a simulated wet refractivity field. Straight-line ray tracing through the predefined refractivity field between the satellite and receiver is used to simulate observations. DD delays, SPD and ZTD can all be simulated. Alternate point meteorological observations can also be simulated.

Simulated GPS integral observations

Numerical integration is used to compute the path delay between each satellite-and-receiver link using the Newton-Cotes quadrature (Stoer and Bulirsch, 1980; Perler, 2011). The usability of satellites in view can be restricted by a cut-off angle and an integration height is limited to the height of the voxel model. A measurement error may be introduced into the delays using a Gaussian distribution in the AWATOS 2 software package. A measurement bias can be introduced by specifying an expectation value of accuracy (μ) and a measurement noise denoted by a variance (σ^2). These values are used to control error magnitudes. The formation of these measurement errors are independent. The simulated SPDs are based on the true theoretical delay ($\overline{SPD}$) and a random noise equal to the measurement error multiplied by a mapping function.

$$SPD = \overline{SPD} + \frac{1}{\cos(\beta)}\varepsilon \tag{4.27}$$

where

$$\varepsilon \sim N(\mu, \sigma^2) \tag{4.28}$$

where $\overline{SPD}$ is the true theoretical delay computed using numerical ray tracing and SPD includes a measurement error (ε) multiplied by a mapping function with respect to the zenith angle (β). GPS DD observations are formed by combining four SPD observations. AWATOS 2 uses the Kruskal's algorithm (Matousek and Nesetril, 1998) to construct the baseline strategy between GPS stations and to build the DD observations. For this simulation study a minimum distance cost function was used, which calculated the ellipsoidal distance between two stations and also defined the minimum distance baselines to construct DD observations (see Figure 4.2).

Simulated point observations

Point observations may also be simulated and used as an additional observation input. These in-situ measurements are simulated using single point coordinates and an interpolation method in the synthetic refractivity function. The following defines the simulated point observation equation

$$N = \overline{N}(\lambda, \phi, h) + \varepsilon \tag{4.29}$$

where

$$\varepsilon \sim N(\mu, \sigma^2) \tag{4.30}$$

where N is the point refractivity observation inclusive of measurement error (ε), $\overline{N}(\lambda, \phi, h)$ is the true refractivity derived from the simulated field using interpolation.

4.4.3. Simulation method

The evolution of the simulated tomographic reconstruction process uses a forward and backward modelling strategy. First, an initial synthetic refractivity field (original field) is defined. Ray tracing is used to simulate integral and point observations through the pre-defined refractivity field – this is the forward modelling process. At this stage measurement errors may be added to the simulation process to obtain simulated observation data, which are then used to reconstruct the refractivity field using a Kalman filtering system – this is the backward modelling process (Figure 4.3). Finally, the estimated field is compared to the pre-determined field for statistical analysis. The update interval iterator then steps from t_k to t_{k+1} and simulates new observations using the forward model, which are then used in the next step of the backward model for the Kalman filter processing.

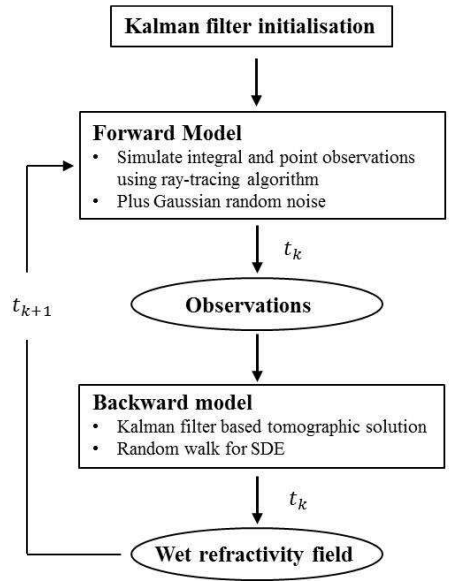

Figure 4.3: The forward and backward model strategy of the GPS tomographic simulation processing using a Kalman filter.

Forward model

The forward model (Figure 4.3) uses a ray-tracing algorithm to simulate the integrated path delay and point observations through a predetermined refractivity field with an integration height of 20000 m. The GPSnet stations and real precise orbit data are used for the ray-tracing with no rays tracing below a zenith angle of 85°. A Gaussian random noise is added to each integrated SPD with a magnitude of 5 mm when mapped to the zenith. This applies measurement error to the ground-based GPS processing to simulate realistic observation models for the reconstruction processes of the backward model. The slant delay estimates are used to construct the DD delays using the minimum distance baseline strategy.

Backward model

The backward model (Figure 4.3) solves the SDE corresponding to the random walk of the refractivity solution. The time evolving SDE solution, along with the simulated observations from the forward model are used in the backward model using a Kalman filtering approach to reconstruct the solution estimate ($\hat{\mathbf{N}}_{wet\,k}(+)$) of the wet refractivity field. The initial state of the SDE is given by the parameters of the initial refractivity field and the predetermined covariance matrix.

4.5. Summary

This chapter presented the fundamental theory of using GPS tropospheric tomography for reconstructing estimates of 4D wet refractivity fields. The software package AWATOS 2 and the fundamental models were introduced for simulated and real data investigations in this thesis. The theory of real and simulated studies using the Kalman filter based GPS tomography strategy was also introduced.

The fundamentals of GPS tropospheric tomography presented in this Chapter were used for a statistical optimisation using simulated data for GPSnet, as described in Chapter 5. Furthermore, a real data analysis investigating two severe weather case studies are presented in Chapter's 6 and 7. These studies are investigated to identify the capability of GPS tomography for sensing the dynamics of wet refractivity during the evolution of severe weather.

Chapter 5. GPS tomographic simulation

5.1. Overview

The feasibility and capability of reconstructing the physical dynamics of wet refractivity using a 4D GPS tomographic technique above the GPSnet was investigated using simulations of a synthetic tropospheric state. This simulation study for parameter optimisation focused on the following five aspects:

- Horizontal grid resolution;
- Vertical layer resolution;
- Layer spacing technique;
- Vertical wet refractivity spike analysis; and,
- The impact of additional observation methods on the tomographic solution.

The evaluation of each simulation result for optimisation was based on:

- Solution convergence rate;
- RMS error analysis; and,
- Solution stabilisation rate.

This section investigated the optimal tomographic model construction and influence of additional observation methods through a series of simulation experiments. Synthetic wet refractivity fields were used for each simulation analysis to statistically optimise variables of the GPS tomographic model setup. Results from this analysis were used for the real observation data presented in Chapters 6 and 7.

5.2. Parameter optimisation study

A theoretical investigation into the capabilities of GPS tomography in the Victorian domain using synthetically constructed refractivity fields in the AWATOS 2 simulation platform was conducted. This is currently a new study for Australia where the terrain is generally flat and the geometry of the GPSnet CORS network is heterogeneous.

As mentioned previously, GPSnet comprises approximately 110 dual-frequency geodetic grade GPS receivers in continuous operation from which 78 were used for this research. The average inter-station

distance was ~70 km with relative homogeneity in distribution. The network is highly dense for Australian standards and has the potential to be a major resource for meteorological data especially in the absence of sufficient meteorological observation systems.

This case study was conducted using simulated wet refractivity fields for a 24 hour period. Two synthetic wet refractivity fields were used for the analysis. First, an exponentially decreasing wet refractivity field was used to approximate a vertical standard atmosphere. Data from a radiosonde profile launched on 1 Dec 2010 was used to approximate this standard atmosphere using an exponential function. Secondly, a constant wet refractivity field with a spike layer was incorporated. This was investigated to identify the capabilities of vertical resolvability using GPSnet for the GPS tomographic algorithm using spherical grid layer geometries. This test was investigated to determine the accuracy and convergence rate of the tomographic solution to reconstruct large vertical anomalies in the atmosphere. This also analysed the capability of detecting and monitoring the dynamic nature of severe weather.

The true coordinates from GPSnet stations, along with the precise IGS orbits, were used in the forward modelling to construct the GPS observations through the simulation field. A standard deviation of 5 mm for the observation errors at the zenith was incorporated in the observation integral using a Gaussian distribution.

The aim of this simulation analysis was to optimise the discretisation parameters for the GPSnet and then to assess the influence of the inclusion of additional observations on the state solution estimate accuracy. This was with the view of using these optimal parameters for real data and severe weather analysis. The optimal 3D voxel resolution was determined based on the RMS errors, the vertical resolvability and the associated convergence rate of the solutions.

Two different types of observation methods were assessed in this section to identify both their strengths and limitations. These were:

- *Profile observations:* these are vertical profile observations for simulating the geometry of both the radiosonde and GPS RO profiles. The influence of this additional profile observation method in the observation matrix on the Kalman filter based GPS tomographic solution was investigated.
- *Synoptic weather observation network observations:* these are ground-based network observations for simulating the geometry of synoptic weather observation network. Usually, ground synoptic networks would be used for this analysis, however the Victorian synoptic weather network has an insufficient number of stations. NWP analysis was used to interpolate meteorological information for the GPSnet station locations and to extract the dry component in the real DD SWD observations. Thus, the coordinates of the GPSnet

stations were used to simulate point meteorological observations within the forward model processing. The influence of this additional network observation method in the observation matrix on the Kalman filter based GPS tomographic solution was investigated.

5.3. Parameter settings

As mentioned previously, the evolution of the simulated tomographic reconstruction process used a forward and backward modelling strategy. Firstly, an initial synthetic refractivity field (Table 5.1) was defined. In the forward model process, ray-tracing was used to simulate integral SWD (Eq. (4.27)) and point observations (Eq. (4.29)) through the synthetic atmosphere (Eq. (5.1)) using spherical grid layer geometry. At this stage, measurement noise was added to the simulation process using a Gaussian distribution error (Eq. (4.28) and (4.30)). Simulated SWD observations derived from ray-tracing using the satellite and receiver coordinates plus measurement noise were used to reconstruct the DD SWD observations, which were then used to solve for the refractivity field using the Kalman filter (Eqs. (4.9) – (4.13)) – this is the backward model process. Finally, the updated estimate ($(\widehat{\mathbf{N}}_{wet\,k}(+)$) was compared to the true atmosphere $\mathbf{N}_{wet}$ (Eq. (5.1)) for statistical analysis of the algorithm performance.

5.3.1. Voxel model construction

The discretisation of the lower atmosphere was defined with a finite curvilinear voxel grid using latitude and longitude boundaries referenced to the WGS84 ellipsoid. The area under investigation ranged from 141^0 to 148^0 E longitude and from -35.8^0 to 38.6^0 S latitude with a height range of 0 – 15000 m. In addition, a boundary layer of 5^0 provided a buffer on the outside of this model to ensure that all rays are within the model and pass through the top boundary. Figure 5.1(a) presents the finite domain from which a horizontal resolution at the surface of 0.5^0 is shown. The vertical layer structure is shown in Figure 5.1(b) with an exponential layer function used.

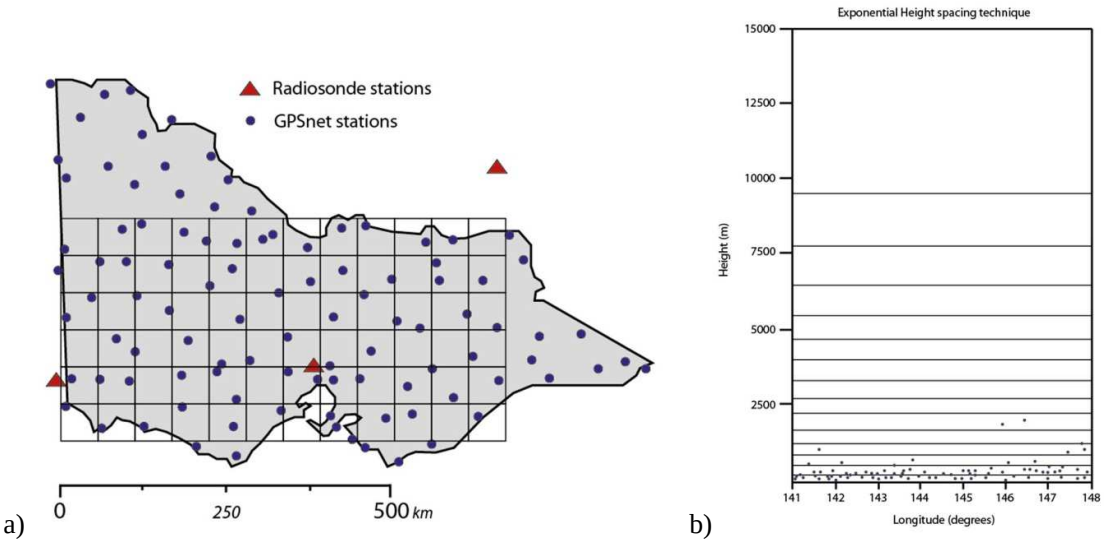

Figure 5.1: The Victorian GPSnet CORS network, radiosonde sites and horizontal discretisation of the voxel grid model (a), and, vertical layer structure defined with an exponential spacing technique (b). This spatial resolution for the voxel construction was also used in real data processing.

5.3.2. Synthetic wet refractivity fields

Two synthetic horizontally homogeneous fields were used for this simulation analysis; Figure 5.2(a) shows an exponential wet refractivity function derived from radiosonde observations of the troposphere and Figure 5.2(b) shows a spike wet refractivity field for investigating vertical resolvability in view of severe weather monitoring.

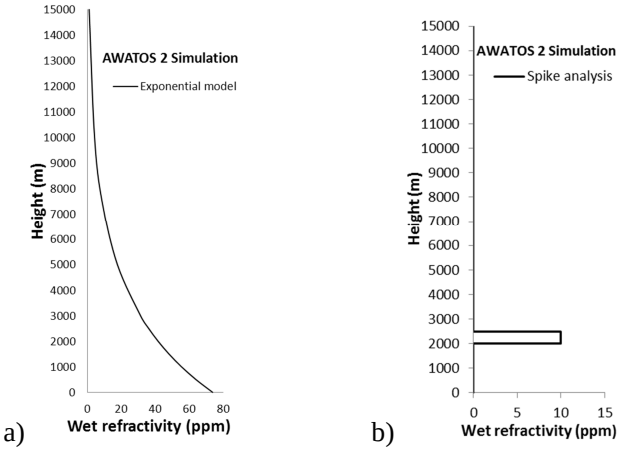

Figure 5.2: Exponentially decreasing refractivity field (a), spike refractivity field (b).

Each synthetic wet refractivity field implements no variation in the horizontal direction because the main limitation in GPS tomography is the vertical resolvability (e.g. Foelsche and Kirchengast, 2001;

Bender and Raabe, 2007; Perler, 2011 and Rohm et al., 2011). Simulations based on a synthetic exponential wet refractivity function (Figure 5.2(a)) were defined using:

$$N_{wet}(h) = N_{wet\,0}\exp\left(-\frac{h}{h_s}\right) \tag{5.1}$$

where, $N_{wet\,0}$ is the surface wet refractivity and h_s is the scale height.

For this research these values were determined using an averaged radiosonde profile from 1 Jan 2011, with values of: $N_{wet\,0} = 67.79$ ppm and $h_s = 2873$ m.

5.3.3. Initial state of the Kalman Filter

The initialisation of the Kalman filter state vector for the SDE included the initial refractivity field and covariance matrix of the backward model. The initial state for the unknown wet refractivity parameters of the 3D grid are set to 0 ppm. This value is deliberately implemented for the initial field to assess the convergence and stabilisation rate of each test tomographic solution for evaluation. The initial covariance and scale height were taken from the averaged exponential profile from radiosonde data on 1 Jan 2011. Equation 5.1 was used to standardise this field. The stochastic evaluation of the SDE used a spatial correlation length matrix to scale values based on the initial state. Parameter settings of the initial state are listed in Table 5.1.

Table 5.1: Parameter settings for the initialisation of the Kalman filter.

Parameter Initial state of backward model	**Value**
Initial state	0 ppm
Initial variance at reference level	134 ppm²
Scaling height of variance model	2873
Horizontal correlation scaling length	55262 m
Vertical correlation scaling length	1216 m

5.3.4. Forward model

The forward model used a ray-tracing algorithm to construct the integrated path delay measurements through a synthetic control field with an integration height of 20000 m. The DD delays were simulated with a sample rate of 30 seconds, which was the same as the real data sampling rate from GPSnet raw data. The 78 GPSnet stations were used (see Figure 5.1(a)) along with precise IGS orbits for the 3D ray tracing with a cut-off angle of 5°. As mentioned previously, an additive Gaussian noise of 5 mm in the zenith direction was incorporated in the integrated SPD equation (see Eq. (4.27)). The error magnitude increased using a mapping function $\frac{1}{\cos(\beta)}$. The DD delays were formed using the

shortest baseline strategy. The parameters are presented in Table 5.2, along with remaining constant values adopted.

Table 5.2: Parameter settings of the forward model.

Parameter *forward model*	**Value**
Simulation date	01-12-2011
Simulation period	24 hrs
Number of GPSnet stations	78
Satellite system	GPS
Additional observations	None
Simulated observations	GPS DD path delays
Baseline strategy	Shortest baseline distance
Sampling rate of measurements	30 sec
Integration height	20000 m
Cuttoff angle	5°
Measurement noise	5 mm (zenith)
Type of measurement noise	Gaussian
Measurement bias	0 mm

5.3.5. Backward model

The time evolving SDE solution was combined with the simulated observations from the forward model in a Kalman filtering approach to solve for the wet refractivity field. The update step size was set equal to the GPS observation rate of 30 seconds. Again, the spatial correlation length matrix and scale height value were defined for the SDE. No additional observations were added. Parameters of the prediction and observation models are listed in Tables 5.3 and 5.4, respectively. These parameters are applicable for all simulation analyses.

Table 5.3: Parameter setting of the Kalman filter prediction model.

Parameters *Prediction model*	**Value**
State vector	Random walk
Prediction step size	30 seconds
Prediction error	Multi-variant Gaussian
Horizontal correlation scaling length	55262 m
Vertical correlation scaling length	1216 m

Table 5.4: Parameter setting of the observation model

Parameter *Observation model*	**Value**
Observations	GPS DD path delays
Pseudo observations	Boundary conditions
Covariance model of the observations	Full covariance model

These simulation configurations of the forward and backward modelling strategy were implemented in order to analyse the capabilities of processing for each parameter optimisation study in this research. Data evaluation methods were then implemented for this analysis (see Section 5.4).

5.4. Data evaluation methods

The data evaluation method compared the estimated wet refractivity obtained from the Kalman filter solution of the backward model against the true (simulated wet refractivity) state. The scalar difference between these two refractivity states were computed for every update step (30s epoch) for the 24-hour simulation campaign with analytical methods. The following three aspects were investigated:

1. *Profile comparison:* The vertical profile located at point (A) is presented in Figures 5.3(a) for the horizontal location, and (b) for vertical location. This profile point was used for a comparison between the estimated refractivity field and the true simulated state.

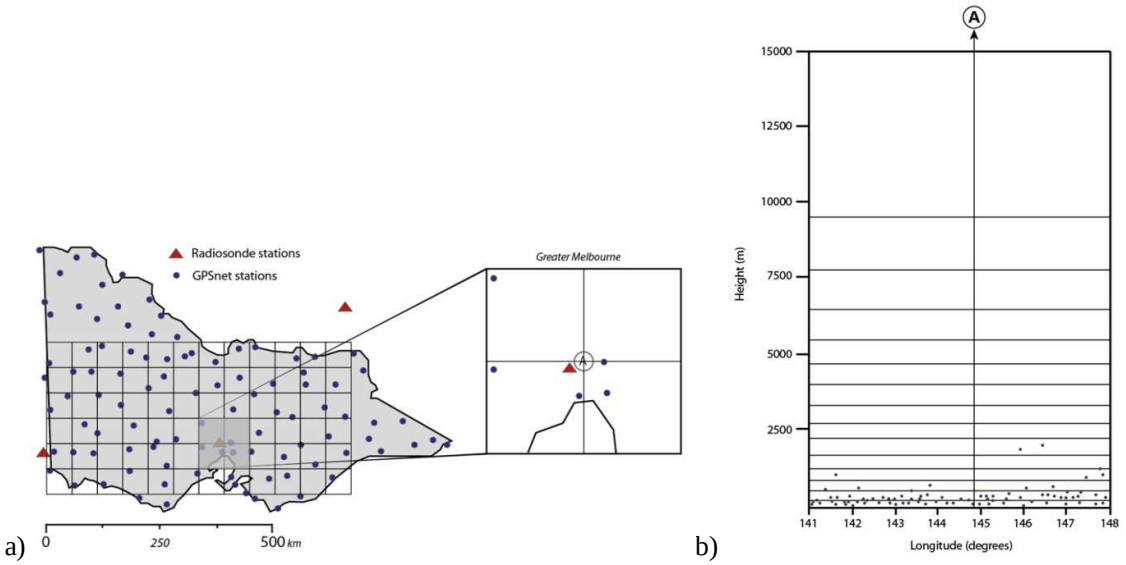

Figure 5.3: Horizontal location of profile (A) along with the GPSnet horizontal distribution and base ellipsoidal voxel model (a), and the vertical location of the profile (A) along with the vertical distribution of GPSnet and vertical layers (b).

The root mean square (RMS) of the differences between the true wet refractivity ($\mathbf{N}_{wet}$) profile and estimated wet refractivity $\widehat{\mathbf{N}}_{wet}$ profile was used to assess the performance of the time evolving tomographic solution. Additionally, the solution convergence rate and vertical resolvability were also assessed.

2. *RMS error of profile solution:* RMS is a statistical measure of the accuracy of the wet refractivity estimates and thus it provides an estimate of the overall accuracy of each tomographic solution. In the case of a set of n parameters ($x_1, x_2, \dots, x_n$), the RMS value is defined as:

$$x_{RMS} = \sqrt{\frac{1}{n}({x_1}^2 + {x_2}^2 + \cdots + {x_n}^2)} \tag{5.2}$$

In this research x_i is a comparison between the true (N_{wet}) and estimated ($\widehat{N}_{wet}$) wet refractivity at a single location. The RMS (x_{RMS}) error was derived for profile solutions, 2D height layers and all unknown parameters over time in order to provide a robust analysis of the tomographic algorithm performance.

3. *Error stabilisation for solution convergence rate:* An RMS error value of 1 ppm was adopted as a stable level of accuracy for the wet refractivity estimate to be considered stable after the initialisation of the Kalman filter. The processing time taken to achieve this level of accuracy using tomographic simulations provides valuable information about the solution convergence rate and vertical resolvability. Overall, this study was primarily aimed at severe weather detection and monitoring where the atmosphere is extremely unstable and the dynamics of WV are highly variable. Therefore analysis on the ability to detect sharp wet refractivity changes due to convective and unstable mechanisms was vital.

5.5. Spatial resolution optimisation

5.5.1. Horizontal resolution

The horizontal grid resolution is an important parameter for optimising the depiction of highly dynamic wet refractivity fields in view of hydrological hazards (Lutz, 2008). High variability of wet refractivity often occurs during the formation and maturity of severe weather due to high atmospheric instability and mechanisms of convection. Determining the optimal grid resolution of GPS tomography in order to detect the dynamic changes in wet refractivity in Australia was a fundamental goal for this research. The potential applications of this study include nowcasting, severe weather and precise positioning.

The optimal horizontal resolution was investigated using statistical analysis comparing the three horizontal voxel resolutions shown in Table 5.5. The base voxel setup remained constant for each experiment variation. Each of these horizontal resolutions implemented an exponential wet refractivity function (Eq. (5.1)) as the simulated wet refractivity state. The objective of this research was to identify the achievable optimal horizontal grid spacing for reconstructing the 4D structure of wet refractivity based on the solution convergence rate and an RMS error analysis using GPSnet. First, a 3×6 voxel grid with 1° resolution (i.e. ~110 km resolution) was tested. Secondly, a 6×12 voxel grid with 0.5° resolution (i.e. ~55 km resolution) was then examined. This is approximately the overall diameter size of the super cell thunderstorm. It was also a similar size to the inter-station GPSnet distance, which is the suggested voxel resolution adoption following the preconditions of GPS tomography from Bender and Raabe (2007). Finally, a 12×24 voxel grid with 0.25° resolution (i.e. ~27.5km resolution) was analysed. This studied the capability of high grid resolution in comparison to the inter-station distance of GPSnet. Again, this would be optimal for severe weather monitoring (Ahrens and Samson, 2010).

Table 5.5: Base voxel setup and the experiments for various horizontal grid resolutions.

Voxel resolution	**Base voxel setup**	**Experiment variations**
Horizontal (grid)	55 km	110 km, 55 km, 27.5 km
Vertical (layers)	15	15
Vertical layer spacing	Exponential function	Exponential function

An increase in the horizontal resolution exponentially increases the number of unknown parameters of wet refractivity to be estimated. As a result the number of observations per unknown parameter decreases dramatically. With finer resolutions, more unknown parameters need to be solved for with a constant number of observations. Solving for these unknowns becomes increasingly more ambiguous above the highest GPS station, especially in the mid-to-upper troposphere because of the under-determined solution. This is where pseudo-observations and vertical constraints have an increasingly greater influence on the solution estimate. In fact the number of pseudo-observations increases proportionally with the exponential increase in resolution and unknown parameters, which minimises both the influence of GPS observations on the solution and the sharp changes in the reconstructed wet refractivity fields. This in turn limits the convergence rate and vertical resolvability of the Kalman filter solution. An additional limiting factor is the flat geometry of the GPSnet. Only 8 stations exceed an altitude of 500 m, with a maximum station height of 1900m. Large differences in receiver heights are beneficial for resolving the vertical structure using tomography (Bender and Raabe, 2007). Because of these limitations, additional meteorological information on the vertical profile of wet refractivity becomes increasingly more important (Gradinarsky and Jarlemark, 2004). For all three horizontal resolutions tested, the vertical layer spacing was kept fixed to 15 layers using the exponential method (Figure 5.4) as shown in Table 5.5.

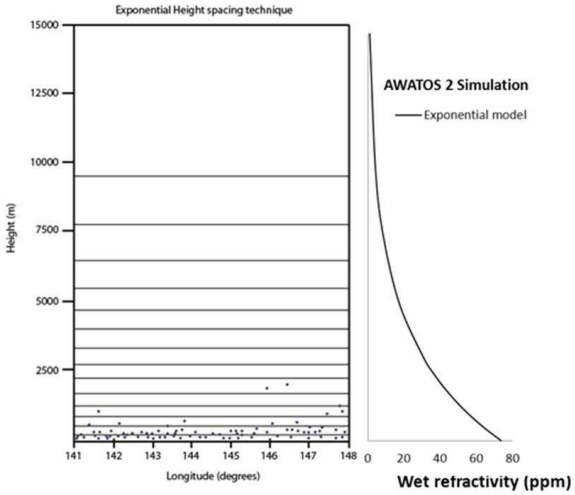

Figure 5.4: Vertical distribution of GPSnet stations in the exponential layer spacing model (left), and exponential refractivity function (right).

The initial refractivity field was input as an initial state of the backward model. This was set to 0 ppm with the covariance matrix and scale height of variance model derived from radiosonde observations on the day of 1 Dec. 2010 (see Table 5.1). The configuration of the initial state was set to 0 ppm such that the convergence rate of each experiment could be investigated and compared.

Results and discussion

a) GPS tomographic wet refractivity solution

Figures 5.5 − 5.7 present colour contour maps of the time series of the reconstructed wet refractivity profile at (A) (see Figure 5.3) for the initial 60 minutes of processing using the 110 km, 55 km and 27.5 km horizontal resolutions, respectively. The profiles on the right show the average value and standard deviation at each height layer along the vertical profile for the total 60 minutes. The time series displays a trend of fast convergence rate below 1500m for the 55 km resolution compared with the 110 km and 27.5 km resolutions. This is evident in the height resolved standard deviations where larger variations exist below 1500m.

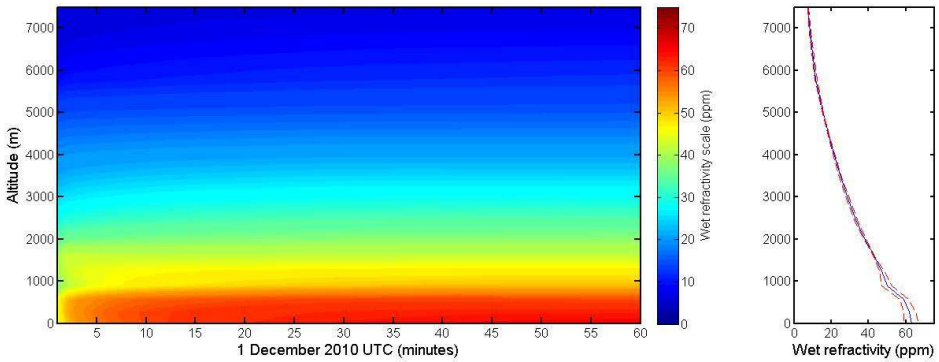

Figure 5.5: Profile time series of the estimated wet refractivity (ppm) field for 110 km horizontal resolution for the initial 60 minutes of processing (left), and the average value and standard deviation for each height layer (right).

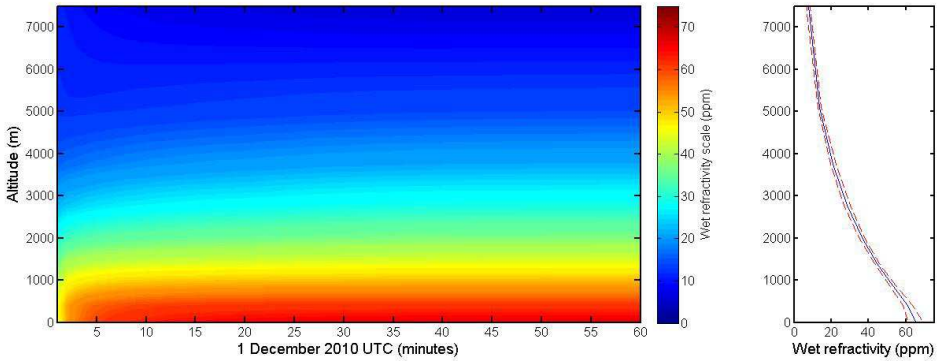

Figure 5.6: Profile time series of the estimated wet refractivity (ppm) field for 55 km horizontal resolution for the initial 60 minutes of processing (left), and the average value and standard deviation for each height layer (right).

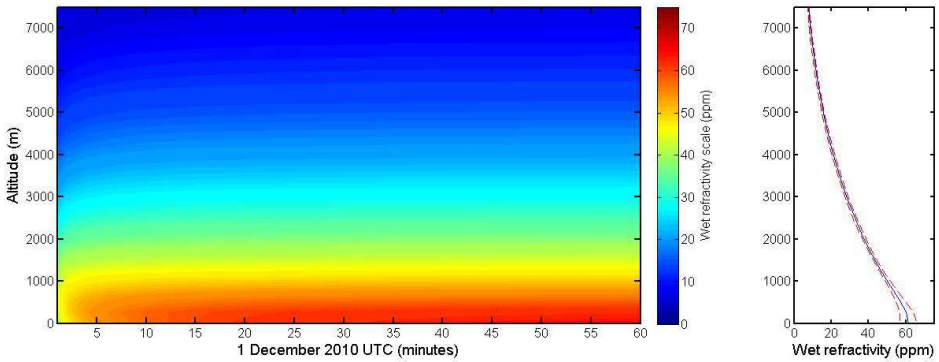

Figure 5.7: Profile time series of the estimated wet refractivity (ppm) field for 27.5 km horizontal resolution for the initial 60 minutes of processing (left), and the average value and standard deviation for each height layer (right).

b) Comparison of estimated and true wet refractivity solutions

Figures 5.8 − 5.10 present the comparison between the estimated and true simulated state for the initial 60 minutes using the 110 km, 55 km and 27.5 km horizontal resolutions, respectively. Each comparison is evaluated at the profile (A) shown in Figure 5.3. The RMS error was derived for each profile using the difference between the estimated solution and true simulated field at each vertical height layer (see Eq. (5.2)). The profile on the right of each figure represents the bias and standard deviation for the comparison at each vertical height layer. The time series of RMS error for the initial 60 minutes of process is also displayed beneath each figure.

The bias and standard deviation of the 110 km resolution, presented in Figure 5.8, indicates an inability to resolve the true state. This is particularly true for height layers below 1400 m. It is suggested that this is due to the Gaussian error in the observation model providing more uncertainty in the prediction due to less unknown parameters. Inaccuracies in multiple observations can have an adverse effect on the update solution (Troller, 2004). Furthermore, a positive bias forms after 10 minutes of processing at an altitude of 500 m reaching a magnitude of 4.5 ppm. This bias anomaly slowly dissipates after 70 minutes. Also, a negative bias becomes evident at ~6000 m altitude of 3 ppm after 15 minutes, which slowly dissipates to a stabilised error of less than 1 ppm after 60 minutes.

The bias and standard deviation for the 55 km resolution (see Figure 5.9) presents a much higher accuracy with the simulated wet refractivity field. The colour contour map presents rapid convergence, especially in the mid to low troposphere from the initial state vector of 0 ppm (Table 5.1). A small positive bias developed again after 10 minutes of processing at an altitude of ~500 m. However, this anomaly only reaches a magnitude of 0.9 ppm. The standard deviation at each height layer for the initial 60 minutes of processing presents a consistently high accuracy.

A similar trend exists for the 27.5 km resolution (see Figure 5.10) when compared to the 55 km resolution. However a much slower convergence rate is evident in the colour contour map. This resolution develops a consistent but larger standard deviation for each height layer. Also an unacceptable bias and standard deviation exists below 1000 m where the error is still not stabilised after 60 minutes of processing. The slow convergence rate is also evident in the time series of the RMS error. This slow convergence in the lower height layers is due to the exponentially increased number of unknowns to be solved for in the estimated state solution. The 27.5 km resolution contains 6882 unknown parameters compared to the 2294 unknowns and 918 unknowns attributed to the 55 km resolution and 110 km resolution, respectively. This quantifies an increase in unknown parameters by a factor of 3 and 7.5, respectively. As the number of integral observations remains constant, the number of observations per unknown significantly decreases. This effect is evident in the slow convergence of the 27.5 km resolution.

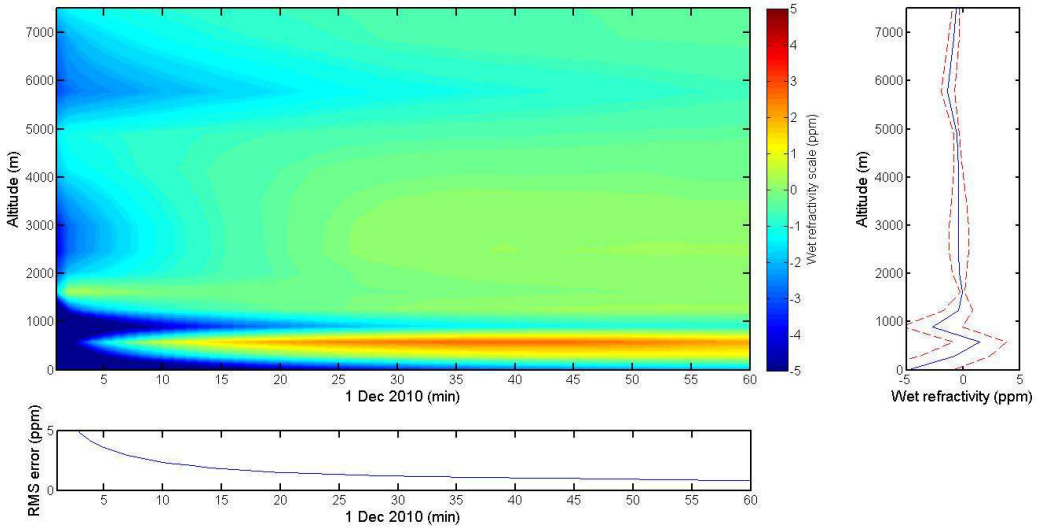

Figure 5.8: Time series colour contour map of the comparison between the estimated state using the 110 km horizontal resolution and the true simulated field for initial 60 minutes of processing (centre). The time series of RMS error (bottom), and bias and standard deviation for each height layer (right).

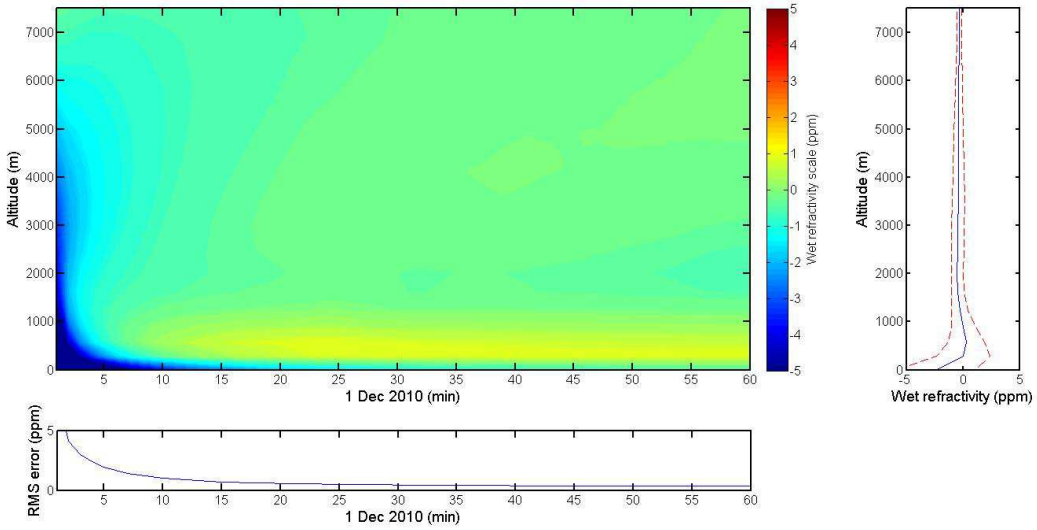

Figure 5.9: Time series colour contour map of the comparison between the estimated state using the 55 km horizontal resolution and the true simulated field for initial 60 minutes of processing (centre). The time series of RMS error (bottom), and bias and standard deviation for each height layer (right).

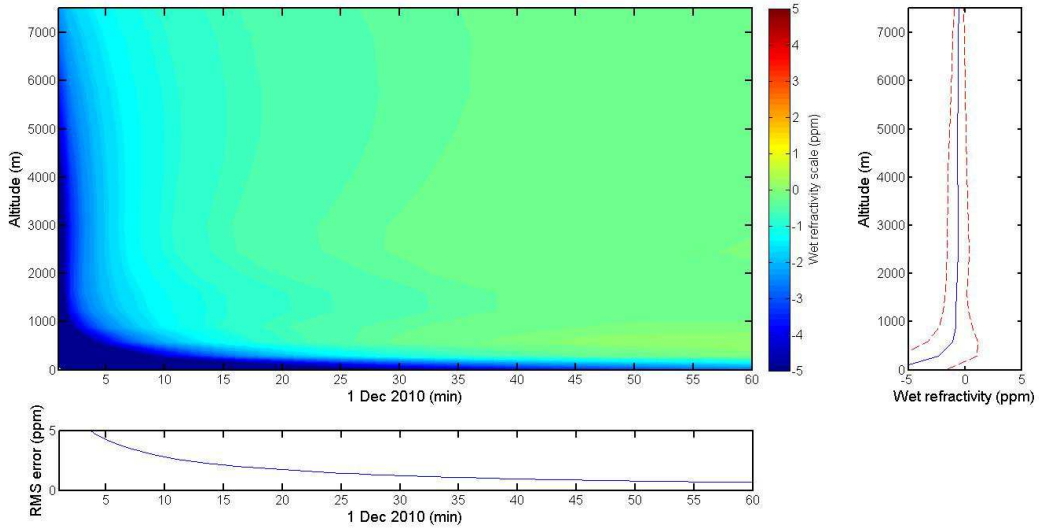

Figure 5.10: Time series colour contour map of the comparison between the estimated state using the 27.5 km horizontal resolution and the true simulated field for initial 60 minutes of processing (centre). The time series of RMS error (bottom), and bias and standard deviation for each height layer (right).

c) Vertical resolvability analysis

The vertical resolvability of the estimated solution is a key consideration for an optimal horizontal voxel resolution. The vertical analysis examines the convergence rate of each height layer. Figures 5.11(a) and (b) present the difference between the estimated wet refractivity state from the GPS tomography solution and the true simulated state at each height layer after the initial 15 minutes and 60 minutes of processing, respectively. Results after 15 minutes of processing revealed the 55 km resolution provided the fastest vertical resolvability. This was due to much lower differences compared with the 110 km and 27.5 km resolutions. Additionally, all three resolutions presented increasing differences above the highest GPS receiver up to approximately 6000 m altitude, with a maximum of 1.8 ppm, 0.6 ppm and 0.8 ppm for the 110 km, 55 km and 27.5 km resolutions, respectively. Furthermore, the 27.5 km and 110 km resolutions showed a slow convergence rate with layers below 1200 m in contrast to the 55 km resolution. Figure 5.11(b) presents the differences for each test at each height layer after 60 minutes of processing. It is evident for all three tests scenarios that the mid troposphere has a much higher correlation with the true wet refractivity state compared with the solution after 15 minutes of processing. The 27.5 km resolution shows the highest agreement below a height of 4000 m altitude. However, the convergence rate of this domain remains the slowest due to the ratio of observations to the amount of unknowns being too low.

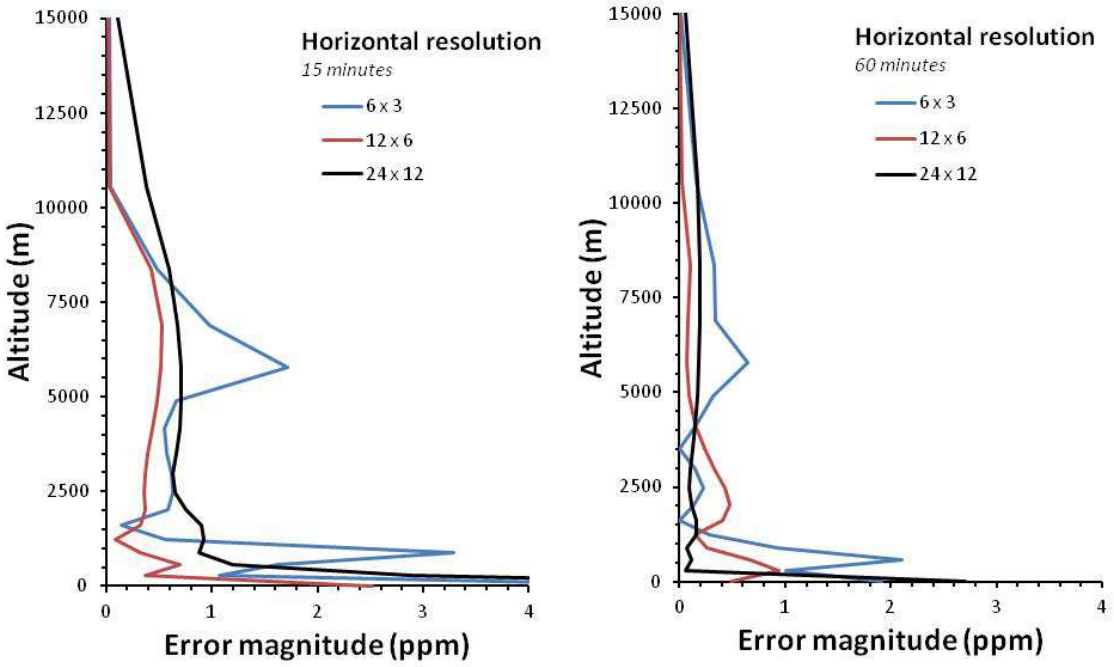

Figure 5.11: Vertical resolvability. Comparison of difference at each height layer for the 3 horizontal resolutions after the initial 15 minutes (left) and 60 minutes (right) of processing. The difference is between the tomographic solution estimate and the true simulated field.

d) Time series of the RMS errors for the horizontal resolutions

Figure 5.12 presents a time series of the RMS error for each test scenario when comparing the tomographic solution estimate with the true simulated state at profile (A). This figure shows the initial 60 minutes of processing. The time evolution for the RMS error of each horizontal grid resolution was used as an accurate method of determining solution convergence rate. Each RMS error profile follows the general trend of an inverse function. Table 5.6 provides statistical results for each test scenario over the 24-hour processing period. The 55 km solution converged below 1 ppm in 13 minutes and has a final RMS error of 0.49 ppm after 24 hours. The 110 km and 27.5 km grid solutions converged below 1 ppm in 45 and 40 minutes, respectively. The final RMS error for both after the 24-hour processing period revealed 0.78 ppm and 0.20 ppm, respectively. The error stabilisation for this resolution was quicker than the 110 km and 27.5 km resolutions by a factor of 3.46 and 3.07, respectively.

The influence of the Gaussian measurement error in the simulated DD SWD observations (see Eq. (4.27)) decreased with the increase in the unknown wet refractivity parameters to be solved for. This increase in unknowns also linearly increased the number of pseudo observations and constraints. Therefore, the highest resolution (27.5 km) revealed the smallest final RMS error after 24-hours, due to the measurement error inflicting less influence over more unknown parameters. However, this

resolution also revealed the slowest convergence rate from initialisation. This is due to a similar problem where the ratio of observations per unknowns is significantly decreased compared to the 55 km and 110 km resolutions.

Based on these results it was concluded that the 55 km solution presented the fastest convergence rate between the update solution of the backward model and the true simulated field.

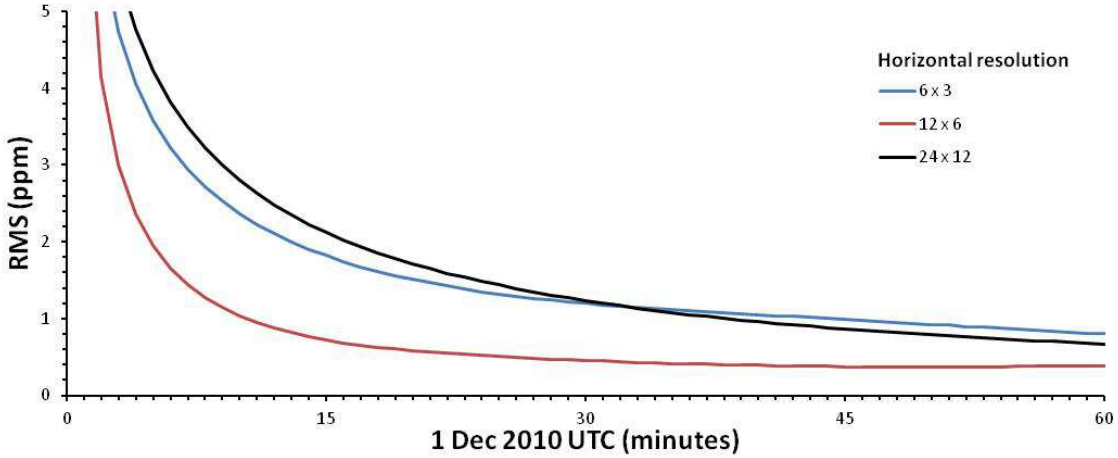

Figure 5.12: Time series of RMS errors for the tomographic solutions of each horizontal resolution test for the initial 60 minutes of processing.

Table 5.6: Final results for the 3 horizontal grid resolutions based on convergence rate and RMS error.

Resolution	**Convergence rate** *(mins)*	**RMS error (ppm)** *After 1 hour*	**RMS error (ppm)** *After 24 hours*
27.5 km	40	0.68	0.20
55 km	13	0.52	0.49
110 km	45	0.81	0.78

5.5.2. Vertical resolution and layer spacing determination

The spatial resolution of the voxel layers in the vertical direction is fundamental for the statistical optimisation of GPS tomographic solutions. It is also paramount to determine the optimal layer spacing technique for accurately reconstructing WV variability. Unfortunately, vertical resolution and layer spacing determination is a challenging task because a major limitation of GPS tomography is the vertical resolvability of the wet refractivity. This is due to the relatively flat vertical distribution of the GPSnet and the restricted geometry of satellite-to-ground observations. This section provides statistical analysis to optimise the vertical resolution and spacing to obtain fast convergence, vertical resolvability and high vertical resolution for the GPS tomographic solution.

Vertical layer resolution

The investigation of wet refractivity fields required the determination of the vertical resolution for optimal analysis. The lower and upper bounds of the vertical layer discretisation are from 0 to 15000 m altitude. The 4D distribution of WV suggests that the highest density exists within the planetary boundary layer (PBL), which is below ~2000m and decreases exponentially with height. The WV at the height of the tropopause is suggested to have a negligible effect on the propagating GPS signal (Nilsson, 2005). The spatial resolution in the lower-to-mid troposphere is a critical issue because the WV distribution from approximately 2 to 7 km has the highest variability during severe weather (Houze, 2004; Song and Grejner-Brzezinska, 2009). Also, the ability to resolve the vertical structure decreases dramatically above the highest receiver.

This section analyses the effect of vertical resolution on the convergence rate, RMS error, and vertical resolvability of the solution at profile (A) represented in Figure 5.3. The optimal 55 km horizontal resolution was used as a constant horizontal resolution based on the final results from Section 5.5.1. Five vertical resolutions were investigated for the vertical discretisation using GPSnet. They include 5, 10, 15, 20 and 25 layers (see Table 5.7). A synthetic exponential wet refractivity field was implemented as the true simulated field (Eq. 5.1) for this experiment.

Table 5.7: Vertical layer resolution experiments.

Voxel resolution	**Experiment variations**
Horizontal	55 km
Vertical (layers)	5, 10, 15, 20, 25
Vertical layer spacing	Exponential function

The determination of the vertical spacing used the function expressed in Eq. (5.3) to define the height layers. The layer spacing was derived as a function of height. An increase in height has an exponential increase in layer spacing. This increase is proportional to a constant growth factor (w) at i^{th} layer. The height subdivision can be expressed as:

$$\Delta h_i = \Delta h_0 w^i \tag{5.3}$$

where Δh_i is the thickness of layer i and Δh_0 is the thickness of the first layer.

A constant growth factor (w) of 1.3 (Perler et al., 2011) was used for the vertical resolution of each vertical spacing. The vertical resolutions for analysis are presented in Figure 5.13.

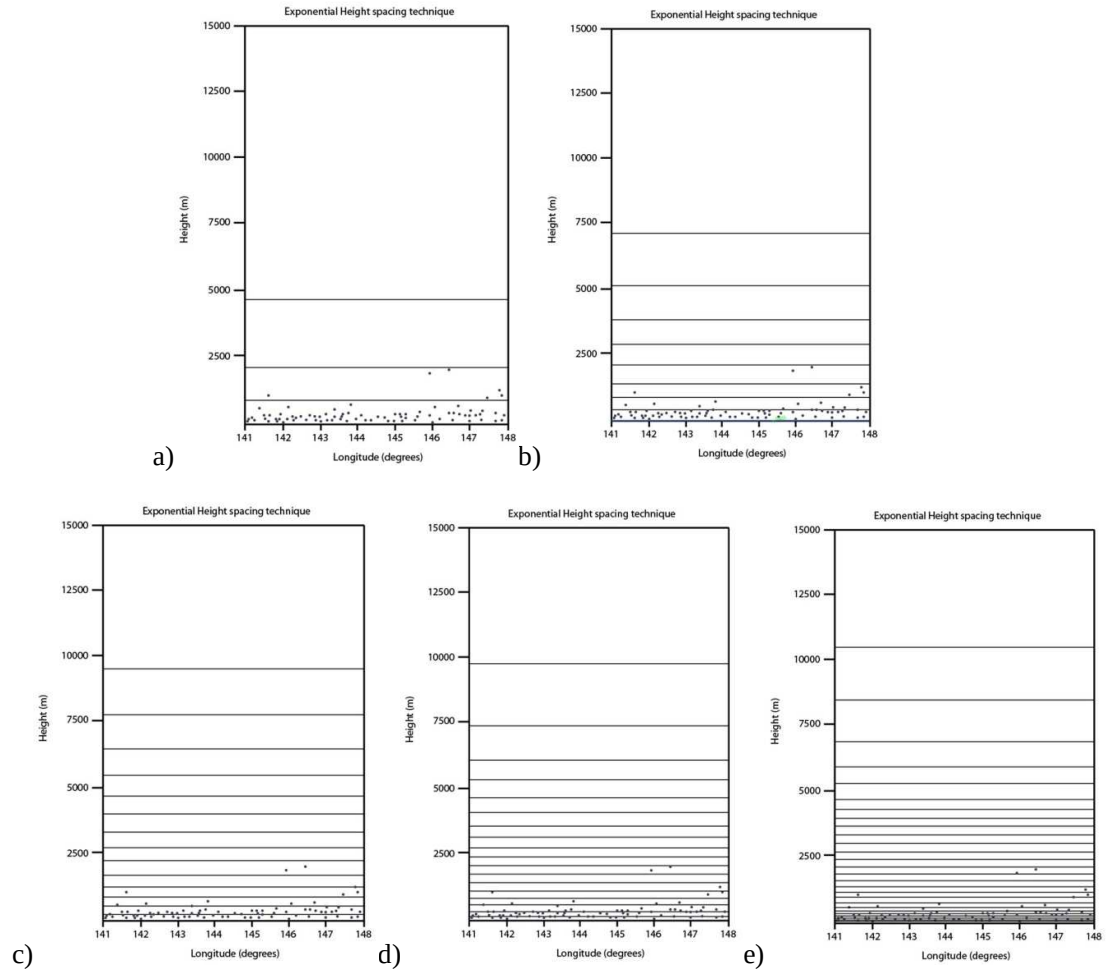

Figure 5.13: Exponential discretisation of the vertical domain using 5 (a), 10 (b), 15 (c), 20 (d) and 25 (e) layers.

As discussed in Section 5.5.1, the GPS tomographic simulation process used simulated GPS integral observations (Eq. (4.27)), constructed using a ray-tracing algorithm through the synthetic exponential wet refractivity field (Eq. (5.1)) with a Gaussian measurement error (Eq. (4.28)). These observations are in turn used for the backward model process (see Tables 5.3 – 5.4). A propagation step size of 30 seconds used in our tests is equal to the sampling rate of the GPS DD observations used in real data analysis for this research.

Results and discussion

a) Comparisons of vertical resolutions

Figures 5.14 – 5.18 show results of the differences between each GPS tomographic solution for the vertical resolutions of 5-, 10-, 15-, 20- and 25-layers respectively, and the true simulated field. These

figures present the initial 60 minutes of processing. The profile accuracy of each solution in the time series is presented as an RMS error value shown at the bottom. The bias and standard deviation at each height layer are presented on the right.

Both the 5- and 10-layer solutions reveal an inability to effectively resolve the vertical structure over the initial 60 minutes of processing, especially in the low-to-mid troposphere from 2000 – 7000 m. However, height layers below 1000 m suggest a fast convergence and a fast convergence with the true simulated field, with differences decreasing below 1 ppm after 10 minutes of processing. The time series for the 15-, 20- and 25-layer resolutions yielded similar results. The 15-layer solution presents slightly quicker overall convergence, especially in the height layers above 2000 m. This is reflected in the bias and standard deviation above 2000 m being slightly smaller than the 20- and 25-layer resolutions.

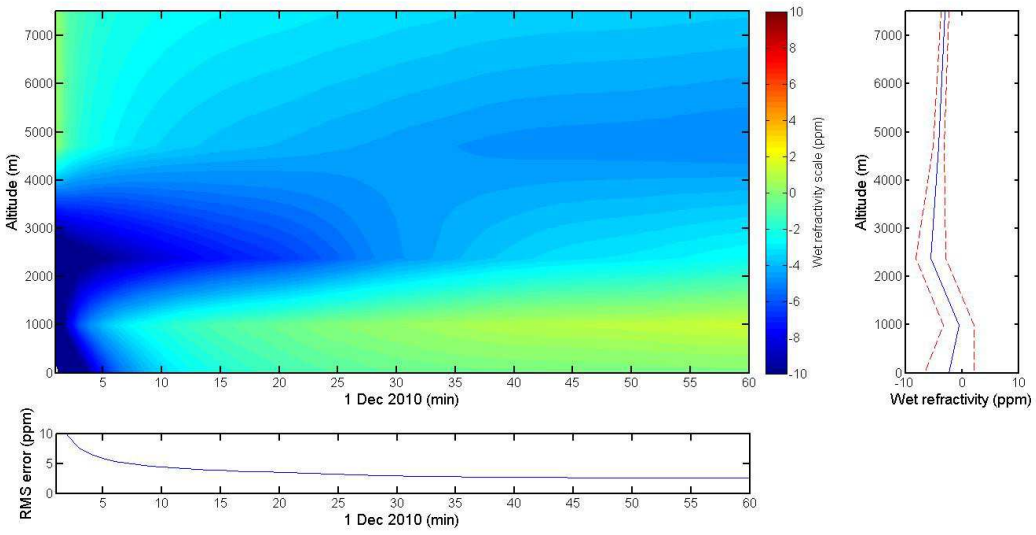

Figure 5.14: Time series colour contour map of the comparison between the estimated state using the 5-layer resolution and the true simulated field for initial 60 minutes of processing (centre). The time series of RMS error (bottom), and bias and standard deviation for each height layer (right).

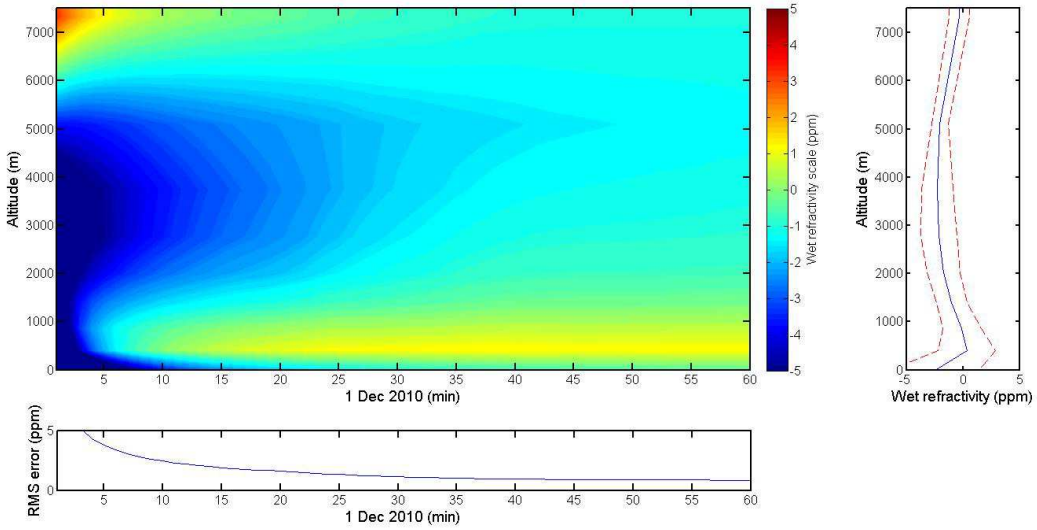

Figure 5.15: Time series colour contour map of the comparison between the estimated state using the 10-layer resolution and the true simulated field for initial 60 minutes of processing (centre). The time series of RMS error (bottom), and bias and standard deviation for each height layer (right).

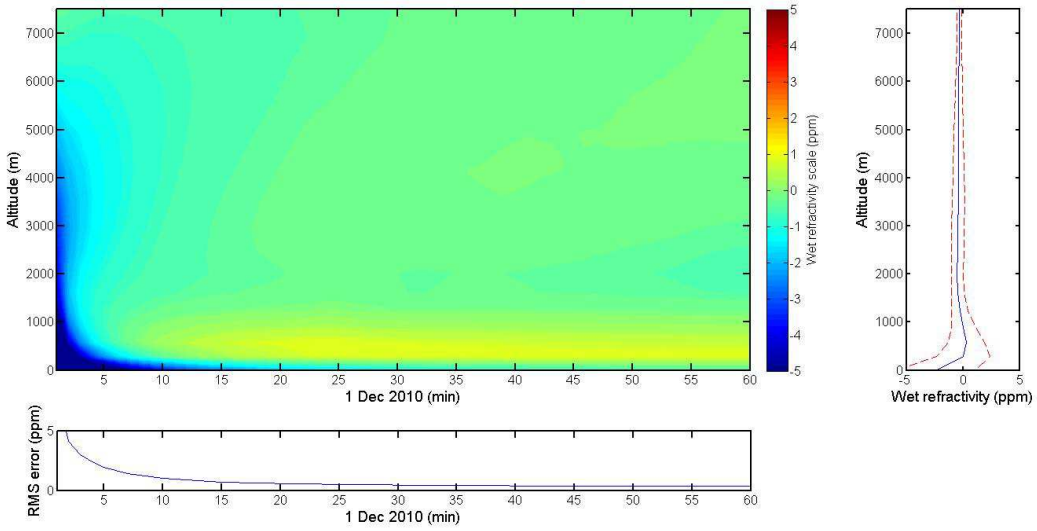

Figure 5.16: Time series colour contour map of the comparison between the estimated state using the 15-layer resolution and the true simulated field for initial 60 minutes of processing (centre). The time series of RMS error (bottom), and bias and standard deviation for each height layer (right).

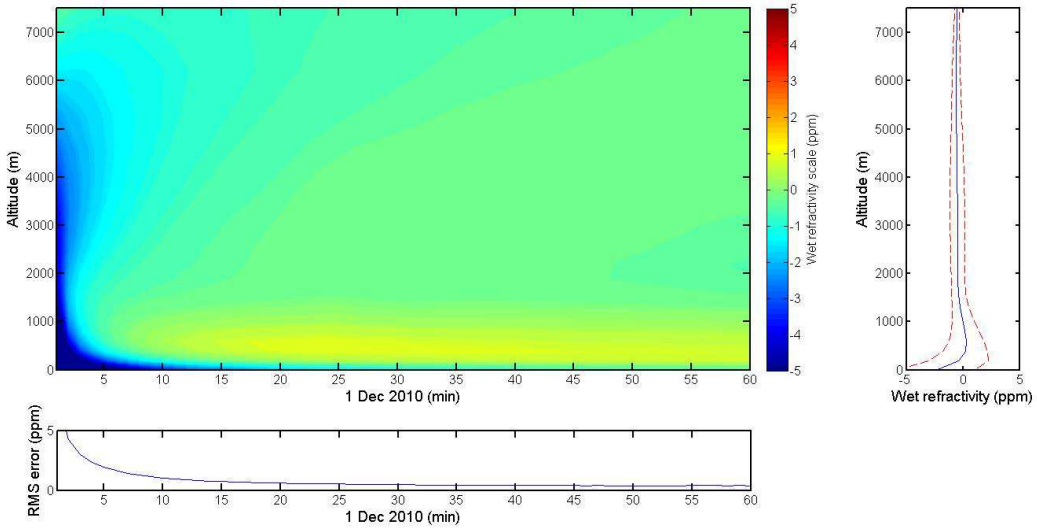

Figure 5.17: Time series colour contour map of the comparison between the estimated state using the 20-layer resolution and the true simulated field for initial 60 minutes of processing (centre). The time series of RMS error (bottom), and bias and standard deviation for each height layer (right).

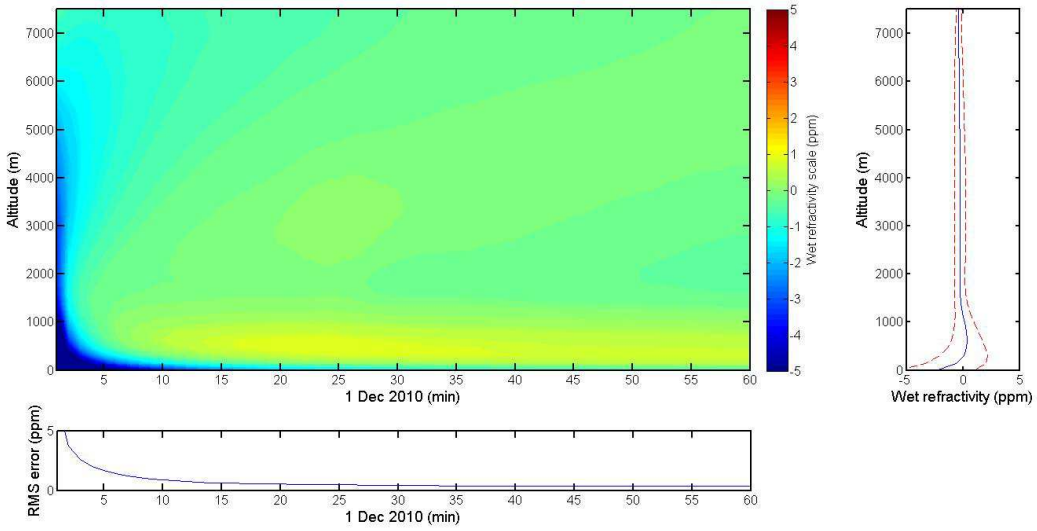

Figure 5.18: Time series colour contour map of the comparison between the estimated state using the 25-layer resolution and the true simulated field for initial 60 minutes of processing (centre). The time series of RMS error (bottom), and bias and standard deviation for each height layer (right).

b) Vertical resolvability analysis

The vertical resolvability of each vertical resolution test was analysed after the initial 15 and 60 minutes of processing and the results are presented in Figures 5.19(a) and (b), respectively. An optimisation of the vertical resolution was determined by the vertical resolvability based on the error magnitudes at each profile point. Results from the 15-layer solution after 15 minutes give a slightly better agreement with the true simulated field, especially at heights above the highest GPS receiver (1900 m) where error magnitudes do not exceed 0.5 ppm. This is a good result as the reliability of solution vertical resolvability decreases above this height. The 20- and 25-layer solutions also show good resolvability with both resolutions producing errors below 1.0 ppm and 0.7 ppm above 1900 m altitude, respectively.

The 5- and 10-layer solutions both present major limitations in resolving the mid-to-upper troposphere after 15 minutes with errors reaching 5 ppm and 3 ppm, respectively. The 10-layer solution presents improved resolvability after 60 minutes (Figure 5.19(b)) with mid tropospheric convergence improved to errors below 1.4 ppm. The 15-, 20- and 25-layer solutions all present good resolvability after 60 minutes of processing, especially height layers above 3000 m, where errors consistently remain below 0.3 ppm. Furthermore these three solutions provide accuracies below 4000 m with error magnitudes < 1 ppm.

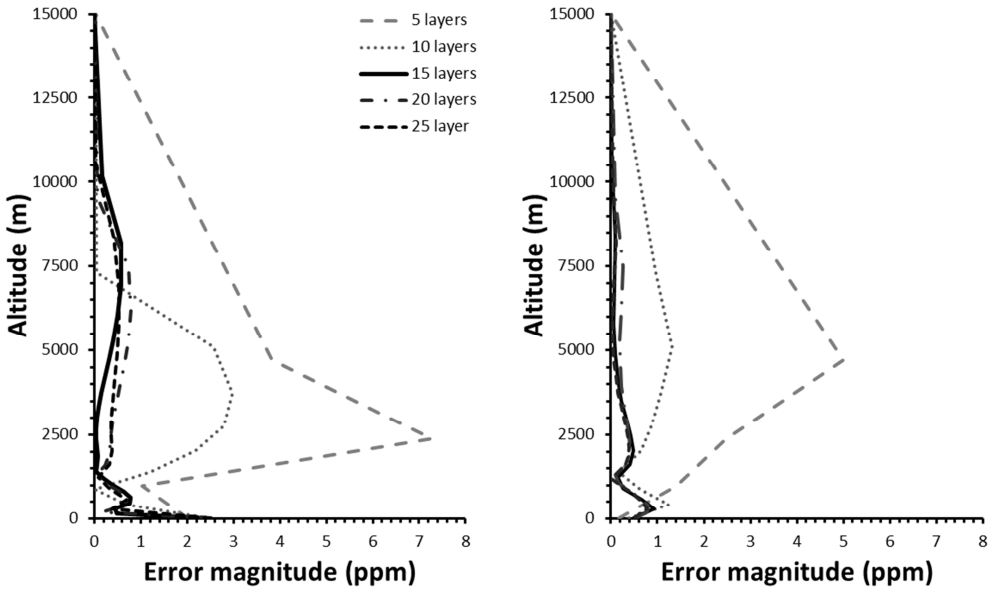

a) b)

Figure 5.19: Vertical resolvability presenting the comparison of error magnitudes at each profile point for the 5 vertical layer solutions after the initial 15 minutes (a) and 60 minutes (b) of processing.

c) Time series of the RMS errors for the vertical resolutions

Figure 5.20 presents the statistical results for the time series of the RMS error for each vertical resolution test over the initial 60 minutes of processing. These results also provide estimates of the tomographic solution convergence rate for each vertical resolution. The 15-, 20- and 25-layer resolutions have the fastest convergence with very similar RMS error trends. An error stabilisation value of < 1 ppm was used similar to the horizontal resolution analysis. Both the 5- and 10-layer solutions appear to have limited ability to resolve the mid-troposphere (see Figures 5.19(a) and (b)), thus affecting the accuracy of the solution resulting generally in higher RMS error solutions. The 5- and 10-layer solutions had an RMS error of 3.81 ppm 1.89 ppm after 15 minutes, and 2.57 ppm and 0.84 ppm after the first 60 minutes, respectively. As a result, the 5-layer solution did not achieve the stabilisation accuracy of < 1 ppm and the 10-layer solution took 37 minutes to do so. The 15-, 20- and 25-layer solutions have similar results with each revealing an RMS error of 0.72 ppm, 0.74 ppm and 0.72 ppm after 15 minutes, respectively, and 0.38 ppm, 0.40 ppm and 0.36 ppm after 60 minutes, respectively. The error stabilisation for each resolution was also quite similar with the 15-, 20- and 25-layer solutions converging on an accuracy of < 1 ppm after 13, 14 and 14 minutes, respectively.

It was therefore concluded that the 15-layer resolution was optimal based on a slightly faster convergence rate and higher vertical resolvability. However, the 20- and 25-layer solutions would also be acceptable for use based on the results from this analysis.

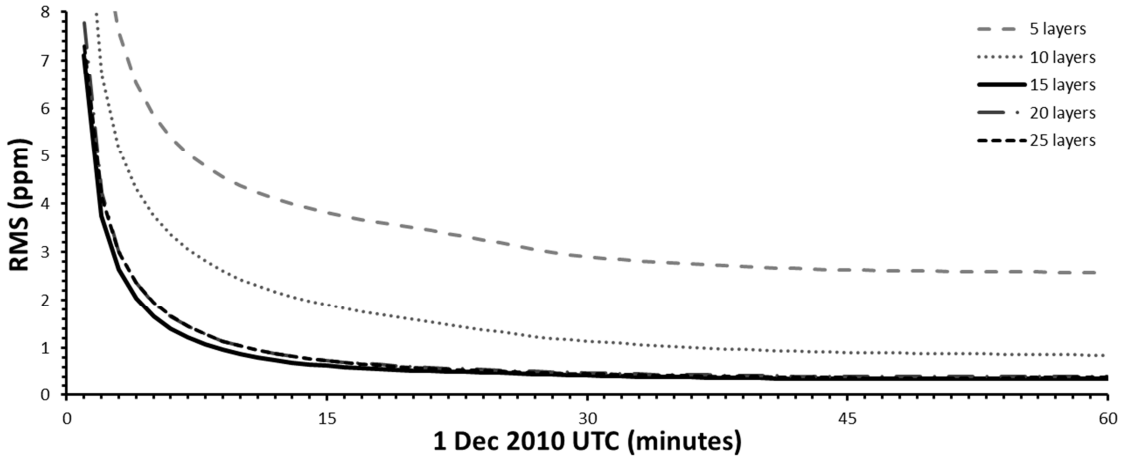

Figure 5.20: Time series of RMS error for the tomographic solutions of 5 vertical resolutions for the initial 60 minutes of processing.

Layer spacing techniques

Past research have adopted two different vertical spacing techniques – constant (Rohm and Bosy, 2011) and exponential (Champollion et al., 2005; Lutz, 2008; Perler, 2011). This test scenario aimed

at comparing both methods using the same number of layers, which corresponded to the same number of unknowns in Eq. (4.24). The vertical resolution was determined using two discretisation methods:

- *The constant method:* divides the vertical component into equal graduations of layer heights.
- *The exponential method:* uses an exponential function of height to determine the layer thickness. This function is proportional to a constant growth factor (w) at i^{th} layer as expressed by Eq. (5.3).

The advantages and limitations of the two methods are as follows:

- The exponential method creates higher resolution in lower layers, where the distribution of GPS stations are located within the initial 7 layers creating a height differential. In theory this will enhance the vertical resolvability compared to the constant technique, which hold nearly all stations in the bottom layer.
- The exponential method provides higher resolution in lower layers where wet refractivity density and variability is high and lower resolution in upper layers where wet values approach 0 ppm.
- The constant method provides a much higher number of observations per unknown parameters in the lower levels of the troposphere, theoretically providing a more robust solution depending on accuracy of observations.

A flat distribution of GPSnet stations is evident with only 8 stations above 500 m altitude and the maximum height is ~1900m. A large range in station heights is beneficial for resolving the vertical structure using tomography (Bender and Raabe, 2007). Inter-voxel constraints and additional information on the vertical profile of refractivity are paramount for a robust tomographic solution (Gradinarsky and Jarlemark, 2004), particularly for a flat ground-based GPS network. The vertical layer spacing techniques are displayed in Figure 5.21.

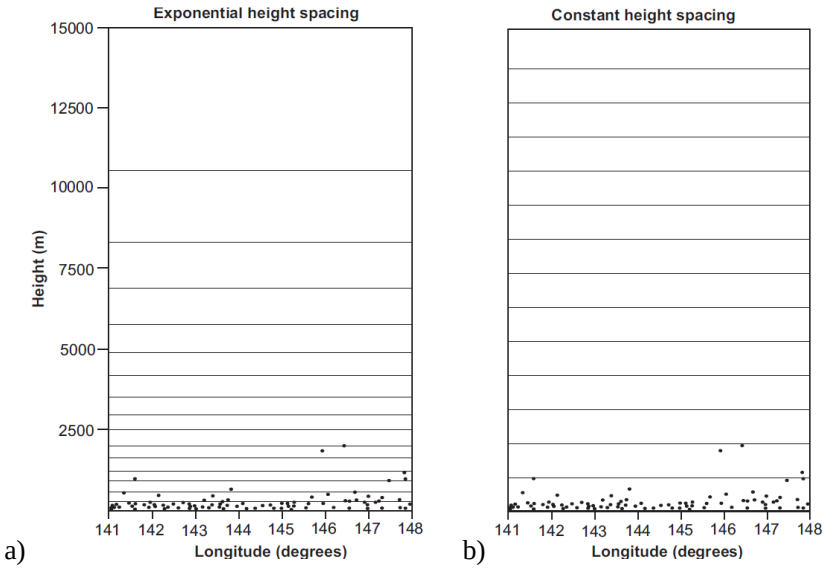

Figure 5.21: GPSnet station distributed in exponential layer spacing technique (a), and constant spacing technique (b).

Table 5.8: Vertical layer spacing method experiments.

Voxel resolution	Experiment variations
Horizontal	55 km
Vertical (layers)	15
Vertical layer spacing	Exponential function, constant spacing

Results and discussion

a) Vertical resolvability of layer spacing tests

Figures 5.22(a) and (b) present the vertical profile of the error magnitudes resulting from the two layer spacing techniques after 15 and 60 minutes, respectively. The exponential method after 15 minute (Figure 5.22(a)) provided a much higher accuracy below 4500 m altitude compared with the constant method. For example, results from exponential method at 2000 m altitude are smaller than the constant method by a factor of 3. Moreover, the exponential method holds a much higher spatial resolution in this domain with 9 vertical layers existing below 4000 m as opposed to 4. In contrast, the constant method resolved the mid-tropospheric region of 4500 – 8000 m with a higher accuracy and convergence rate. Results after 60 minutes (Figure 5.22(b)) revealed a generally higher accuracy using the exponential method, especially in the low-to-mid troposphere. The vertical resolvability after 15 and 60 minutes of processing also revealed that the exponential method estimates were generally more consistent over all layers.

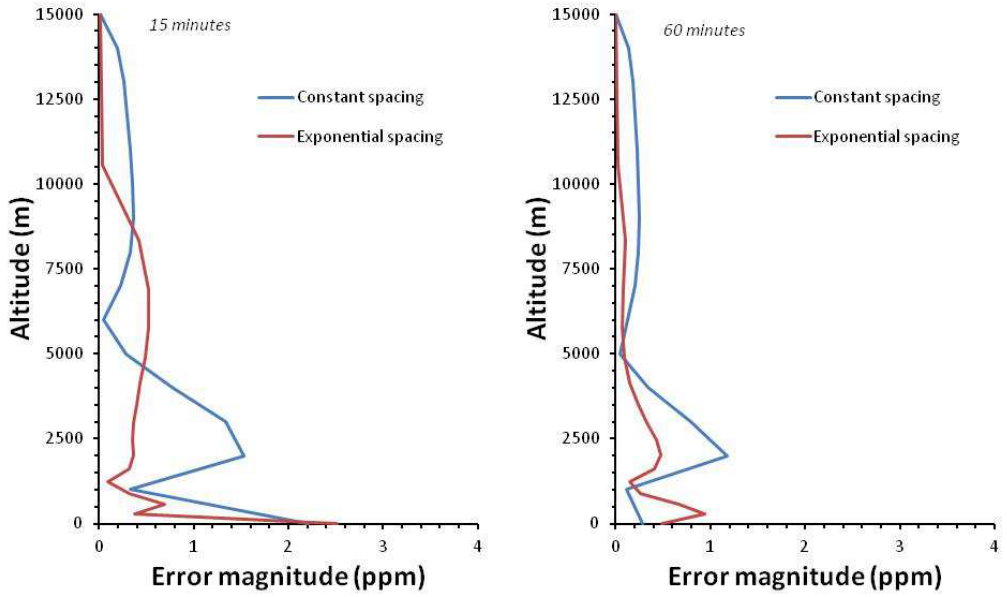

Figure 5.22: Vertical resolvability. Comparison of error magnitude at each height layer for the 2 vertical layer spacing techniques after the initial 15 minutes (left) and 60 minutes (right) of processing. The error magnitude is the difference between the tomographic solution and the true simulation wet refractivity field.

c) Time series of the RMS errors for the vertical layer spacing techniques

Figure 5.23 presents the time series of the RMS errors resulting from the two layer spacing techniques, for investigating solution convergence rate. As stated previously, an error of < 1 ppm was used to assess the convergence rate for error stabilisation. The results indicated a highly similar error trend with the exponential and constant methods achieving the error stabilisation of < 1ppm RMS error after 13 and 14 minutes, respectively.

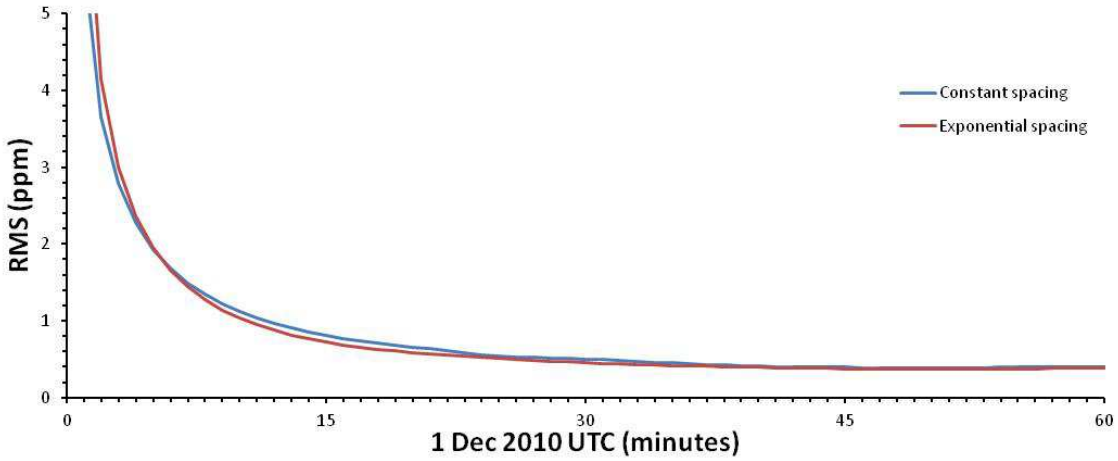

Figure 5.23: Time series of RMS error resulting from the tomographic solution of two vertical layer spacing methods for the initial 60 minutes of processing.

Based on the vertical resolvability, the exponential layer spacing method was concluded to be optimal. This is due to the higher resolution in the lower troposphere where wet refractivity is the highest and a generally more accurate vertical resolvability.

5.6. Spike layer analysis

This section presents results from a simulated spike wet refractivity field (Rohm and Bosy, 2011; Perler 2011) for investigation of the limitation of the vertical resolvability when confronted with sharp vertical changes of wet refractivity. Sharp vertical spikes in wet refractivity are evident in the formation and lifecycle of severe weather events. This is caused by large-scale updraft of warm, moist air in the convective processes and rapid inflow jets of dry, dense air in the stratiform processes (Ahrens and Samson, 2010). This analysis used a constant wet refractivity field of 0 ppm and implemented a wet refractivity spike layer of 10 ppm from 2000 m to 2500 m altitude (see Eq. (5.4)), which is situated at ~100 m above the altitude of the highest ground-based GPS station. This altitude is where the confidence of solution vertical resolvability decreases with increasing height. This test scenario used the same parameter settings for the simulated observations of the forward model and tomographic model setup of the backward model as stated in Table 5.2 and 5.3. The base voxel setup was also used for the discretisation of the model field as stated in Table 5.5. The Earth's curvature has a positive influence on the vertical resolvability of the solution due to the geometry of the spheroidal grid layers as opposed to a planar grid geometry (Perler, 2011).

$$N(\lambda, \phi, h) = \begin{cases} 10 & if\ h \in [2000, 2500] \\ 0 & all\ else \end{cases} \tag{5.4}$$

Figure 5.24 presents the time series profiles of the GPS tomographic solution estimates for the initial 20 minutes of processing. The true simulated spike profile is represented by red dots and the increasingly darker shades of grey represent the GPS tomographic solution every 5 minutes. After 20 minutes of process the RMS error for the solution was 0.94ppm. The speed of solution convergence for estimating the true simulated state of the wet refractivity spike was slightly slower than resolving the exponential simulated state (See Table 5.6) by a factor of 1.54. Conclusions for this analysis suggest that GPS tomography has the ability for sensing dynamic changes to the vertical structure of wet refractivity above the highest GPS station with a high accuracy and fast convergence.

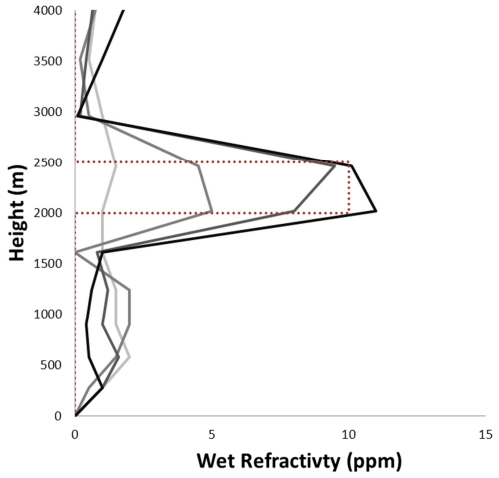

Figure 5.24: Time series of the GPS tomographic solution for the spike layer analysis for the initial 20 minutes of processing. The true simulated spike field is represented with red dots, and the increasingly darker shades of grey profiles depict the evolving solutions every 5 minutes.

5.7. Influence of additional observations

Assessing the influence of additional types of observations on the GPS tomographic solution is of high importance. This is because they have the potential to significantly increase the solution accuracy and reliability. This influence was initially analysed using simulated data. Two different types of observation methods were used for this investigation, comparing the influence of the observation geometry, number of observations and temporal resolutions on the RMS error, vertical resolvability and convergence rate of the GPS tomographic solution. The two different types of observation methods were:

- *Ground-based synoptic weather network observations:* A ground-based network of weather stations with data provided at a temporal resolution of 15 minutes was simulated. The GPSnet network distribution was used in this test scenario. This is because the real data analysis used interpolated meteorological point data at each GPSnet station for the additional point observations in the multi-observational GPS tomography analysis (see Chapter 7)
- *Profile observations:* the profile geometry of radiosonde and GPS RO was simulated, which provide meteorological parameters along the vertical profile. The MELB radiosonde station was used for the location of the profile, which was located close to the middle of the voxel model (see Figure 5.3). A sample rate of 12 hours was set to simulate the temporal resolution of real data.

Parameters for the forward and backward model remain constant (see Tables 5.1 – 5.3). For both methods, the observation data ($N_{(\lambda,\phi,h)}$) were simulated for each station and profile point ($p_{\lambda,\phi,h}$)

using Eq. (4.29) with a standard deviation of 2 ppm using Eq. (4.30), and were included into the observation and covariance matrix, respectively. The objective of this investigation was to identify the magnitude of influence of the inclusion of additional data on the accuracy of the GPS tomographic solution estimates.

Results and discussion

a) GPS tomographic wet refractivity solution

Figures 5.25 and 5.26 present the time series of wet refractivity derived from two GPS tomographic tests, including additional synoptic network observations and profile observations in the solutions, respectively. The standard deviation and average value for each height layer is presented on the right of each figure. It can be seen that both tests present similar results and very fast convergence.

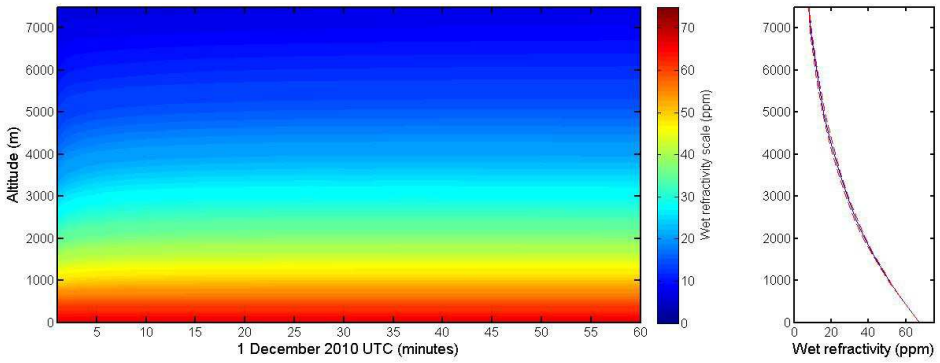

Figure 5.25: Profile evolution of simulated wet refractivity (ppm) field for solution including additional synoptic observations for the initial 60 minutes of processing (left). The average value and standard deviation for each height point are presented (right).

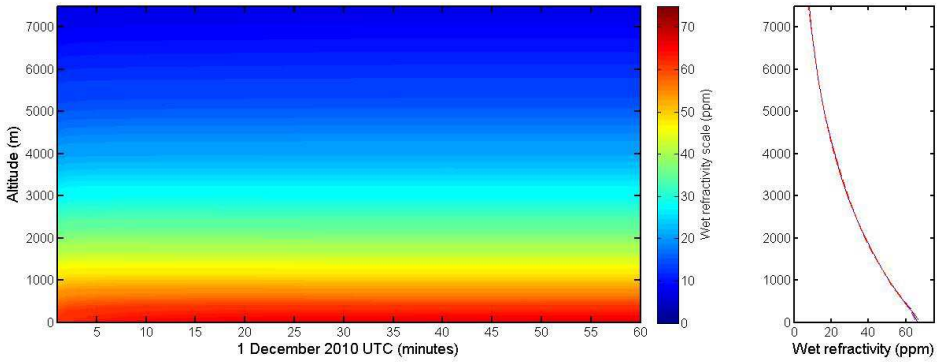

Figure 5.26: Profile evolution of simulated wet refractivity (ppm) field for solution including additional profile observations for the initial 60 minutes of processing (left). The average value and standard deviation for each height point are presented (right).

b) Vertical resolvability analysis

Figures 5.27(a) and (b) present the difference between the GPS tomographic solution estimate and the true simulated field for both the solution including additional synoptic network observations and the solution including additional profile observations after 15 and 60 minutes, respectively. Furthermore, the original GPS tomographic solution (see Section 5.5.1), which included no additional data, was introduced into each figure to analysis the influence. The vertical resolvability of the two solutions after the initial 15 minutes of processing (Figure 5.27(a)) revealed significant improvement in the convergence rate. This was especially evident in the solution which included additional profile observations, where the accuracy for heights between 1000 – 4000 m was better than 0.1 ppm. The solution including additional synoptic network observations showed a large improvement in accuracy below 1000 m altitude. The error of this at 270 m altitude was smaller than the original solution by a factor of 3.2.

Again, the synoptic solution provided the highest accuracy below 1500 m after 60 minutes (Figure 5.27(b)) and the solution including additional profile observations resolved the vertical profile from 1500 – 9000 m altitude with the highest accuracy. This result is logical as the geometry of the profile information complements the limitation of resolving the vertical structure. Therefore, profile observation methods such as radiosonde provide higher accuracy, faster convergence rate and a more robust operation when processing GPS tomographic solution. However, the major limitation was with the temporal resolution of this observation method as only 2 profiles were provided per day. The addition of synoptic meteorological network information provided valuable information on the state of refractivity at the surface. However, this method provided no additional information on the vertical structure. Furthermore, in contrast to the radiosonde method, the temporal resolution of synoptic network observations was quite high, with information available every 15 minutes. The difference in temporal resolutions between the two additional data methods was the reason why the accuracy of the synoptic solution was slighter higher than the profile solution after the initial 60 minutes of processing.

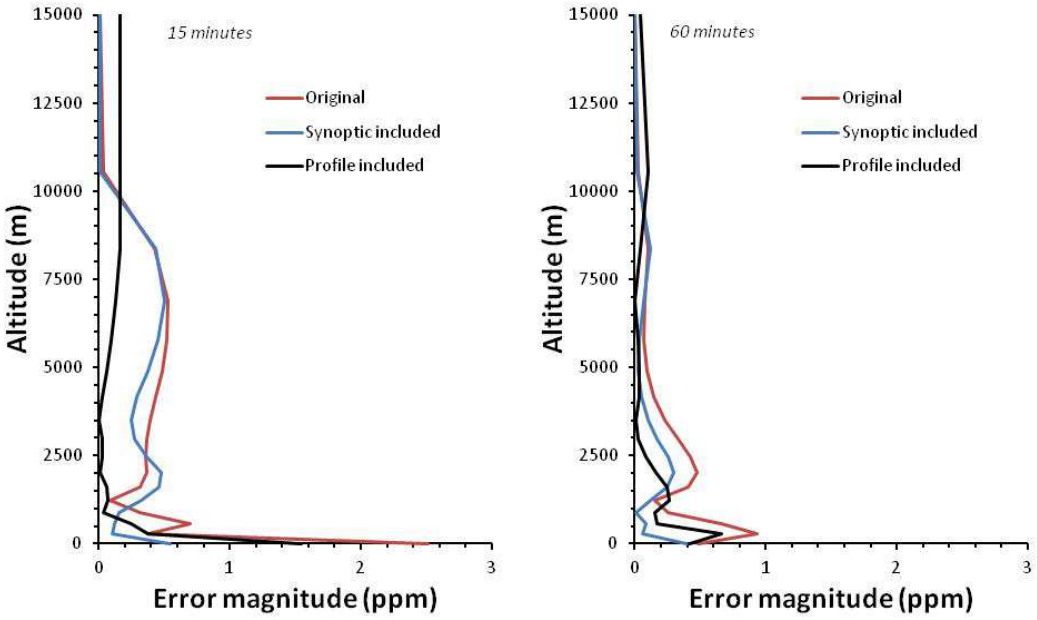

a) b)

Figure 5.27: Vertical resolvability. Comparison of the error magnitude at each height layer for the two GPS tomographic test scenarios including the additon of synoptic (blue) and profile (red) observations after the initial 15 minutes (left) and 60 minutes (right) of processing. The original profile of the GPS tomographic solution with no additional data is present (black). The error magnitude is the difference between the tomographic solution and the true simulation wet refractivity field.

c) Time series of the RMS errors for additional observations analysis

Figure 5.28 presents the time series of RMS errors for both the test scenario with the addition of synoptic network observations and the addition of profile observations. The original solution with no additional observations is included for analysis. The synoptic solution presented an error stabilisation of < 1 ppm after 4 minutes and a final RMS error of 0.22 ppm after 24 hours. The profile solution reached this stabilised state after 3 minutes with a final RMS error of 0.1 ppm after 24 hours. Compared to the results from the original GPS tomographic solution, the convergence rate of the synoptic and profile solutions are faster by a factor of 3.3 and 4.3, respectively. Therefore, it was concluded that the initialisation, accuracy and vertical resolvability of the Kalman filter based GPS tomographic solution is enhanced when additional synoptic network and profile observations are introduced.

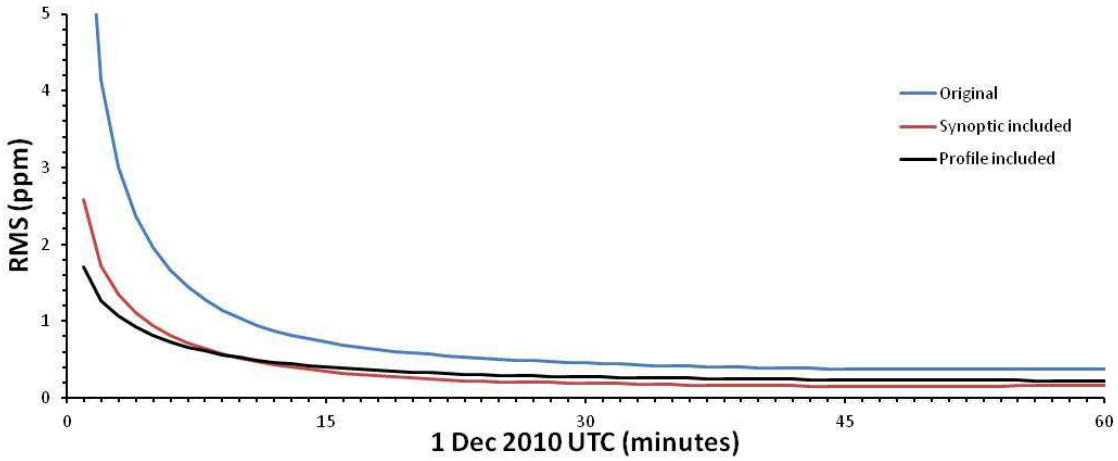

Figure 5.28: The time series of RMS error for the 2 tomographic solutions including additional meteorological observation methods against the original solution containing no additional data for the initial 60 minutes of processing.

5.8. Summary

In this chapter, the Kalman filter based GPS tomographic model implemented multiple tests using two simulated synthetic wet refractivity fields to statistically optimise parameters based on the GPSnet infrastructure. This investigation used the RMS error, the convergence rate and the vertical resolvability of each estimated state to analysis and compare varying parameters. The two synthetic simulated wet refractivity fields were used for these simulation tests. These included, an exponential refractivity field and a spike layer field. The statistical optimisation analysis included:

- Optimisation of the discretised horizontal and vertical voxel resolutions. This was investigated to determine the most robust solution, which provided a high resolution, fast solution convergence and high accuracy;
- The optimal layer spacing technique. This was analysed to determine the optimal layer spacing for reconstructing wet refractivity in the troposphere;
- The vertical resolvability and capability of reconstructing a spike layer. This was investigated to determine the capability of the tomographic algorithm for detecting large vertical anomalies in wet refractivity during severe weather beyond the height of the GPSnet; and,
- The influence of including additional synoptic network and profile observations on the GPS tomographic solution of wet refractivity estimates were investigated.

Simulation tests into the spatial discretisation of the horizontal resolution were investigated for the GPSnet. Results indicated that the horizontal resolution of 55 km produced the best solution in terms

of high accuracy and fast solution convergence. This resolution produced the fastest convergence rate by a factor of 3.46 and 3.07 when compared with the 110 km and 27.5 km resolutions, respectively.

It was also concluded that the increase in spatial resolution beyond the optimal 55 km resolution minimises the influence the observations on the convergence of tomographic solution. This was due to the large increase of unknown parameters compared with the unchanged amount of observations. This affected the ratio of observations per unknown parameter, and presented a smoothing effect on the Kalman filter solution estimates. This resulted in slower convergence. It appeared that when using the higher resolution of 27.5 km, a much slower convergence rate was evident due to the amount of unknowns to be solved, increasing by a factor of 3 in comparison to the 55 km resolution.

The vertical resolution and layer spacing techniques were also investigated to identify the optimal resolution. Final results concluded a 15-layer solution with an exponential layer spacing function was optimal. This was because it presented the fastest solution convergence and highest vertical resolvability in the low-to-mid troposphere.

A spike layer test was investigated for analysing the vertical resolvability of the GPS tomographic solution above the geometry of the GPSnet. This test is in view of monitoring the dynamics mesoscale convective mechanisms during severe weather events. The solution error stabilisation of 1 ppm accuracy was achieved after the initial 20 minutes of processing. The convergence rate appeared to be only slightly slower by a factor of 1.54 compared with a simulated stable atmosphere represented by the original exponential field. This result suggested that GPS tomography has the potential to monitor the mesoscale convective processes in 4D.

Two simulation tests were conducted to investigate the influence of additional synoptic network and profile observations on the GPS tomographic solution estimates. Results from these two simulation tests showed that the inclusion of additional observations significantly improved the accuracy, the convergence rate and the vertical resolvability of the solutions estimates. These results were compared with the original tomographic simulation results, which included no additional observations. Results indicated that the addition of profile data lead to the quickest convergence rate as the improvement on the original solution was increased by a factor of 4.3. The synoptic network also provided a significant improvement with a faster convergence rate by a factor of 3.3 when compared with the original solution.

The results from this simulation study for parameter optimisation will be used in Chapters 6 and 7 for the real data modelling analysis for severe weather using 4D GPS tomography.

Chapter 6. Case study 1: Severe weather monitoring using GPS tomography

6.1. Overview

As stated previously, the dynamics of WV have a strong influence on the formation, lifecycle and dissipation of severe mesoscale convective storm systems due to the large energy transfers in the hydrological processes in the neutral atmosphere. Therefore, WV becomes one of the most important parameters to measure in response to severe weather detection. However, atmospheric WV remains inadequately measured due to the current limitations of spatial and temporal resolutions for atmospheric observation and sounding stations. This is particularly evident in Australia and more broadly the southern hemisphere due to large areas of unoccupied land.

This research investigated a new platform in Australia and initially Victoria for the improvement of forecasts of precipitation and severe weather using 4D GPS tomography. The spatial and temporal resolutions are imperative parameters for optimising the depiction of hydrological hazards using highly dynamic WV modeling (Lutz, 2008). Ground-based GPS tomography within Australia has the potential to utilise the dense ground-based GPSnet infrastructure and potentially the NPI to provide reconstructed wet refractivity fields with a high spatial and temporal resolution. This will potentially improve early detection and prediction of severe weather and precipitation systems.

The research investigated two case studies of severe weather for the analysis of GPS tomography using GPSnet.

- *A severe convective supercell storm system that occurred during March 2010:* was used to analyse the evolution of wet refractivity dynamics using GPS tomography. The vertical and horizontal gradients of wet refractivity were assessed in comparison to precipitation radar intensities to resolve the mesoscale processes of severe weather (Chapter 6).
- *A severe precipitation and storm system that occurred during January 2011:* was used to assess the accuracy of GPS tomography solutions with the addition of alternate observations methods to the observation model in comparison to the original GPS tomography campaign. This analysis is termed multi-observational GPS tomography and is presented in Chapter 7.

Both, the spatial resolution of the discretised three dimensional field and the Kalman filter processing parameters for the GPS tomographic solutions were set for this real data analysis based on simulation studies described in Chapter 5 and are also published in Manning et al. (2014).

6.2. Characteristics of severe mesoscale convective storm systems

Thunderstorms form in unstable atmospheric environments when warm, moist air rises due to instability of air masses. The warmer the parcel of air (less dense) the greater the acting upward-directed buoyant force and in turn the stronger the convection. The forcing mechanisms needed to start air moving upward may be: unequal heating at the surface; the effect of terrain, or the lifting of air along shallow boundaries of converging surface winds; diverging upper-level winds, coupled with converging surface winds and rising air; and, warm air rising along a frontal zone. Usually a combination of several mechanisms is needed together with vertical wind shear to generate severe thunderstorms (Ahrens and Samson, 2010).

Supercell thunderstorms are uniquely characterised during the mature stage by the ratio of cold air downdraft being undercut by moist air updraft. This causes horizontal spin of a singular violent updraft, which develops a supercell. These storms have the ability to suspend hailstones of considerable size, produce high-speed winds and heavy precipitation, threatening safety, significant damage and flash flooding to communities. These mesoscale convective storm systems contain regions of both convective and stratiform precipitation. The convective region consists of intense, vertically extending cores, while the stratiform region hold a more stabilised lighter precipitation (Houze, 2004). See Figure 1.1.

After heavy precipitation, the storm becomes dominated by downdraft. This process cuts off the inflow and updraft and the storm begins to dissipate (Ahrens and Samson, 2010). The fundamental elements of the storm structure require a much finer resolution where the mature cell and convective region can cover less than 30 km. The stratiform on the other hand is much larger with a spatial coverage of up to ~125 km.

To identify the size, intensity of precipitation and path of severe convective thunderstorms, weather radar images are commonly used. Radar signals are sent out as short pulses, which may intercept elements such as precipitation and in turn scatter and reflect part of the energy back to the radar. From this returned information the radar is able to tell where the precipitation is occurring and how much

precipitation exists. The intensity of precipitation is represented as a colour scale in a radar image and is based on the size, number and state of the particle (Masunaga et al., 2002).

Radar images are able to detect the general domain of severe convective storm systems and depict the convective and stratiform precipitation regions. Figure 6.1 shows the extent of the storm that can be observed using radar.

This research used the March 2010 severe supercell thunderstorm event (Choy et al., 2011; Manning et al., 2012) as *case study 1* for analysing the capability of modelling the time evolving wet refractivity dynamics using 4D GPS tomography. Wet refractivity is a function of partial WV pressure and temperature (Eq. (2.5)). Radar image intensity data were used to track the path, domain and intensity of the severe supercell thunderstorm phenomena during its manifestation and evolution to identify correlations and mechanisms of convection, precipitation and dissipation in the GPS tomographic wet refractivity fields.

6.3. March 2010: Victorian severe supercell storm event

The focus of this case study was to examine the development and evolution of a series of supercell convective thunderstorms, that passed through Victoria, Australia from 6 – 8 of March 2010. This event brought heavy rainfall, lightning, flash flooding, strong winds and large hailstones. The storm was initiated by a large warm, humid air mass travelling from southern Queensland and developed in western Victoria due to a low-pressure system. The unstable atmosphere developed into a severe supercell thunderstorm on 6-March, which travelled across the state from the northwest to the southeast. Warm, moist pre-frontal air was identified in the greater Melbourne region approximately 1 day prior to the event. At the storm's peak strength a 400 km band of heavy rain and large hail extended across the state reaching Melbourne at approximately 14:40 AEDT (5:40 UTC). The synoptic weather station network revealed that the total rainfall for the day was the highest in historical record for March in Victoria. In Melbourne a total of 61 mm was measured for 6-March, which is more than the monthly average of 50mm. At approximately 14:40 (5:40 UTC) Melbourne experienced 19 mm in 18 minutes and 26 mm within 60 minutes. In addition, wind speeds in excess of 100 km/h and hailstones of ~ 2 – 5 cm were recorded throughout Melbourne (Choy et al., 2011; Manning et al., 2012).

Figure 6.1 presents the radar reflectivity image from the Melbourne radar at 14:00, 14:48 and 15:24 AEDT (5:00, 5:48, and 6:24 UTC) on 6-March as the storm passed over central Melbourne. This

event caused danger to civilians, flash flooding, immense commercial and residential damage, and vast traffic and transport delays. Further rain and flash flooding continued throughout the night and into 7-March. It can be seen that the storm region of highest precipitation denoted by dark-red passes directly over central and greater Melbourne during this period.

Figure 6.1: Radar reflectivity images from the Melbourne radar (Laverton) at 14:00, 14:48 and 15:24 (AEDT) (5:00, 5:48, and 6:24 UTC) on 6 March 2010 (Bureau of Meteorology, 2011).

6.3.1. Experiment setup

The GPS tomographic campaign covered a 7-day period from the 3 – 10 March. This time interval allowed an in-depth analysis of the finite atmosphere over Victoria during periods before, during and after the severe supercell convective storm system. The scope of analysis was to, 1) identify the physical dynamics and distribution of wet refractivity during the lifecycle of this severe weather event and then, 2) to identify mechanisms of convection and precipitation regions in the wet refractivity and gradient analysis.

As discussed previously, the discretisation of the lower atmosphere was defined with a finite curvilinear voxel grid using latitude and longitude boundaries referenced to the WGS84 ellipsoid. The area under investigation ranged from 141^0 to 148^0 E longitude and from -35.8^0 to -38.6^0 S latitude (Figure 6.2(a)) with a height domain of 0 to 15000 m (Figure 6.2(b)). A 10^0 boundary buffer borders the outside of this model domain to ensure that all rays were within the model and pass through the top boundary. The horizontal resolution was set to 0.5^0 (Figure 6.2(a)), which is approximately the overall diameter size of the super cell thunderstorm and is slightly denser than the inter-station GPSnet distance of 70 km. This was the suggested voxel adoption following the preconditions of GPS tomography from Bender and Raabe (2007). To comprehensively depict the dynamics of the individual convection and stratiform domains of a severe supercell storm, a much finer horizontal resolution would be needed. However, this discretisation is limited by the resolution of GPSnet where an increase in the number of unknowns in Eq. (4.24) does not add additional observations and

ultimately, in the presence of horizontal constraints a smoothing affect is generated as concluded in Section 5.5.

Approximately 50% of WV is located in the planetary boundary layer (PBL) making it imperative to model the dynamic and vertical structure of WV below ~2000 m with high resolution. Therefore, the vertical resolution is set to 15 layers with exponential layer spacing as presented in Figure 6.2(b). This produced high resolution in the lower troposphere and low resolution in the upper troposphere (Manning et al., 2013). See Chapter 5 for full analysis on the optimisation of the discretised field resolution.

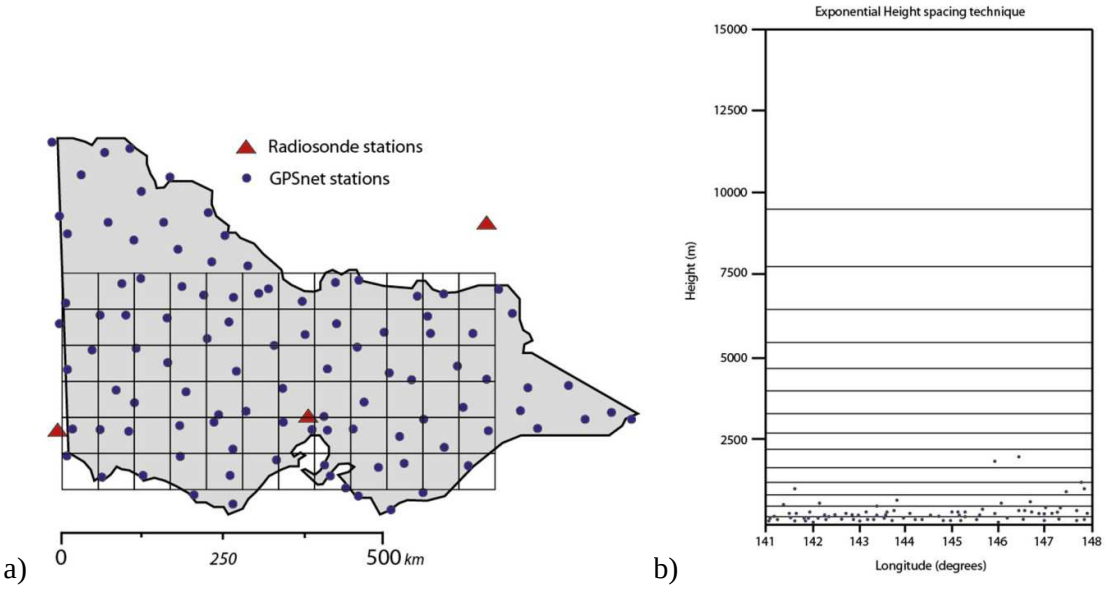

Figure 6.2: The Victorian GPSnet CORS network as of March 2010, radiosonde sites and horizontal discretisation of the grid model (a), and, vertical layer structure defined with an exponential spacing technique (b).

6.3.2. GPS DD processing

A total of 69 GPSnet CORS stations were used for this case study, which covered a large amount of the state of Victoria. Raw GPS phase data in the form of RINEX files were collected for each GPS CORS station operational within the GPSnet infrastructure during March 2010. The sample rate was set to 30 seconds for processing. The *maximum number* baseline strategy (Dach et al., 2007) was used to construct the baselines for DD processing and an ionosphere-free linear combination was used in the Bernese GPS processing campaign. The campaign was segmented into daily batches. Precise orbits from the IGS were used to attain the highest accuracy, although rapid orbits should be considered in near real-time and real-time applications. The Niell mapping function was used to compute the slant path delays (Niell, 1996). Apriori values were calculated with the Saastamoinen

hydrostatic model (Saastamoinen, 1973) and dry Niell mapping function. These apriori values were corrected by a piecewise linear function with a step size of 1 hour. The Niell wet mapping function was used for estimating these corrections. Table 6.1 presents the parameters of the configuration used for the GPS processing. For full details on the method of processing using the Bernese GPS processing software refer to section 2.3.2.

Table 6.1: Parameters of the Bernese GPS processing software.

Parameter	**Value**
Time period	3 – 10 March 2010
Processing method	Double difference
Number of stations	69
Baseline strategy	Maximum number of baselines
Estimation period	Daily
Ionosphere correction	Ionosphere free linear (L_3) combination
Orbits	IGS precise orbits
Sampling rate	30 s
Cutoff angle	5°
Additional corrections	Ocean loading, solid Earth tide, axis rotation corrections
Apriori tropospheric model	Saastamoinen dry model
Mapping function	Niell mapping function
Output data	ZTD, DD residuals, final station coordinates

6.3.3. GPS Tomographic setup

As discussed previously, GPS tropospheric delays from the GPSnet (Figure 6.2) were computed using the Bernese V5.0 using the maximum number of observations baseline strategy and a DD approach. The estimated hourly ZTD, plus DD residuals, interpolated meteorological data from NWP model ACCESS-R and satellite and receiver coordinates were all used to reconstruct the DD SWD observations (see Eq. (4.3)) These were the primary input observations for the tomographic inversion during each update step of the Kalman filter. The trilinear voxel parameterisation method (Eq. (4.6)) was adopted based on a long-term GPS tomographic study conducted by Perler (2011). The initialisation of the state vector in the Kalman filter used an exponential wet refractivity field. This field was modelled on average wet refractivity profiles from radio sounding balloons during the 7 day campaign. Table 6.2 lists the initialisation parameter settings for the Kalman filter.

Table 6.2: Parameter settings of the initial state of the Kalman filter.

Parameter *Initial State of the Kalman filter*	**Value**
Initial surface value	75 ppm
Initial variance at reference level	10000 ppm²
Scaling height of variance model	2873 m
Horizontal correlation length	55262 m
Vertical correlation length	1216 m

Table 6.3 presents parameters of the Kalman filter prediction model along with horizontal and vetical correlation lengths resulting from statistical optimisation of resolution concluded in the simulation tests of Chapter 5. AWATOS 2 implements a random walk process on the refractivity estimates with the prediciton process noise modelled as Gaussian.

The data sampling size is set to 30 seconds, which coincides with the epoch rate of the GPS data processing, and the update step size of the Kalman filter is set to 5 minutes.

Table 6.3: Parameters of the Kalman filter (KF) prediction model.

Parameter *Prediction model*	**Value**
Prediction model	Random walk
Sample size	30 s
Step size	300 s
Prediction error type	Multivariate additive Gaussian
Prediction error at surface	346 ppm
Scaling height of the prediction error	2873 m
Vertical scaling length of the correlation	1216 m
Horizontal scaling length of the correlation	55262 m

GPS-derived DD SWD observations, along with vertical constraints and boundary layer conditions were introduced into the observation Equation (Eq. (4.24)). Table 6.4 presents the observation types and parameters.

Table 6.4: Parameter settings of the observation model.

Parameter *Observation model*	**Value**
Integral observations	GPS DD observations
Number of stations	69
Inter-station distance	~70 km
Sampling rate	30 s
Cutoff elevation angle	5°
Point observations	None
Pseudo-observations	Boundary layer, top layer and vertical constraints
Additional observations	None
Covariance model	Full model

Integral observations

- *GPS DD SWD*: These DD observations, as the primay observables in the observation model, were considered independent of each other if there was not a common SWD between two DD observations. As stated previously, on average 69 GPS CORS stations from the GPSnet were taken into account for our study as they were the total number operational in Victoria during March 2010. The covariance model implemented a standard deviation of measurement errors which were associated with the DD observations in the order of 5mm at the zenith for STD (Troller, 2004; Perler, 2011; Manning et al., 2013). This value was based on investigations and the final results presented in Section 3.5. The standard deviation will increase when the mapping function of $1/\cos(\beta)$ is used. The cutoff angle was set to 5°, which is the same as the one used in the GPS DD processing of the Bernese GPS software.

Pseudo-observations

- *Boundary layer constraints*: A 10° boundary voxel buffer was constructed around the inner voxel model to ensure all traversing integral measurements pass through the top of the voxel model. Pseudo grid point observations were added to this boundary layer using a synthetic exponential wet refractivity model expressed in Eq. (5.1). The weighting strategy was controlled by the prediction error at each boundary point.
- *Top layer constraints*: 15000 m was the altitude limit for the grid model and this layer was assumed to have a wet refractivity value of 0 ppm. Similar to boundary layer constraints the top layer grid points are input with pseudo-observations of value 0 ppm with weight matrix controlled by the prediction error.
- *Vertical constraints*: The weighting strategy was chosen to minimise the variability between GPS tomographic processing and validation from radiosonde during this March 2010 severe weather event. The gradient of the vertical constraints were based on the exponential wet refrctivity function presented in Eq. (5.1).

6.3.4. Data evaluation methods

Multiple evaluation methods were used in order to compute quantifiable accuracies of the GPS tomographic solutions and also to identify tomographic model dynamics and processes in comparison to convective storm and precipitation intensities. The MELB radiosonde station was used to validate the tomographic wet refractivity solution over the Victorian region during the severe weather event. Two radiosondes were released daily providing a temporal resolution of 12 hours. The profile point data were interpolated to the height of each tomographic voxel layer for comparison. This provided 15 comparison points along the vertical profile from 0 to 15000 m altitude. Figure 5.3 presents the location of the profile point (A) used for this analysis and also for the comparison and validation against radiosonde profile data from the MELB station.

The evaluation using alternate intensity measurements of the dynamic WV processes before, during and after the lifecycle of a supercell thunderstorm identified the capability of GPS tomography to depict 4D wet refractivity structure of severe weather. Special interest was taken in detecting the formation and path of severe thunderstorms to aid in early detection and prediction of severe weather. The three evaluation methods used were:

1. *The cumulative rainfall data* from the Melbourne observatory weather station were used to identify precipitation intensities in the inner Melbourne region. This provided a direct link with the passage of the storm and times of extreme hazard. This time series was plotted against the time series of a tomographic profile selected from the model above this weather station.
2. *An average wet refractivity index* was computed from a tomographic profile selected from the model. The average refractivity index (RI), developed by Sharma et al. (2009) is a measure of atmospheric instability using GPS RO derived refractivity measurements. The advantage of implementing this index is its direct correlation with refractivity, without the need for retrieving temperature, pressure and WV measurements. The average value of RI is a mean of the values from height layers above the planetary boundary layer (PBL) (~2000 m) to the tropopause. This study adopted a wet RI (RI_{wet}) using the wet refractivity solutions from GPS tomography processing. This formula is expressed as follows (Manning et al., 2012):

$$\mathrm{RI}_{wet} = \left(\sum_{l}^{k} N_{wet,l} \right) \Big/ n \qquad (6.1)$$

where l and k represent the first and last N_{wet} terms relating to the initial term above the planetary boundary layer (~2000 m) and the last term at the top of the tomographic model (15000 m), respectively. The variable n is the number of terms. As the voxel model

discretisation was fixed, n was set to 11 for this research. This optimised the sensitivity to moisture content as it excluded the dominating dry component of refractivity. This index was primarily used to identify early mechanisms of *lift* due to warm, moist air convection during the formation and lifecycle of severe weather. This convective region (see Figure 6.3) was identified at the front of the storm system incorporating the mature cell structure and heavy precipitation regions. The RI_{wet} was used in the GPS tomographic analysis section for results shown in Figures 6.5 – 6.7.

3. *Vertical and horizontal wet refractivity gradients* were used to depict the 4D distribution of wet refractivity in comparison to radar image intensities. The differences between radar images and the GPS tomographic 2D cross sections could be summarised as: 1) the wavelength of the signal, and 2) the signal path. The radar pulse sent towards the mesoscale convective system (MCS) (5GHz frequency) is partially reflected by the rain drops, snow and ice crystals contained in all MCSs. GPS signals (1.5 GHz frequency), however are refracted by the WV particles suspended in the air or that are moving upward/ downward in air parcels and are afterwards recorded in GPS receivers as phase delay. Therefore, 2D GPS tomographic gradients are capable of sensing the increase of humidity before a MCS, as well as a decrease during heavy rain and in the stratiform region. Both the convective and stratiform regions are identified in Figure 6.3.

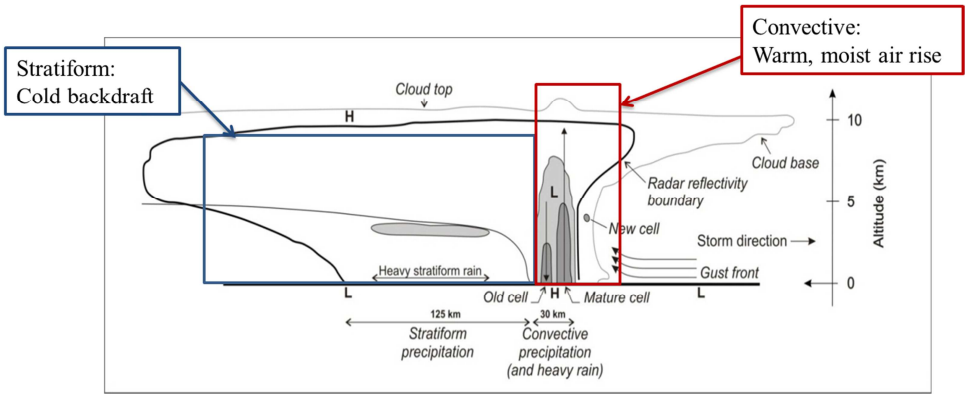

Figure 6.3: 2D profile of a severe convective supercell thunderstorm. Radar reflectivity boundary presented as thick black line, and the approximate convective and stratiform precipitation regions identified within the red and blue boxes, respectively (based on Houze, 2004).

Vertical 2D cross sections were extracted from the GPS tomographic solution along the path of the supercell storm analysed for *case study 1*. Horizontal 2D cross sections were extracted at 3 different altitude layers (i.e. 578 m, 1613 m and 5780 m) to analyse the horizontal gradients in comparison to the path, domain and intensity of the severe weather phenomena. Gradient magnitudes denoting the dynamic wet refractivity field changes were calculated according to the equation (Manning et al., 2012):

$$\nabla 2DN_{wet} = \left(\frac{\partial N_{wet}}{\partial x} i + \frac{\partial N_{wet}}{\partial h} k + \frac{\partial N_{wet}}{\partial t} p\right) \quad (6.2)$$

The first two elements denote the horizontal and vertical gradients in wet refractivity within one epoch. The last element denotes the time derivative of wet refractivity and it is only this element that is being analysed as a measure of the troposphere activity parameter. These time evolving gradients are mapped against the weather radar intensities to identify any trend of wet refractivity within the storm anomaly. This evaluation method was used for the vertical and horizontal gradient analyses presented in Figures 6.9 – 6.13.

6.4. Results and discussion of case study 1

The data analysis focused first on the time series of GPS-derived PWV estimates from the Melbourne observatory GPS CORS station (MOBS). Secondly, this analysis investigated 4D GPS tomography during the 7 day severe supercell convective storm system on March 2010 (Manning et al., 2012). The following results will compare trends and accuracies of both products.

6.4.1. GPS-derived PWV

As discussed previously, GPS-derived PWV estimates were constructed using the ZTD from the Bernese GPS processing software (see Section 2.4.1). Using the surface pressure measurements from ACCESS NWP analysis data and the associated mean sea level height (H) and geographic latitude (ϕ) of the GPS station (MOBS), the hydrostatic components of the delay at the zenith (ZHD) can be computed using the Saastamoinen hydrostatic equation (Saastamoinen, 1973). This leaves the GPS-derived ZWD estimate (Δ_a^{ZWD}), which can be converted into PWV using a mean temperature value in a conversion factor Π (Bevis et al., 1992). See Section 2.4.1 for full derivations.

Figure 6.4 presents the evolution and comparison between GPS-derived PWV estimates and cumulative rainfall measurements 3 days prior to, during, and 3 days after the severe supercell storm system. The data represents observations from the Melbourne observatory (MOBS) station (Choy et al., 2011; Manning et al., 2012).

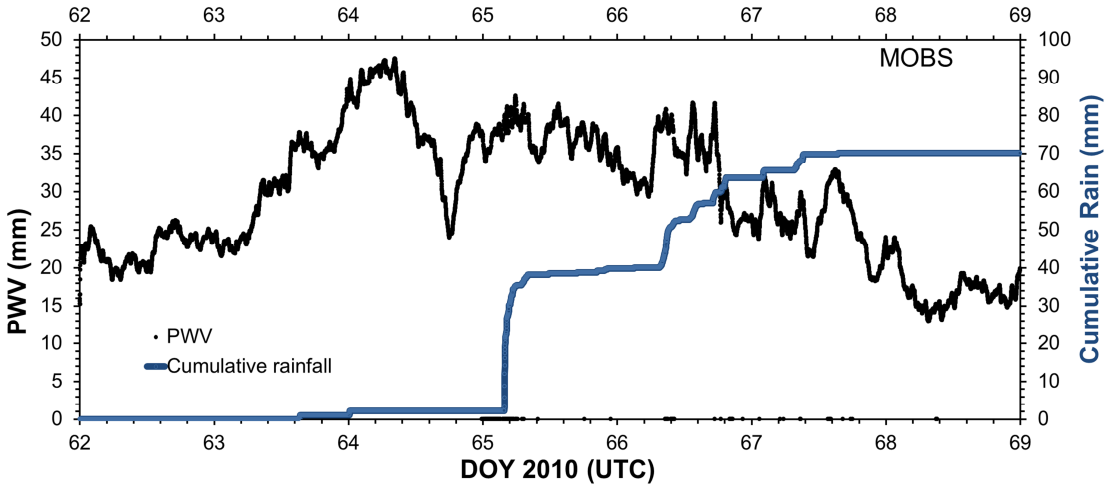

Figure 6.4: Time series comparing GPS PWV (mm) to the cumulative rainfall (mm) over the 7 day case study campaign (AEDT).

The large increase from 20 mm to 47 mm (PWV) from day-of-year (DOY) 63 to 64 corresponds to the steady increase in warm moist air attributed to a pre-frontal air mass. Pre-frontal warm air holds more WV than the cold post-frontal air. Thus, Figure 6.4 presents this clear signature of increasing PWV to 47 mm representing the warm pre-front air and the immediate atmospheric procession of a sharp drop back to approximately 23 mm characterising the arrival of cold, dry post-front air mass. A sharp increase in PWV is then evident 8 – 10 hours prior to the extreme precipitation storm anomaly reaching Melbourne at 5:40 (UTC) on DOY 65. The sharp drop in PWV coincides with the passing of intense precipitation. This correlation between PWV and precipitation intensity repeats on DOY 66 with a sharp rise 3 hours prior to, and then a dramatic drop after the precipitation anomaly. The trend between PWV and rain intensity is also supported by similar severe weather studies conducted by Champollion et al. (2005), Boniface et al. (2009) and Seko et al. (2004, 2010), which used ZTD for the investigation.

Validation of the GPS-derived PWV estimates with radiosonde observations concluded an overall RMS error of 2 – 3 mm for greater Melbourne, as presented in Choy et al. (2011) and Manning et al. (2012). This initial result identified the ability to use GPS state-wide networks to map the passage of WV in the pre- and post-frontal air mass of a severe weather event with a high temporal resolution. Based on this analysis, it is concluded that GPD-derived PWV estimates can resolve the synoptic dynamics and precursors to severe weather, and also has the potential to strengthen NWP models and forecasts in view of severe weather. However, the limitation of this 1D solution is that the mesoscale storm processes are not able to be fully resolved due to the integral observation geometry of GPS-derived PWV estimates. To monitor the 4D dynamics and mesoscale processes of severe weather, GPS tomography was adopted.

6.4.2. GPS tomographic analysis

The formation of a convective storm system must involve three conditions. The first is *moisture* in the lower to mid troposphere. The second is atmospheric *instability*, which can be a good indicator for storm intensity. The last condition is a *lift* or convective mechanism. This analysis identified the mesoscale convective and stratiform processes of wet refractivity during the early formation and maturation of the March 2010 severe weather event using 4D GPS tomography in Victoria.

Figure 6.5 presents the time series of the tomographic wet refractivity profile solution at the voxel profile point (A) (see Figure 5.3) over the 7-day campaign. Below this is the time series of RI_{wet} over the same period. A RI_{wet} value of 12.73 ppm was adopted as a standard value for a stable atmosphere, derived using MELB radiosonde observations from Feb-May 2010. The cumulative rainfall is referenced to the right y-axis with a supercell storm occurring on DOY 65 depicted by a significant spike where ~40 mm was recorded in less than 2 hours.

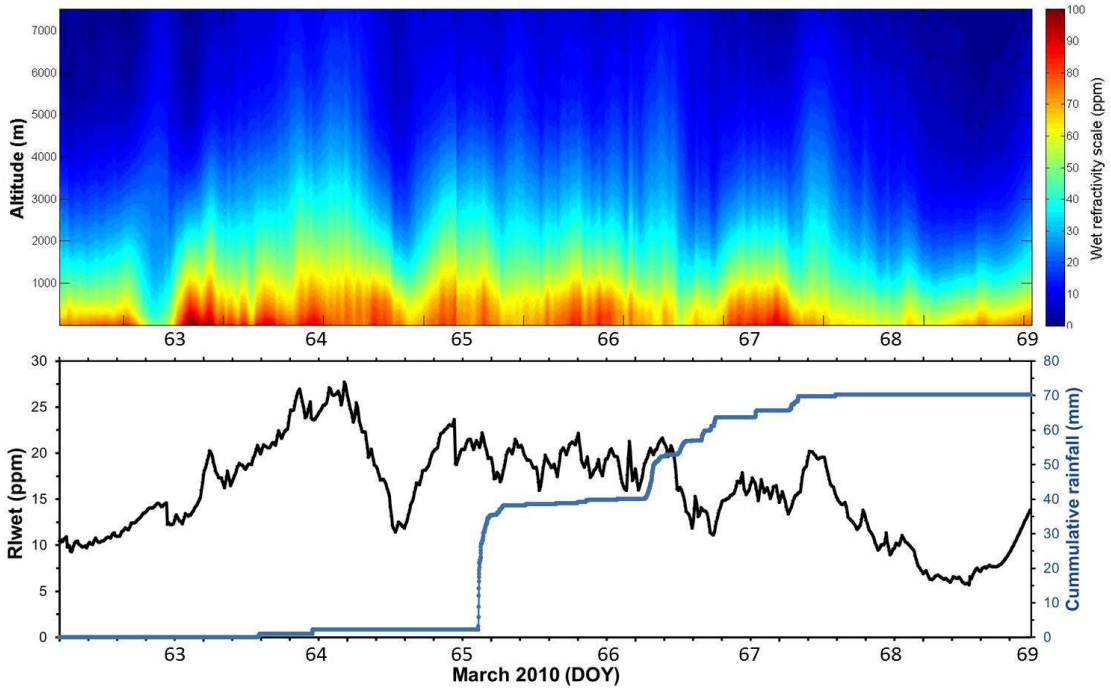

Figure 6.5: Time series of tomographic profile solution for wet refractivity every 10 minutes from 3-8 March 2010 (UTC). The blue line presents cumulative rainfall (mm) from MOBS synoptic station during this period. The bottom graph is the evolution of the RI_{wet}.

The RI_{wet} index presents an approximately linear rise from day of year (DOY) 63 to 64.3 coinciding with the large amounts of warm, moist air and the process of strong *lift* or convection in the pre-frontal, unstable atmosphere. This process is consistent with the large warm, humid air mass detected

moving down from southern Queensland, which triggered the atmospheric instability. The index reached 28 ppm, which is an increase on the standard RI_{wet} by a factor of 2.2. This is followed by a dry, cold post frontal air triggering a sharp drop in the RI_{wet}. There is then a sharp rise until the heavy rainfall, hail and flash flooding reached Melbourne. The tomographic profile evolution presents a similar signature to the RI_{wet}. However, the highly dynamic distribution of wet refractivity in the vertical direction is detected. Distinctive patterns of convective updraft due to warm, moist air and atmospheric instability are revealed. Also periods of cool, dry air are detected – represented by sharp drops in wet refractivity down through the vertical layers caused by cold air mass advection associated with the stratiform region (Figure 6.3). This occurs during the mature and dissipating phase of the storm lifecycle due to heavy precipitation.

The GPS tomographic solutions were validated at profile point (A) (Figure 5.3) with observations from the co-located radiosonde station MELB. This radiosonde station provided 2 profiles per day with 14 in total for comparison. A tomographic solution every 12 hours was selected and presented in Figure 6.6(a) to coincide with the temporal resolution of the radiosonde. Figure 6.6(b) presents the vertical colour map for the time evolving radiosonde profiles against the cumulative rainfall data. Due to the low temporal resolution, the signature and distribution of wet refractivity remains poorly resolved. The RI_{wet} was interpolated for the same height layers as the tomographic solution and presented below. The colour contour map (Figure 6.7) presents the difference between radiosonde and tomography profiles at the co-located MELB station. The RMS error for each profile comparison is consistent considering the highly unstable nature of WV in the model field during the severe weather event.

The bias and standard deviation at each height layer is displayed in the profile on the right of Figure 6.6 with total values of 1 ppm and 6.2 ppm, respectively. The majority of variability is presented below ~4000 m, which would be expected especially during severe weather due to the highly variable nature of WV in an unstable atmosphere.

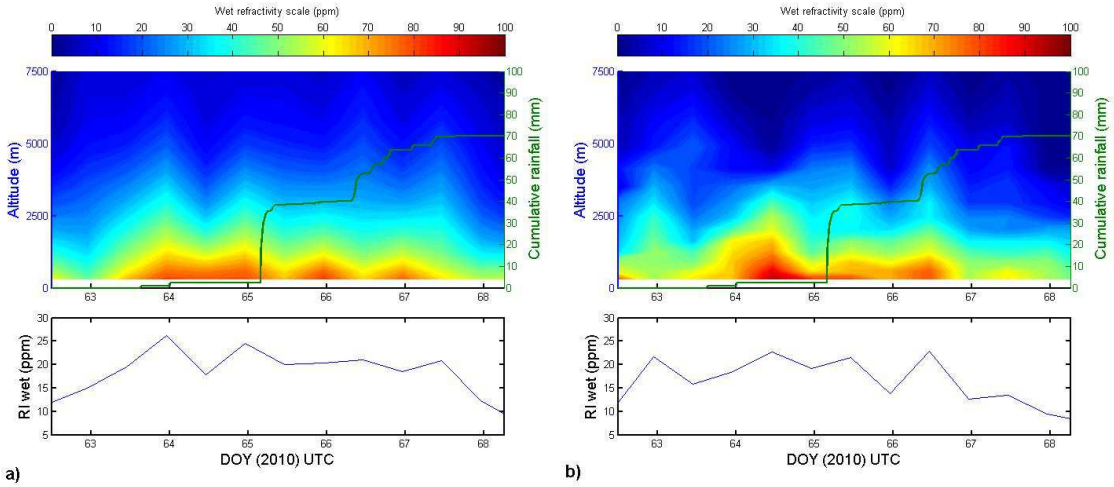

(a) GPS tomography (b) Radiosonde

Figure 6.6: Time series of tomographic profile solution of wet refractivity every 12 hours with RI_{wet} index profile (a), and, evolution of radiosonde profiles with 12 hour resolution from the Melbourne Airport station including RI_{wet} profile (b). Green line represents cumulative rainfall (mm) from 3-8 March 2010 (UTC).

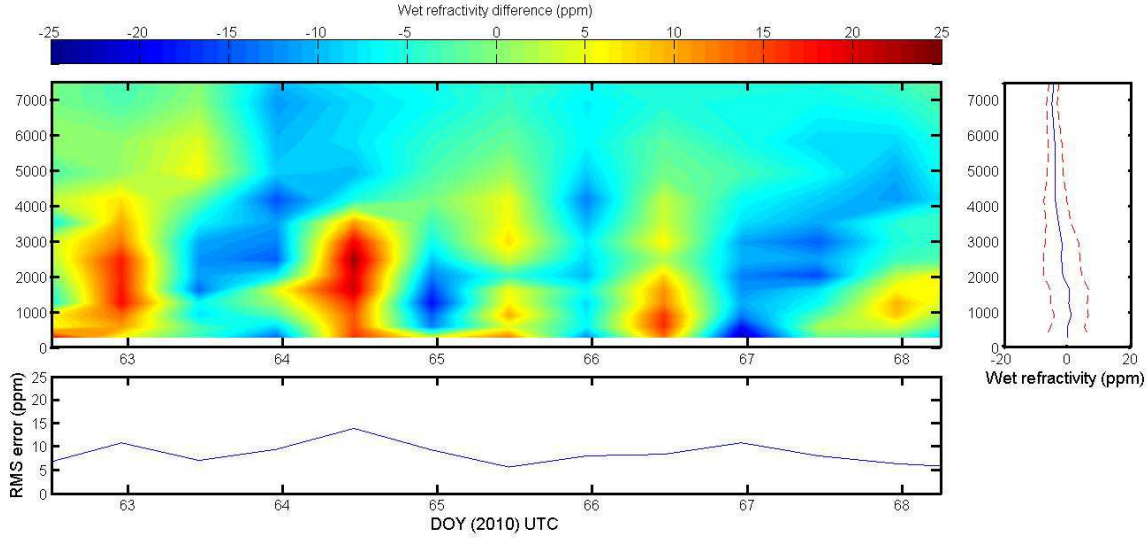

Figure 6.7: Wet refractivity of radiosonde minus tomography profile at the Melbourne International Airport every 12 hours. RMS error of each profile solution (below) and the bias and Standard deviation at each height layer (right).

Tables 6.5 and 6.6 present the RMS error of the GPS tomographic profile at voxel point (A) compared with the radiosonde data (see Figure 5.3). The RMS error of each GPS tomographic solution is presented in Table 6.5. This time series suggests a consistent level of accuracy, not affected by the highly dynamic and unstable atmospheric conditions during the severe weather. The RMS error over the 7 days for each layer is listed in Table 6.6. The mid-tropospheric layers from approximately 2000 to 5000 m altitude present the lowest accuracy. Furthermore, this height range also presents an

increasing error up to 5000 m. The RMS error then trends to drop uniformly with increasing altitude to 0.53 ppm at 15000 m. This is because the top layer was constrained to 0 ppm in the tomographic model and thus this constraint had a significant influence on higher layers. The RMS error was relatively constant in the low troposphere. This is due to the GPS receiver height distribution ranging from ~0 m MSL up to ~1900 m altitude. Table 6.6 shows a decrease in reliability of the wet refractivity estimates from GPS tomographic solutions in layers above the highest GPS receiver. The inclusion of vertical constraints (see Section 4.3.8) as pseudo-observations were implemented to minimise this effect. The final RMS error for each profile comparison remained relatively constant throughout the campaign with an average RMS error of 8.58. The largest error of 12.19 ppm occurred on the 5-March (DOY 64) at 00:00 UTC (11:00 5 Mar 2010 AEDT). This period presented large atmospheric instability (as evident in Figure 6.8) as part of the pre-frontal warm, moist air-mass, which incurred high strength convection. This effect of sensing wet refractivity using GPS tomography was however minimal during these periods with RMS errors remaining relatively constant.

This accuracy analysis is consistent with past research in validating GPS tomography (Nilsson and Gradinarsky, 2006; Lutz, 2008; Rohm and Bosy, 2011; Perler, 2011). This was particularly positive as this analysis was conducted during the effects of severe weather, which seemed to have no adverse effect on the time series of RMS error. Therefore, this method has the potential to be a reliable observational model for NWP analysis and forecasts due to the high temporal and spatial resolution. This is especially important for Australia and the southern hemisphere where meteorological sensors are currently spatio-temorally sparse.

Table 6.5: RMS error of GPS tomographic solutions when compare with radiosonde observations. Voxel profile (A) (figure 5.3) used for this analysis.

Time (DOY)	RMS (ppm)
62.5	10.04
63	6.43
63.5	8.30
64	12.19
64.5	10.18
65	9.40
65.5	7.52
66	9.44
66.5	7.35
67	10.10
67.5	11.85
68	8.77
68.5	7.93
Average RMS	**8.58**

Table 6.6: RMS error of GPS tomographic solutions for each altitude layer during the campaign.

Altitude (m)	RMS (ppm)
279	11.73
578	9.12
897	8.38
1241	8.55
1613	8.95
2019	10.68
2466	12.41
2961	13.66
3518	14.74
4153	14.01
4894	9.68
5780	5.18
6886	3.62
8054	3.51
9501	2.51
15000	0.53
Average RMS	**8.58**

Only 3 radiosonde stations operated within greater Victoria, of which only one (MELB) is located within Victoria. Figure 6.7 presents the comparison between the radiosonde and tomographic RI_{wet} index. The major difference between the two data sets is the much higher temporal resolution of the tomography, which provided a solution every 5 minutes. The comparison of the radiosonde and tomographic RI_{wet} values gave an overall of 3.8 ppm (RMS).

Due to the sparse spatial and temporal distribution of the radiosonde network it can be concluded that this observation system is unable to resolve the physical dynamics of WV during severe weather. This restricts the ability for early detection and prediction. The RI_{wet} index comparison (Figure 6.8) illustrates the limitations of radiosonde profiles on the ability to depict sharp temporal changes associated with convection and mechanisms of *lift* for wet refractivity in an unstable atmosphere. An example of this is the pre- and post- frontal air anomaly during DOY 64. The tomographic solution provides a conclusively resolved index evolution, whereas the dynamic changes of the atmospheric anomaly remain totally unresolved using radiosonde profiles.

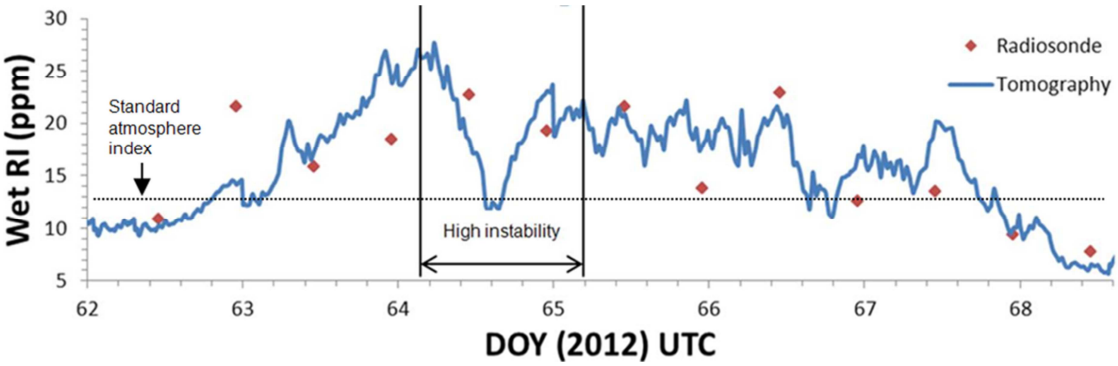

Figure 6.8: Average wet refractivity index (RI) for radiosonde and tomography profiles at respective temporal resolutions of 720 and 10 minutes, respectively. High instability domain indicated.

6.4.2.1. 2D gradient cross section analysis

A 2D cross section was extracted from the tomographic solution to spatially and temporally depict the generalised pattern of wet refractivity dynamics during a mesoscale convective storm system. The path and precipitation intensity of the March 2010 supercell storm is presented using a colour scale of the weather radar intensity at hourly intervals in Figure 6.9. This figure presents the lifecycle and direction of this supercell convective storm from formation to dissipation. The grid points depict the tomographic voxel resolution and the red circles present the area of interpolation for the radar image intensity. The diagonal tomographic grid profiles were selected to reconstruct a 2D profile for comparison with the radar intensity. The theoretical size and dynamics of mesoscale convective systems suggest that a much finer horizontal resolution than the 55 km resolution used for this tomography was needed to conclusively depict the mesoscale convective dynamics, stratiform inflow dynamics and mature cell of the storm (see Figure 6.3). However, this was constrained by the spatial resolution of GPSnet.

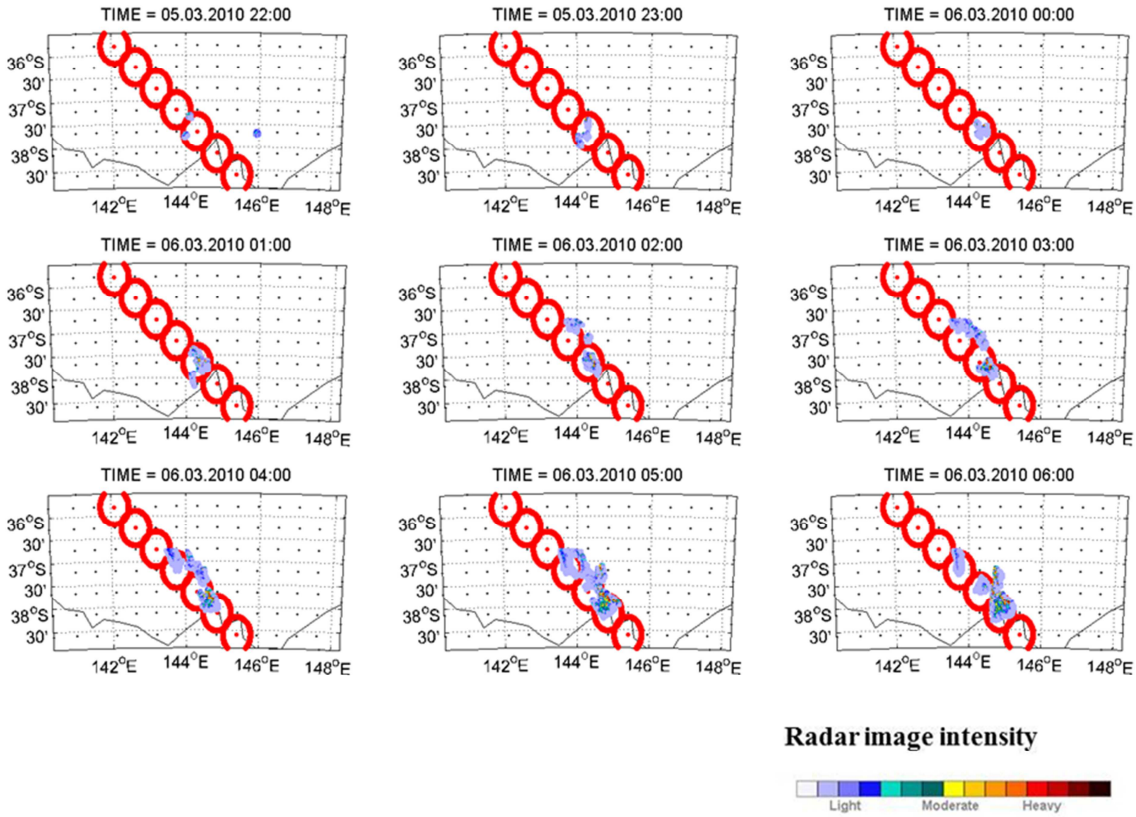

Figure 6.9: Tomographic domain presented with black dots corresponding to grid corners, red dots presenting profile grid points used to construct the tomographic 2D cross section, weather radar image intensity, and, red circles representing the interpolation domain for the weather radar image. The time series from 5 Mar 2010 22:00 to 6 Mar 2010 06:00 (UTC) presents the lifecycle of the extreme supercell thunderstorm passing over greater Melbourne.

Figure 6.10 presents the time evolving tomographic solution gradient along the cross section profile with the interpolated radar image intensity mapped to the right hand y-axis. A 9-hour section of processing is presented from 22:00 on 5-March UTC (7:00 on 6-March AEDT) to 06:00 on 6-March UTC (15:00 on 6-March AEDT) at hourly intervals. The storm motion is from the NW to SE. As the convective system matures the precipitation domain increases in size and intensity. The major events in the time series were the areas of intense precipitation that display a distinct drop in wet refractivity over all layers and especially in the mid troposphere. Furthermore, regions in front of the storm path present a large increase in wet refractivity gradients up through each layer. This dynamic trend at the front of the storm depicts the convection process of warm, moist air in the violent updraft of the gust front and formation of the mature cell (see Figure 6.3). This is particularly evident from 03:00 to 05:00 (UTC) on 6 Mar 2010 as the supercell storm reached greater Melbourne with 26 mm of rain falling within 60 minutes and with record precipitation logged for this day. The cross sections from 03:00 to 04:00 UTC at the front of the radar intensity show very strong gradient increases through all layers up to 10,000m altitude and especially in the mid to low troposphere. Gradient increases in wet

refractivity from tomography are also evident behind the storm precipitation system and stratiform region. These are also depicted using the radar intensities. This coincides with dissipation of the storm beyond the stratiform precipitation in a stabilising atmosphere and the melting and evaporation of precipitation parcels in the stratiform clouds (Manning et al., 2012).

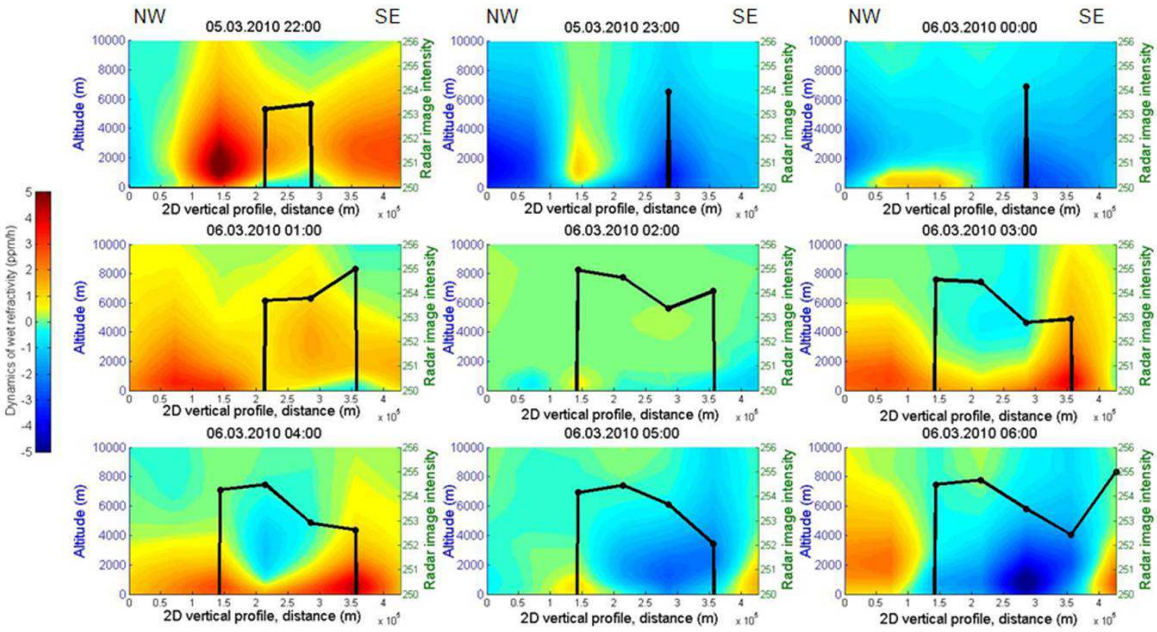

Figure 6.10: The time series from 5 Mar 2010 22:00 to 6 Mar 2010 06:00 (UTC) presenting 2D tomographic cross section against the weather radar image intensity.

To determine the horizontal movement of wet refractivity using 4D GPS tomography, the horizontal gradients were determined at hourly intervals for the passing of the severe convective storm phenomena. As stated previously, these gradient changes were determined for three height layers (i.e. 578 m, 1613 m, 5780 m altitude) extracted from the tomographic solution. The weather radar image intensity was superimposed over the top of each figure to depict the storm path, location and precipitation intensities.

Figures 6.11 – 6.13 present the horizontal gradient distribution of wet refractivity from the tomographic solution at 6:00, 7:00 and 8:00 on DOY 65 2010 (UTC), respectively. Additionally, hourly 2D horizontal gradients from 15:00 DOY 64 to 12:00 DOY 65 (2010) are presented in Appendix A. The results depict an increase in wet refractivity over most of Victoria several hours prior to the manifestation and mature stages of the severe storm phenomena and the high intensity precipitation event that passed over Melbourne. These gradients identified the synoptic scale precursors to severe weather, where distinct patterns of increasing moisture were detected several hours prior to the manifestation of the severe weather phenomena. As the convective storm system

intensified moving from the north-west towards Melbourne on DOY 65 from 4:00 am distinct patterns in the wet refractivity gradients began to form. Steep increases in gradients are visible at the front of the supercell storm structure through each layer. These represent significant convective updraft, which are identified from 6:00 to 8:00 (DOY 65) shown in Figures 6.11 – 6.13, respectively. Also, significant decreases in gradients are identified, where cool, dry air form downdraft and inflow jets through the back of the storm forming the larger stratiform region. From 4:00 to 9:00 (DOY 65) large decreases in gradient are evident within the heavy precipitation regions detected by the radar image intensity and spanning out toward the back of the storm. These represent down draft and inflow jet mechanisms of the stratiform region. The patterns remained visible throughout the mature stage of the mesoscale convective storm system (Figures 6.11 – 6.13) providing solid evidence that the mesoscale passage and processes of severe storm phenomena can be detected using 4D GPS tomography during highly unstable and rapidly changing conditions. The dissipation of the supercell storm system (Appendix A) then brings on widespread dry air-masses into the mid troposphere (5780 m altitude).

These findings demonstrate that 4D GPS tomography has the capability to detect and monitor the mesoscale convective and stratiform processes of severe weather in the Victorian region. Therefore, this GPS platform has the potential to provide state wide continuous observations of wet refractivity in 4D for the potential improvement and early detection of severe weather.

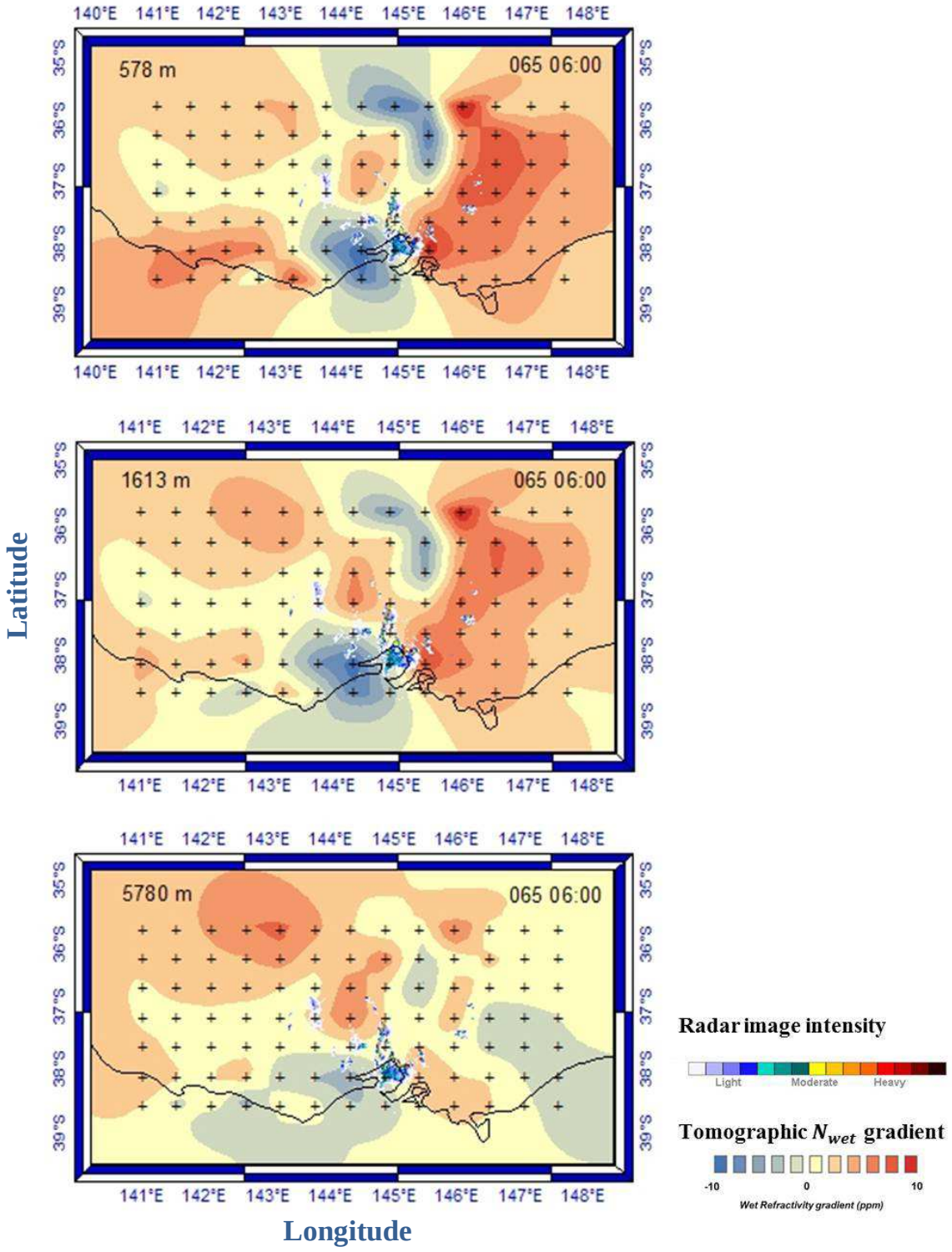

Figure 6.11: Presents the horizontal gradient distribution of wet refractivity from the tomographic solution at 6:00 DOY 65 2010 (UTC). The 2D horizontal gradients are presented for height layers: 578m, 1614m and 5780m, respectively. The Melbourne radar image intensity is overlaid to identify relative path and intensity of the convective storm system.

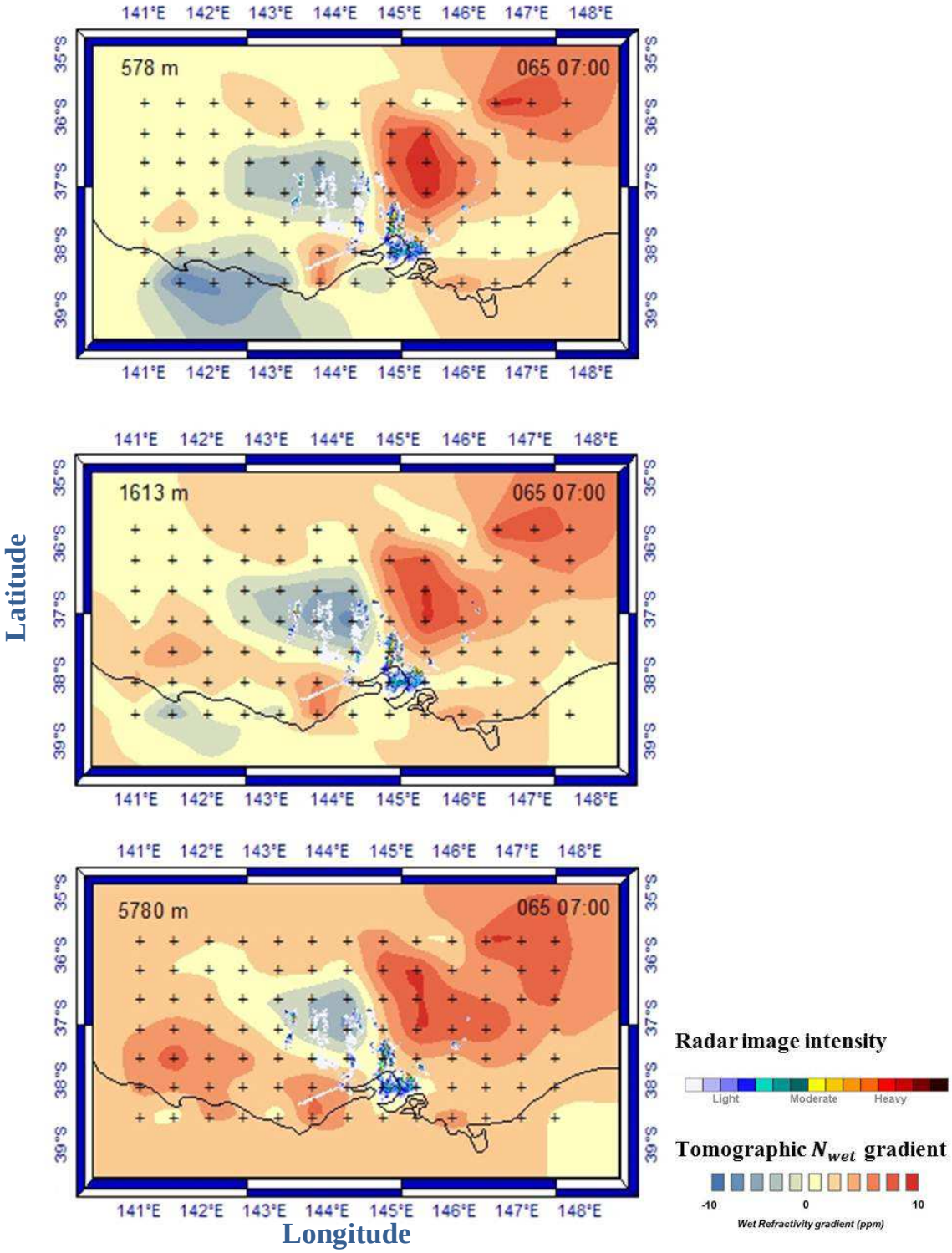

Figure 6.12: Presents the horizontal gradient distribution of wet refractivity from the tomographic solution at 7:00 DOY 65 2010 (UTC). The 2D horizontal gradients are presented for height layers: 578m, 1614m and 5780m, respectively. The Melbourne radar image intensity is overlaid to identify relative path and intensity of the convective storm system.

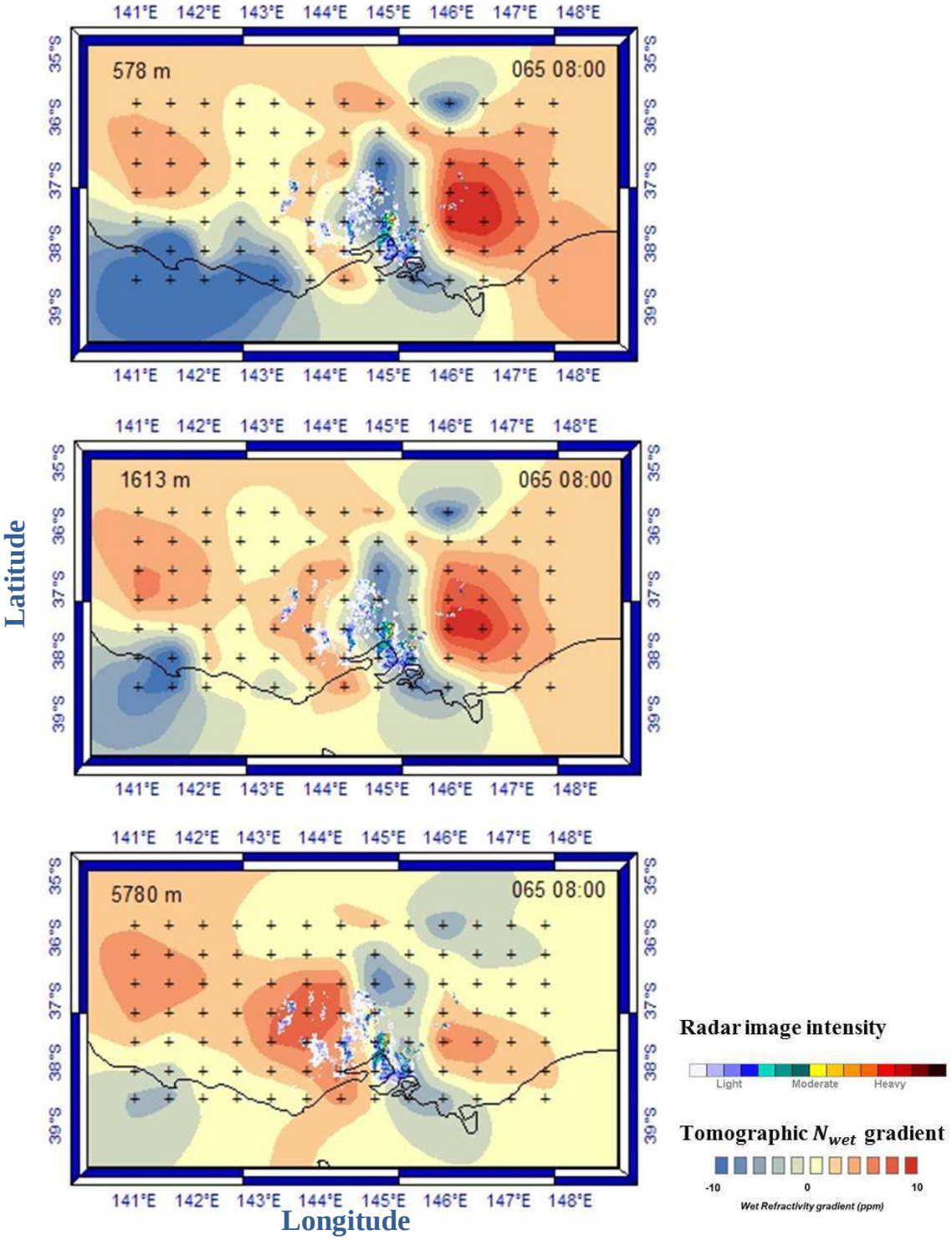

Figure 6.13: Presents the horizontal gradient distribution of wet refractivity from the tomographic solution at 8:00 DOY 65 2010 (UTC). The 2D horizontal gradients are presented for height layers: 578m, 1614m and 5780m, respectively. The Melbourne radar image intensity is overlaid to identify relative path and intensity of the convective storm system.

6.5. Summary

Results presented in this section conclude that 4D GPS tomography is an effective method for reconstructing the dynamics of wet refractivity during the formation and lifecycle of severe weather. This research also reveals that by using the GPSnet for tomographic modelling, the mesoscale convective and stratiform processes of severe storm phenomena are able to be resolved to a horizontal resolution of 55 km. There was a high correlation when comparing the passage of the severe storm and precipitation anomaly depicted by radar intensity images and cumulative rainfall data with the horizontal and vertical gradients of the time evolving wet refractivity fields. The GPS tomographic solutions were validated against radiosonde profiles to achieve an RMS error of 8.58 ppm. This accuracy was particularly positive as the RMS error of the GPS tomographic solution showed no adverse effect when reconstructing of wet refractivity during the severe weather event. Therefore, it was concluded that this method has the potential to be a reliable observational model for NWP analysis and forecasts due to the high temporal and spatial resolution of the GPS tomographic solutions. This is especially important for Australia and the southern hemisphere where meteorological sensors are currently spatio-temorally sparse. This study also concluded that a state-wide GPS tomographic modelling strategy can identify mechanisms of convection up through the vertical layers at the front of the storm and inflow jets in the stratiform region.

Chapter 7. Case study 2: Multi-observational GPS tomography

7.1. Overview

In this chapter, the influence of additional point observations as apriori information to the observation model of the Kalman filter for GPS tomography processing are assessed and analysed. This multi-observational analysis is investigated during the formation, maturation and dissipation of a severe storm and precipitation system, which passed over Melbourne and greater Victoria during Jan 2011. The additional types of point observation methods used for this case study include:

- Radiosonde observations;
- Synoptic meteorological station network observations; and,
- GPS RO observations.

Each additional type of observations is input into the same base GPS tomographic configuration for comparisons during stable and unstable atmospheric conditions. Furthermore, a combination of all additional types of observations are assimilated in a test scenario for comparison.

7.2. January 2011: Victorian severe storm event

Case study 2 covers the severe precipitation and storm event, which occurred during January 2011 to investigate the influence of different apriori observations and to test the concept of a combined multi-observational GPS tomography platform. Different types of observations were assimilated with the GPS-derived DD SWD observations in different test scenarios to anaylse the magnitude of influence on the time series of derived wet refractivity solutions.

The severe storm event for this case study passed over Victoria from 9 – 15 January 2011 (9 – 15 Jan) led to a monthly rainfall three times that of the long-term average, making January 2011 the wettest January on record. The state average rainfall for this period was 118.58 mm compared to the long-term average of 39.72 mm. The storm precipitation intensity resulted in widespread and flash flooding across northern, western and central Victoria. Two thirds of the state received rainfall totals of 100 – 300 mm during this period. Heavy rainfall plus already wet catchments led to widespread flooding, which remained until the end of January. This resulted in most gauges reaching their highest flood levels on record, far exceeding levels set during the September 2010 event. The wettest single day

during this severe storm event was 12-Jan, with rainfall totals reaching 146.8 mm followed closely by 14-Jan recording totals reaching 146.6 mm. Figure 7.1 presents the daily rainfall totals for the 15 day analysis across the state of Victoria.

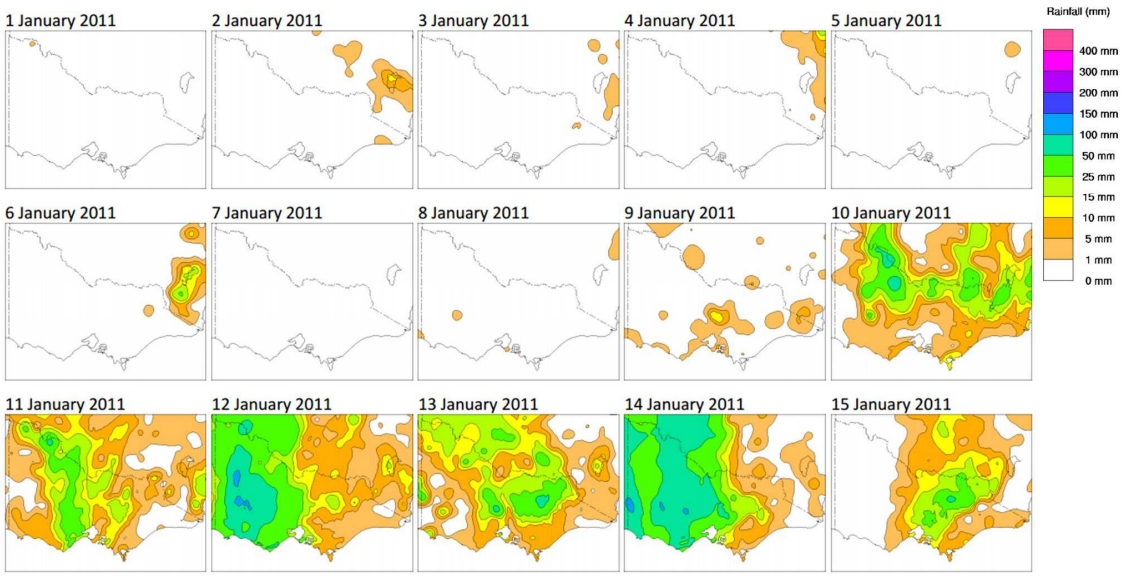

Figure 7.1: Daily rainfall totals across Victoria from the 1 – 15 Jan (Australian Bureau of Meteorology).

Cumulative rainfall data from the Melbourne observatory weather station were used to provide precipitation in the Melbourne region for this severe weather event. The temporal resolution of the cumulative precipitation is 60 seconds from 1 – 15 Jan (Figure 7.2). For Melbourne the wettest 2 days were 13 – 14 with 38 mm and 12 mm accumulated, respectively. Furthermore, the mature stage of this weather event revealed the two largest downpours with 27.1 mm falling in 10 hours (13-Jan) and 23 mm falling in 4 hours (13 – 14 Jan).

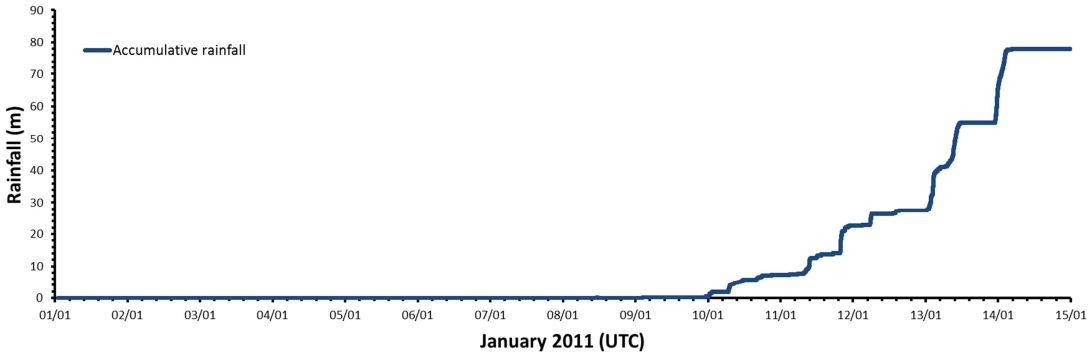

Figure 7.2: Time series of cumulative rainfall for the Melbourne observatory office station from 1 – 15 Jan. Time resolution in 60 seconds.

7.3. Observation parameters

7.3.1. GPS double difference processing

A total of 78 GPSnet CORS stations were used for *case study 2* over the greater extent of Victoria. The processing strategy used the parameter settings described in Section 6.3 for *case study 1* (Figure 6.2). Table 7.1 presents parameters of the configuration used for the GPS DD processing.

Table 7.1: Parameters of the Bernese GPS processing software.

Parameter	**Value**
Time period	1 – 15 Jan 2011
Processing method	Double difference
Number of stations	78
Baseline strategy	Maximum number of observations
Estimation period	Daily
Ionosphere correction	Ionosphere free linear (L_3) combination
Orbits	IGS precise orbits
Sampling rate	30s
Cutoff angle	5°
Additional corrections	Ocean loading, solid Earth tide, axis rotation corrections
Apriori tropospheric model	Saastamoinen dry model
Mapping function	Niell mapping function
Outputs	ZTDs, DD residuals, final station coordinates

Radiosonde profiles

Radio sounding data from MELB were used in this case study for two purposes:

1. As an additional profile observation input for a GPS tomography test scenario.
2. The reference data to validate each test scenario.

The radio sounding balloons produce profile data at a 12-hour resolution. The periodical launch times are 11:00 and 23:00 (UTC). The observation parameters used for this analysis were pressure (hPa), temperature (K) and relative humidity (%). A dry bias exists within the radiosonde profile, which needs to be noted in the context of comparison (see Section 3.5).

Figure 7.3 presents the time series of the computed wet refractivity values for the radiosonde profile over the 15 days. A total of 30 radiosonde profiles were used in this time series to depict the vertical structure of this severe precipitation system during its manifestation and lifecycle. The sparse temporal resolution was the reason for the limited detail revealed in the time series of the wet refractivity dynamics. Furthermore, the MELB station is the only active radiosonde site in Victoria (see Figure 3.13)

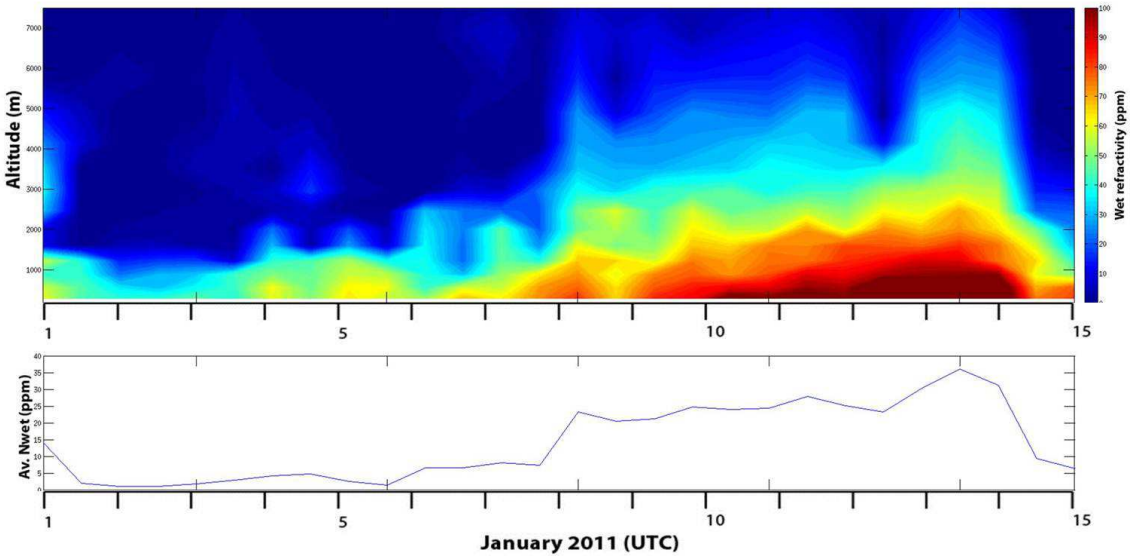

Figure 7.3: The top section presents the evolution of radiosonde wet refractivity profiles every 12 hours on 1 – 15 Jan (UTC). The bottom section presents the evolution of the RI_{wet} during the same time period.

Accuracies of radiosonde estimates of wet refractivity were derived from the National Oceanic and Atmospheric Administration (1997), which published accuracies of pressure, temperature and relative humidity measurements (see Table 3.1). This equates to an overall accuracy for wet refractivity of $\sigma = 2$ ppm.

7.3.2. Synoptic ground meteorological data

Ground-based synoptic meteorological network data were used as an additional data source in the observation model of the 4D tomographic processing in order to determine the influence on the solution estimate. This dataset was tested due to its dense ground-based geometry, homogeneity, and high temporal resolution. The Victorian synoptic weather network was insufficient for providing accurate meteorological parameters at the location of each ground-based GPS station. Therefore, this research implemented an interpolation function (see Section 3.4.2) using the ACCESS-R NWP analysis model. This interpolated network data computed for each GPS station provided a homogeneous data set describing the atmospheric state at each GPS receiver. The data set has a temporal resolution of 1 hour.

The synoptic ground-based meteorological data were also analysed as an additional point observation method for the observation model in the GPS tomographic reconstruction. The standard deviation for this dataset was set to 2 ppm for the covariance model in the Kalman filter (see Section 4.3.5).

7.3.3. GPS RO observations

GPS RO as a satellite-to-satellite tracking technique using radio signals transmitted by the GPS satellites, has emerged as a powerful and relatively inexpensive approach for sounding the global atmosphere with high accuracy, and high vertical resolution in all weather and over both land and ocean (Hajj et al., 2002; Anthes et al., 2008). The advancements of this vertical profiling technique from COSMIC (Constellation Observing System for Meteorology, Ionosphere and Climate) RO have permitted a much closer penetration to the Earth's surface, i.e. 70% – 90% of the soundings reach to within 1 km of the surface on a global basis. The data have been used operationally for weather forecasting and a positive impact has been demonstrated (Le Marshall et al., 2010; Norman et al., 2013b).

This method of observation has also been tested as an additional observation source due to its low cost, homogeneous distribution, high accuracy and high vertical resolution. The post processing RO products include wet refractivity and are routinely generated by UCAR/NOAA. The RO event tangent point distribution is presented in Figure 7.4. These events were incorporated in this case study as a test scenario to assess the influence of additional profile data on the GPS tomographic solution estimate. The benefit of this observation method over radiosonde observations is that the profiles are not restricted to a single location. The limitation, however, is the spatial resolution of events. For example only 10 RO profile events out of 53 occurred in the inner finite voxel grid during the 15-day campaign whereas, radiosonde produced 29 profiles at a temporal resolution of 12 hours. There is, however, a major opportunity for the development of RO as the numbers of LEO satellites increase thus producing a much higher spatial resolution and potentially increasing the reliability of low tropospheric observations (Anthes et al., 2008). This includes next generation GNSS and the development of the proposed COSMIC 2 follow-on mission.

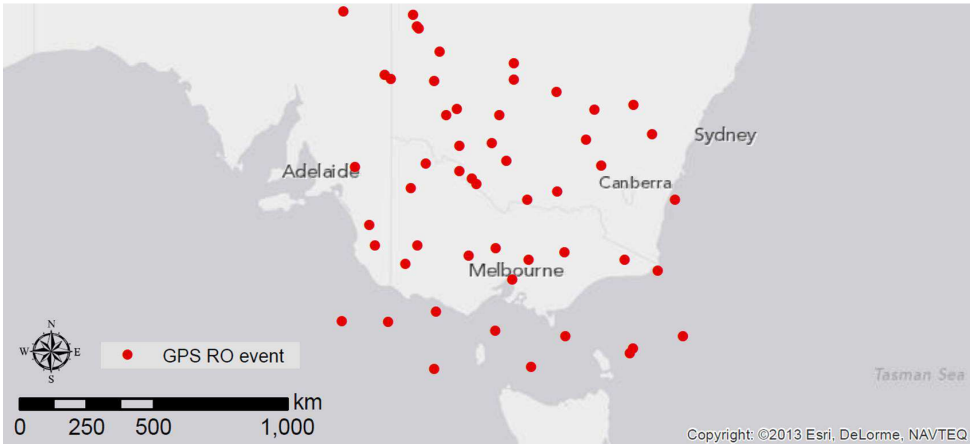

Figure 7.4: The location of 53 GPS RO events in the greater Victorian region during the severe weather event from 1 – 15 Jan 2011.

It should be noted that the UCAR wet refractivity profile data using COSMIC in the troposphere was derived using a one-dimensional variational (1D-Var) analysis combining the F3C RO parameters with a given apriori atmospheric state, and then used in a statistically optimal way, to obtain the most probable atmospheric state (Norman et al., 2012; Li et al., 2013).

The GPS RO dataset was used as an additional point observation method for the observation model in the GPS tomographic processing to assess the influence on the solution estimate. The standard deviation for this dataset was set to 5 ppm for the covariance model in the Kalman filter (see Section 4.3.5). This accuracy is derived from multiple studies of comparing profiles from COSMIC RO of refractivity (ppm) to radiosonde profiles in the troposphere (Kuo et al., 2004; Ho et al., 2010; Fu, 2011).

7.4. GPS tomographic setup

GPS tropospheric delays from GPSnet were computed using the Bernese GPS processing software, a maximum number baseline strategy and the DD approach. The estimated hourly ZPD, the DD residuals, interpolated meteorological data from the ACCESS-R NWP model and satellite and receiver coordinates were all used to reconstruct the DD SWD observations following the same procedure as Section 6.3. Again, a trilinear parameterisation method was adopted. The initialisation of the state vector in the Kalman filter (Table 7.2) and the boundary layer model used an exponential wet refractivity field modelled on average wet refractivity profiles from MELB radiosonde observations.

Table 7.2: Parameter settings of the initial state of the Kalman filter

Parameter *Initial State of the Kalman Filter*	**Value**
Initial surface value (1-1-2011)	55.2 ppm
Initial variance at reference level	10000 ppm²
Scaling height of variance model	1562
Horizontal correlation scaling length	55262 m
Vertical correlation scaling length	1216 m

Table 7.3 presents parameters used in the prediction model. AWATOS 2 assumes a random walk process on the refractivity estimates with the prediciton error as Gaussian. As per *case study 1*, the data sampling rate was set to 30 seconds, the same as the GPS data processing, and the update step size of the Kalman filter was set to 5 minutes.

Table 7.3: Parameters of the prediction model of the Kalman filter

Parameter *Prediction model*	**Value**
Prediction model	Random walk
Sample rate	30 s
Update step size	300 s
Prediction error type	Multivariate Gaussian
Prediction variance at surface	346 ppm²/day
Scaling height of the prediction error	2873
Horizontal scaling length of the correlation	55262 m
Vertical scaling length of the correlation	1216 m

7.4.1. Multi-observation model setup

Five test scenarios were processed using the same GPS tomographic parameter settings with the addition of different observation data types. The initial test scenario introduced no additional data and was used to identify the influence of each additional observation method on the GPS tomographic solution. Each setup used a different type of addition observation sensor to assess the overall accuracy and strength of configuration during a severe weather event. The distribution, sampling rate and geometry of additional meteorological data were assessed using solution estimate accuracy. Table 7.4 presents the parameters of the observation model including the additional observations.

Table 7.4: Parameter settings of the observation model for each GPS tomographic test scenario.

Parameter *Observation model*	**Value**
Integral observations	GPS DD SWD observations
Number of stations	78
Inter-station distance	68 km
Pseudo-observations	Boundary layer, top layer and vertical constraints
Covariance model	Full model
Additional observations	
Test scenario 1 (Tomo)	
Additional observations	None
Test scenario 2 (Tomo + RS)	
Additional observations	Radiosonde (RS)
Number of stations	1
Profile points	17
Sample rate	12 hr
Std. Dev.	2 ppm
Test scenario 3 (Tomo + Synoptic)	
Additional observations	Synoptic meteorological network data (Synoptic)
Number of stations	78
Sample rate	1 hr
Std. Dev.	2 ppm
Test scenario 4 (Tomo + GPS RO)	
Additional observations	GPS RO
Total number of profiles	53
Profile points	17
Sample rate	~7 hr (average)
Std. Dev.	5 ppm
Test scenario 5 (Tomo + RS + Synoptic + GPS RO)	
Additional observations	RS + Synoptic + GPS RO

7.5. Results and discussion of case study 2

In this section results for the January 2011 severe weather event initially include first, the 1D GPS-derived PWV estimates at the KEPK station and comparisons with radiosonde-derived PWV estimates from the MELB station. Secondly, the results on the 4D analysis of wet refractivity using GPS tomography are then presented. Finally, the test scenarios of the multi-observational GPS tomographic solutions are discussed. This case study has an aim of developing GPS meteorology in

the form of ZTD or PWV estimates, and, 4D tomography to increase the capability of resolving the spatial and temporal dynamics of severe weather.

Final results from the simulation experiments (see Section 5.7) revealed that the influence of additional apriori information in the form of synoptic networks or profile data provided a higher accuracy, an improved vertical resolvability as well as a faster solution convergence of the Kalman filter based GPS tomographic solutions.

7.5.1. GPS-derived PWV

As stated in Chapter 6, GPSnet has currently installed ~110 dual-frequency geodetic grade GPS receivers in continuous operation from which 78 were available during the period of *case study 2*. This network holds 9 more stations than *case study 1* (March 2010, see Chapter 6). As discussed previously, the GPSnet is currently considered to be highly dense and homogeneous by Australian standards and has the potential to be a major resource for meteorological data especially in the absence of sufficient meteorological observation systems. The method of processing for GPS-derived PWV estimates was described in Section 6.5.1.

Figure 7.5 presents the results of GPS and radiosonde derived PWV estimates with 1 and 12-hour resolutions, respectively. The initial increase in warm, moist air during the unstable conditions of severe weather were evident from 8-Jan as the dynamics of the severe convection forced WV up through the atmospheric layers. This created higher moisture content in the vertical column. Consequently, the PWV estimates increased from an average 17 mm during a stable atmosphere to a maximum of 62 mm during the severe storm and precipitation processes. The cumulative rainfall series is presented to provide a correlated time scale of the precipitation intensities over the greater Melbourne region during the severe weather event. As evident in the comparison, a sharp increase in PWV from both GPS and radiosonde occurred at 00:00 (UTC) on the 8-Jan approximately 12-hours prior to initial developments of the extreme precipitation system. The mature storm passed over the Melbourne region from 10 – 15 Jan with the maximum intensity occurring during 13 – 14 Jan. A sharp decrease in PWV estimates from both GPS and radiosonde measurements occurred from 14-Jan with values of less than 20 mm estimated by 6am (UTC). This coincided with the final and most intense precipitation front passing over Melbourne. The sharp drop in PWV coincided with the final precipitation system with the time series dropping back to stable values.

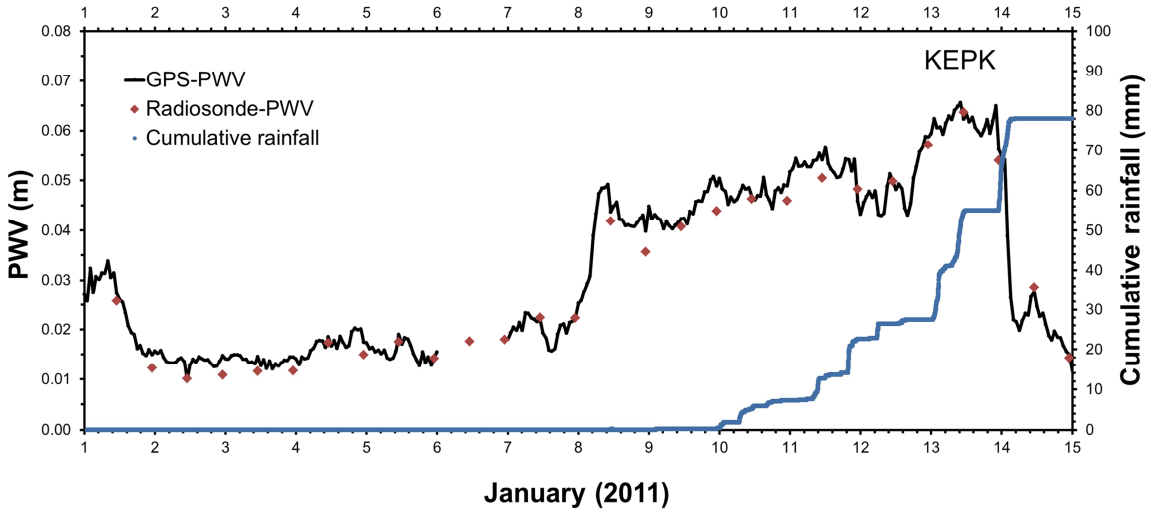

Figure 7.5: Time series of GPS-dervied PWV (mm) from the KEPK station, radiosonde-derived PWV from the MELB station and the cumulative rainfall (mm) during this severe precipitation case study period from 1 – 15 Jan.

The GPS- and radiosonde-derived PWV estimates revealed similar results throughout the 15-day campaign. The storm period from 8 – 15 Jan had minimal effect on the accuracy of GPS-derived PWV, with an RMS error during this period of 1.90 mm (Table 7.5). This equates to a 13% increase compared to results of RMS error derived in Section 3.5. The bias of 0.51 mm is quite significant and indicates a dry bias in the measurement of parameters using radiosonde.

Table 7.5: Final results of the PWV comparison between the ground-based GPSnet station KEPK and radiosonde station MELB.

Station	**Comparison**	Δ_{max}	Δ_{min}	**RMS**	**Bias**	**Std. Dev.**
KEPK	29	4.96	-3.21	1.90	0.51	1.57

To identify trends between the gradient of PWV from GPS and the total rainfall intensity (mm/hr) the first derivative was calculated as shown is Figure 7.6. This figure depicts the gradient time series of PWV and rainfall intensity with respect to time during the *case study 2* period. Initially a large positive gradient occurred in the first 8 hours during 8-Jan approximately 2 days prior to the start of the severe precipitation system. The estimated PWV gradient has a dependency on the rainfall intensity and shows a significant rise in PWV prior to, and during rainfall. There is a direct negative gradient detected immediately after the rainfall. The calculated increase of PWV gradient indicates the capability of GPS-derived PWV estimations for resolving the precursors to severe weather on a synoptic scale. This particular PWV trend was detected approximately 15 and 6 hours prior to the mature stage of the precipitation event from 13 – 14 Jan. This anomaly is depicted by large positive

gradient of PWV during 12-Jan. Significant negative gradients of PWV were recorded directly after this final and most intense rainfall period (13-Jan 23:00 UTC) alluding that the severe weather had passed.

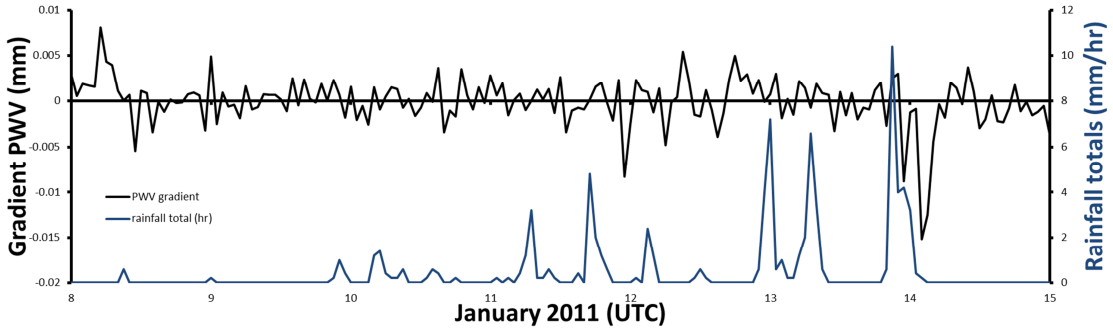

Figure 7.6: Time series of gradient GPS-derived PWV with respect to time and rainfall totals (mm/hour) during the case study period from the 8 – 15 Jan.

These results depict the sensitivity of any GPS state-wide network to be able to measure the integrated amount of WV in the column above each GPS station during the manifestation and lifecycle of severe precipitation systems. The combination of such data from all stations can be used to map the passage of severe weather anomalies with a high horizontal and temporal resolution. In the future this could potentially be used as a continuous, real time application.

However, GPS-derived PWV estimates are integral measurements, therefore they cannot be used to detect or resolve the mesoscale mechanisms of convection in the formation and maturity of severe convective storm systems. For this reason, a 4D GPS tomographic reconstruction method was applied to partly resolve the horizontal and vertical dynamics of wet refractivity for a severe weather event.

7.5.2. GPS tomographic solution

This section presents the performance of *case study 2* using multi-observational GPS tomographic methods and the AWATOS 2 tomography software. This investigation was conducted to analyse the influence of additional observations on the GPS tomographic solution under both stable and unstable atmospheric processes. This was to identify the optimal configuration of the observation model including multiple observation types. The GPS-derived DD SWD observations were the primary input for all test scenarios with additional types of observations for each analysis (see Table 7.4). Unfortunately, GPSnet data were unavailable during the 6-Jan. Also, the GPSnet was reduced from 78 stations to 29 on 9-Jan resulting in smoothing of the tomographic wet refractivity field.

The RI_{wet} (see Eq. (6.1)) was computed for the time series of tomographic profiles extracted from the 4D solution estimates of each campaign (see chapter 6 for full details). As mentioned previously, the

average value of refractivity (RI) was an index of the mean values from altitude layers above the PBL (~2000 m) up to the tropopause. In this study, RI was adopted and applied to the wet refractivity profile computed using GPS tomography in order to produce RI_{wet}. This optimised the sensitivity to moisture content as it excluded the dominating dry component of refractivity (Eq. (2.3)). The index was applied to identify early mechanisms of *lift* due to warm, moist air convection during the formation and lifecycle of severe weather.

7.5.2.1. Detecting severe weather with GPS tomography

Initially, *test scenario 1* (Tomo) was used to investigate the ability of GPS tomography to detect and monitor the highly dynamic mechanisms of moisture in the formation and maturation of a severe weather event.

Figures 7.7 presents the time series of wet refractivity (ppm) profiles at 10-minute intervals at the profile location (A) (Figure 5.3). The profiles extend from the surface to 7500 m altitude for a detailed look at the dynamics of wet refractivity during the 15-day period. The vertical and temporal resolutions made it possible to assess and detect rises in wet refractivity associated with mechanisms of convection due to warm, moist air masses rising through the vertical layers. For example, distinct increases of wet refractivity are estimated on 12-Jan, which start 6 hours prior to the heavy precipitation on 13-Jan. These mechanisms coincide with the convective processes at the storms front.

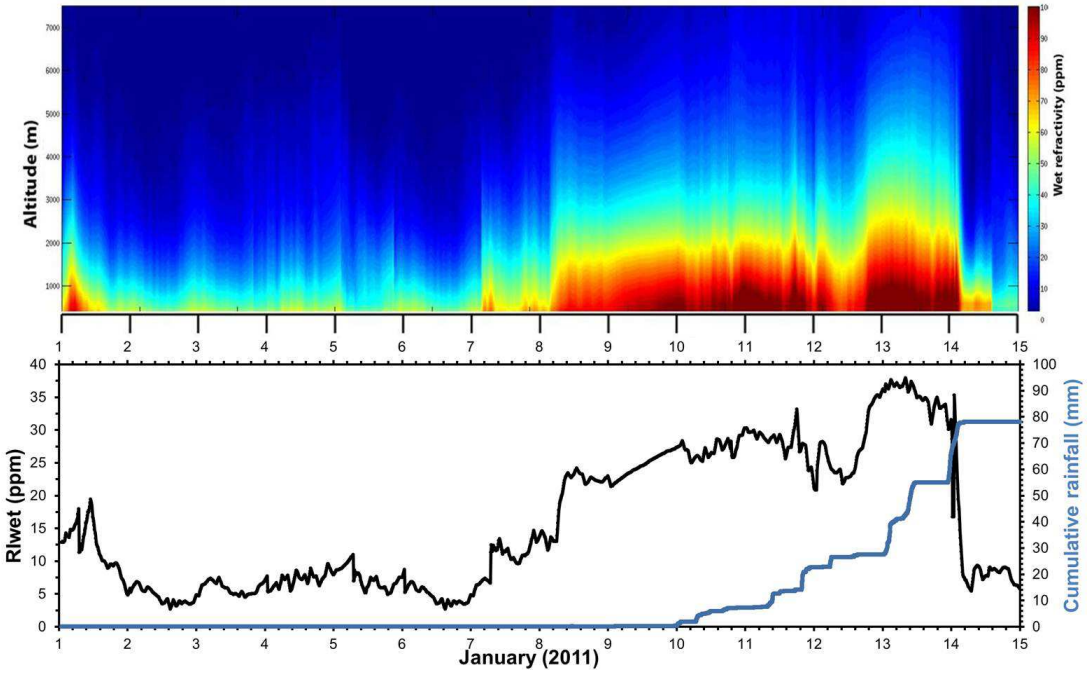

Figure 7.7: *Test scenario 1* (Tomo): time series of tomographic profile solution at profile point (A) using no additional observation data in the observation model. The profiles are values of wet refractivity (ppm) with a solution every 10 minutes from 1 – 15 Jan (UTC). Time series of the RI_{wet} index and cumulative rainfall (below).

The time series presents low but stable levels of wet refractivity from 1 to 7 Jan with minimal significant movement of moisture in the vertical direction. The RI_{wet} also reveals a stable pattern of wet refractivity dynamics during this period. At the start of 7-Jan, a sharp and distinct rise in wet refractivity through each layer occur, with values of 40 ppm rising up above 5000 m altitude. These distinct increases are associated with the precursors of severe weather on a synoptic scale. The RI_{wet} presents a similar trend, showing a distinct rise in the integral measurement of convection. The heaviest cumulative rainfall periods occur on 13 – 14 Jan. The RI_{wet} present a high sensitivity to cumulative rainfall intensity with sharp rise just before, and fall directly after the last and most significant precipitation event. A smoothing effect is identified during 9-Jan (evident in the colour time series of wet refractivity and RI_{wet}). This is due to the number of operational GPSnet stations for this day reduced from 78 to 29.

The dynamics of wet refractivity, with respect to the time series of cumulative rainfall, presents a distinct trend. There was a large rise in wet refractivity through the vertical layers prior to, and during the precipitation extremes with a significant fall directly after the event. The manifestations of these large rises through the vertical layers occur approximately 6 – 12 hours prior to the heavy precipitation anomaly. The most conclusive example of this can be from the time series of wet refractivity over the last 3 days of processing from 12 – 15 Jan. This incorporates the most significant and final rainfall period. Rapid increases in wet refractivity are evident on 12-Jan with large rises in moisture ascending the vertical layers approximately 6 hours prior to the precipitation extreme. This identified the precursors of severe weather and the mesoscale process of strong convection. After the last storm and precipitation anomaly, a sudden drop in wet refractivity is evident through all vertical layers identifying the passing of the severe weather event.

Consequentially, it can be concluded that the sensitivities of the GPS tomographic reconstruction of wet refractivity are highly correlated with periods of heavy rain and hail during the formation and maturity of severe weather. These results show the ability of GPS tomography for monitoring the mesoscale convective and stratiform processes associated with severe weather.

7.5.2.2. Multi-observational GPS tomography

The influence and potential benefits of the inclusion of additional observation types for GPS tomography were investigated during the severe weather event of *case study 2*. The original GPS tomographic model and the same Kalman filter processing was used (see Section 7.4 for parameter settings). The additional observations and their associated covariances were input into the observation model during the update set of the Kalman filter.

Five test scenarios were included in this analysis using different observation types to investigate the influence on the wet refractivity solution estimate. The parameters for the observation model of each

test scenario are presented in Table 7.4. *Test scenario 1* (Tomo) (Figure 7.7) had no additional observations included to the GPS tomographic processing. *Test scenario 2* (Tomo + RS) included radiosonde observations from the MELB station. These observations were added to the observation model with a sample rate of 12hrs. *Test scenario 3* (Tomo + synoptic) included ground meteorological data from a network of 78 ground-based stations. The sample rate was 1hr. *Test scenario 4* (Tomo + GPS RO) included GPS RO profiles. The observation geometry provided profile data with relative homogeneity at different locations dependent on the location of GPS and LEO satellites. A total of 53 GPS RO events occurred within the model field during the 15 day period with an average sample rate of ~7hrs. However, the current limitation of this observation method is that only 10 RO events were recorded within the inner voxel grid (Figure 7.4). *Test scenario 5* (Tomo + RS + Synoptic + GPS RO) assimilated all additional observation types in the observation model.

Time series of wet refractivity profiles from multi-observational GPS tomography

Figures 7.8 – 7.11 present the time series profiles of wet refractivity from the surface to 7500 m altitude, for each additional test scenario. The RI_{wet} is presented at the bottom of each time series along with the cumulative rainfall. These figures present similar patterns of wet refractivity and RI_{wet} with *test scenario 1* (Tomo) shown in Figure 7.7. The same mesoscale convective processes of wet refractivity dynamics through the vertical layers are evident in each figure along with the synoptic precursors.

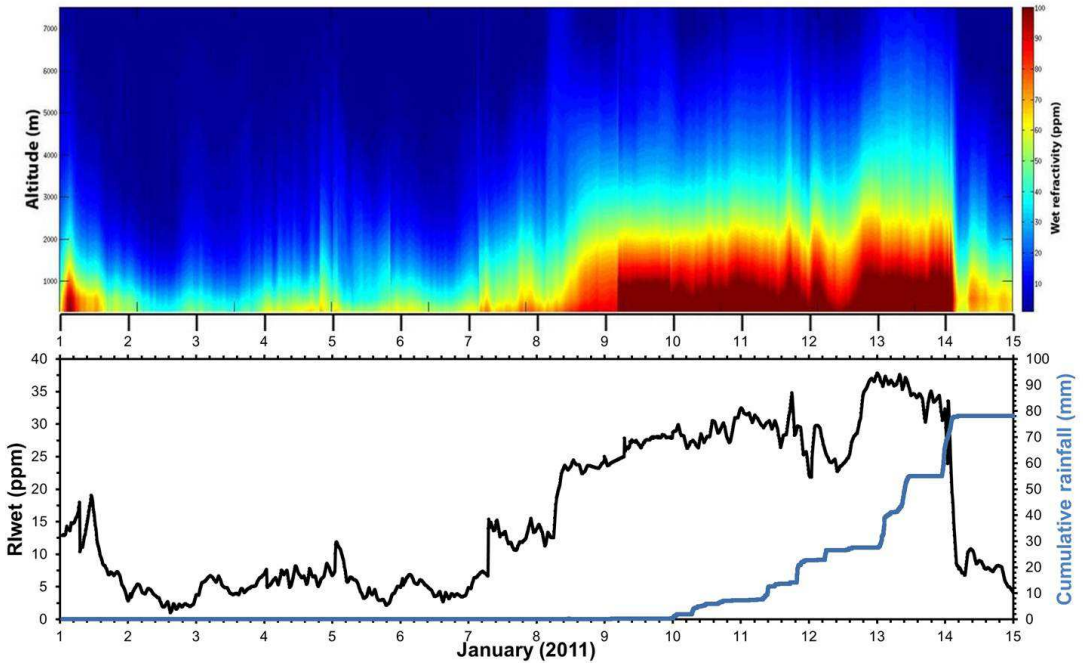

Figure 7.8: *Test scenario 2* (Tomo + RS): time series of tomographic profile solution using radiosonde profiles as an additional observation source. The profiles are values of wet refractivity (ppm) with a solution every 10 minutes from 1 – 15 Jan (UTC). Time series of the RI_{wet} index (black) and cumulative rainfall (blue) shown below.

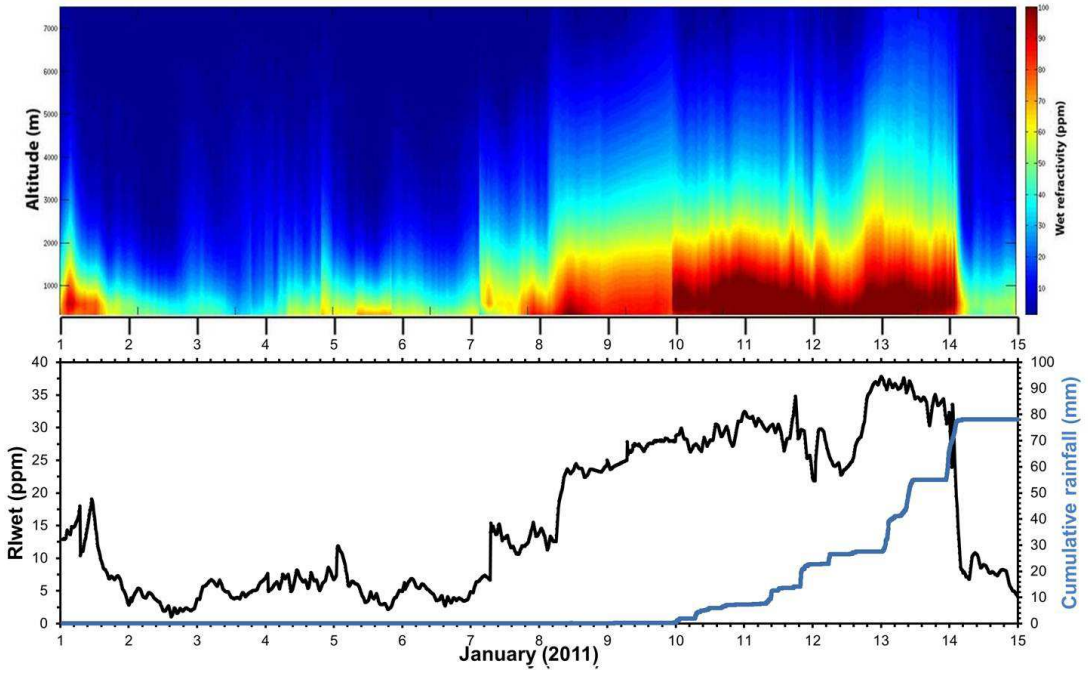

Figure 7.9: *Test scenario 3* (Tomo + Synoptic): time series of tomographic profile solution using synoptic ground meteorological data as an additional observation source in the observation model. The profiles are values of wet refractivity (ppm) with a solution every 10 minutes from 1 – 15 Jan (UTC). Time series of the RI_{wet} index (black) and cumulative rainfall (blue) shown below.

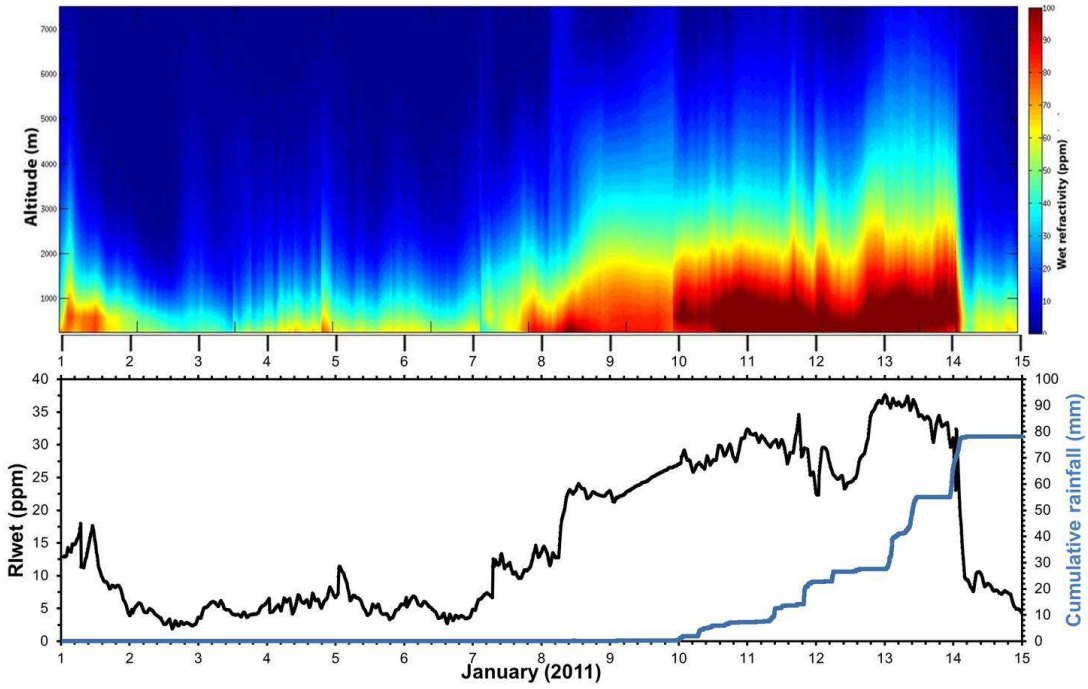

Figure 7.10: *Test scenario 4* (Tomo + GPS RO): time series of tomographic profile solution using GPS RO profiles as an additional observation source in the observation model. The profiles are values of wet refractivity (ppm) with a solution every 10 minutes from 1 – 15 Jan (UTC). Time series of the RI_{wet} index (black) and cumulative rainfall (blue) shown below.

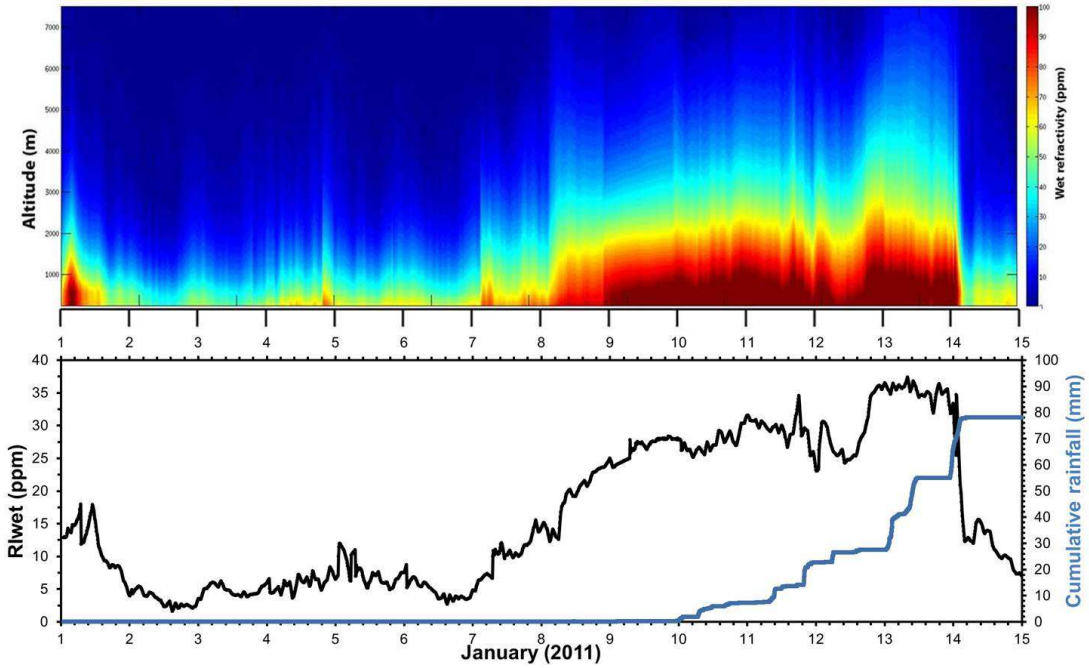

Figure 7.11: *Test scenario 5* (Tomo + RS + Synoptic + GPS RO): time series of tomographic profile solution using radiosonde profiles, synoptic ground meteorological data and GPS RO profiles as additional observation sources in the observation model. The profiles are values of wet refractivity (ppm) with a solution every 10 minutes from 1 – 15 Jan (UTC). Time series of the RI_{wet} index (black) and cumulative rainfall (blue) shown below.

The time series of RI_{wet} for each multi-observational GPS tomographic test in this investigation presented minimal variation between all solutions. It appears that the majority of high turbulence, uncertainty and dynamics of wet refractivity occur within the PBL. The time series of RI_{wet} presented in Figures 7.8 – 7.11 show a significant low during 2 – 6 Jan where values drop to < 4 ppm in contrast to the average value or stable index of 12 ppm. After this period, there was significant rise depicting large amounts of warm, moist air rising up above the PBL via convective dynamics. These processes are the precursors to the formation of the severe weather event. The RI_{wet} reached values > 35 ppm during 13-Jan, which exceed the stable index by a factor of 2.92. Within 4 hours, directly after the severe storm system, the RI_{wet} drops by approximately 25 ppm back to 10 ppm, suggesting the end of the severe weather event and a stabilising atmosphere.

Each GPS tomographic test scenario was compared with the radiosonde observations from the MELB station at a sample rate of 12 hours. According to the National Oceanic and Atmospheric Administration (1997), the accuracy of the radiosonde technique within the troposphere is 1 – 2 hPa for pressure, 0.5°C for temperature and 5% for relative humidity.

Validation analysis of multi-observational GPS tomography

Figures 7.12 – 7.16 present the comparisons between each tomographic solution and radiosonde-derived wet refractivity (ppm). To the right is the bias and standard deviation, and below is the time series of RMS error for each profile solution. Figure 7.12 presents the results for *test scenario 1* (Tomo) using DD SWD observations only. A large positive bias existed below 1500 m with a contrasting negative bias from 1500 to 4000 m altitude during 1 – 6 Jan. This period presents a relatively dry period, recording wet refractivity values of less than 5 ppm above 1500 m in contrast to values exceeding 90 ppm above this altitude during the formation of the severe weather event. Figures 7.13 – 7.16 show a significant improvement during this period compared with *test scenario 1* (Tomo) (Figure 7.12). This additional data improved the solution accuracy by providing valuable supporting information on the atmospheric structure below 4000 m. Significant improvements were also evident during the 12-Jan, where a large outlying RMS error of 18.02 ppm exists at 11:00am (UTC) during *test scenario 1* (Tomo) (Figure 7.12) and the influence of each additional data source (Figure 7.13 – 7.16) significantly reduced these errors to less than 5 ppm. Overall, the time series of *test scenarios* 2 – 4 present increased stability and accuracy in RMS error compared with *test scenario 1* over the 15-day period. However, the use of all observation types for the GPS tomographic processing in *test scenario 5* (Tomo + RS + Synoptic + GPS RO) suggests that this combination of observation geometries and a higher number of observations provides the most accurate and robust result. An overall comparison suggests a smaller standard deviation at every layer and an overall lower RMS error value for periods of both a stable and unstable atmosphere.

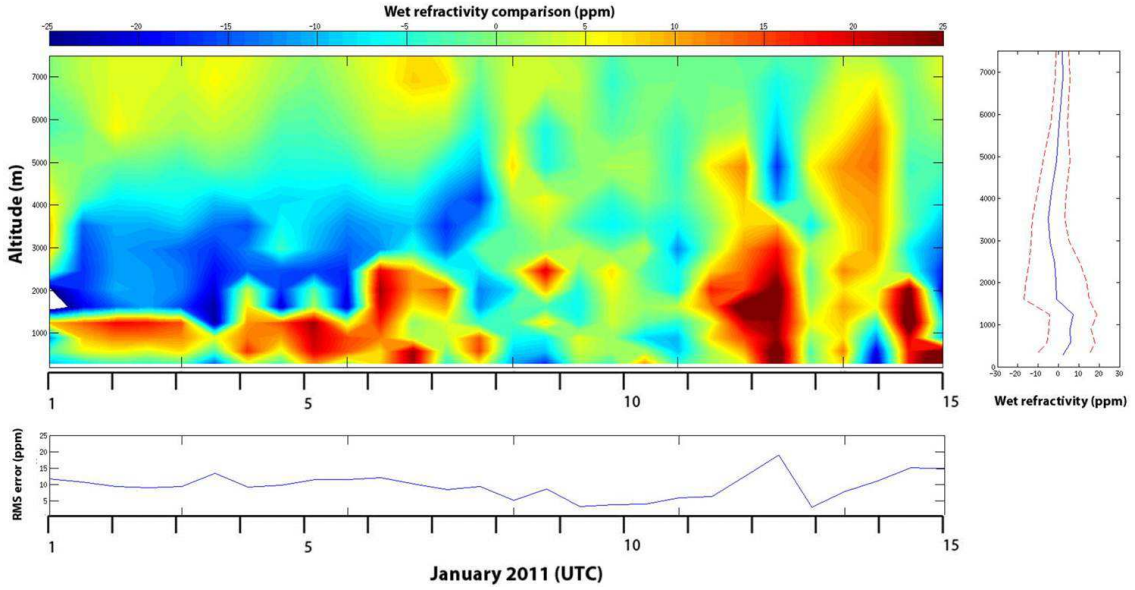

Figure 7.12: *Test scenario 1* (Tomo): Time series profile of wet refractivity derived from radiosonde minus tomographic solution for profile point (A). RMS error of each profile comparison (below) and the bias and standard deviation of each height layer (right).

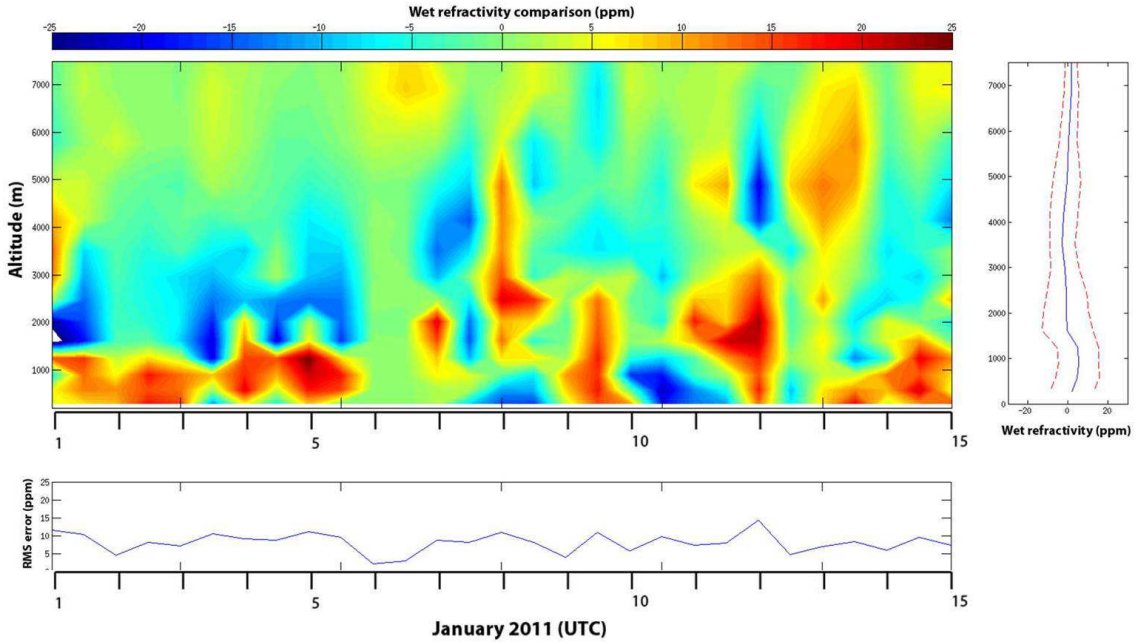

Figure 7.13: *Test scenario 2* (Tomo + RS): Time series profile of wet refractivity derived from radiosonde minus tomographic solution for profile point (A). RMS error of each profile comparison (below) and the bias and standard deviation of each height layer (right).

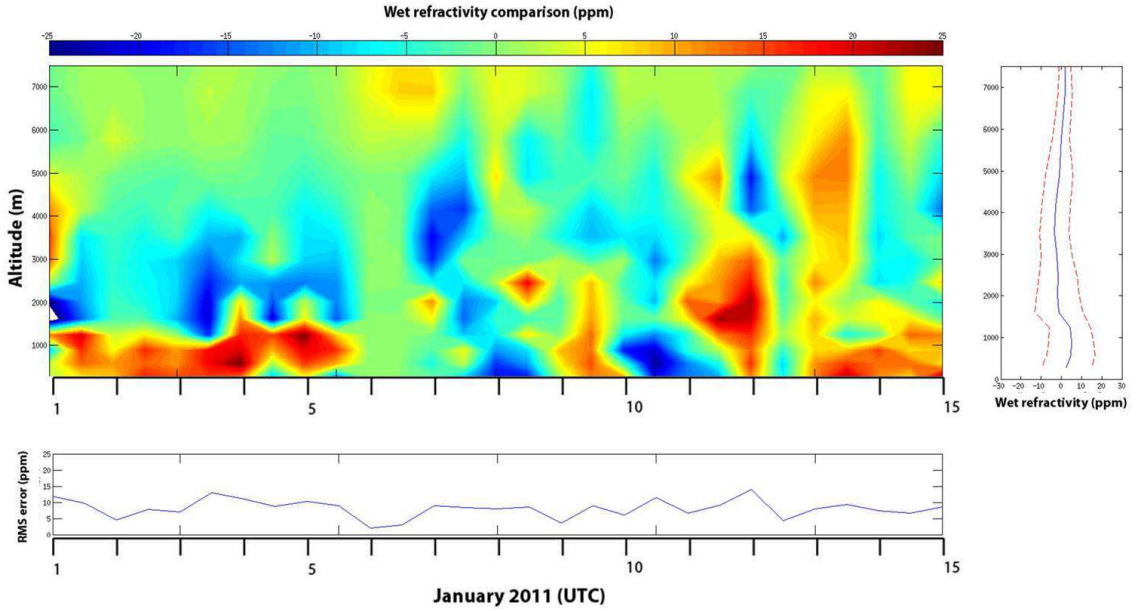

Figure 7.14: *Test scenario 3* (Tomo + Synoptic): Time series profile of wet refractivity derived from radiosonde minus tomographic solution for profile point (A). RMS error of each profile comparison (below) and the bias and standard deviation of each height layer (right).

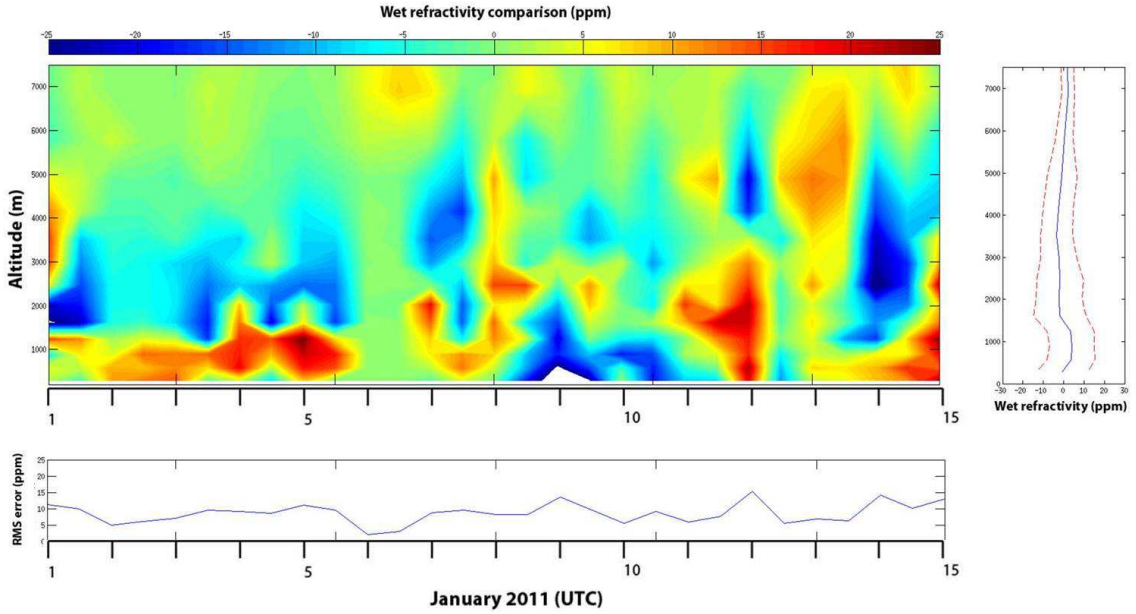

Figure 7.15: *Test scenario 4* (Tomo + GPS RO): Time series profile of wet refractivity derived from radiosonde minus tomographic solution for profile point (A). RMS error of each profile comparison (below) and the bias and standard deviation of each height layer (right).

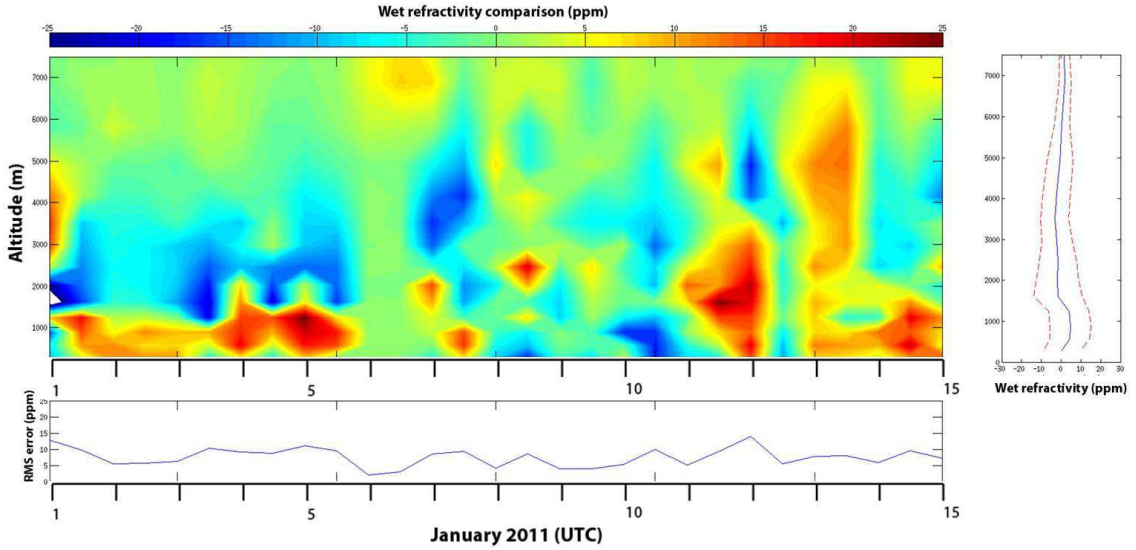

Figure 7.16: *Test scenario 5* (Tomo + RS + Synoptic + GPS RO): Time series profile of wet refractivity derived from radiosonde minus tomographic solution for profile point (A). RMS error of each profile comparison (below) and the bias and standard deviation of each height layer (right).

Comparison of time series of wet refractivity at different altitudes

Figures 7.17, 7.19 and 7.21 present the time series of wet refractivity computed for each multi-observational GPS tomographic test scenario along with radiosonde-derived wet refractivity at altitude layers: 578 m, 1613 m and 5780 m (see Figure 5.3), respectively. Additionally, Figures 7.18,

7.20 and 7.22 present the difference in wet refractivity between the radiosonde-derived estimates and each test scenario solution for the same time series and height layers. As mentioned previously, the number of operational GPS receivers on the 9-Jan decreased from 78 to 29, thus introducing a smoothing effect on each tomographic solution.

Once again, each multi-observational GPS tomographic test scenario were compared against the original *test scenario 1* (Tomo), which includes no additional data. This was to identify the influence of each test scenario at difference heights of the tomographic model. Radiosonde-derived wet refractivity estimates observed at each height layer were used as the truth data. These three layers were selected to track the behaviour of wet refractivity just above the surface, at the approximate height of the planetary boundary layer and at the mid tropospheric altitude at approximately 500 hPa pressure, respectively. The influence of each additional observation type was identified at each height layer. However, it became apparent that the highly dynamic and unstable nature of the troposphere during this severe weather event did introduce a limitation and uncertainty in the final conclusions and results.

In comparison to *test scenario 1* (Tomo), the inclusion of additional information provided a higher overall accuracy when compared to the radiosonde-derived wet refractivity time series. Evidence of this conclusion are listed as follows:

- A significant spike increase in wet refractivity occurred on 1-Jan at each altitude under investigation (Figure 7.17, 7.19 and 7.21). *Test scenarios 2 – 5* which include additional observations present a significant increase in accuracy at 578 m altitude (Figure 7.18) compared with *Test scenario 1* (Tomo). Differences decrease from 17 ppm to below 10 ppm for *Test scenarios 2 – 5*.

- At lower altitudes, it was assumed that the additional interpolated synoptic measurements would have the most significant effect on accuracy and would ultimately be the most robust solution due to the density and homogeneity of the ground-based geometry and hourly temporal resolution. Evidence of this conclusion occurred at 1613 m altitude (Figure 7.19 – 7.20) during 5 – 10 Jan for *test scenario 3* (Tomo + Synoptic), where the most significant improvements of accuracy were identified.

- High instability on 11 – 12 Jan for each of the three height layers indicated mechanisms of convection for the precursor to the severe precipitation event. This period of high instability identified the enhancement in resolvability for the *test scenarios 2 – 5* in comparison to *test scenario 1*. Figures 7.18, 7.20 and 7.22 present a significant increase in accuracy for this period when assessing the differences when compared with radiosonde at each height layer. Accuracies increase by more than 50% for all height layers during this period.

- The final decrease in wet refractivity occurred on 14-Jan with wet refractivity values decreasing by half in 4 hours. This tropospheric anomaly is reconstructed with a high trend between all GPS tomographic test scenarios. The pattern of wet refractivity during this anomaly coincided with the pattern of cold, dense downdraft and inflow jets at the back of the storm and stratiform structure.

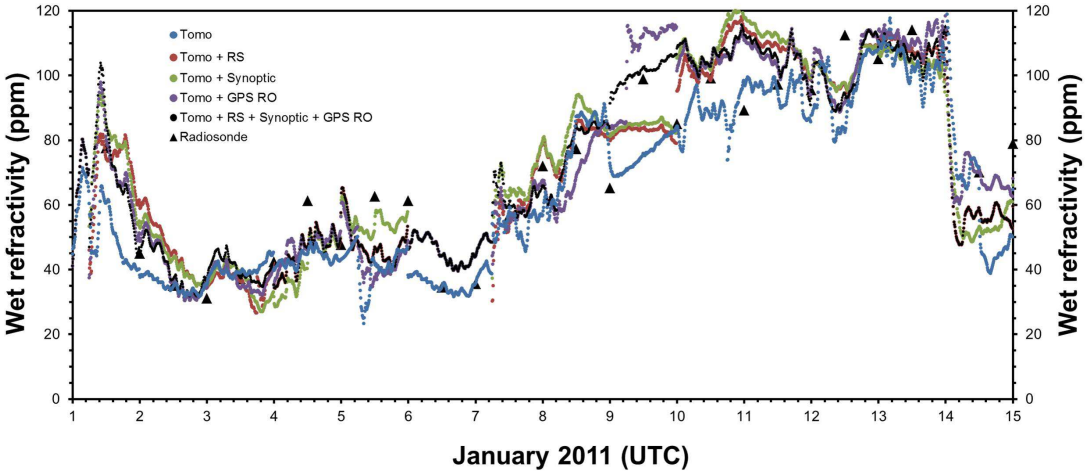

Figure 7.17: Time series of the wet refractivity (ppm) solution for all test scenarios at height layer 578 m. Radiosonde-derived wet refractivity (ppm), expressed as black triangles were the reference values.

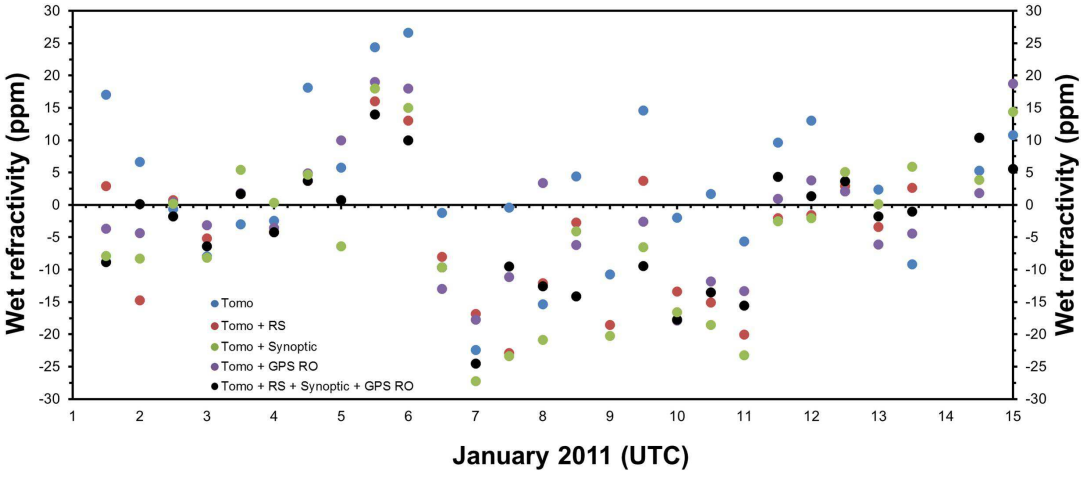

Figure 7.18: Time series of the difference in wet refractivity (ppm) between the radiosonde-derived estimate and each GPS tomographic test scenario at height layer 578 m.

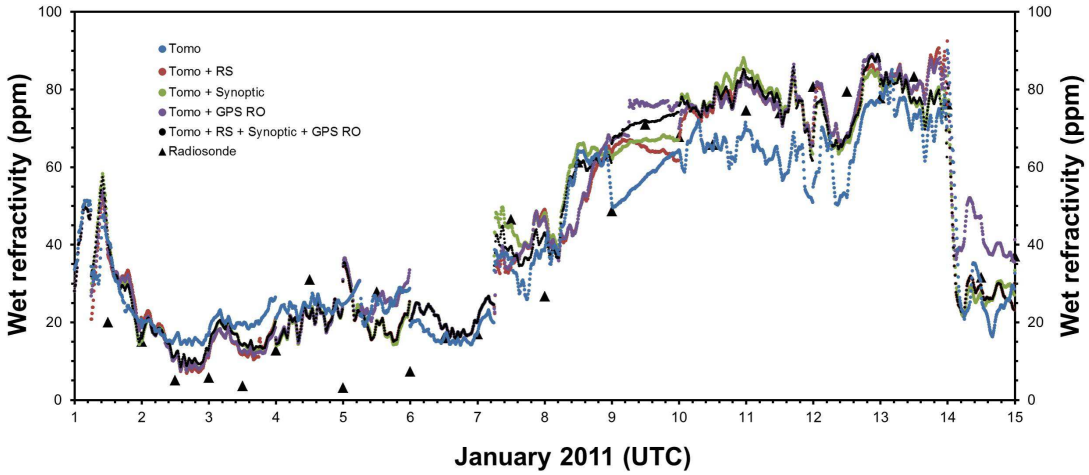

Figure 7.19: Time series of the wet refractivity (ppm) solution for all test scenarios at height layer 1613 m. Radiosonde-derived wet refractivity (ppm), expressed as black triangles were the refrence values.

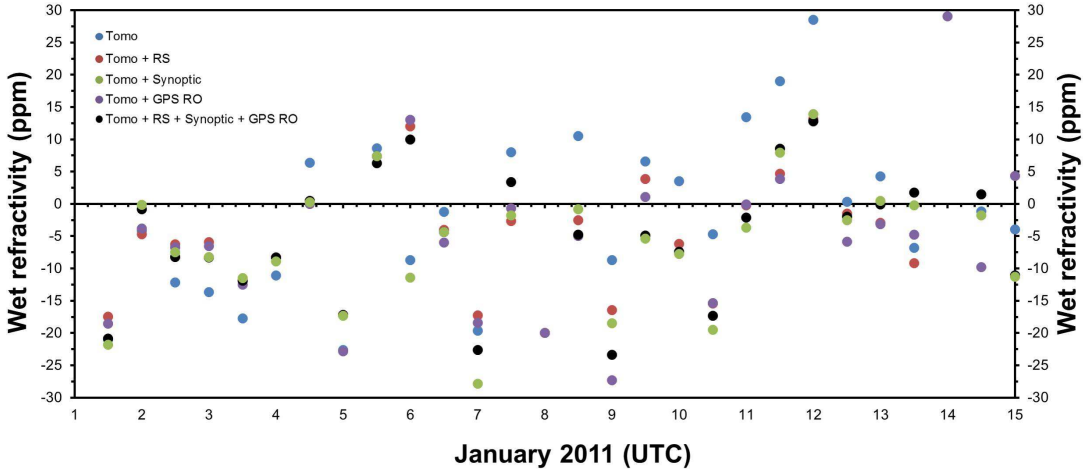

Figure 7.20: Time series of the difference in wet refractivity (ppm) between the radiosonde-derived estimate and each GPS tomographic test scenario at height layer 1613 m.

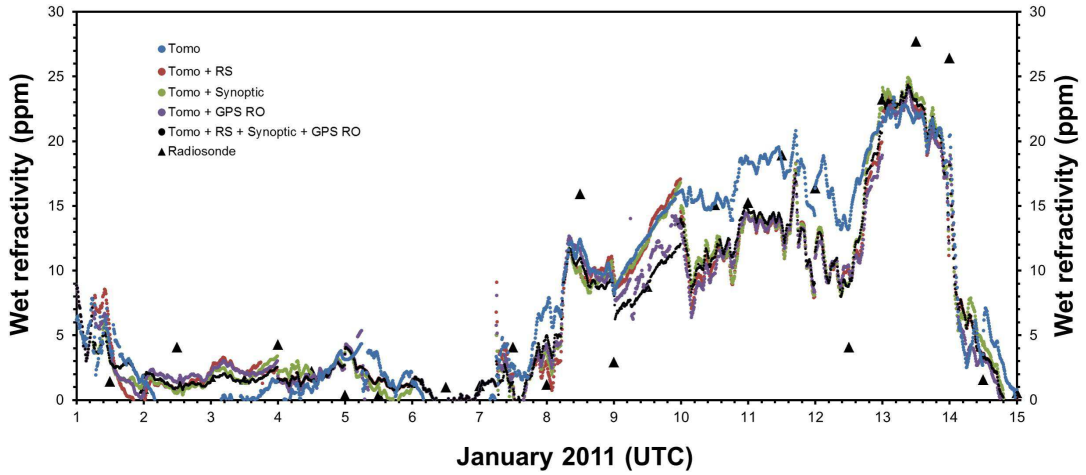

Figure 7.21: Time series of the wet refractivity (ppm) solution for all test scenarios at height layer 5780 m. Radiosonde-derived wet refractivity (ppm), expressed as black triangles were the refrence values.

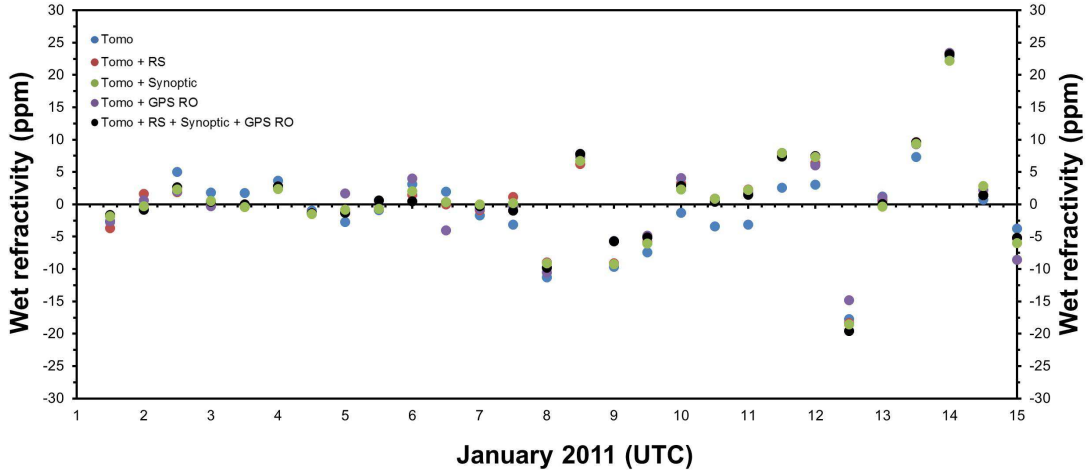

Figure 7.22: Time series of the difference in wet refractivity (ppm) between the radiosonde-derived estimate and each GPS tomographic test scenario at height layer 5780 m

Time series of RMS error

The time series of RMS error for the 15-day analysis present a relatively consistent pattern of error during periods of both stable and unstable atmosphere conditions (Figure 7.23). The period from 12 – 15 Jan produced predominantly all of the rainfall associated with this storm precipitation system. Significant decreases in RMS error were evident during this period for each multi-observational GPS tomographic test scenario when compared with *test scenario 1* (Tomo). The test with the inclusion of radiosonde observations (*test scenario 2* (Tomo + RS)) and the ground meteorological synoptic network observations (*test scenario 3* (Tomo + Synoptic)) revealed the largest increase in accuracy. The results of the test including GPS RO observations (*test scenario 4* (Tomo + GPS RO)) revealed

slight improvements. However, as mentioned previously, limitations existed in the time and frequency of RO events in the Victorian region, eg: only 10 of these events occurred within the inner voxel model. The rest occurred within the boundary layer of the voxel construction. The results from *test scenario 5* (Tomo + RS + Synoptic + GPS RO) revealed a higher overall accuracy in comparison to all other solutions. This is particularly true during the period of highly unstable wet refractivity conditions during the formation and maturity of the severe weather event.

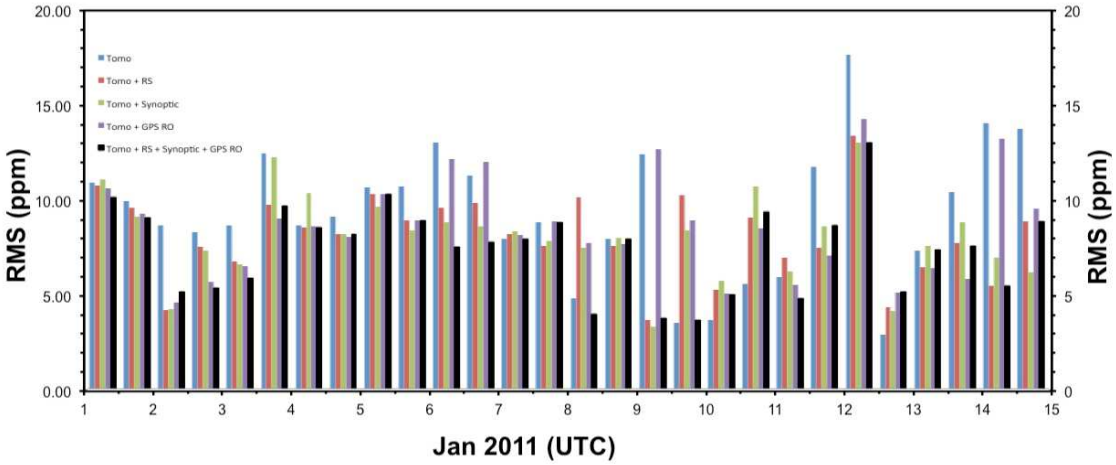

Figure 7.23: Time series of RMS error values for all 5 test scenarios. Radiosonde-derived wet refractivity from the MELB station was used for reference values.

These findings are significant, as the RMS error of the GPS tomographic solution showed no adverse effect when reconstructing wet refractivity fields during the severe weather event. Furthermore, the inclusion of additional observations to the GPS tomographic solution provided, on average, a significantly higher accuracy and more robust solution. Therefore, this GPS platform has the potential to monitor the convective and stratiform mechanisms of wet refractivity in 4D and ultimately enhance the early detection and prediction of severe weather when assimilated into NWP forecast and analysis.

7.5.2.3. Results for multi-observational GPS tomographic solutions

Table 7.6 presents the average RMS accuracies of each multi-observational GPS tomographic test scenario compared with the reference: radiosonde-derived wet refractivity during the 15-day case study. This period encompassed approximately 8 days of dry stable atmospheric conditions (1 – 8 Jan), followed by 7 days of unstable atmospheric storm and precipitation phenomena (9 – 15 Jan). The average accuracies for the period prior to, and during the severe weather conditions are shown in Table 7.7. Each multi-observational tomographic test revealed a noticeable improvement in accuracy compared with *test scenario 1* (Tomo). This strongly suggests that including additional observations on the state of the wet refractivity has a positive influence on the accuracy improvements of the GPS

tomographic solution. This was especially evident during periods of unstable atmospheric conditions. The introduction of radiosonde profiles produced the most significant improvement on the overall accuracy. This is most likely because the geometry of the radiosonde provides better information on the vertical structure of wet refractivity. Resolving the vertical structure above the ground-based GPS network is the major limitation in GPS tomography.

In summary, *test scenario 4* (Tomo + GPS RO) provided an overall improvement of 8.57% compared to *test scenario 1* (Tomo). This is assumed to have provided the least influence on the accuracy due to the sparse and infrequent nature of ROEs in the inner voxel model. *Test scenario 3* (Tomo + Synoptic) and *test scenario 2* (Tomo + RS) resulted in improvements of 13.09% and 14.29%, respectively. The improvement of accuracy for *test scenario 3* (Tomo + Synoptic) can be attributed to the high spatial and homogeneity and high temporal resolution of data in the lower altitudes. The solution with the most improvement in accuracy using only one additional observation method was *test scenario 2* (Tomo + RS) (see Table 7.6 and 7.7). This is predominantly due to the high vertical resolution and accuracy of profile information of radiosonde observations. However, a limitation existing in the time resolution, with only 2 profiles provided per day.

The assimilation of all additional observation methods into the GPS tomographic model (*test scenario 5* (Tomo + RS + Synoptic + GPS RO)) provided the largest improvement of all, with a 19.15% increase in accuracy. This is attributed to the increased amount of redundancy in observations and constraints for the unknown parameters, and the combination of good observation distribution and geometries. This provided the most comprehensive distribution of information on the lower levels due to the synoptic meteorological network, and information on the vertical structure from the radiosonde and GPS RO profiles. Therefore it can be concluded that this multi-observational GPS tomographic strategy is the most accurate and robust for detecting and monitoring severe weather events using GPS.

Table 7.6: Average RMS error results from each GPS tomographic test scenario.

Test scenario	**Observation model**	**Average RMS (ppm)**
1.	Tomo	9.363
2.	Tomo + RS	8.025
3.	Tomo + Synoptic	8.137
4.	Tomo + GPS RO	8.561
5.	Tomo + RS + Synoptic + GPS RO	7.570

Table 7.7: Average RMS error results from each GPS tomographic test scenario for comparisons prior to storm and during storm periods.

Test scenario	Observation model	RMS (ppm) *1 – 8 Jan*	RMS (ppm) *9 – 15 Jan*
1.	Tomo	10.319	8.470
2.	Tomo + RS	7.984	8.062
3.	Tomo + Synoptic	8.232	8.048
4.	Tomo + GPS RO	7.861	9.214
5.	Tomo + RS + Synoptic + GPS RO	7.960	7.206

Table 7.8 provides further statistical results for each multi-observational GPS tomographic test scenario when compared with radiosonde-derived wet refractivity estimates. A bias between the radiosonde and *test scenario's 1, 2, 3 and 5* is evident. This may be due to the suspected dry bias in the radiosonde observations.

The standard deviation of each GPS tomographic campaign (Table 7.8) reveals a similar pattern to the RMS accuracy analysis presented in Table 7.6. Again, there was a significant decrease in the standard deviation between *campaign 1* (Tomo) and all multi-observational GPS tomography campaigns. *Campaign 5* (Tomo + RS + Synoptic + GPS RO) provided the highest accuracy reducing the standard deviation by 19.30%.

Table 7.8: Bias and standard deviation results for each GPS tomographic test scenario.

Test scenario	Observation model	Bias (ppm)	Std. Deviation (ppm)
1.	Tomo	0.516	8.786
2.	Tomo + RS	0.289	7.663
3.	Tomo + Synoptic	0.401	7.676
4.	Tomo + GPS RO	-0.026	8.023
5.	Tomo + RS + Synoptic + GPS	0.758	7.090

These results suggest that on average, increased additional observations provided a more robust and higher accuracy for the overall GPS tomographic solutions. The *test scenario 1* (Tomo) provided a time series of wet refractivity, but with limitations in the vertical resolvability especially during periods of a highly unstable troposphere and severe precipitation events. These limitations were evident during 12- and 14-Jan (Figure 7.12) for the low to mid troposphere. This vertical resolvability limitation may be associated with the flat ground-based GPSnet geometry. Although boundary conditions and vertical constraints provide some apriori model information, there are no direct measurements included. Therefore, the inclusion of additional observations will have a significant

positive influence on the solution accuracy, especially during severe weather anomalies. The combination of additional vertical profile and ground-based station observation geometries are complementary with each other and provide solution strength for the reconstruction of wet refractivity.

7.6. Summary

This chapter presented an investigation into the use and capability of multi-observational GPS tomography during the formation and lifecycle of *case study 2*: severe weather event. The results show that the accuracy of 4D GPS tomography was improved with the inclusion of additional types of observation systems. Four multi-observational GPS tomographic test scenarios were validated against radiosonde-derived wet refractivity to assess the influence of the inclusion of each observation system, in comparison with *test scenario 1* (Tomo), which included no additional data. Furthermore, the influence of all additional observation systems assimilated into the GPS tomographic solution was investigated in *test scenario 5* (Tomo + RS + Synoptic + GPS RO). Results showed that the most significant improvement was from *test scenario 5* (Tomo + RS + Synoptic + GPS RO) with an increase in accuracy of 19.15% (RMS).

These findings are significant, as the RMS error of the GPS tomographic solution showed no adverse effect when reconstructing wet refractivity fields during the severe weather event. Furthermore, the inclusion of additional observations to the GPS tomographic solution significantly increased the accuracy and reliability of reconstructing the wet refractivity fields. Therefore, multi-observational GPS tomography has the potential to be a reliable observational model for NWP analysis and forecasts especially during the formation and lifecycle of severe weather, due to the high temporal and spatial resolution of the GPS tomographic solutions. As mentioned previously, this is especially important for Australia and the southern hemisphere where meteorological sensors are currently spatio-temorally sparse.

Finally, results showed that 4D GPS tomography is able to detect the mesoscale convective and stratiform processes of wet refractivity during severe weather. This was proven by monitoring the dynamics of the 4D reconstructed wet refractivity fields in relation to the evolution of cumulative rainfall in the Melbourne region.

Chapter 8. Conclusions, recommendations and outlook

8.1. Conclusions

This research has demonstrated that ground-based GPS meteorology is a highly effective and robust observation technique for detecting the dynamics of WV, particularly in the context of severe weather. This is especially significant for Australia and the southern hemisphere where other sensors are sparse in space and time. This research developed a new effective GPS meteorological platform using Kalman filter based GPS tomographic modelling to reconstruct the 4D dynamics of wet refractivity for the GPSnet CORS network. A high spatio-temporal resolution was obtained during the formation and lifecycle of severe weather phenomena, which was achieved by exploiting the high spatial and unbiased network resolution, and continuous operability of the GPSnet. This GPS-derived 4D modelling strategy has the potential to improve weather prediction, climatology and the early detection and prediction of severe weather events. Results for this research also indicate that 1D GPS-derived PWV estimates have a high accuracy and reliability, and also hold a high sensitivity to the dynamics of WV during the formation and lifecycle of severe weather.

This research presented a pioneer study into GPS tomography for the Australian region, with a particular interest in detecting and monitoring severe weather events. The Kalman filter based GPS tomography package AWATOS 2 was implemented and parameters were optimised for the GPSnet to reconstruct the dynamics of wet refractivity in the troposphere in Australia. Results indicated a high sensitivity and trend to depicting the mesoscale structure, including the convective and stratiform regions in the formation and lifecycle of severe weather using dense CORS networks.

Two case studies were implemented to analyse the dynamics of wet refractivity derived from GPS tomography during the influence of severe weather. These were:

- *Case study 1*: March 2010 Victorian severe supercell storm event
- *Case study 2*: January 2011 Victorian severe storm event

Both case studies presented a high correlation between the passage of the severe storm/ precipitation anomaly depicted by radar intensity images and cumulative rainfall data and the horizontal and vertical gradients of the time evolving wet refractivity fields. Results suggest that a state-wide GPS tomographic solution can identify mechanisms of convection in the vertical layers at the front of the

storm and also gradients of rear inflow jets in the stratiform region. Radiosonde-derived wet refractivity estimates were used as the reference for the validation of the GPS tomographic solutions of wet refractivity. Average RMS errors of 8.58 ppm and 9.36 ppm, respectively were achieved for both case studies. These accuracies are consistent with past research in validating GPS tomography (Nilsson and Gradinarsky, 2006; Lutz, 2008; Rohm and Bosy, 2011; Perler, 2011). This result was particularly significant because this analysis was conducted during a severe weather event, and showed no adverse effects on the time series of the RMS error for the GPS tomographic solution. Therefore, GPS tomography has the potential to be a reliable observational model for assimilation into NWP analysis and forecasts. This GPS platform will potentially enhance the early detection and prediction of severe weather due to the high temporal and spatial resolution of data. This is especially important for Australia and the southern hemisphere where meteorological sensors are currently spatio-temorally sparse.

An investigation into multi-observational GPS tomography was carried out during the *case study 2* severe weather event. Five test scenarios were tested and assessed, which incorporated three different types of additional observations to identify the influence on the GPS tomographic solution. These were: radiosonde observations; Synoptic meteorological station networks observations; and, GPS RO observations.

The five test scenarios investigated were:

- *Test scenario 1* (Tomo): No additional data added to the original GPS tomographic model;
- *Test scenario 2* (Tomo + RS): Radiosonde observations added;
- *Test scenario 3* (Tomo + Synoptic): Synoptic network observations added;
- *Test scenario 4* (Tomo + GPS RO): GPS RO observations added; and,
- *Test scenario 5* (Tomo + RS + Synoptic + GPS RO): All additional types of observations added.

Results from these analyses suggested that additional meteorological observations significantly and consistently improve the accuracy of the reconstructed wet refractivity field and provide a more robust GPS tomographic solution. Additional observations providing information on the vertical structure of wet refractivity yielded the highest improvement in accuracy. This was primarily due to the limitation of GPS tomography alone to vertically resolve wet refractivity. Final results for each multi-observational test scenario were compared against *test scenario 1* (Tomo). This test incorporated the original GPS-derived DD SWD observations only into the tomographic solution. The inclusion of additional GPS RO observations (*test scenario 4* (Tomo + GPS RO)) resulted in an average improvement of 8.57%. It appears that this provided the least improvement in accuracy because only 10 RO events were observed in the voxel model during the 15-day period. The use of additional ground-based synoptic weather station network observations (*test scenario 3* (Tomo +

Synoptic)) yielded an improvement of 13.09%. The inclusion of additional radiosonde observations (*test scenario 2* (Tomo + RS)) provided an improvement in accuracy of 14.29%. This proved to be the largest for the addition of a single observation type. *Test scenario 5* (Tomo + RS + Synoptic + GPS RO) included all additional types of observations in the GPS tomographic model. This produced an increase in accuracy of 19.15%. This result was the largest improvement, and it appears to be due to the greater redundancy available in observations used to solve the same number of unknown wet refractivity parameters. Based on these results it was concluded that the inclusion of additional observations to the GPS tomographic model significantly increased the accuracy and reliability of reconstructing the wet refractivity fields. Therefore, multi-observational GPS tomography has the potential to enhance the accuracy of original GPS tomographic techniques providing a more robust solution, particularly in the outlook of monitoring severe weather events. Again, this is especially paramount for Australia where meteorological data are sparse.

Statistical optimisation for the GPS tomographic model parameter settings was also investigated via multiple tests using synthetic refractivity fields in simulation studies. The statistical optimisation was based on the RMS error, vertical convergence and stabilisation rate of the solution. The discretisation issue of the voxel grid over the GPSnet was investigated and it was concluded that a horizontal resolution of 55 km and a vertical resolution of 15 layers with exponential layer divisions are optimal. Horizontal and vertical correlation parameters of the Kalman filter were set to these optimal voxel resolutions. The vertical resolvability of wet refractivity using the optimal voxel resolution was tested by investigating the solution convergence, above the highest GPS receiver, using a constant synthetic wet refractivity field that had a wet refractivity spike layer of 10 ppm. Past research has suggested that there is a limitation in resolving the vertical structure. The vertical convergence took 20 minutes for the solution to resolve the wet refractivity spike with an accuracy of < 1 ppm. The speed of solution convergence for estimating the wet refractivity spike was only slightly slower by a factor of 1.54 than resolving the original simulated exponential wet refractivity field. Conclusions from this analysis suggest that the GPS tomographic algorithm is highly robust and has the ability to quickly adapt to highly dynamic changes in wet refractivity. This is particularly significant for severe weather monitoring where fast convergence is needed to resolve mesoscale convective processes.

A final simulation study investigated the influence of additional types of simulated meteorological observations introduced into the GPS tomographic solution. Two types of additional observations were simulated and included in this study. These were:

- Profile observations; and,
- Synoptic network observations.

Both GPS tomographic simulations, each including an additional observation type were compared against the original GPS tomographic solution, which included no additional data. The solution with additional simulated profile observations produced the quickest convergence rate with an improvement on the original solution by a factor of 4.3. The solution with additional synoptic network data also concluded a significant increase in convergence rate with an improvement on the original solution by a factor of 3.3. These results appear to show that a higher redundancy in observations per unknown wet refractivity parameter to be solved for, provides a faster convergence rate for the tomographic algorithm. These findings are particularly significant for severe weather monitoring using GPS tomography. This is due to the high dynamic nature of wet refractivity during these events.

Investigations into GPS-derived PWV estimates using the GPSnet in the Victorian region revealed a high accuracy and reliability when compared with radiosonde-derived PWV. The Bernese GPS processing software V5.0 was used to determine accurate estimates of ZTD using a DD approach. Additional meteorological data with an empirical model and a scaling factor were used to determine PWV. Radiosonde-derived PWV estimates were used as truth data to validate the GPS-derived PWV. Three GPSnet stations were co-located with respective radiosonde stations to examine the accuracy over a 30-day period, which included 6 days of severe weather. The three co-located sites produced an average RMS error of 1.59 mm. The RMS error was 1.9 mm during the severe weather event. This validation study provided the fundamentals for the GPS-derived PWV estimation process in Victoria. Currently 110 GPS CORS stations are operational in Victoria as the GPSnet infrastructure, and an additional 130 are operational within New South Wales. Therefore, this combined infrastructure has the potential to be of significant benefit for assimilation into the Australian NWP model to improve forecasting and nowcasting. The advantages are a high spatio-temporal resolution of measurements compared to radiosonde, a dynamic capability for detecting sharp changes in PWV at the zenith and high accuracy.

Results of GPS-derived PWV estimates also indicate high sensitivity to the formation and precursors of severe weather events at a synoptic scale. *Case studies 1 and 2* were used to assess the dynamics and sensitivity of PWV to WV during severe weather. Both case studies presented significant increases in PWV approximately 48 hours prior to the storm front and precipitation extremes. These are associated with the synoptic scale precursors of warm, moist air creating unstable atmospheric conditions with a cold front. However, identifying the mesoscale convective processes in the evolution of GPS-derived PWV estimates is too ambiguous. Sharp increases in PWV occurred several hours prior to heavy rain. These events coincide with warm, moist air convection. Also, sudden decreases are evident with the passing of the storm front. However, this PWV correlation is unable to resolve the vertical structure of the reconstructed atmosphere. Due to this limitation, it is concluded that a 4D GPS tomographic strategy for reconstructing the dynamic and evolution of wet refractivity

is a superior methodology for depicting and monitoring the mesoscale convective processes of severe weather.

8.2. Recommendations and Outlook

The results from this research have demonstrated that ground-based GPS meteorology in the form of PWV estimation and 4D tomographic modelling of wet refractivity have the potential to be valuable additional observation platforms for operational NWP analysis and forecasting. This is especially true in view of severe weather. A number of new research initiatives can be developed in the outlook of this research. These include:

- It is suggested that 1D and 4D ground-based GPS observation platforms be extended with the development of the Australian NPI project to provide a wide-scale national coverage of additional meteorological observations. This will be introduced at almost no further cost, as the CORS networks are currently operational. The New South Wales CORS network and the Victorian GPSnet have currently 130 and 110 operational GPS stations, respectively. This provides good coverage and continuous operability of observations in space and time.
- With the development of next generation GNSS constellations including: GPS, GLONASS, Galileo, Compass, etc., the average number of satellites in view will triple. This will have a profound influence on the accuracy of the GPS tomographic solutions and PWV estimates. It is recommended that research be undertaken to investigate the full benefit of GNSS for meteorological platforms.
- The development of COSMIC 2 will provide continuous additional observations for the platform of multi-observational GPS tomography, potentially producing a higher accuracy, refined coverage and more robust solution. The high accuracy and high vertical resolution of measurements provide much needed information on the vertical structure of wet refractivity. Research should be undertaken in the capabilities of COSMIC 2 and its potential use for creating a more robust GPS tomographic solution.
- Further research should be undertaken to investigate the capabilities of near real-time and real-time methodologies for both 1D and 4D GPS observation platforms in view of assimilation into operational NWP analysis and forecasting models.

Currently, the research collaboration between the SPACE Research Centre, RMIT and the Australian Bureau of Meteorology are in the development stage of assimilating ground-based GPS-derived ZTD estimates from GPSnet into the ACCESS NWP model. The aim is to investigate their effect on analysis and forecasting. For this assimilation to become operational in the ACCESS model, the

methodology of producing ZTD estimates in near real-time and real-time needs to be developed and tested. Future research collaboration should look into the potential benefits of including 4D wet refractivity fields derived from GNSS tomography into the assimilation process of the operational ACCESS NWP modelling, particularly in view of severe weather detection and prediction.

References

Ahrens, D., and P. Samson (2010). Extreme weather and climate. *Brooks/Cole Pub Co*

Alber, C., R. Ware, C. Rocken and J. Braun (2000). Obtaining single path phase delays from GPS double differences. *Geophys. Res. Letters 27*(17), 2661–2664

Anthes, R., D. Ector, D. Hunt, Y. Kuo, C. Rocken, W. Schreiner, S. Sokolovskiy, S. Syndergaard, T. Wee, Z. Zeng, P. Bernhardt, K. Dymond, Y. Chen, H. Liu, K. Manning, W. Randel, K. Trenberth, L. Cucurull, S Healy, S. Ho, C. McCormick, T Meehan, D. Thompson and N. Yen (2008). The COSMIC/FORMOSAT-3 mission: Early results. *B. Am. Meteorol. Soc 89*, 313–333

Bai, Z. (2004). Near-Real-Time GPS Sensing of Atmospheric Water Vapour. PhD thesis. *Queensland University of Technology*

Ball, M. (2011). Australia's Nation Positioning Infrastructure Effort Promises Economic gains. Asian Surveying and Mapping. http://www.asmmag.com/201108181998/australias-national-positioning-infrastructure-effort-promises-economic-gain.html. *Viewed 12/04/2013*

Bender, M., and A. Raabe (2007). Preconditions to ground-based GPS water vapour tomography. *Ann. Geophys 25*(8), 1727–1734

Bender M., G. Dick, J. Wickert, T. Schmidt, S. Song, G. Gendt, M. Ge, and M. Rothacher (2008). Validation of GPS slant delays using water vapour radiometers and weather models. *Meteorologishe Zeitschrift 17*(6), 807–812

Bennitt, G. and A. Jupp (2012). Operational Assimilation of GPS Zenith Total Delay Observations into the Met Office Numerical Weather Prediction Models. *Mon. Wea. Rev 140*, 2706–2719

Bevis, M., S. Businger, T. Herring, C. Rocken, R. Anthes, and R. Ware (1992). GPS Meteorology: Remote Sensing of Atmospheric Water Vapor Using the Global Positioning System. *J. Geophys 97*(15), 787–801

Bevis, M., S. Businger, S. Chiswell, T. Herring, R. Anthes, C. Rocken, and R. Ware (1994). GPS Meteorology: Mapping Zenith Wet Delays onto Precipitable Water. *J. Appl. Meteor 33*, 379–386.

Bi, Y., J. Mao, and C. Li (2006). Preliminary Results of 4-D Water Vapor Tomography in the Troposphere Using GPS. *Adv. Atmos. Sci 23*(4) 551–560

Boniface, K., V. Ducrocq, G. Jaubert, X. Yan, P. Brousseau, F. Masson, C. Champollion, J. Chery and E. Doerflinger (2009). Impact of high-resolution data assimilation of GPS zenith delay on Mediterranean heavy rainfall forecasting. *Ann. Geophys 27*, 2739–2753

Borkowski, A., J. Bosy, and B. Kontny (2002). Meteorological data and determination of heights in local GPS networks–preliminary results. *Electronic Journal of Polish Agricultural Universities*, Geodesy and Cartography

Bosy, J., W. Rohm, A. Borkowski, K. Kroszczynski, M. Figurski (2010). Integration and verification of meteorological observations and NWP model data for the local GNSS tomography. *Atmos. Res. 96*, 522–530

Braun, J., C. Rocken and R. Ware (2001). Validation of line-of-sight water vapor measurements with GPS. *Radio Sci. 36*(3), 459–472

Braun, J., C. Rocken, and J. Liljegren (2003). Comparisons of line-of-sight water vapor observations using the Global Positioning System and a pointing microwave radiometer. *J. Atm. and Oce. Tech. 20*, 606–612

Braun, J. (2004). Remote Sensing of Atmospheric Water Vapor with the Global Positioning System, PhD thesis. *Aero. Eng. Sci.*, University of Colorado

Champollion, C., F. Mason, M. Bouin, A. Walpersdorf, E. Doerflinger, O. Bock, and J. van Baelen (2005). GPS water vapour tomography: preliminary results from the ESCOMPTE field experiment. *Atmos. Res. 74*, 253–274

Choy, S., K. Zhang, C. Wang, Y. Li, and Y. Kuleshov (2011). Remote Sensing of the Earth's Lower Atmosphere during Severe Weather Events using GPS Technology: a Study in Victoria, Australia. *ION GNSS 2011*. Portland, Oregon, USA, 20–23 September.

Crompton, R., and J. McAneney (2008). The cost of natural disasters in Australia: the case for disaster risk reduction. *The Aust. J. Emer. Management 32*(4), 43–46.

Dach, R., U. Hugentobler, and P. Fridez (2007). Bernese GPS Software Version 5.0. *Astronomical Institute*. University of Bern, Bern.

Dach, R., and P. Walser (2013). Bernese GNSS Software Version 5.2. *Astronomical Institute*. University of Bern, Bern.

Department of Environment and Primary Industries (2013). Vicmap Position – GPSnet. http://www.dse.vic.gov.au/property-titles-and-maps/maps-imagery-and-data/data/gpsnet, *viewed 12/04/2013*

Dow, J.M., R. Neilan, and C. Rizos (2009). The International GNSS Service in a changing landscape of Global Navigation Satellite Systems. *J. of Geodesy 83*, 191–198

Essen, L., and K. Froome (1951). The Refractive Indices and Dielectric Constants of Air and its Principal Constituents at 24,000 Mc/s. *In Proceedings of the Society, Section B 60*(10), 862–875

Flores, A. (1999). Atmospheric Tomography Using Satellite Radio Signals. PhD thesis, *Institute d'Estudis Espacials de Catalunya*, Barcelona

Flores, A., G. Ruffini, and G. Rius (2000). 4-D tropospheric tomography using GPS slant wet delays, *Annales Geophysicae 18*, 223–234

Flores, A., J. de Arellano, L. Gradinarsky, and A. Rius (2001). Tomography of the Lower Troposphere Using a Small Dense Network of GPS Receivers. *IEEE Transactions on Geoscience and Remote Sensing 39*(2) 439–447

Fu E., K. Zhang, K Marion, X. Xu, J. Marshall, A. Rea, G. Weymouth, and Y. Kuleshov (2009). Assessing COSMIC GPS radio occultation derived atmospheric parameters using Australian radiosonde network data. *The 6th International Conference on Mining Science & Technology*, Proc. Earth and Planetary Science 1

Fu, E., (2011). An Investigation of GNSS Radio Occultation Atmospheric Sounding Technique for Australian Meteorology. PhD thesis, *Mathematical and Geospatial Sciences*, RMIT University

Foelsche, U. and G. Kirchengast (2001). Tropospheric water vapor imaging by combination of ground-based and spaceborne GNSS sounding data. *Journal of Geophysical Research 106*

Gendt, G., C. Reigber, and G. Dick (2001). Near Real-Time Water Vapor Estimation in a German GPS Network: First Results from the Ground Program of the HGF GASP Project. *Phys. Chem. Earth* 26(6-8) 413–416

Genio, A. and J. Hansen (2001). The Role of Remote Sensing Displays in Earth Climate and Planetary Atmospheric Research. *Interpreting Remote Sensing Imagery: Human Factors.* 207–224

Geoscience Australia (2011). Severe weather basics. http://www.ga.gov.au/hazards/severe-weather/severe-weather-basics/causes.html, *viewed 12/04/2013*

Gradinarsky, L. (2002). Sensing atmospheric water vapor using radio waves. Ph.D thesis, *Chalmers University of Technology*, Technical report No 436

Gradinarsky, L., and P. Jarlemark (2004). Ground-based GPS tomography of water vapour: Analysis of simulated and real data. *J. Meteorol. Soc. Japan 82,* 551–560

Gradinarsky, L., J. Johansson, H. Bouma, H Scherneck, and G. Elgered (2002). Climate monitoring using GPS. *Phys. Chem. Earth 27*, 335–340

Grewal M., and L. Weill (2002). Frontmatter and Index. Global Positioning Systems, Inertial Navigation, and Integration. *John Wiley & Sons* Inc. 1054–1059

Grewal, M., L. Weill amd A. Andrews (2007). Global Positioning Systems, Inertial Navigation and Integration , *Second Edition, John Wiley and Sons* Inc.

Grzeschik, M., F. Zus, H. Bauer, V. Wulfmeyer, J. Wickert, G. Dick and G. Gendt (2006). Assimilation of GPS water vapor observations into the MM5 4D-Var system. *In Proceedings of the 1st MAP D-PHASE Scientific Meeting*, 28–31

Gutman, S., S. Sahm, S. Benjamin, and T. Smith, (2004). GPS Water Vapour Observation Errors. *In 8th Symposium on Integrated Observing and Assimilation Systems for Atmosphere, Oceans, and Land Surface*

Hajj, G., E. Kursinski, L. Romans, W. Bertiger, and S. Leroy (2002). A technical description of atmospheric sounding by GPS occultation. *Journal of Atmospheric and Solar-Terrestrial Physics 64*(4) 451–469

Herring, T. (1992). Modelling atmospheric delays in the analysis of space geodetic data. *Refraction of trans-atmospheric signals in geodesy*, Netherlands Geodetic Commission, 157–164

Ho, S., X. Zhou, Y. Kuo, D. Hunt and J. Wang (2010). Global evaluation of radiosonde water vapor wystematic biases using GPS radio occultation from COSMIC and ECMWF analysis. *Remote Sens. 2*, 1320–1330

Hofmann-Wellenhof, B., H. Lichtenegger, and J. Collins (2001). Global Positioning System: Theory and Practice. Springer.

Houze (Jr) R. (2004). Mesoscale convctive systems. *Reviews of Geophysics 42*

Isaac, V., W. Van Wijngaarden (2012). Surface Water Vapor Pressure and Temperature Trends in North America during 1948–2010. *J. Climate, 25*, 3599–3609

Ishikawa, (2012). Data Assimilation of GPS Precipitable Water Vapor into the JMA Mesoscale Numerical Weather Prediction Model. *Numerical Prediction Division*, Japan Meteorological Agency

Jain, A. (1989). Fundamentals of Digital Image Processing. *Englewood Cliffs*: Prentice-Hall.

Kleijer, F. (2004). Troposphere Modeling and Filtering for Precise GPS Leveling. PhD thesis. *Department of Mathematical Geodesy and Positioning*, University of Technology, Netherlands

Kopken, C. (2001). Validation of Integrated Water Vapor from Numerical Models Using Ground-Based GPS, SSM/I, and Water Vapor Radiometer Measurements. *J. Appl. Meteor. 40*, 1105–1117

Kruse, L. (2001), Spatial and Temporal Distribution of Atmospheric Water Vapor using Space Geodetic Techniques. *GeArbeiten in der Schweiz 62*, Swiss Geodetic Commission

Kuo, Y, S. Sokolovskiy, R. Anthes and F. Vandenberghe (2000). Assimilation of GPS Radio Occultation Data for Numerical Weather Production. *Atmos. Oceanic Sci. 11*(1), 157–186

Kuo, Y., T. Wee, S. Sokolovskiy, C. Rocken, W. Schreiner, D. Hunt and R. Anthes (2004). Inversion and Error Estimation of GPS Radio Occultation Data. J. *Meteor. Soc. Japan, 82*(1B), 507–531

Kursinski, E., G. Hajj, K. Hardy, L. Romans, and J. Schoeld (1995). Observing tropospheric water vapor by radio occultation upositioning system. *Geophys. Res. Lett. 22*(17), 2365–2368

Kursinski, E., G. Hajj, J. Schofield, R. Linfield and K. Hardy (1997). Observing Earth's atmosphere with radio occultation measurements using the Global Positioning System. *J. Geophys. Res. 102*, 23429–23465

Kursinski, E., and G. Hajj (2001). A comparison of water vapor derived from GPS occultations and global weather analyses. *J. Geophys. Res. 106*(D1)

Lambeck, K. (2010). The science of climate change: Questions and answers. *Australian Academy of Science*, Canbarra

Le Marshall J., Y Xiao, R. Norman, K. Zhang, A. Rea, L. Cucurull, R. Seecamp, P. Steinle, K. Puri, and T. Le (2010). The beneficial impact of radio occultation observations on Australian region forecasts. *The Australian Meteorological and Oceanographic Journal 60*, 121–125

Le Marshall, J., Y. Xiao, R. Norman, K. Zhang and P. Steinle (2012). Use of Radio Occultation Observations for Climate Monitoring and Numerical Weather Prediction in the Australian Region. *Australian Meteorological And Oceanographic Journal*

Li, Y., G. Kirchengast, B. Scherllin-Pirscher, S. Wu, M. Schwaerz, J. Fritzer, S. Zhang, B. A. Carter and K. Zhang (2014). A new dynamic approach for statistical optimization of GNSS radio occultation bending angles for optimal climate monitoring utility. *J. Geophysical Res. (in press, accepted 27/10/2013)*

Liou, Y., and C. Huang (2000). GPS observations of PW during the passage of a typhoon. *Earth Planets Space 52*, 709–712

Liu, Y. (2000). Remote Sensing of Atmospheric Water Vapour using GPS Data in the Hong Kong region. PhD thesis. *Department of Land Surveying & Geo-informatics*, The Hong Kong Polytechnic University. Kong Kong

Lutz, S. (2008). High-resolution GPS tomography in view of hydrological hazard assessment. PhD thesis No. 17675. *ETH Zurich*, Switzerland

MacDonald, A., Y. Xie and R. Ware (2002). Diagnosis of Three-Dimensional Water Vapor Using a GPS Network. *Monthly Weather Review 130*, 386–397

McDonald, K. (1999). The Modernization of GPS: Plans, New Capabilities and the Future Relationship to Galileo, *JoGPS 1*(1), 1–17

Manning, T., K. Zhang, W. Rohm, S. Choy, F. Hurter (2012). Detecting Severe Weather using GPS Tomography: An Australian Case Study. *JoGPS 11*(1), 58–70

Manning, T., W. Rohm, K. Zhang, F. Hurter, and C. Wang (2014). Determining the 4D dynamics of wet refractivity using GPS tomography in the Australian region. *IAG Symp*. 139

Masunaga H., T. Iguchi, R. Oki, and M. Kachi (2002). Comparison of Rainfall Products Derived from TRMM Microwave Imager and Precipitation Radar. *J. Appl. Meteor. 41*, 849–862

Matousek, J., and J. Nesetril (1998), Invitation to Descrete Mathematics. *Oxford University Press*

Melbourne, W., E. Davis, C. Duncan, G. A. Hajj, K. Hardy, E. Kursinski, T. Meehan, and L. Young (1994). The application of spaceborne GPS to atmospheric limb sounding and global change monitoring. *Jet Propulsion Laboratory 94*(18)

Mendes, V., and R. Langley (1998). Optimization of tropospheric delay mapping function performance for high-precision geodetic applications. *In Proceedings of DORIS Days*, Toulouse, France

Miloshevich, L., H. Vömel, D. Whiteman, B. Lesht, F. Schmidlin and F. Russo (2006). Absolute accuracy of water vapor measurements from six operational radiosonde types launched during AWEX-G and implications for AIRS validation. *J. Geophys. Res. 111*

Mockler, S. (1995). Water vapour in the climate system: special report. AGU Chapman Conference on Water Vapor in the Climate System. *American Geophysical Union*. 0-87590-865-9

Nakamura, H., and A. Shimpo (2004). Seasonal variations in the Southern Hemisphere storm tracks and jetstreams asrevealed in a reanalysis dataset. *J. Clim. 17*, 1828–1844

National Oceanic and Atmospheric Administration, (1997). Federal meteorological handbook: Rawinsonde and Pibal observations. *Department of Commerce/National Oceanic and Atmospheric Administration*, Washington, 191.

Nicholson N., S. Skone, M. Cannon, G. Lachapelle, and N. Luo (2005). Regional tropospheric tomography based on real-time double difference observables. *Proceedings of ION GNSS 2005*, Long Beach, California, U.S.A. 269–280

Niell, A. (2001). Preliminary Evaluation of Atmospheric Mapping Functions Based on Numerical Weather Models. *Phys. Chem. Earth, 26*(6-8), 475–480

Niell, A. (1996). Global mapping functions for the atmospheric delay at radio wavelengths, *J. Geophys. Res. 101*, 3227–3246

Nilsson, T., and L. Gradinarsky (2006). Water Vapor Tomography Using GPS Phase Observations: Simulation Results. *IEEE Transactions on Geoscience and Remote Sensing 44*(10), 2927–2941

Nilsson, T., L. Gradinarsky and G. Elgered (2004). GPS Tomography Using Phase Observations. *In Geoscience and Remote Sensing Symposium 4*, 2756–2759

Nilsson, T. (2005). Assessment of tomographic methods for estimation of atmospheric water vapor using ground-based GPS. PhD thesis. *Chalmers University of Technology*, Göteborg, Sweden.

Norman, R., J. Le Marshall, B. Carter, C. Wang, S. Gordon and K. Zhang (2012). A new pseudo three-dimensional Segment Method Analytical Ray Tracing (3-D SMART) Technique. *IEEE Transactions on Antennas & Propagation 60*(12), 5818–5824

Norman, R., J. Le Marshall, B. Carter, J. Bennett, S. Wu, S. Zhang, N. Yen and K. Zhang (2013a). Platform technologies for space, atmosphere and climate - A project from the Australian Space Research Program, *International Conference on GPS Radio Occultation*, Taipei, Taiwan

Norman R., J. Le Marshall, K. Zhang, C. Wang, B. Carter, T. Manning , S. Gordon and Y. Li (2013b). Comparing GPS Radio Occultation observations with Radiosonde measurements in the Australian region. *IAG Symposia 139*, Springer-Verlag

Nolet, G. (1987). Waveform tomography, in Seismic Tomography, with Applications in Global Seismology and Exploration Geophysics. 301–322, ed. Nolet, G., Reidel, Dordrecht

Owens, J. (1967). Optical Refractive Index of Air: Dependence on Pressure, Temperature and Composition. *Applied Optics, 6*(1), 51–59

Perler, D. (2011). Water vapour tomography using global navigation satellite systems, PhD thesis No. 20012, *ETH Zurich*, Switzerland

Perler D., A. Geiger, and F. Hurter (2011). 4D GPS water vapor tomography: New parameterized approaches. *J. of Geodesy, 10*.1007/s00190- 011-0454-2

Rankine, W. and E. Bamber (2009). Useful Rules and Tables Relating to Mensuration, Engineering, Structures and Machines, *BiblioBazaar*, LLC

Ray, R. (1999). A Global Ocean Tide Model From TOPEX/POSEIDON Altime- try: *GOT99.2. Technical report*, Goddard Space Flight Center

Remondi, B. (1984). Using the Global Posititioning System (GPS) Phase Observable for Relative Geodesy: Modeling, Processing, and Results. *Noaa reprint*, University of Texas at Austin

Rius, A., G. Runi and L. Cucurull (1997). Improving the vertical resolution of ionospheric tomography with GPS occultations. *Geophys. Res. Lett. 24*(18), 2291–2294

Rocken, C., T. van Hove, J. Johnson, F. Solheim, R. Ware, M. Bevis, T. Chiswell and S. Businger (1995). GPS/STORM: GPS sensing of atmospheric water vapor for meteorology. *J. Atmos. Oceanic Technol. 12*, 468–478

Rocken, C., S. Sokolovskiy, J. Johnson and D. Hunt (2001). Improved Mapping of Tropospheric Delays. *J. Atmos. Oceanic Technol. 18*, 1205–1213

Rocken, C., R. Ware, T. van Hove, F. Solheim, C. Alber, J. Johnson, M. Bevis and S. Businger (1993). Sensing atmospheric water vapor with the Global Positioning System. *Geophys. Res. Lett. 20*(23), 2631–2634

Rocken, C., T. van Hove and R. Ware (1997). Near real-time GPS sensing of atmospheric water vapor. *Geophys. Res. Lett. 24*(24), 3221–3224

Rohm, W., and J. Bosy (2009). Local tomography troposphere model over mountains area. *Atmos. Res. 93*(4), 777–783

Rohm, W., and J. Bosy (2011). The verification of GNSS tropospheric tomography model in a mountainous area. *Adv. in Space Res. 47*, 1721–1730

Rohm, W., K. Zhang and J. Bosy (2013). Unconstrained, robust Kalman filtering for GNSS troposphere tomography. *Atmos. Meas. Tech. Discuss.*, 6, 9133-9162

Rueger, J. (2002). Refractive index formulae for electronic distance measurement with radio and millimetre waves. *School of Surveying and Spatial Information Systems*, University of New South Wales, *Unisurv Rep 68*

Ruffini, G., E. Cardellach, A. Flores, L. Cucurull and A. Rius (1998). Ionospheric calibration of radar altimeters using GPS tomography. *Geophys. Res. Lett. 25*(20), 3771–3774

Saastamoinen, J. (1973). Contributions to the theory of atmospheric refraction. *Bull. Geod. 105*, 279–298

Saastamoinen, J. (1972). Atmospheric correction for troposphere and stratosphere in radio ranging of satellites. In: Henriksen SW, Macini A, Chovitz BH (eds) *The use of artificial satellites for geodesy. Geophysics monograph 15.* American Geophysical Union, Washington D.C, 247–251

Schneider, E., B. Kirtman and R. Lindzen (1999). Tropospheric Water Vapor and Climate Sensitivity. *J. Atmos. Sci., 56*, 1649–1658

Seko, H., S. Shimada, H. Nakamura and T. Kato (2000). Three-dimensional distribution of water vapor estimated from tropospheric delay of GPS data in a mesoscale precipitation system of the baiu front. *Earth Planets Space, 52*, 927–933

Seko, H., H. Nakamura, Y. Shoji and T. Iwabuchi (2004), The Mesoscale Water Vapor Distribution Associated with a Thunderstrom Calculated from a Dense Network of GPS Receivers. *J. Meteor. Soc. Japan, 82*(1B), 569–586

Seko, H., M. Kunii, Y. Shoji and K. Saito (2010). Improvement of Rainfall Forcast by Assimilation of Ground-Based GPS Data and Radio Occultation data. *SOLA 6*, 81–84

Sharma N., D. Jagadheesha, P. Joshi, and P. Pal (2009). Atmospheric stability estimation using radio occultation data over India and surrounding region. *Indian Journal of Radio and Space physics. 38*, 317–325

Shrestha, S. (2003). Investigations into the Estimation of Tropospheric Delay and Wet Refractivity Using GPS Measurements. Master's thesis. *Department of Geomatics Enineering*, University of Calgary, Calgary, Alberta

Skone, S. and V. Hoyle (2005). Troposphere modeling in a regional GPS network. *Journal of Global Positioning Systems*, 4(1-2), 230–239

Smith, (Jr) E. and S. Weintraub (1953). The Constants in the Equation for Atmospheric Refractive Index at Radio Frequencies. *In Proceedings of the Institute of Radio Engineers, volume 41*(8), 1035–1037

Smith, T., S. Benjamin, S. Gutman and S. Sahm (2007). Short-Range Forecast Impact from Assimilation of GPS-IPW Observations into the Rapid Up- date Cycle. *Monthly Weather Review, 135*, 2914–2930

Soden, B., R. Wetherald, G. Stenchikov and A. Robock (2002). Global Cooling After the Eruption of Mount Pinatubo: A Test of Climate Feedback by Water Vapor. *Science, 296*, 727–730

Solomon, S., D. Qin, M. Manning, M. Marquis, K. Averyt, M. Tignor, H (Jr) Miller and Z. Chen (2007). Climate Change 2007: The Physical Science Basis. Contribution of Working Group I to the Fourth Assessment Report of the Intergovernmental Panel on Climate Change. *Cambridge University Press*, Cambridge and New York

Song, D. and A. Grejner-Brzezinska (2009). Remote sensing of atmospheric water vapor variation from GPS measurements during a severe weather event. *Earth Planets Space, 61* (10), 1117–1125

Song, S., W. Zhu, J. Ding and J. Peng (2006). 3D water-vapor tomography with Shanghai GPS network to improve forecasted moisture field. *Chin. Sci. Bull. 51*(5), 607–614

Stull, R. (1999). An Introduction to Boundary Layer Meteorology. *Kluwer Academic Publishers*, Dordrecht. Reprint

Stoer, J. and R. Bulirsch (1980). Introduction to Numerical Analysis. *New York:* Springer-Verlag.

Thayer, G. (1974). An improved equation for the radio refractive index of air. *Radio Science, 9*, 803–807

Tregoning P., R. Boers, and D. O'Brien (1998). Accuracy of absolute precipitable water vapor estimates from GPS observations. *J. of Geophysics. Res. 103*(28), 701−719.

Trenberth, K. (1999). Conceptual framework for changes of extremes of the hydrological cycle with climate change. *Climatic Change 42,* 337–339

Troller, M., B. Burki, M. Cocard, A. Geiger and H. Kahle (2002). 3-D refractivity field from GPS double difference tomography. *Geophys. Res. Lett*.

Troller, M. (2004). GPS based Determination of the Integrated and Spatially Distributed Water Vapor in the Troposphere. *Swiss Geodetic Commission*

Troller M., A. Geiger, E. Brockmann, and H. Kahle (2006). Determination of the spatial and temporal variation of tropospheric water vapour using CGPS networks. *Geophys J Int Vol. 167*(2), 509–520

Van Baelen J., M. Reverdy, F. Tridon, L. Labbouz, G. Dick, M. Bender, and M. Hagen (2011). On the relationship between water vapour field evolution and the life cycle of precipitation systems. *Quarterly Journal of the Royal Meteorological Society 137*, 204–223

Ware R., C. Alber, C. Rocken, and F. Solheim (1997). Sensing integrated water vapor along GPS ray paths. *Geophys. Res. Lett. 24*, 417–420

Ware, R., D. Fulker, S. Stein, D. Anderson, S. Avery, R. Clark, K. Droegemeier, J. Kuettner, J. Minster and S. Sorooshian (2000). A Real-Time National GPS Network for Atmospheric Research and Education. *Bull. Am. Meteorol. Soc. 81*(4), 677–694

Wolfe, D. and S. Gutman (2000). Developing an Operational, Surface-Based, GPS, Water Vapor Observing System for NOAA: Network Design and Results. *J. Atmos. Oceanic Technol., 17,* 426–440

Wickert, J., C. Reigber, G. Beyerle, R. König, C. Marquardt, T. Schmidt, L. Grunwaldt, R. Galas, T. Meehan, W. Melbourne and K. Hocke (2001). Atmosphere sounding by GPS radio occultation: First results from CHAMP. *Geophys. Res. Lett. 28,* 3263–3266

Zhang, K., E. Fu, D. Silcock, Y. Wang and Y. Kuleshov (2011). An investigation of atmospheric temperature profiles in the Australian region using collocated GPS radio occultation and radiosonde data. *Atmospheric measurment techniques, 4*(10) 2087–2092

Zhang K., Wang C.S., Bennett J., Carter B., Norman R. and Wu S. (2013). The Australian Space Research Program Project − Platform Technologies for Space Atmosphere and Climate: Progress and Preliminary Results, *IAG Symposia 139*, Springer-Verlag, 19–25

List of Tables

List of Figures

APPENDIX A

The following figures present the GPS tomographic time series from 5 Mar 2010 15:00 to 6 Mar 2010 12:00 (UTC) of the horizontal gradient distribution of wet refractivity every hour. Gradient solutions for height layer's: 578m, 1614m and 5780m, respectively are presented. The Melbourne radar image intensity is overlaid to identify relative path and intensity of the convective storm system.

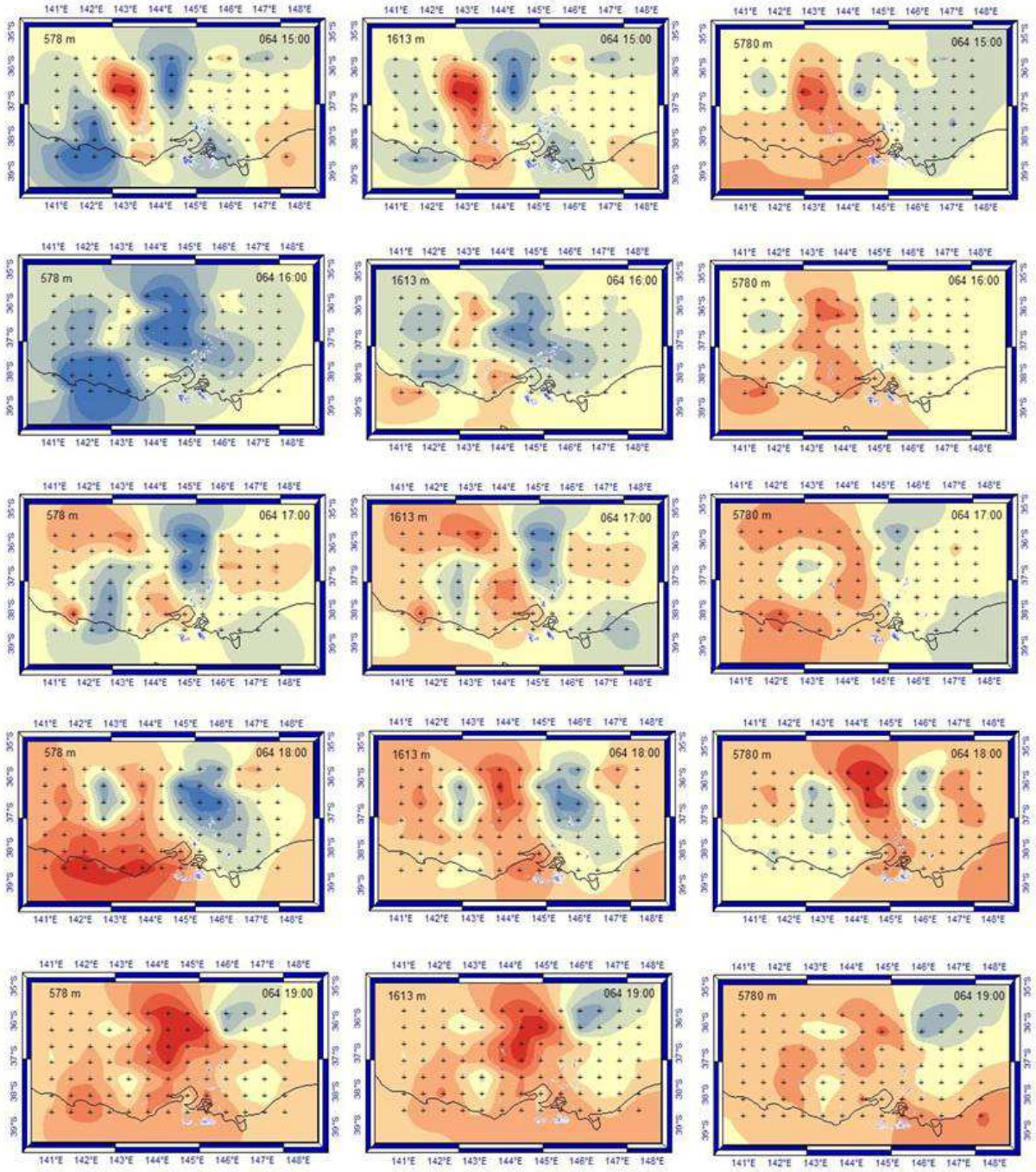

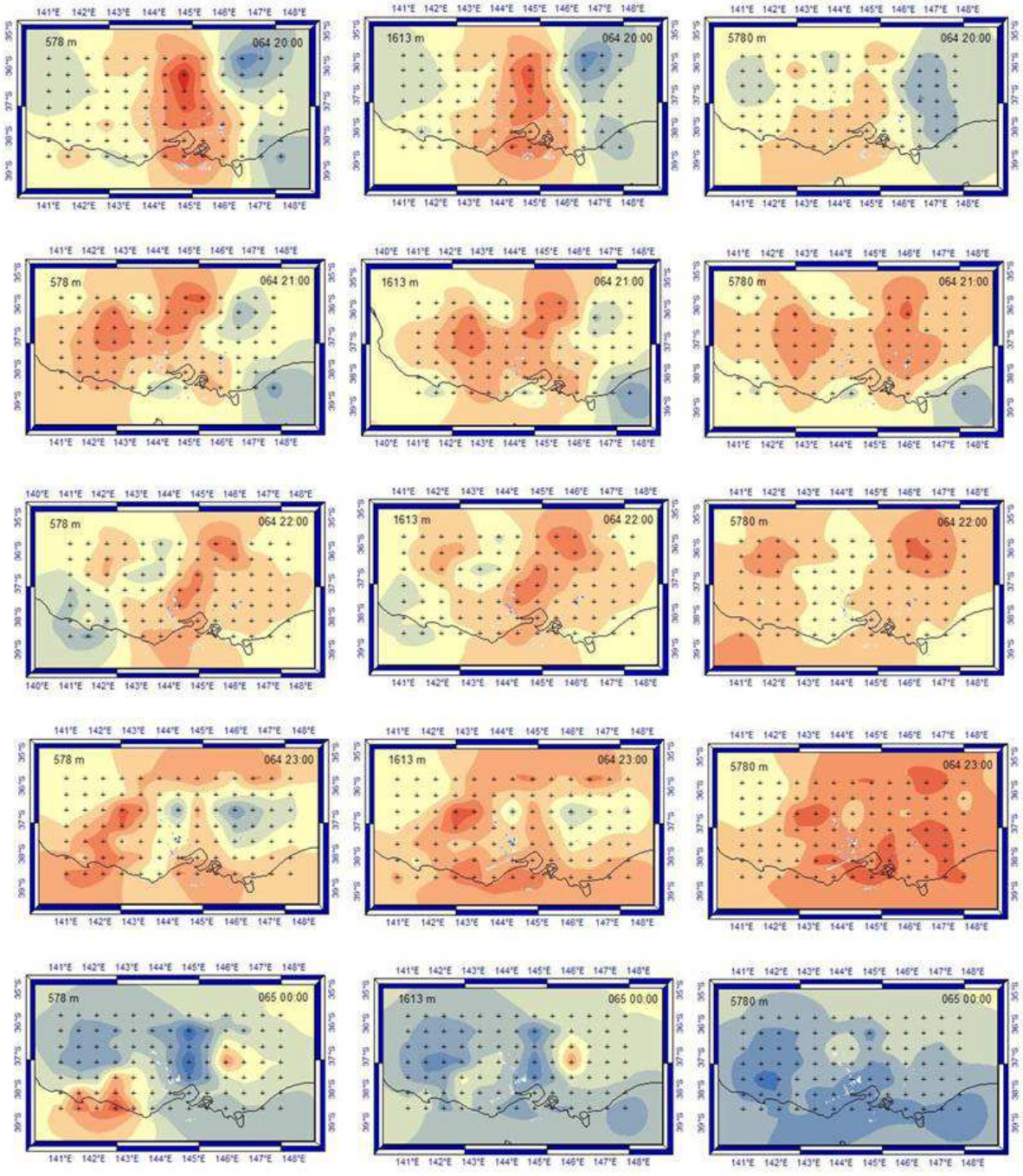
578 m
064 20:00
1613 m
064 20:00
5780 m
064 20:00
578 m
064 21:00
1613 m
064 21:00
5780 m
064 21:00
578 m
064 22:00
1613 m
064 22:00
5780 m
064 22:00
578 m
064 23:00
1613 m
064 23:00
5780 m
064 23:00
578 m
065 00:00
1613 m
065 00:00
5780 m
065 00:00
Radar image intensity
Light
Moderate
Heavy
Tomographic N_{wet} gradient
-10
0
10
Wet Refractivity gradient (ppm)

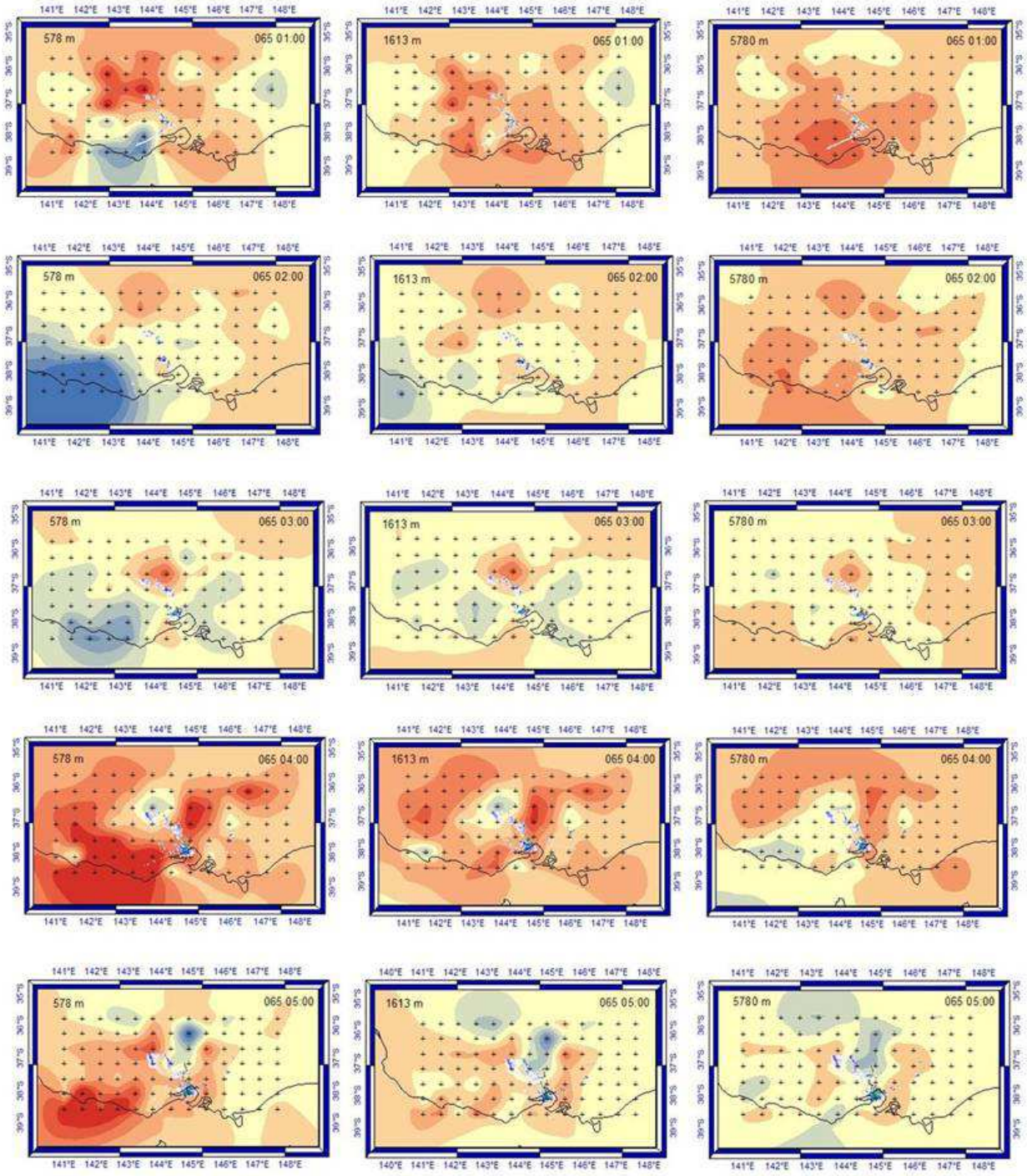
578 m
065 01:00
1613 m
065 01:00
5780 m
065 01:00
578 m
065 02:00
1613 m
065 02:00
5780 m
065 02:00
578 m
065 03:00
1613 m
065 03:00
5780 m
065 03:00
578 m
065 04:00
1613 m
065 04:00
5780 m
065 04:00
578 m
065 05:00
1613 m
065 05:00
5780 m
065 05:00
Radar image intensity
Light
Moderate
Heavy
Tomographic N_{wet} gradient
-10
0
10
Wet Refractivity gradient (ppm)

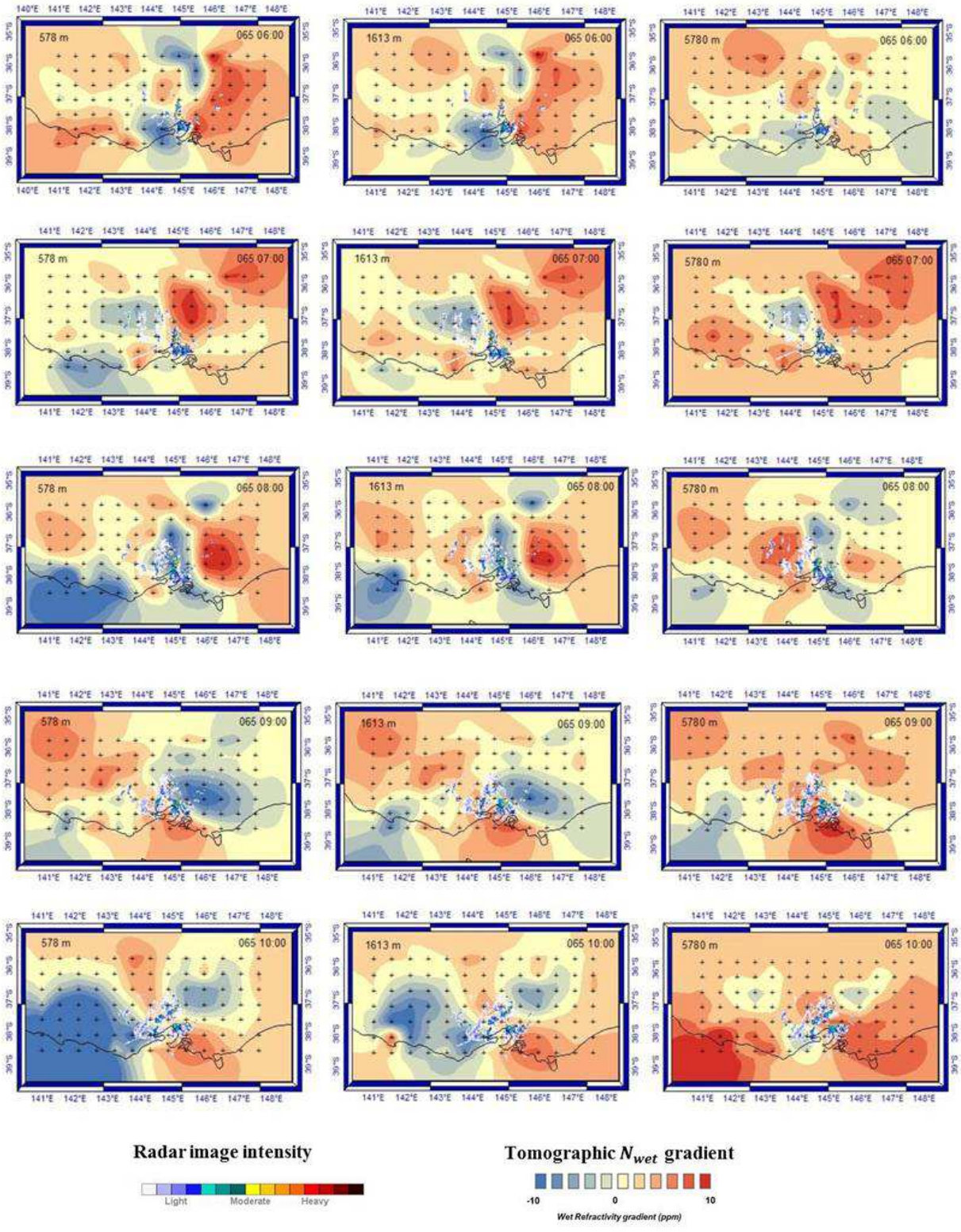
578 m
065 06:00
1613 m
065 06:00
5780 m
065 06:00
578 m
065 07:00
1613 m
065 07:00
5780 m
065 07:00
578 m
065 08:00
1613 m
065 08:00
5780 m
065 08:00
578 m
065 09:00
1613 m
065 09:00
5780 m
065 09:00
578 m
065 10:00
1613 m
065 10:00
5780 m
065 10:00
Radar image intensity
Light
Moderate
Heavy
Tomographic N_{wet} gradient
-10
0
10
Wet Refractivity gradient (ppm)

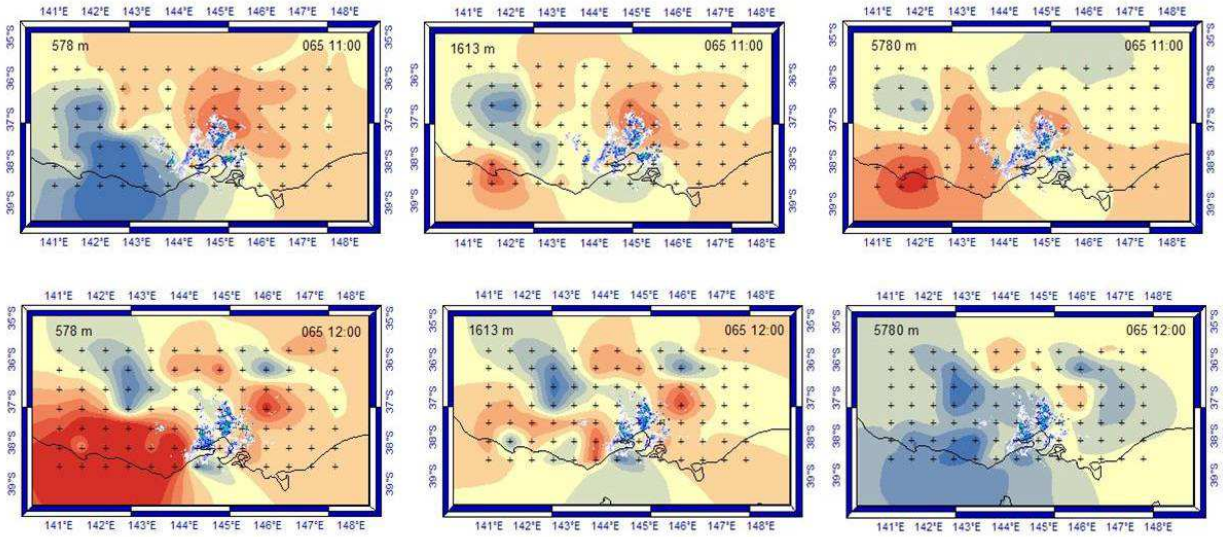

Radar image intensity

Tomographic N_{wet} gradient